2013

N-DOPED MULTIWALLED CARBON NANOTUBES: FUNCTIONALIZATION, CHARACTERIZATION AND APPLICATION IN LI ION BATTERIES

Aman Preet Kaur
University of Kentucky, apkaur2@g.uky.edu

STUDENT AGREEMENT:

I represent that my thesis or dissertation and abstract are my original work. Proper attribution has been given to all outside sources. I understand that I am solely responsible for obtaining any needed copyright permissions. I have obtained and attached hereto needed written permission statements(s) from the owner(s) of each third-party copyrighted matter to be included in my work, allowing electronic distribution (if such use is not permitted by the fair use doctrine).

I hereby grant to The University of Kentucky and its agents the non-exclusive license to archive and make accessible my work in whole or in part in all forms of media, now or hereafter known. I agree that the document mentioned above may be made available immediately for worldwide access unless a preapproved embargo applies.

I retain all other ownership rights to the copyright of my work. I also retain the right to use in future works (such as articles or books) all or part of my work. I understand that I am free to register the copyright to my work.

REVIEW, APPROVAL AND ACCEPTANCE

The document mentioned above has been reviewed and accepted by the student's advisor, on behalf of the advisory committee, and by the Director of Graduate Studies (DGS), on behalf of the program; we verify that this is the final, approved version of the student's dissertation including all changes required by the advisory committee. The undersigned agree to abide by the statements above.

Aman Preet Kaur, Student

Dr. Mark S. Meier, Major Professor

Dr. John E. Anthony, Director of Graduate Studies

N-DOPED MULTIWALLED CARBON NANOTUBES: FUNCTIONALIZATION, CHARACTERIZATION AND APPLICATION IN LI ION BATTERIES

DISSERTATION

A dissertation submitted in partial fulfillment of the
requirement for the degree of Doctor of Philosophy in the
College of Arts and Science
at the University of Kentucky

By
Aman Preet Kaur
Lexington, Kentucky

Director: Dr. Mark S. Meier, Professor of Department of Chemistry
Lexington, Kentucky

2013

ABSTRACT OF DISSERTATION

N-DOPED MULTIWALLED CARBON NANOTUBES: FUNCTIONALIZATION, CHARACTERIZATION AND APPLICATION IN LI-ION BATTERIES

The focus of this dissertation is to utilize chemical functionalization as a probe to investigate the reactivity of N-doped multiwalled carbon nanotubes (N-MWCNTs). The surface of N-MWCNTs, being a set of potentially reactive graphene edges, provides a large number of reactive sites for chemical modification, so considerable changes in chemical and physical properties can be envisaged. We observed that both reduction (dissolving metal reduction/alkylation) and oxidation (H_2SO_4/HNO_3 and $H_2SO_4/KMnO_4$ mixtures) of N-MWCNTs lead to formation of interesting spiral channels and spiraled carbon nanoribbons. A variety of techniques, including TGA, SEM, TEM, XRD and surface area measurements were used to analyze these new textural changes. We have developed methods to demonstrate that specific chemistry has occurred on these new structures. To this end, we introduced metal-binding ligands that could be used as probes in imaging and spectroscopic techniques including TEM, STEM, EDX, and EELS. A proposal for the underlying structure of N-MWCNTs responsible for the formation of the new textures is presented. We have investigated the performance of our materials as potential negative electrodes for rechargeable lithium ion batteries.

Keywords: *N-MWCNTs, chemical functionalization, spiral channels, spiraled carbon nanoribbons, lithium ion batteries.*

Aman Preet Kaur

05/03/2013

N-DOPED MULTIWALLED CARBON NANOTUBES: FUNCTIONALIZATION, CHARACTERIZATION AND APPLICATION IN LI-ION BATTERIES

By

Aman Preet Kaur

Dr. Mark S. Meier

Director of Dissertation

Dr. John E. Anthony

Director of Graduate Studies

05/03/2013

Date

Dedicated to my grandparents and parents

ACKNOWLEDGEMENTS

At the outset I would like to express my deepest gratitude to Manindar Kaur (mam) and Virendra Singh (sir) who motivated me to pursue Ph.D. studies. I am indebted to the efforts they have put in setting up research as my career path. I am thankful to them to provide me with love and strength at all times in my life. I would like to dedicate this dissertation to my late grandparents and my mom (Nirmal Kaur Dhillon) and dad (S. H. S. Dhillon). Their unconditional love and affection provided me the strength to accept all the challenges in my life. I would like to express my love to my brother (Simranjit Dhillon) and cousin (Navneep Sandhu) with whom I shared all my joys and sorrows. I sincerely thank my relatives who always kept me in their prayers especially, my aunt (massi).

I would like to express my deepest acknowledgement to my advisor, Dr. Mark S. Meier, who continuously guided and supported me throughout my Ph.D. career. He provided me useful and critical suggestions whenever I approached him. He introduced me to various inter-disciplinary research projects as part of my Ph.D. He gave me the freedom to try and explore new ideas. He always motivated me to think independently and develop as a researcher. I am thankful to Dr. Rodney Andrews for giving me ideas and suggestions during our scientific meetings. I am also thankful to him for allowing me to use the instruments of his lab and other facilities at CAER. Thank you Dr. Andrews to serve as the external examiner during my final defense. I would like to thank Dr. John Selegue for sparing time to meet with me whenever I requested and giving his useful insights into the projects I was working on. I would like to thank Dr. Mark Watson for giving his critical comments and suggestions as he came across my work. I cannot forget the moral support and confidence he gave me, as I was standing nervous just before my oral qualifying exam. Many thanks to Dr. Selegue, Dr. Watson, Dr. Janet Lumpp and Dr. Leonidas Bachas for serving on my advisory committee.

My special thanks to Dr. Y. T. Cheng at Department of Chemical and Materials Engineering for the wonderful collaboration that we had along with his student Dr. J.C. Li. Dr. YT is a wonderful person to talk to and we had very interesting meetings related to work on Li-ion batteries. I would like to thank JC for introducing me to energy storage research. I am very thankful for another collaboration, involving work

on Lignin deconstruction, with Dr. Mark Crocker at CAER. I wish to thank Dr. Dali Qian for synthesizing nanotubes for all my projects and for TEM analyses of my samples. I thank John Craddock for annealing the tubes.

I would like to thank Department of Chemistry, Department of Chemical and Materials Engineering and CAER at UK for allowing me to use the facilities as and when I required.

I want to thank all my past and present group members for maintaining healthy work environment in the lab. During this Ph.D. journey, I have made many friends, both related and unrelated to work. I would like to extend sincere thanks to all my friends who have made this part of my life special. I will always cherish the moments that I spent with my friends (a long list of names). Many thanks to Rituraj and Mahendra who participated and made our research discussions fun and productive. Many thanks and love to my cute little friends (Shubhu, Gugdu and Dominick) for the fun time we had. I thank God for giving me a good friend, Subrahmanyam, who stood by me at all times, encouraging and motivating me throughout my graduate career. I thank Almighty for the choicest blessings He showered and the opportunities He gave me to shape myself.

TABLE OF CONTENTS

LIST OF FIGURES

LIST OF TABLES

LIST OF SCHEMES

Chapter 1

Introduction

1.1. Carbon nanotubes

Carbon nanotubes (CNTs), a form of filamentous carbon, have presented unparalleled potential for use as advanced materials since their discovery[1-3]. This potential can be attributed to the inherent combination of extraordinary structural, mechanical, electrical, and thermal properties[4-7]. The physico-chemical properties of CNTs can be altered by reactions on the outer CNT walls, and these alterations also impact the basic electronic structure, potentially expanding the possibilities for application of CNTs as nanoelectronic devices[6], catalyst support materials[8] and nanocomposites[9]. A large number of publications and patents have been produced in this quickly expanding field[6, 10].

CNTs can be either a single layer of graphene rolled to form a cylinder and forming a singlewalled carbon nanotube (SWCNT), or multiple concentric cylinders forming a multiwalled carbon nanotube (MWCNT). Different morphologies of MWCNTs can be produced, depending on the conditions and the method chosen for synthesis[11]. These morphologies include:

a) hollow tube: the axis of graphene plane is parallel to tube axis;
b) herringbone: the axis of graphene plane is formed at an angle to tube axis; and
c) bamboo: similar to herringbone except that the nanotube is periodically closed along the length, forming compartments as in bamboo or in stack of paper cups.

hollow tube MWCNTs | herringbone MWCNTs | bamboo or stacked cup MWCNTs

Figure 1-1 Representation of different morphologies of MWCNTs[11].

An ideal hollow (cylindrical) nanotube will have no edges, except at one open end of the tube. The surface becomes more graphitic and less curved than SWCNTs, and thus should have reactivity similar to that of graphite. In the latter two cases, the axis of graphene plane is at an angle to the tube axis. As a result, the graphene sheets must terminate at the surface of the nanotube, giving rise to a large number of edge/plane-like defect sites along the surface of the tube[11].

Considerable research has explored the effect of changes in the local electron density in these materials by doping them with various atoms and/or ions, including Co, P, K, Si, N, B, S and O[12-17]. Doping is the process of intentionally introducing impurities into a pure material to enhance its desired property. In layered sp^2 carbon nanosystems, it is possible to tailor the electronic, structural and mechanical properties by introducing non-carbon atoms in different manners at small concentrations (from parts per million to small weight percentages)[18]. There are three main ways of doping carbon: intercalation, encapsulation and substitutional doping.

These doping procedures generally involve one of the following processes: drawing low-melting-point liquid metals into nanotube cores through capillary forces (encapsulation); intercalation of metals (Ag, Co) into nanotube bundles; and incorporation of atoms (B, N, Si, S) directly into graphene layers of nanotubes (substitutional doping) during the nanotube synthesis process. Among these, boron and nitrogen atoms are most conveniently used as dopants, since they have atomic sizes similar to that of carbon- a property that provides them a strong probability of entering into the carbon lattice.

1.2. N-doped multiwalled carbon nanotubes (N-MWCNTs)

The substitutional doping with nitrogen has received attention because significant changes in mechanical properties, electrical conductivity, and chemical reactivity have been predicted[19-22] and experimentally observed[11, 22-24]. When electron-rich nitrogen substitutes for carbon in a graphitic layer, the band gap of the CNTs is reduced, leading to metallic CNTs[25]. In general, doping with nitrogen produces a

texture which is reportedly known as “bamboo or stacked cup” type MWCNTs[26-31] and hence facilitates in ease of chemical functionalization[32].

Methods to prepare N-MWCNTs include magnetron sputtering[33], laser ablation[34], pyrolysis of mixtures of organometallic and nitrogen-containing organic compounds[35], chemical vapor deposition (CVD) of nitrogen-containing hydrocarbons over heterogeneous catalysts like Fe, Co or Ni[36], and controlled rapid detonation of common carbon-containing explosives like *m*-dinitrobenzene and picric acid[37]. However, not all stacked cup MWCNT structures involve nitrogen. Saito *et al.* first observed bamboo shaped CNTs in the products from arc discharge evaporation of Ni-loaded graphite[38]. The relative ease of CVD methods allow their use in the large scale production of CNTs[39]. The nitrogen-containing precursors used in CVD MWCNT synthesis include ammonia[40], pyridine[41], melamine[42], triazine[43], acetonitrile[44], dimethyl formamide[45], metal phthalocyanines[46], and zinc cyanamide[27].

The amount and type of nitrogen incorporated into CNTs strongly depends on the synthesis conditions, particularly the precursor, catalyst, reaction temperature and gas flow. N-MWCNTs produced at the University of Kentucky Center for Applied Energy Research (CAER) are made by a catalytic CVD method as developed by Andrews *et al.*[41]. The following steps towards the synthesis are proposed (Figure 1-2):

a) C/N clusters adsorb on the conical catalyst particle;
b) diffusion of the adsorbed carbon atoms through the catalyst to form a graphene cup;
c) the cup lifts off the catalyst by graphene layer slipping due to high stress. The graphene shell then elongates to form the tube wall;
d) second and third cups form and lift off to form bridges in the core;
e) continuous formation and lifting of graphene cups to thicken the tube wall with bridges in the core.

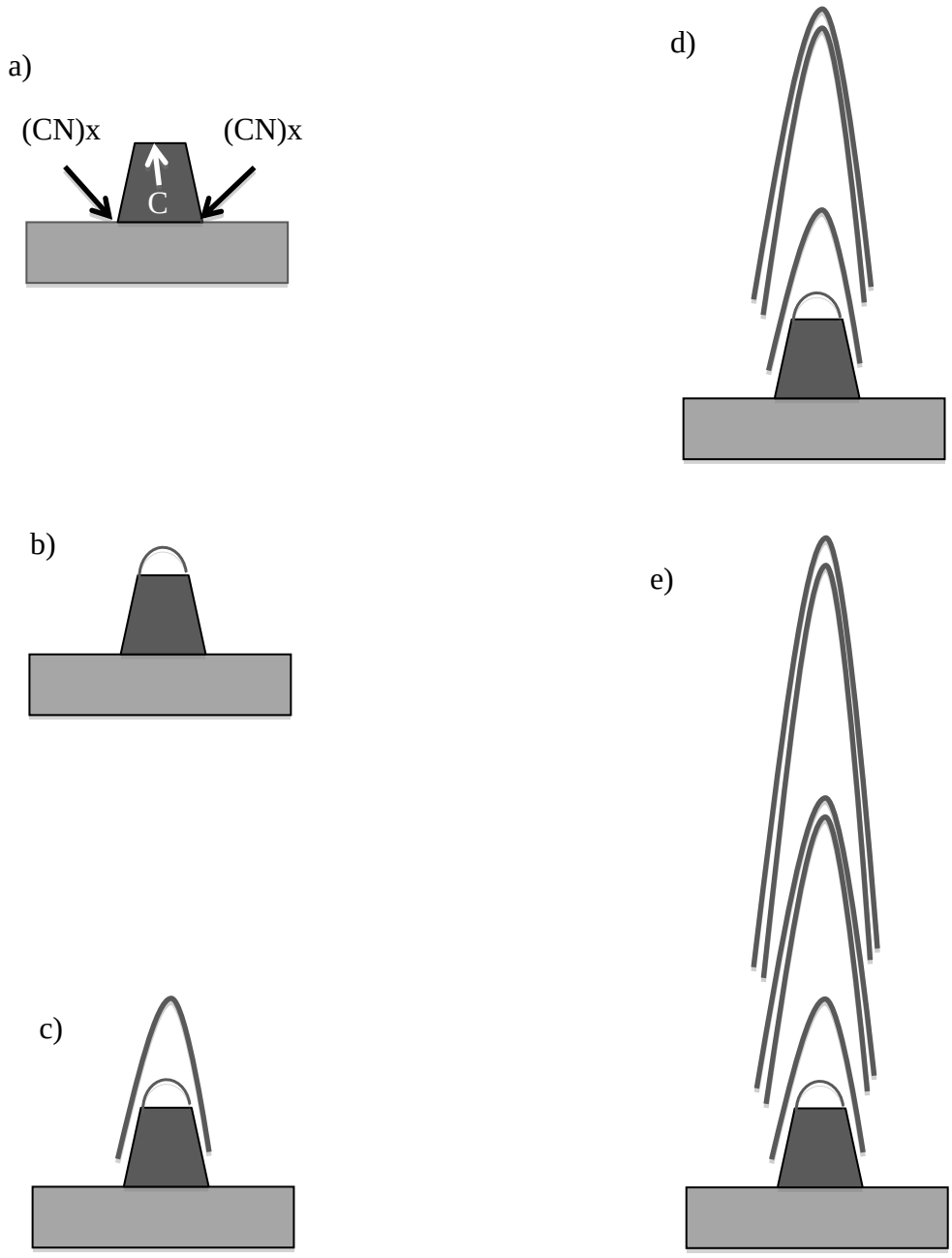

Figure 1-2 Illustration of catalyzed root growth of N-MWCNTs during CVD.

The type of metal catalyst and the reaction temperature determine the rate of diffusion of carbon through the catalyst. Reports on the fate of carbon atom in the catalyst deal with the solubility of carbon in transition metals connected to phase diagrams of Fe_3C[47], Co_2C[48] and Ni_3C[49]. Bitter *et al.*[50] studied how the morphology of N-MWCNTs is affected by varying the C/N precursor (acetonitrile, pyridine, dimethylformamide), the growth catalyst (Fe, Co, Ni) and the reaction temperature

(823-1123 K). They found that N/C ratio of the N-MWCNTs decreased with increasing temperature for all C/N sources and growth catalysts used. Also, Co and Ni catalysts produced cylindrical MWCNTs, while Fe catalyst gave stacked cup type. This difference in morphology was attributed to the difference in the thermodynamic stability of metal carbides. Although considerable research has been done on the physical properties of N-MWCNTs, the chemical reactivity is relatively unexplored.

1.3. Chemical functionalization of CNTs

Considerable efforts have been devoted to the chemical modification of CNTs, as their use in a range of potential applications is hindered due to agglomeration caused by strong inter-tube van der Waals forces. Functionalization of CNTs involves the generation of chemical moieties on their surface that can improve the dispersability and processibility, which might pave the way to many useful applications, including composite preparations[51]. Thus far, covalent and non-covalent functionalizations have been widely investigated approaches to modify these materials. Covalent functionalization encompasses many techniques, including carboxylation[52], amidation[53], thiolation[54], halogenations[55], hydrogenation[53], addition of free radicals[53], cycloadditions[56] and the Diels-Alder reaction[53].

Hence, CNTs can be functionalized using the rich chemistry of carbon[57]. The chemical reactivity is likely to be highest at sites of high curvature, as well as at defect sites[58, 59]. Typical defects, including kinks, bends, and partial or complete breaks in carbon shells, are more reactive than regions of perfect graphene[59].

1.4. Characterization of CNTs

Traditional analytical methods used for characterization of small molecules, such as NMR, IR, MS, are not viable for characterizing the products of chemical reactions on these materials. This is because the products and starting materials are insoluble, highly conductive, strongly absorb light across a broad region of the electromagnetic spectrum, and are poorly dispersible in most solvents and polymer matrices.

In the literature, commonly used methods[60] for the characterization of CNTs include thermal analysis, Raman spectroscopy, X-ray diffraction (XRD) and surface area analysis. All of these are used to analyze bulk material. Surface modification is usually studied with X-ray photoelectron spectroscopy (XPS)[61] which has a very

small penetration length. Electron microscopy[62] techniques like scanning electron microscopy (SEM), transmission electron microscopy (TEM) and scanning transmission electron microscopy (STEM) are used for analysis of individual tubes for information about the texture. Reflectance IR[63] has also been used to characterize chemically functionalized MWCNTs, but this method has proven problematic in our hands. Solid state NMR[64] has only rarely been used. This method, however, has a great deal of promise.

1.5. Applications

N-MWCNTs have received much attention due to enhanced conductivity compared to their undoped counterparts and hence have been suggested to be suitable for applications in nanoelectronics[65]. Some reports deal with the catalytic potential[66] of N-MWCNTs and their use as negative electrodes in lithium ion batteries[67]. N-MWCNTs can also be used as gas sensors[68].

1.6. Scope and outline of the thesis

Although there are many reports of chemical modification of SWCNTs and MWCNTs, N-MWCNTs are much less investigated. The texture of these materials is repeatedly referred to as "bamboo or stacked cup structure". In this arrangement the axis of graphene planes are at an angle to the tube axis, hence there are many graphene edges that could be available for reactions. The aim of this thesis is to investigate chemical reactivity of N-MWCNTs produced at CAER and to develop techniques that demonstrate that new chemistry has occurred on the specific structural target.

In **chapter 2**, the focus is on chemical modification of N-MWCNTs using three different approaches and characterization of the chemistry with available analytical techniques. Observed trends with different oxidizing agents with respect to extent of oxidation will be discussed.

The formation of interesting spiral channeled N-MWCNTs and spiraled carbon nanoribbons upon modifications under specific reaction conditions will be addressed in **chapter 3.** The ribbons are formed over a wide range of reaction conditions and

their formation is independent of the source of nitrogen in CVD method. Discussion of techniques used to unfurl these structures further will also be presented.

Chapter 4 deals with discussion of models reported for stacked cup type materials. A proposal on our view of structure of our material will be presented with experiments leading to such proposal.

Chapter 5 includes the application of starting and functionalized N-MWCNTs as negative electrodes for Li ion batteries. Four materials will be discussed. Effect of microstructure and texture of these on Li storage capacity will also be discussed.

I will conclude my thesis with summary (broader impacts and future directions) of my research.

Chapter 2

Chemical functionalization of N-MWCNTs[†‡]

2.1. Overview

There are many reasons that make researchers interested in investigating ways to attach chemical functionalities to the walls or ends of CNTs. These chemical bonds might be used to tailor the interaction of the nanotube with other entities, such as a solvent, a polymer matrix, or other nanotubes. The chemically functionalized CNTs might have properties that are different from the unfunctionalized CNTs and thus might be used for various applications. The challenge is to find a way to reproducibly and reliably chemically alter CNTs which, like graphite, are fairly unreactive. The characterization of chemically altered CNTs is another challenge, limited by the available resources for use to answer some important structural questions.

In the work described here, different reaction conditions are studied to see the effects of various reagents, oxidizing and reducing in particular, on the texture of N-MWCNTs. Various microscopic and spectroscopic characterizations are utilized to study these changes. An important outcome here was the development of a novel technique to characterize *sites of reactivity* on functionalized N-MWCNTs. We also discovered a hitherto unknown "form" of filamentous carbon - spiraled carbon nanoribbons.

2.2. Introduction

With appropriate surface modifications of CNTs, the properties of CNTs can be harnessed in a variety of applications[69, 70]. Thus far, covalent and non-covalent functionalizations[71] have been widely investigated approaches to modify carbon materials. Chemical reactions, such as electrophilic aromatic substitution, oxidation and reduction, that are known to functionalize the aromatic systems, can be used to covalently functionalize CNTs. In N-MWCNTs, the graphene planes are not parallel

[†] Part of this chapter is taken from our manuscript; Kaur, A.; Meier, M. S.; Andrews, R.; Qian, D. Discontinuous spiraled carbon nanoribbons resulting from coiling of thin graphite subunits formed during oxidation of N-doped multiwalled carbon nanotubes (Carbon, in Press).

[‡] XPS analysis: courtesy Dr. Doo Young Kim.

to the tube axis, thus the surface is a set of edges. In the reported 'bamboo or stacked cups' arrangement[27-31] there are many graphene edges which could be available for reaction in comparison to the true tubular arrangement where graphene edges are only available at defect sites. This feature led us to investigate their chemistry.

Classical dissolving metal reduction, followed by protonation or alkylation, of aromatic systems is well documented and offers means of introducing different functional groups. Similar reactions have been reported on carbon materials[57]. Our group is using dissolving metal reduction followed by alkylation for covalent functionalization[72, 73], a method which has proved to be a reliable, reproducible method for modifying CNTs[57]. This reaction is an example of uniform functionalization of CNTs as we assume that this n-fold reduction creates carbon anion of charge n^- leaving CNTs separated in reaction mixture due to electrostatic repulsion. Presumably this approach can modify the tubes not only at defect sites but also on more graphitic surfaces.

Other common method for modification of CNTs is chemical oxidation[74], and this approach provides dual advantages of purification of the raw material as well as improving the dispersibility of CNTs. The chemical literature includes several reports on methods[75, 76] and the effects[77-79] of oxidation of SWCNTs and MWCNTs under both acidic and basic conditions. Commonly used methods include treating CNTs with HNO_3,[80, 81] mixtures of H_2O_2/H_2SO_4 (piranha solution)[75], H_2SO_4/HNO_3,[79, 82] and NH_4OH/H_2O_2,[76] $KMnO_4$,[83, 84] O_3[85] and others.

Dissolving metal reductions of N-MWCNTs that were carried out in our group (Dr. Kelby Cassity), lead to the formation of linear deep cuts/channels within the walls of nanotubes[72]. The resulting channels reach all the way from the outer surface to the core, and are microns in length. My goal was to further explore this channeling reaction and to:

a) develop methods for functionalizing the new graphene edges that are formed in the course of the channeling reaction;

b) develop methods to demonstrate that desired chemistry has occurred on the specific structural target; and

c) investigate reactions other than dissolving metal reduction that may also result in channeling to gain some mechanistic insight.

2.3. Results and discussion

N-MWCNTs are produced at CAER from a pyridine feedstock containing dissolved ferrocene as catalyst at a temperature of 800 °C using N_2 as the carrier gas[41]. We refer to these as as-produced N-MWCNTs (as-prod-N-MWCNTs). Also, this CVD synthesis enables to prepare a range of nanotube structures with varying diameter, length and morphology by changes in synthesis temperature, feedstocks, and other parameters (including carrier gas, reactor furnace type, etc). Figure 2-1 shows the SEM, STEM and TEM of the as-prod-N-MWCNTs. The conical white (SEM) or black (STEM and TEM) particles are the catalyst (Fe) particles. These look different than carbon based on the principle of Z-contrast and look bright or dark depending on whether the technique involves bright field or dark field imaging. The texture of these tubes is likely a function of these catalyst particles generated during the CVD process.

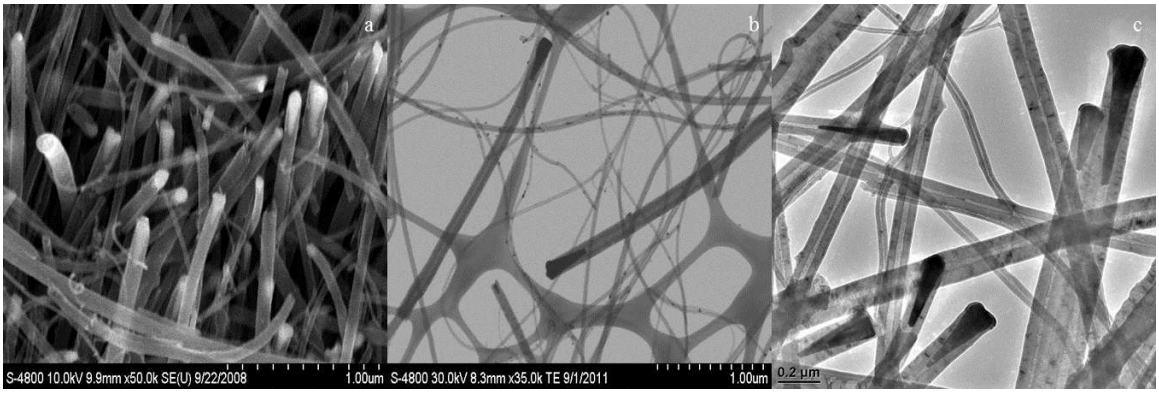

Figure 2-1 As-prod-N-MWCNTs (a) SEM; (b) STEM and (c) TEM with conical catalyst particles.

HRTEM image (Figure 2-2) suggests that there are many edges at the surface available for reaction. So, in principle both electrophilic aromatic substitution and addition reactions should work on these edges. From previous studies in our group,

based on quantitative EELS analysis, the average N concentration is high (~ 8 at.%) at the core position, dropping to less than 3 at.% at the mid-wall with almost no N detected in the outer layers[41]. Thus, we can predict that the presence of nitrogen in these nanotubes will probably not have profound effects on the reactivity of the exposed outer edges of these stacked aromatic systems.

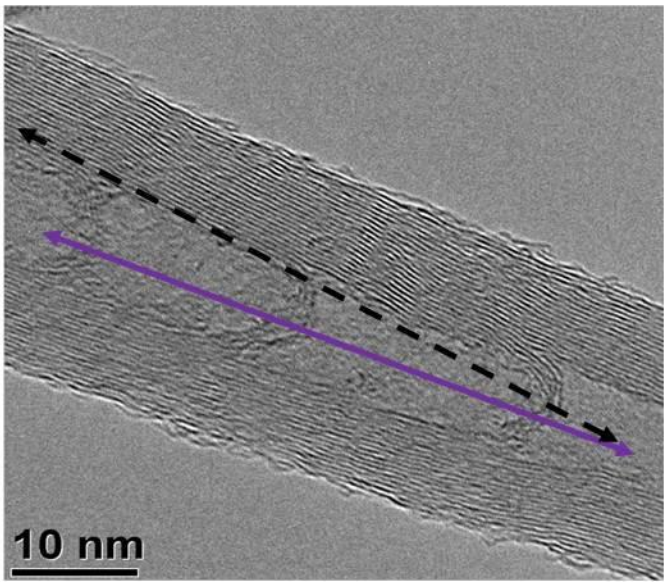

Figure 2-2 HRTEM image of as-prod-N-MWCNTs.

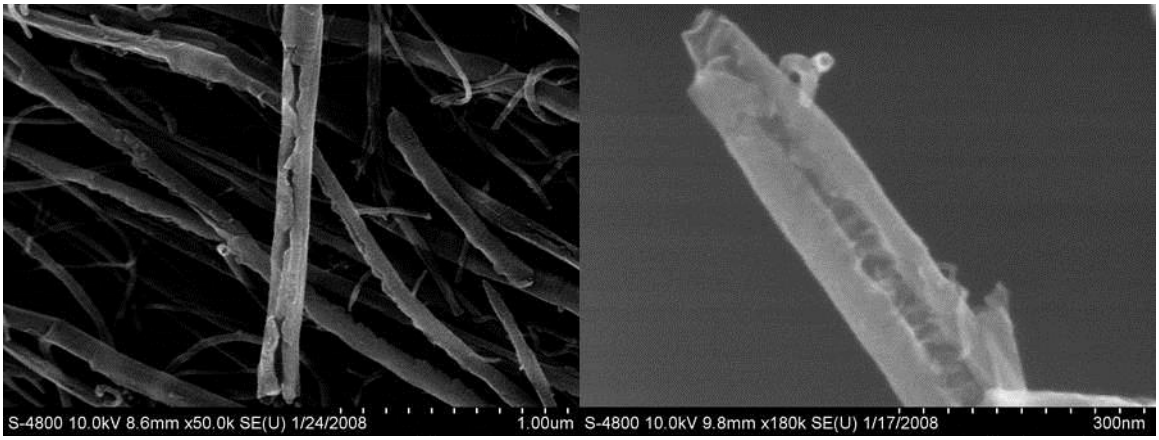

Figure 2-3 SEM images of channels on reduced/alkylated as-prod-N-MWCNTs.

The project started with the investigation of the reactivity of the graphene edges formed in the channels in the course of dissolving metal reduction, as now these edges are available for chemical functionalization, along with those existing before reaction, for chemical functionalization. Figure 2-3 represents SEM of the channeled tubes[72].

In some cases, the channel is quite parallel to the axis of tube, but in other cases the channel gently curves around the nanotube.

We started with the question: Is it possible to functionalize the surface while still maintaining the textural integrity of N-MWCNTs? If yes, then can channels be formed afterwards? We wanted to find a functionalization that can occur without forming channels and another leading to channels during the dissolving metal reduction process. The real challenge was to make N-MWCNTs with functionality inside the channel different from the functionality on the surface.

The first attempt was to functionalize the surface of the as-prod-N-MWCNTs with Friedel-Crafts acylation[86] to completely exploit all the edges and defect sites on the surface. Then the acylated N-MWCNTs were to be reduced in ammonia to form channels and to introduce a new functionality in those channels. When as-prod-N-MWCNTs were benzoylated under Friedel-Crafts conditions (Scheme 2-1) using nitrobenzene as a solvent, the benzoylated N-MWCNTs (2-1) so formed show no evidence of any channels (Figure 2-4(a)). When these benzoylated N-MWCNTs (2-1) are reduced in Li/ammonia followed by alkylation with ethyl bromoacetate, the tubes (2-8) show the presence of channels as seen in SEM (Figure 2-4(b)).

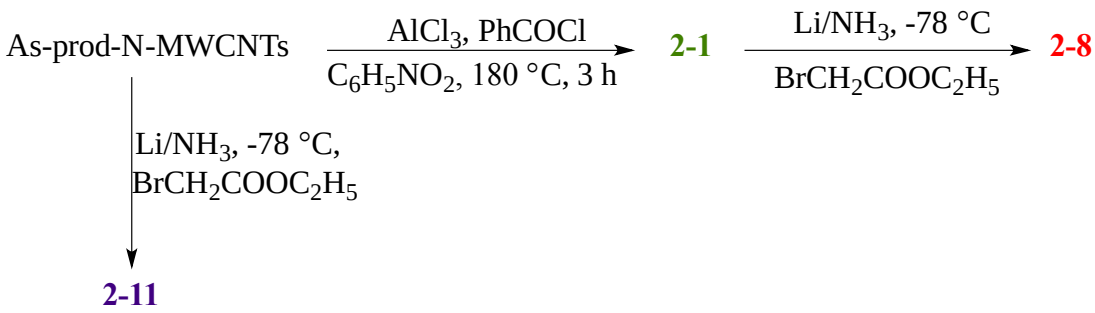

Scheme 2-1 Reaction of as-prod-N-MWCNTs under Friedel-Craft acylation (2-1) and dissolving metal reduction (2-8 and 2-11) conditions.

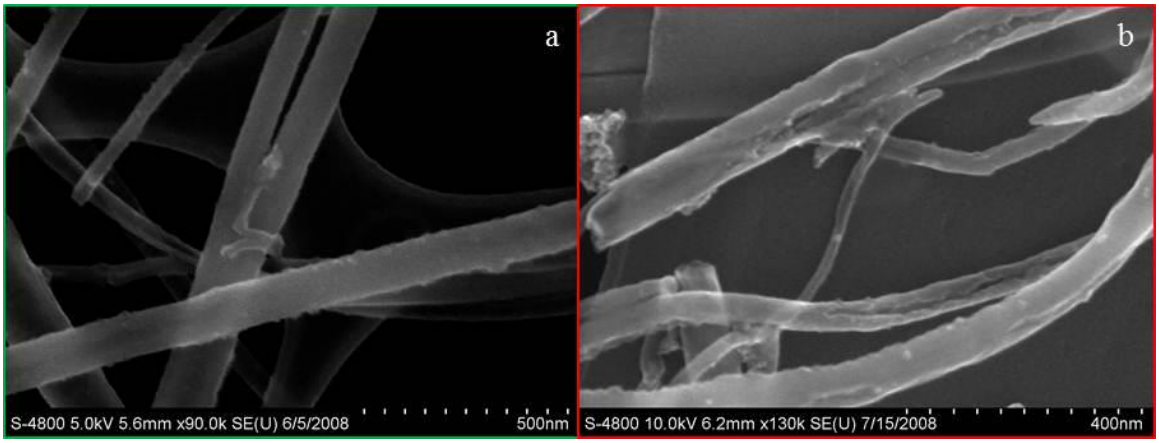

Figure 2-4 SEM images of (a) Benzoylated as-prod-N-MWCNTs and (b) Benzoylated as-prod-N-MWCNTs reduced/alkylated (ethyl bromoacetate).

The products of scheme 2-1 were characterized by thermogravimetric analysis (TGA). TGA is an analytical technique used to determine thermal stability of a material. When carried out in an oxidizing atmosphere (air rather than N_2), the onset temperature of oxidation (T) and the temperature of the maximum rate of oxidation (T_o) can reflect the oxidative stability of a material[59]. Plotting the derivative of the weight vs. temperature curve reveals T_o. The shift of T to the right (to higher temperatures) in benzoylated N-MWCNTs (green curve, Figure 2-5) suggests they have higher resistance to oxidation than the starting as-prod-N-MWCNTs (black curve, Figure 2-5). If we think that our chemistry had worked the way we wanted it to be, then benzoylated N-MWCNTs (2-1) would end up having electron deficient benzene rings (linked to –C=O) on the surface that might be responsible for their resistance to oxidation. Also, the amount of residue is lowered compared to the starting as-prod-N-MWCNTs. Residual iron has a catalytic role in oxidative thermal degradation (Figure 2-30), which might also be responsible for the increased resistance to oxidation in benzoylated N-MWCNTs. The amount of residue in esterified benzoylated sample (red curve, Figure 2-5) was lowered as both the reactions involve acids in the work-up that react with Fe catalyst present in the as-produced tubes.

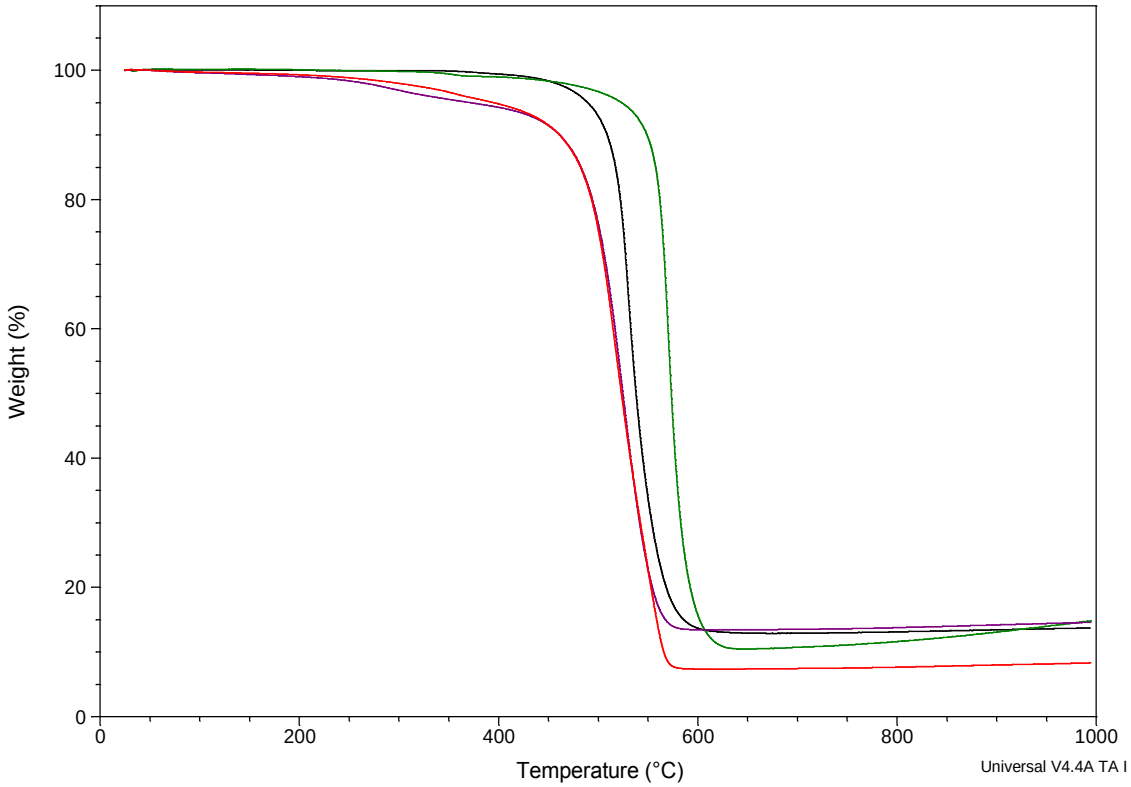

Figure 2-5 TGA plot comparing as-prod-N-MWCNTs (black) with various products from scheme 1.

But, when the as-prod-N-MWCNTs were subjected to only dissolving metal reduction conditions using ethyl bromoacetate as the alkylating agent, the product (2-11, purple curve, Figure 2-5) just lay on top of the reduced benzoylated product (2-8, red curve, Figure 2-5) in TGA. The similar TGA plots of two different products (2-8 and 2-11) implies either the Friedel-Craft acylation was not working in the first step, or the benzoylated product was not stable under reduction conditions in the second step.

We thought of first hydrogenating as-prod-N-MWCNTs under dissolving metal reduction conditions using ammonium chloride as a proton source. Now these hydrogenated N-MWCNTs (2-5) have more –C-H sites (we expected to see an easy substitution of –C-H sites similar to that in fullerenes) to be substituted by the acyl group in the Friedel-Crafts step. The solvent was also varied from nitrobenzene to carbon disulfide, but many questions remained unanswered about the extent of functionalization via Friedel-Crafts acylation after TGA measurements. So we thought of using only dissolving metal reduction for functionalization.

A bigger challenge was to find a technique to characterize the chemistry we desired to do. Designing a chemical transformation to bind metals to the functionalized N-MWCNTs was the next goal to prove the functionalization using imaging as a characterization tool. The scheme used was the following.

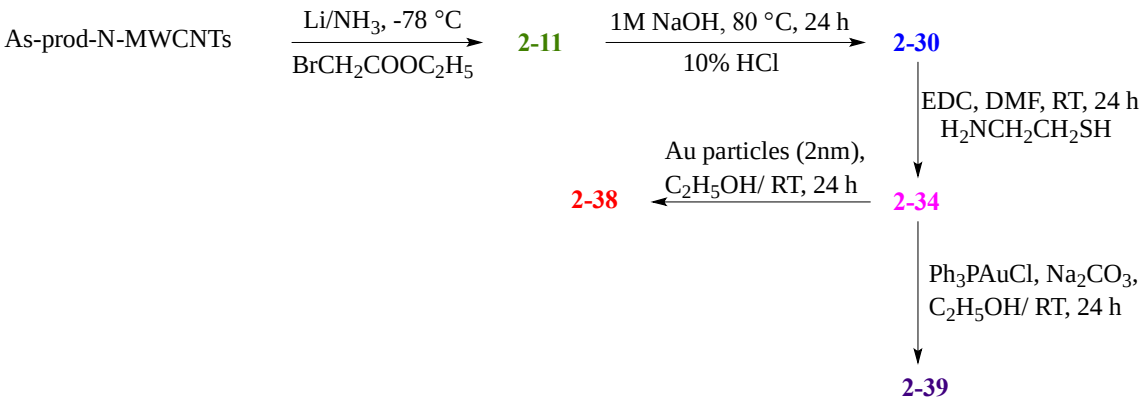

Scheme 2-2 Reaction sequence for binding metals on thiol functionalized as-prod-N-MWCNTs.

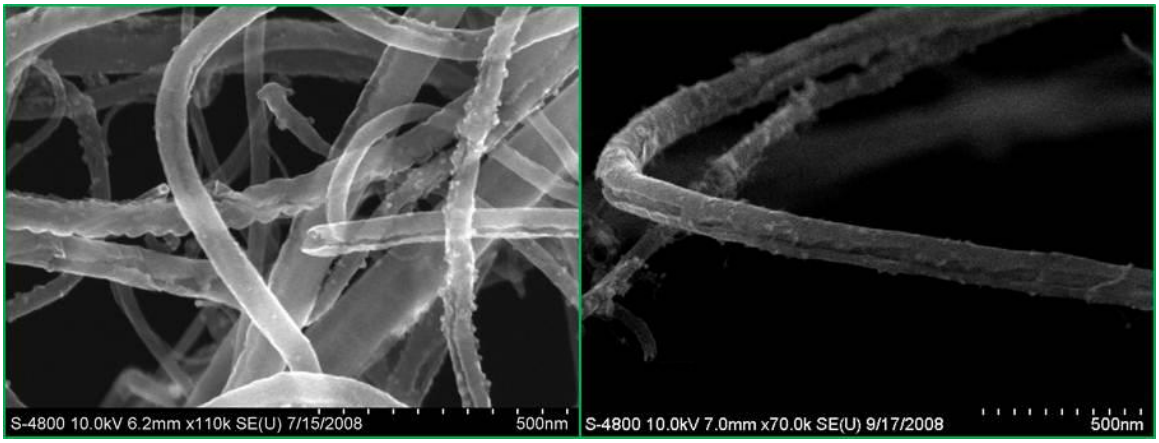

Figure 2-6 SEM images of as-prod-N-MWCNTs reduced with ethylbromoacetate in ammonia (2-11).

As-prod-N-MWCNTs were esterified (2-11) using ethyl bromoacetate as the alkylating agent and then saponified (2-30) to carboxylic acid under basic hydrolysis conditions. Acid functionalized N-MWCNTs (2-30) were then coupled (2-34) in the presence of EDC with cysteamine, that has thiol functionality at the end, which can then be bound to metals like gold and platinum.

The SEM images of the esterified as-prod-N-MWCNTs (Figure 2-6) clearly show the presence of channels. The STEM images (Figure 2-7) of the products resulting from complexation reaction with Au nanoparticles (2-38) and the Au complex (2-39), failed to conclusively prove that the observed black spots were metal particles or were they due to pre-existing materials (like amorphous carbon) on the as-prod-N-MWCNTs. So, we resorted to annealing of the as-prod-N-MWCNTs as a means of removing adhered material and eliminating this ambiguity.

Figure 2-7 STEM images of (a) as-prod-N-MWCNTs and products of complexation reaction; (b) 2-38 and (c) 2-39 of scheme 2-2.

As-prod-N-MWCNTs were subjected to high temperature treatment at 2800 °C, which results in removal of amorphous carbon, most structural defects, residual catalyst particles and nitrogen. This produces a more graphitic material, although not necessarily following the Bernal stacking; we refer to the resulting tubes as G-N-MWCNTs[87]. Figure 2-8 compares the STEM images as-prod-NMCNTs (Figure 2-8(a)) and G-N-MWCNTs (Figure 2-8(b)) and suggests that G-N-MWCNTs are largely free from other forms of carbon and catalyst.

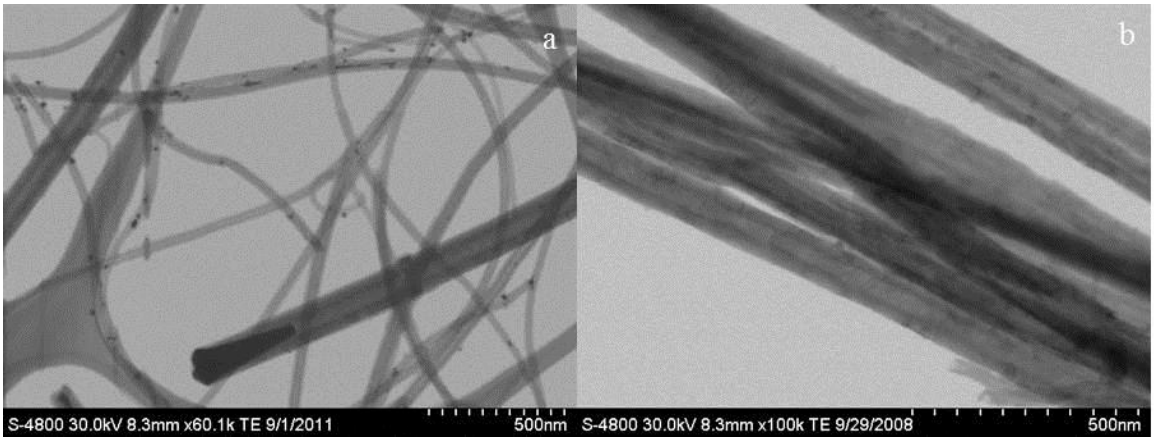

Figure 2-8 STEM images of (a) as-prod-N-MWCNTs (b) G-N-MWCNTs.

G-N-MWCNTs were then treated following two reaction schemes (2-3 and 2-4) to obtain desired functionalization to bind metals.

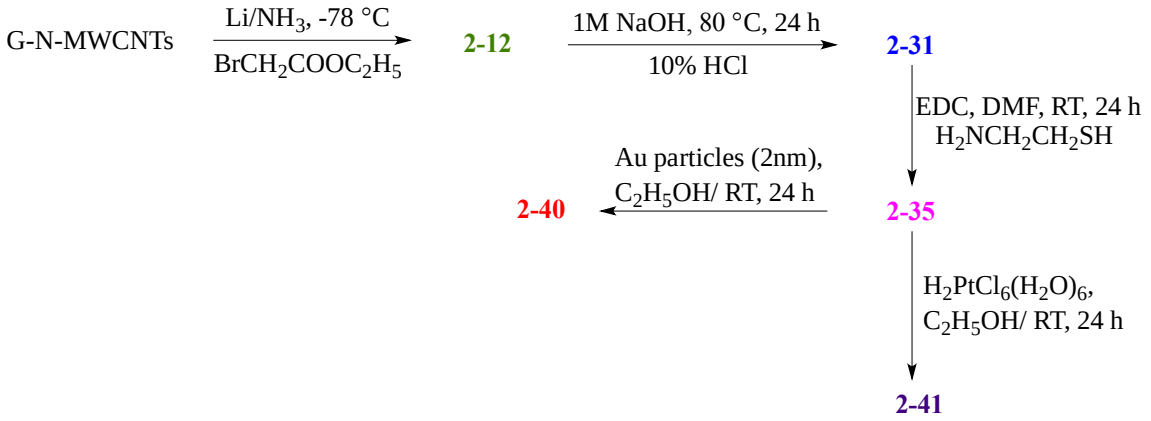

Scheme 2-3 Reaction sequence to bind metals all over (surface and channels) G-N-MWCNTs.

In **scheme 2-3** G-N-MWCNTs were first alkylated with ethyl bromoacetate (2-12), which were then base hydrolyzed to form acid G-N-MWCNTs (2-31). Acid G-N-MWCNTs were then coupled with an amine in presence of EDC to form an amide (2-35) that has thiol functionality at the end which can then be complexed with Au nanoparticles (2 nm) (2-40) and hexachloroplatinate complex (2-41). G-N-MWCNTs will be channeled in the first step of the scheme 2-3 (2-12). After the complexation reaction, all the edges, present on the surface as well as of the channels, should be decorated with these metals, i.e. should have metals at reactive sites all over the surface and also in the channels.

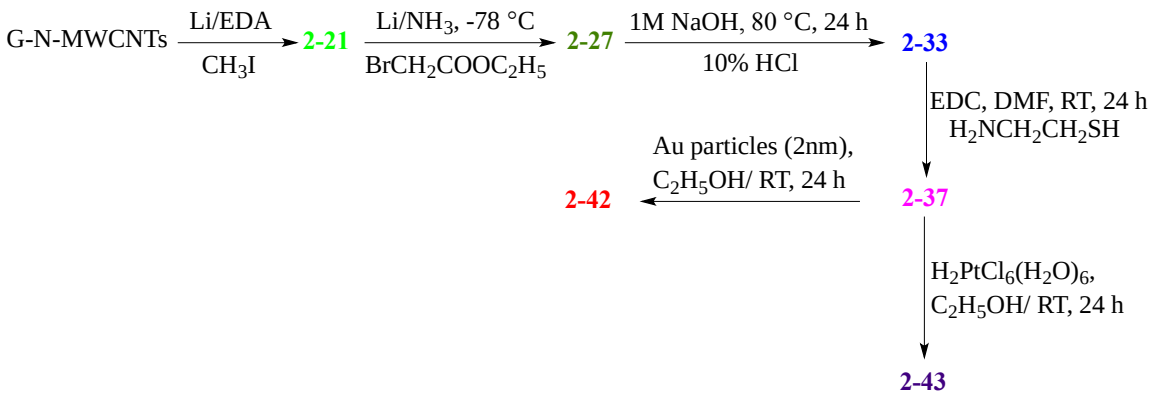

Scheme 2-4 Reaction sequence to bind metals on channeled G-N-MWCNTs.

In **scheme 2-4,** G-N-MWCNTs were first methylated (2-21) in ethylenediamine (EDA) under dissolving metal reduction conditions. As N-MWCNTs do not channel in EDA (already proven by Dr. Kelby Cassity), it was thought that methyl groups would cap all the surface edges. Further following scheme 2-4 on the methylated product, should decorate the channels with metals and not the surface. We were still unable to observe metals in STEM, which led us to question if G-N-MWCNTs really had the required thiol functionality to bind metals, i.e. whether or not the desired chemistry (described in schemes 2-3 and 2-4) was working. This question was examined by elemental analysis for sulphur using electron energy loss spectroscopy (EELS).

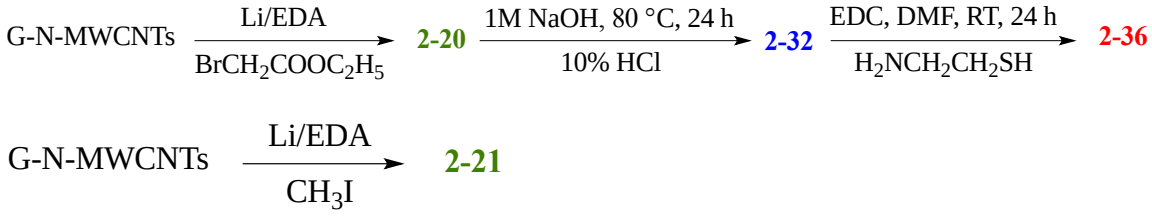

Scheme 2-5 Synthesis of compounds for EELS analysis.

EELS is based on the principle that when electron beam impinges on a sample, a portion of the electrons is inelastically scattered with corresponding energy loss. Differences in the energy lost distinguish elements in the sample. EELS is used for the analysis of light elements like C, N, O etc. The products (2-36 and 2-21) from scheme 2-5 were used for analysis.

The putative amide N-MWCNTs (2-36) didn't show the presence of nitrogen and sulfur in EELS, but oxygen (20 at.%) was present in considerable amount. This lead us to think that the multistep reaction (synthesizing an ester first and then converting it to acid and then to amide) may not be that efficient in these materials and that the amide forming step is not working at all, that there is considerable amount of oxygen already present in the starting material (G-N-MWCNTs), or that the reaction conditions and workup (H_2O used for quenching and washing to remove Li salts) is resulting in increased amount of oxygen.

To narrow these possibilities methylated N-MWCNTs (2-21) were synthesized under same conditions (Li/EDA). Both G-N-MWCNTs and methylated N-MWCNTs (2-21) showed almost zero percent of oxygen in EELS analysis. So, there was no problem with the starting material and the reaction conditions as well as the work-up conditions. These results suggest that multistep synthesis was not working for our material. So, we thought of synthesizing thiol-containing ligands first and then using them in reduction to have functionalization to bind Au nanoparticles.

In the meantime we ran out of stock of the starting material. The material used so far was produced in a large, continuous reactor while the newer material was produced in a 4-inch diameter tube reactor but under same conditions. *All the experiments from this point till the end of my research are performed on this new material synthesized in a 4-inch diameter tube reactor*. The material showed subtle differences in morphology (Figure 2-9 (a) like fewer cup bottoms and larger diameters (80-150 nm) compared to the old as-prod- material. As-prod-N-MWCNTs were then subjected to high temperature treatment at 2800 °C to anneal them (G-N-MWCNTs). Figure 2-9(b) shows the morphology of G-N-MWCNTs as obtained by HRTEM. These have a texture with the appearance of stacked cups and periodically bridged central cores surrounded by a thick outer wall. The observation of very few layers in cup bottoms as compared to outer wall suggests that these tubes may not be a true stack of cups.

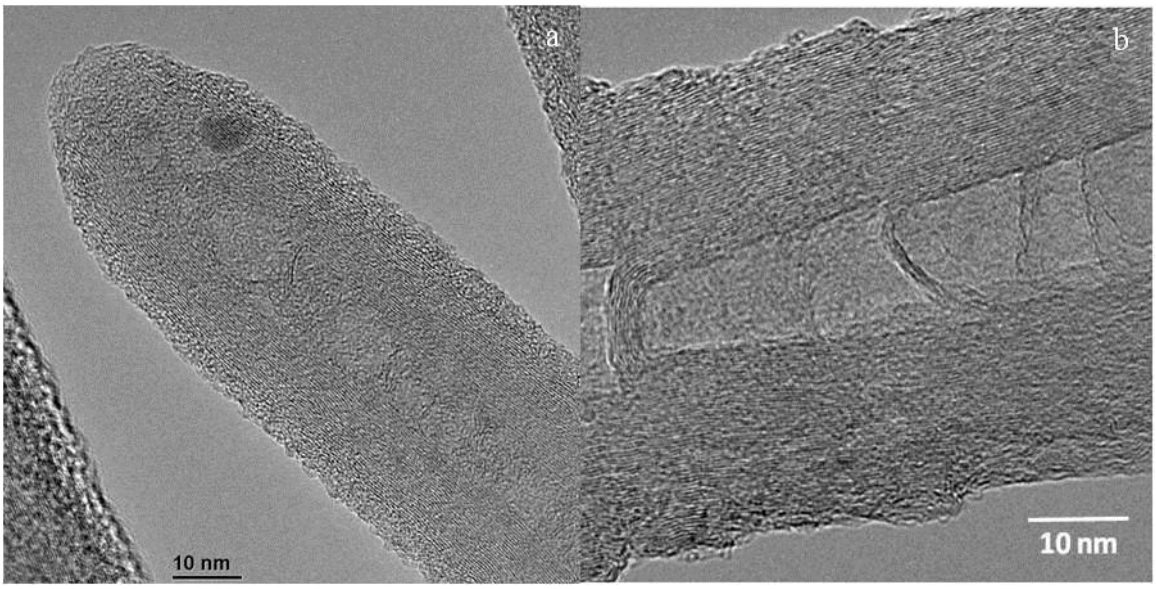

Figure 2-9 TEM images of (a) as-prod-N-MWCNTs produced in 4-inch reactor and (b) corresponding G-N-MWCNTs.

Figure 2-10(a) represents TGA plot comparing oxidative stability of as-prod-N-MWCNTs (black curve) and G-N-MWCNTs (red curve). The TGA plot shows zero residue, as all of the residual Fe catalyst is removed and an increase in the thermal stability of material, reflecting low defect density and more perfect structure[59].

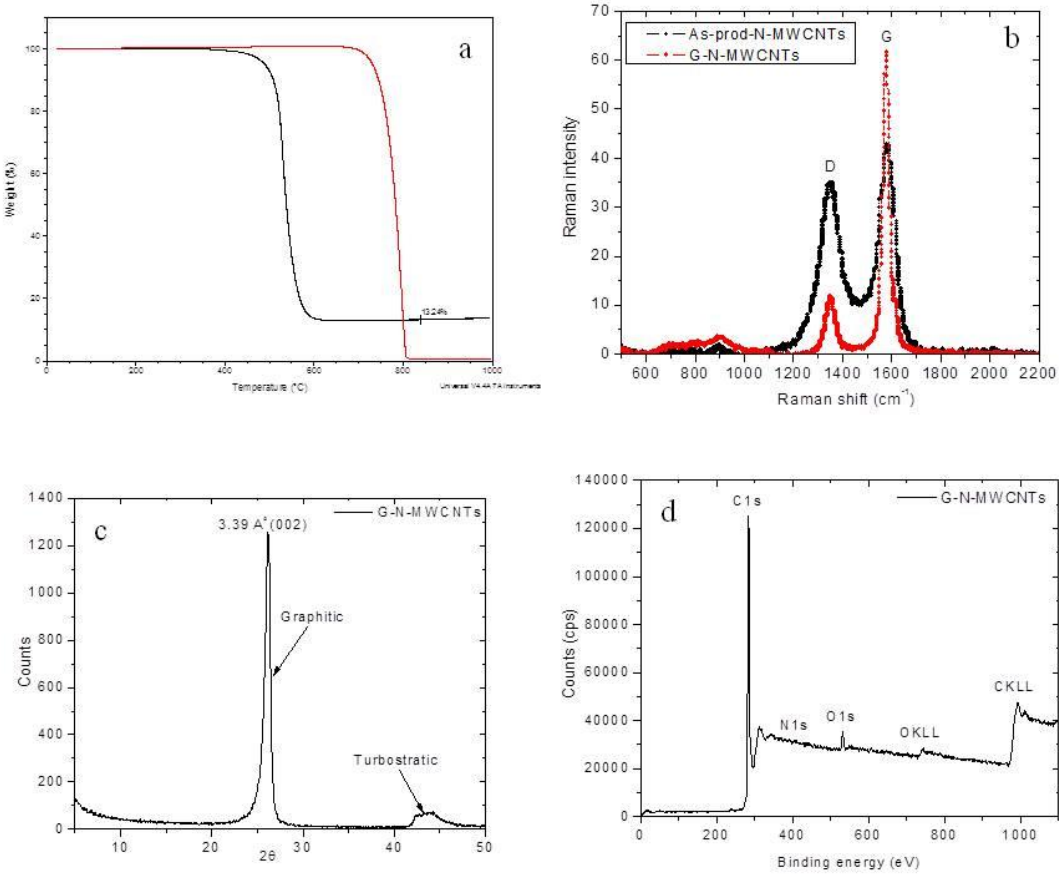

Figure 2-10 (a) TGA plots; (b) Raman spectra comparing as-prod-N-MWCNTs and G-N-MWCNTs; (c) XRD and (d) XPS of G-N-MWCNTs.

The degree of order of the graphitic layers within G-N-MWCNTs was examined using Raman spectroscopy, as shown in Figure 2-10(b). As reported, the I_D/I_G ratio describes degree of disorder in carbonaceous material[88]. The D band is ascribed to disordered carbon, edge defects, and other defects (sp^3 bonded carbon, dangling bonds, vacancies, and topological defects) while the G band indicates ordered sp^2 carbon. Before annealing, the CNTs mainly consist of disordered carbon and the ratio of intensities of the D-band to the G-band (I_D/I_G) is 0.82. After annealing, the ratio of

intensities decreased to 0.2, clearly indicating that high-temperature annealing reduces the defect density, producing more perfect graphitic structure[59].

The XRD pattern of G-N-MWCNTs is shown in Figure 2-10(c). The sharp peak at a 2θ value of 26.2˚ indicates that the average interlayer spacing is 3.39Å, in a good agreement with crystalline graphite (3.35 Å)[89]. The broad asymmetric peak around 43˚ indicates a small amount of turbostratic structure in G-N-MWCNTs[90]. The XPS spectrum (Figure 2-10(d)) demonstrates that after annealing the material is nearly pure carbon with ~3% oxygen and virtually no nitrogen.

Now, we wanted to achieve our goal of functionalization and characterization using metals, with this new material. To demonstrate that the chemistry has occurred on the specific structural targets, we designed a chemical transformation at the reduction step of synthesis. We introduced ligands that could bind metals, and could later be used as probes in imaging technique to prove desired functionalization. The recipe followed here involved synthesizing thiol-containing ligands (Scheme 2-6) to use in the reduction/alkylation step and then binding 2 nm Au particles to the thiol groups. Not surprisingly the benzyl thioether was also deprotected under reductive conditions[91]. Hence the desired functionalization should be achieved in a single step rather than multisteps.

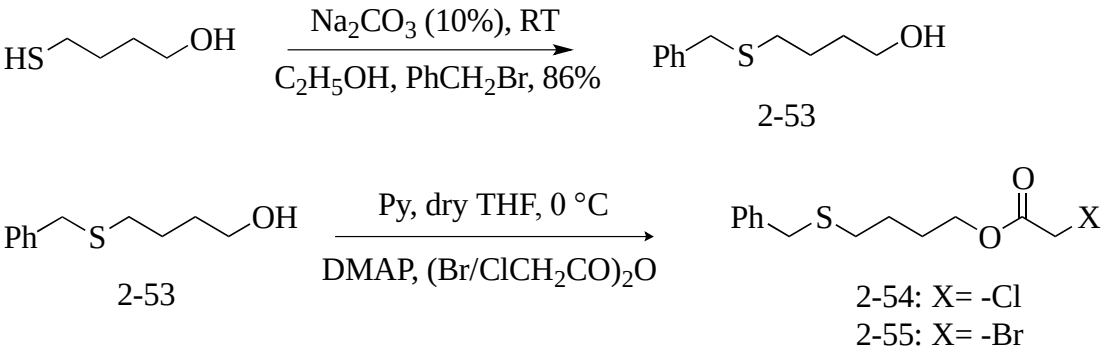

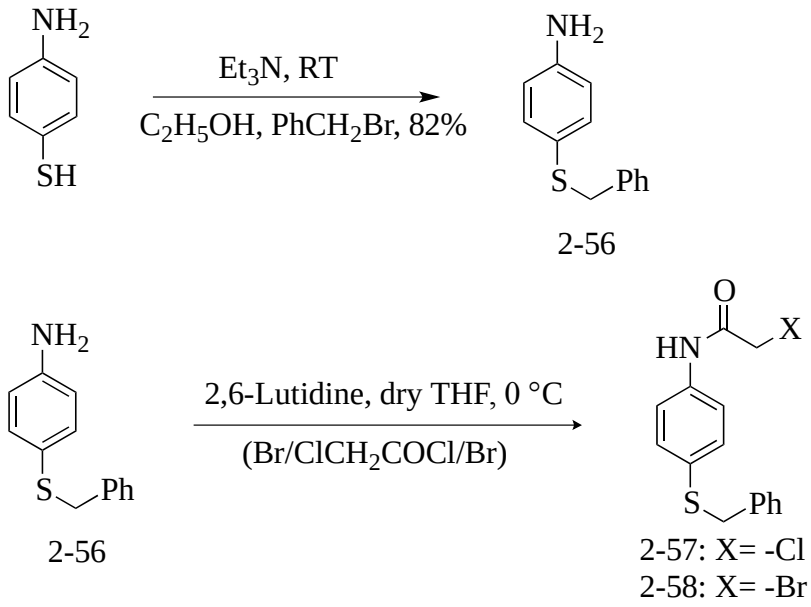

Scheme 2-6 Synthesis of thiol-containing alkylating agents to be used in dissolving metal reduction conditions.

When G-N-MWCNTs were subjected to reductive alkylation in ammonia with thiol-containing ligands (2-54, 55, 57 and 58), to our surprise, we observed the formation of spiral channels (Figure 2-11) instead of linear ones. The majority of the tubes in the samples were channeled in a tight spiral manner. The channeling of the tubes will be discussed in greater detail in chapter 3.

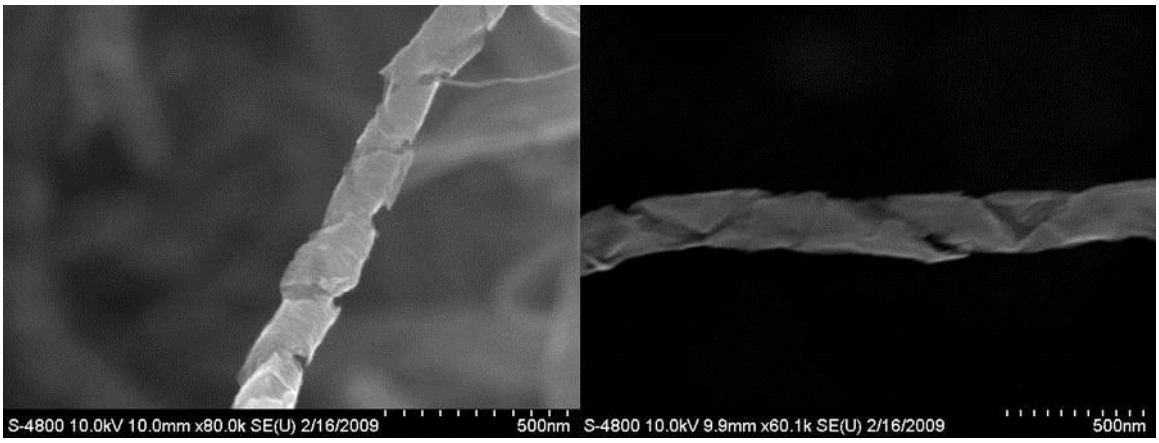

Figure 2-11 SEM images of G-N-MWCNTs showing spiral channels.

With the original material with which we began our work, it was observed that it channeled when ammonia was used as a solvent and not with other amine solvents like EDA. The new G-N-MWCNTs do channel even in EDA (Figure 2-12(a)), but form linear channels rather than spiral. When these channeled G-N-MWCNTs were subjected to another reductive alkylation in ammonia, the G-N-MWCNTs (Figure 2-12(b)) opened dramatically. In the first reduction with EDA, G-N-MWCNTs form linear channels. So these channels are the most prone sites for the second reduction to occur. This might be the reason for the resultant G-N-MWCNTs to be so opened up.

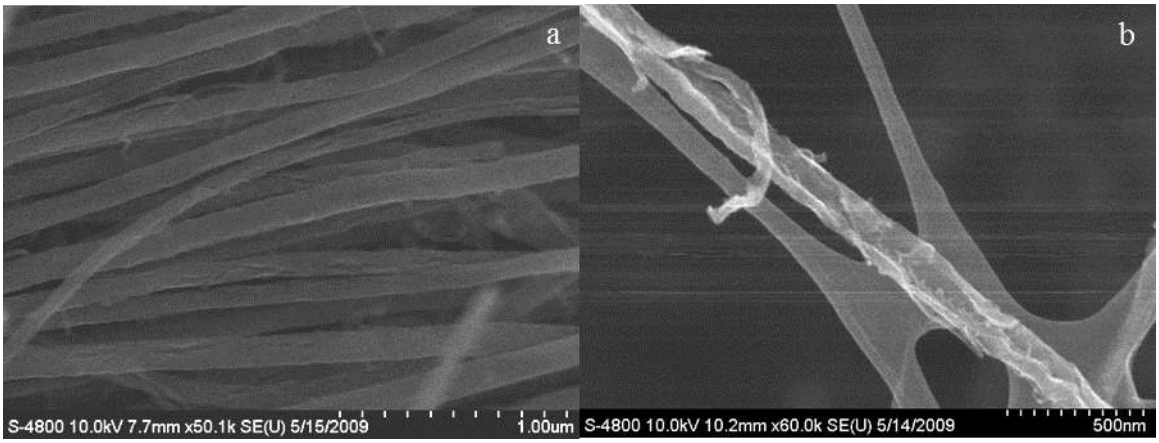

Figure 2-12 SEM images of G-N-MWCNTs (a) reduced in EDA and (b) reduced in EDA and then in ammonia.

After dealing with above-mentioned structural issues, it seemed that to differentially functionalize N-MWCNTs (i.e. to create different functionality in the channels than on the surface) would not be successful. However, we wanted to attempt to prove functionalization using electron microscopy, as there are few other probes that can help confirm that the desired chemistry is taking place. Accordingly we complexed these functionalized G-N-MWCNTs with Au particles (2 nm) using scheme 2-7.

Scheme 2-7 Complexation of functionalized G-N-MWCNTs with thiol-containing ligands.

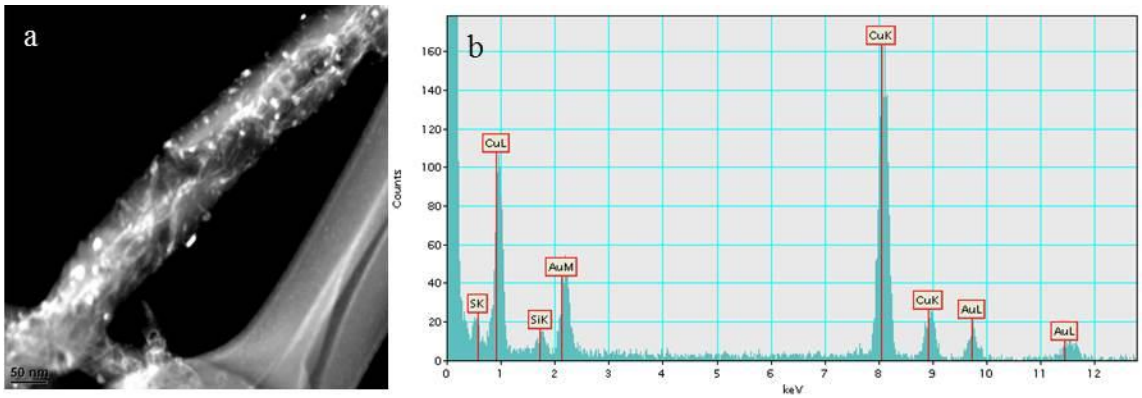

Figure 2-13 (a) STEM and (b) EDX of 2-46.

The STEM image (Figure 2-13(a)) showed white spots; some were around 2 nm in diameter and some were bigger (5-10 nm). We analyzed these spots with energy dispersive X-ray spectroscopy (EDX). EDX is a technique that relies on the investigation of a sample through interactions with electromagnetic radiation, analyzing x-rays emitted by the sample in response to being hit with charged particles. Its characterization capability is based on the fundamental principle that each element has a unique atomic structure allowing x-rays that are characteristic of that element's atomic structure to be identified uniquely. The EDX spectra (Figure 2-13(b)) confirmed that the bigger white spots are Si and the smaller are Au. Also, EDX spectra confirms the presence of S. This was encouraging. The source of the Si might be the quartz substrate on which the arrays of N-MWCNTs are grown.

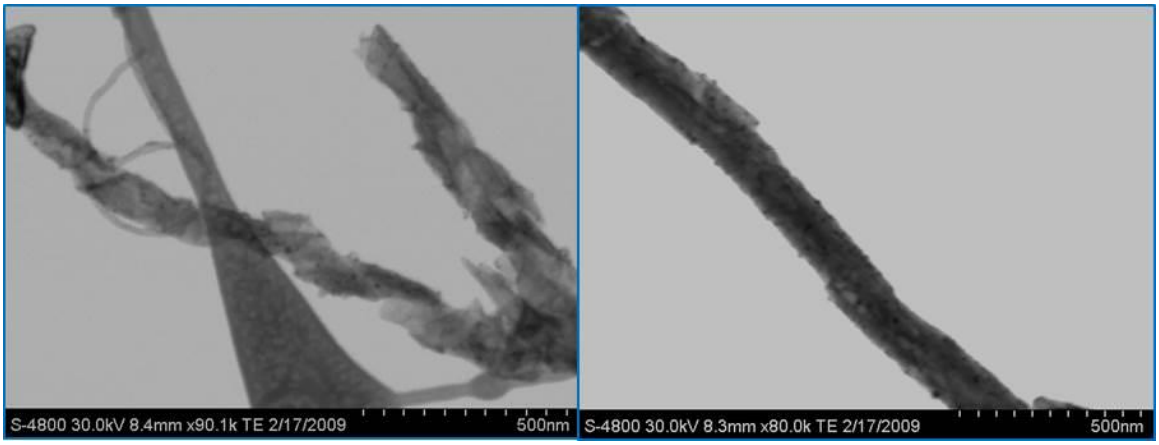

Figure 2-14 STEM images of 2-46.

Au nanoparticles (black spots) seen in STEM images (Figure 2-14) can be thought to be occupying the edges of the channels. This was hard to prove, as it was really hard to image 2 nm Au particles. Also, the concentration of Au nanoparticles was quite low in the original solution, so, we thought of going to larger particle size such as 10 nm, which is available at higher concentrations. The larger size may also help in specifically locating bigger particles, and the channels are wide enough to accommodate 10 nm particles. The reaction conditions were the same, only the size of Au particles was changed from 2 to 10 nm (Scheme 2-8).

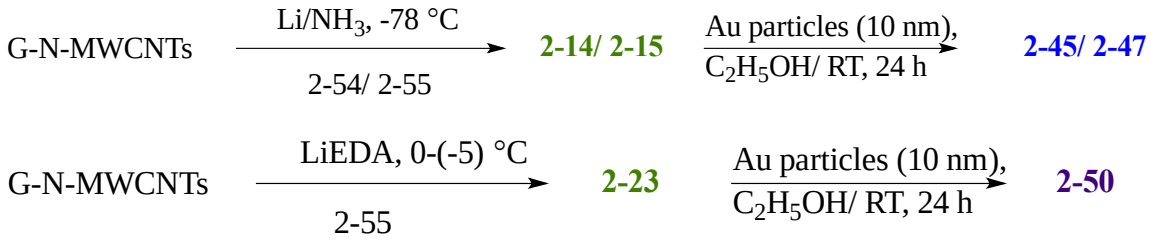

Scheme 2-8 Complexation of functionalized G-N-MWCNTs with thiol-containing ligands in ammonia and EDA.

STEM images of G-N-MWCNTs reduced in ammonia (Figure 2-15) or in EDA (Figure 2-16) quantitatively show that Au nanoparticles were mostly concentrated in the channels and very few were present on the surface. So the original surface of the tubes seems unaffected, opposite to what we expected. EDX (TEM mode) (Figure 2-17) of the sample reduced in ammonia revealed that these black spots are Au particles and are 10 nm in diameter.

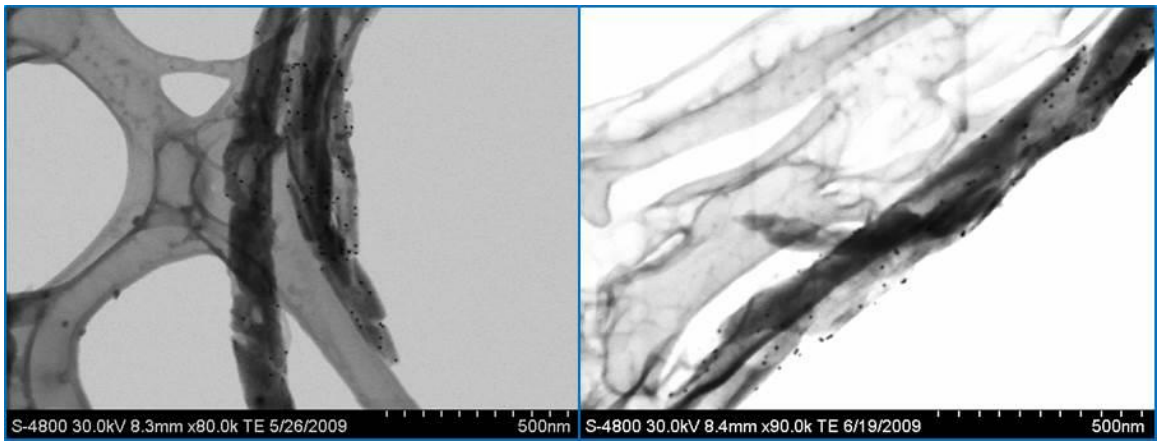

Figure 2-15 STEM images functionalized G-N-MWCNTs with thiol-containing ligands in ammonia (2-45).

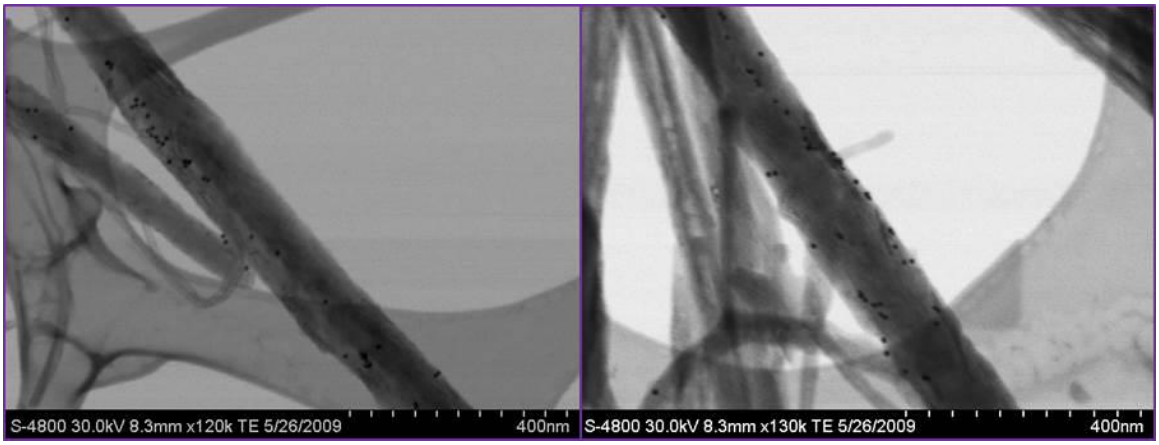

Figure 2-16 STEM images functionalized G-N-MWCNTs with thiol-containing ligands in EDA (2-50).

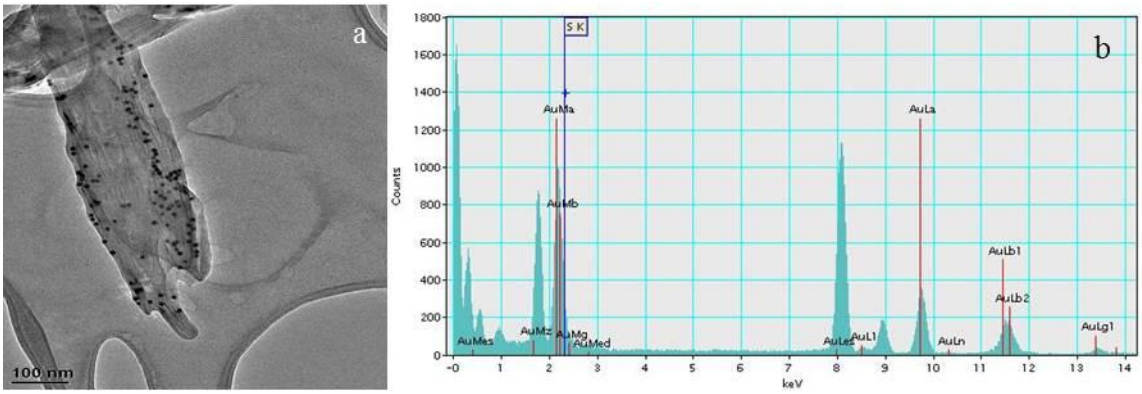

Figure 2-17 (a) TEM and (b) EDX of 2-47.

The electron microscopy results (STEM and TEM images and EDX) suggested that we were able to bind the metals. Another ligand, an amide, was also tried (Scheme 2-9). The STEM images (Figure 2-18 and 2-19) again suggested preferential binding of Au nanoparticles to the newly formed edges of channels. It seemed that these edges are more reactive compared to the surface of the G-N-MWCNTs.

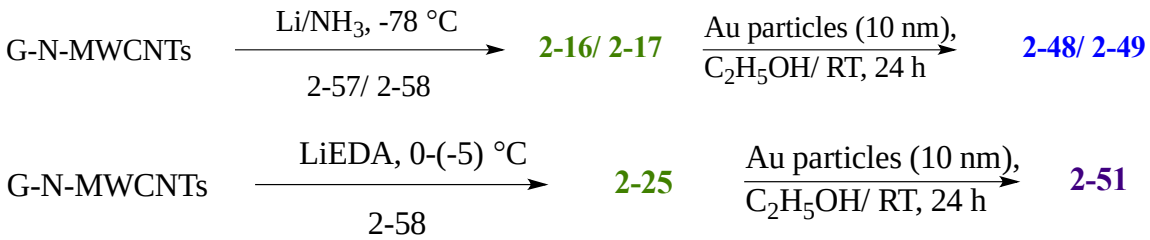

Scheme 2-9 Complexation of functionalized G-N-MWCNTs with thiol-containing ligands in ammonia and EDA.

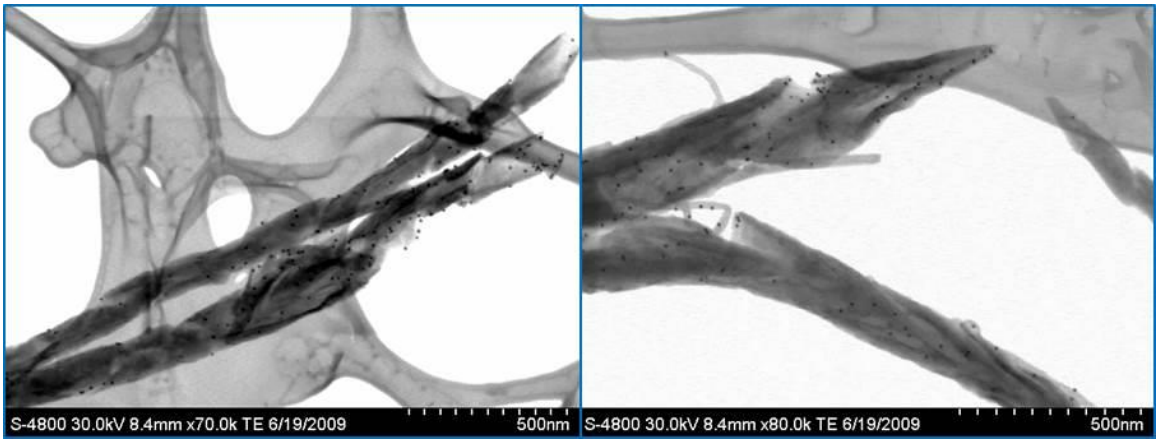

Figure 2-18 STEM images functionalized G-N-MWCNTs with thiol-containing ligands in ammonia.

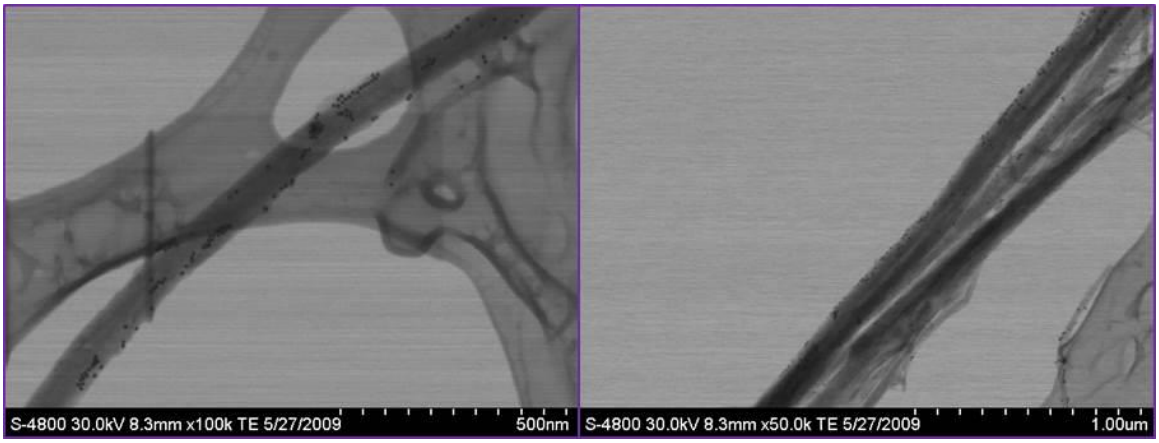

Figure 2-19 STEM images functionalized G-N-MWCNTs with thiol-containing ligands in EDA.

The results of reductive functionalization of G-N-MCWNTs suggest that the desired chemistry was working. To prove that it is covalent functionalization and not non-specific binding (Au particles complexing as such with the starting material without any requirement of thiol functionality or just sliding in the channels) we carried out control experiments. G-N-MWCNTs and G-N-MWCNTs methylated in EDA were treated with Au nanoparticles under same reaction conditions (as the other samples) to produce 2-60 and 2-61 respectively. The STEM images (Figure 2-20(a) and (b)) showed no indication of binding with Au nanoparticles but we can see a few of them trapped in agglomerated tubes in some images.

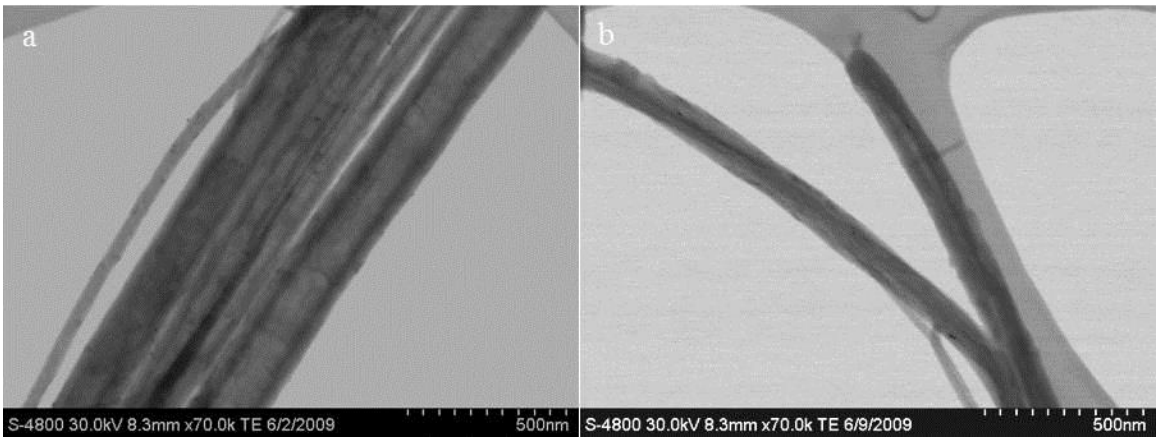

Figure 2-20 STEM images of (a) 2-60 and (b) 2-61.

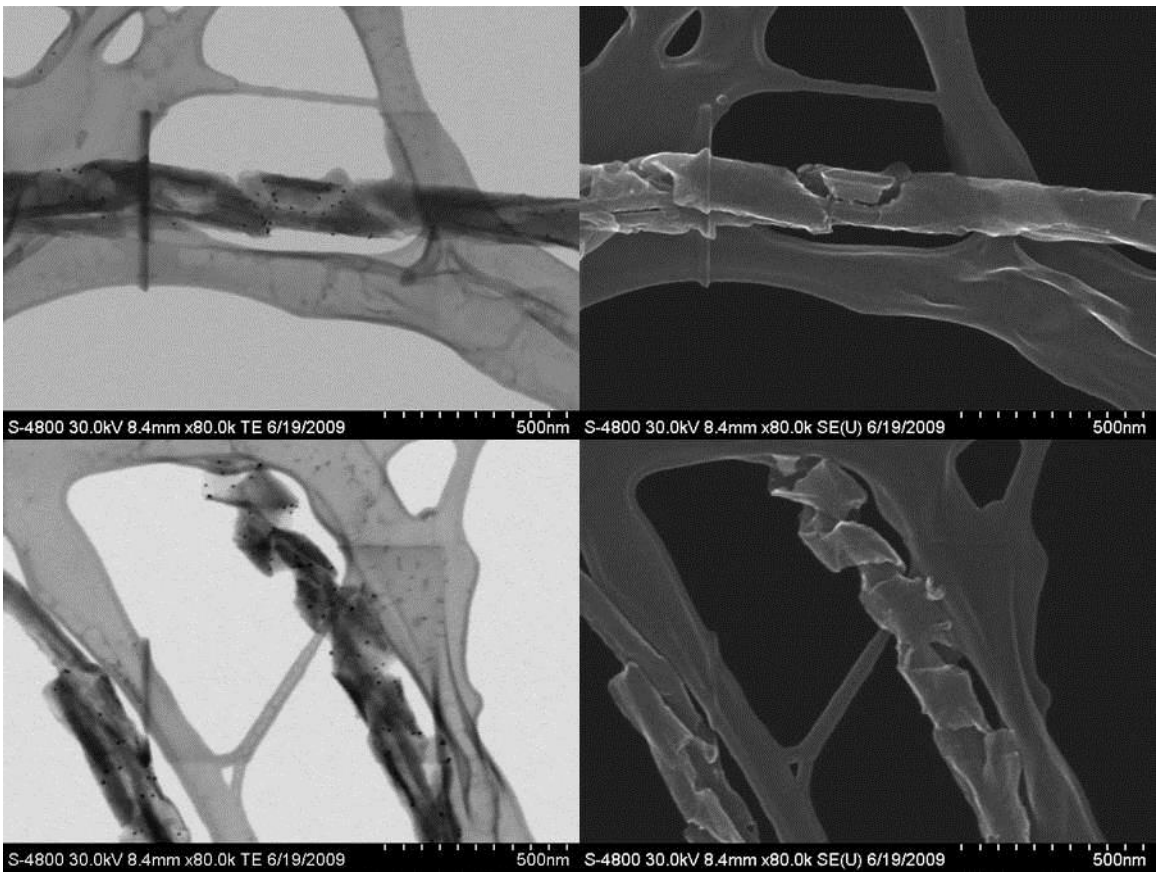

Figure 2-21 STEM and SEM done sequentially on functionalized G-N-MWCNTs with thiol-containing ligands in ammonia.

The project started particularly with the functionalization of N-MWCNTs as their morphology is such that they have more edges available on the surface that can be targeted. But the STEM and TEM images of our functionalized materials so far,

showed that the outer surface seemed quite unreactive, only the edges of the channels were the binding sites for the metals. This was also confirmed by sequentially imaging the samples in SEM and TEM mode (Figure 2-21). Channels can be seen in the SEM images (right hand side) and the corresponding STEM images (left hand side) show how these channels are decorated with Au nanoparticles.

A prominent change that occurs during annealing at 2800 $^{\circ}$C is the formation of loops (Figure 2-22) connecting adjacent graphene layers on both the outer and inner surfaces of the tubes. When other types of carbon materials are heated to high temperatures, similar loops can also form[87]. The formation of stable loops in the G-N-MWCNTs might also be the reason for the non-reactivity of the outer surface as now the outer surface is not a stack of edges, but instead a stack of folds.

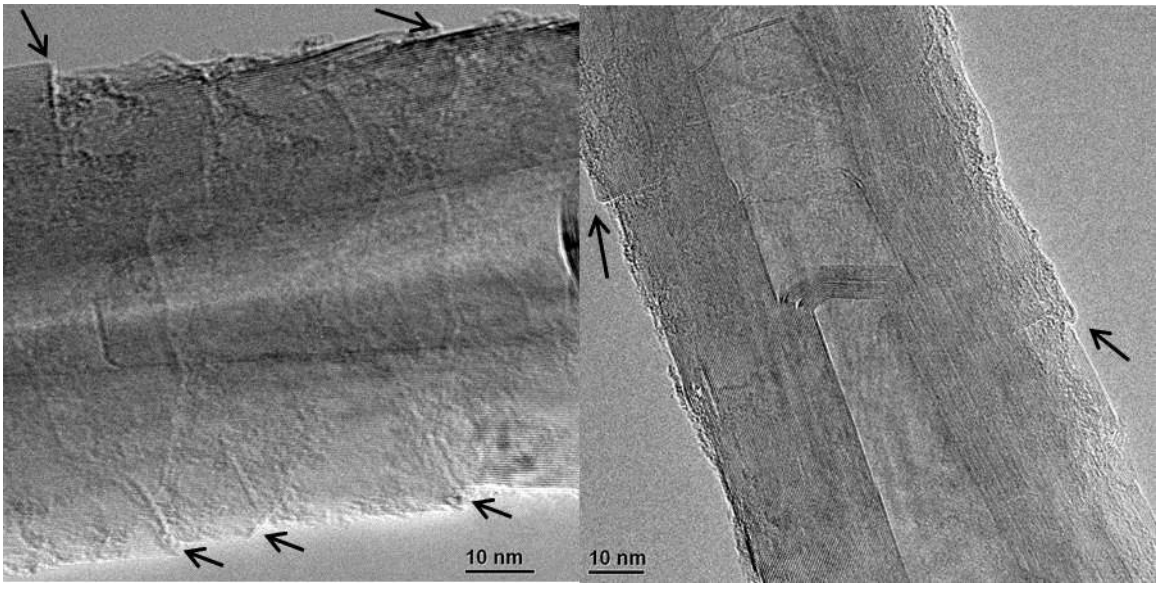

Figure 2-22 TEM of G- N-MWCNTs showing formation of loops (black arrows).

We thought of using more severe conditions for the functionalization of G-N-MWCNTs. Although several oxidation techniques have been employed on SWCNTs and MWCNTs, stacked carbon materials like N-MWCNTs, have not been studied to such an extent.

G-N-MWCNTs were subjected to five different sets of oxidizing conditions: 1) HNO_3; 2) H_2SO_4/H_2O_2; 3) $FeSO_4/H_2O_2$; 4) H_2SO_4/HNO_3; and 5) $KMnO_4/ H_2SO_4$.

Oxidation with HNO_3 (2-62, 63 and 64):

Treatment of SWCNTs with hot HNO_3 helps with efficient removal of metal impurities and graphitic platelets[80]. Bower et al.[92] have reported the intercalation of nitric acid molecules into SWCNT bundles, and prolonged exposure leads to exfoliation and to etching of carbon. Shortening of MWCNTs and formation of amorphous carbon were observed with prolonged exposure to concentrated HNO_3[81]. High temperature annealing following nitric acid-treatment has also been used to remove amorphous carbon[93].

The low-temperature thermal degradation and the shift of the onset of the oxidative decomposition to lower temperature (Figure 2-23) in G-N-MWCNTs that were subjected to sonication (30 min) followed by reflux in conc. HNO_3 for 6h (blue), 12h (green) and 24h (red), compared to G-N-MWCNTs suggested the introduction of functional groups and defects upon acid treatment. The TGA plots (for all oxidation reactions) are rescaled to show regions of interest.

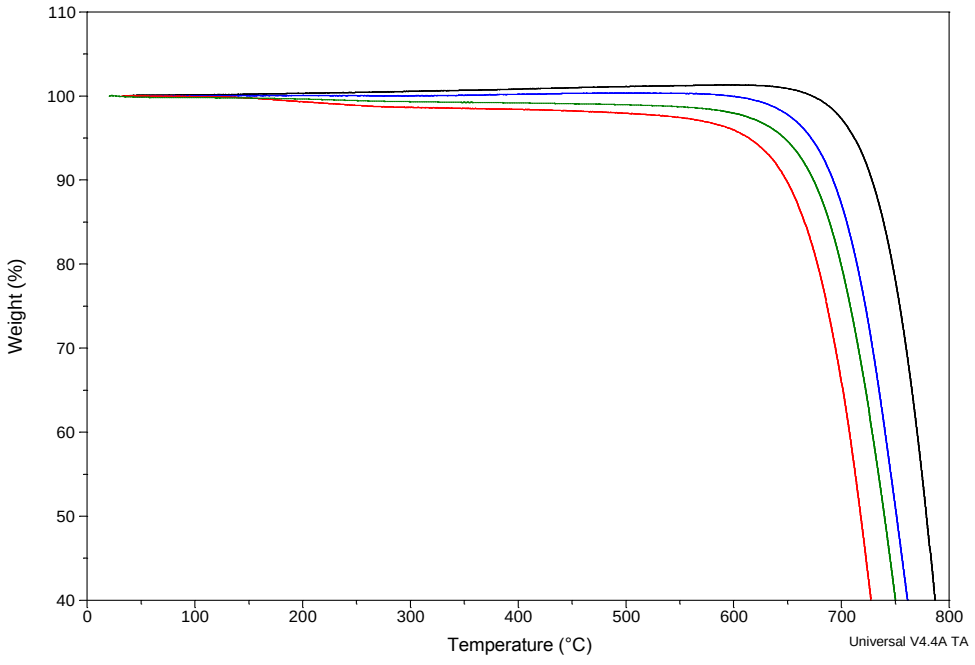

Figure 2-23 TGA plot comparing G-N-MWCNTs (black) with products of conc. HNO_3 oxidation for periods of: 6h (blue), 12h (green) and 24h (red).

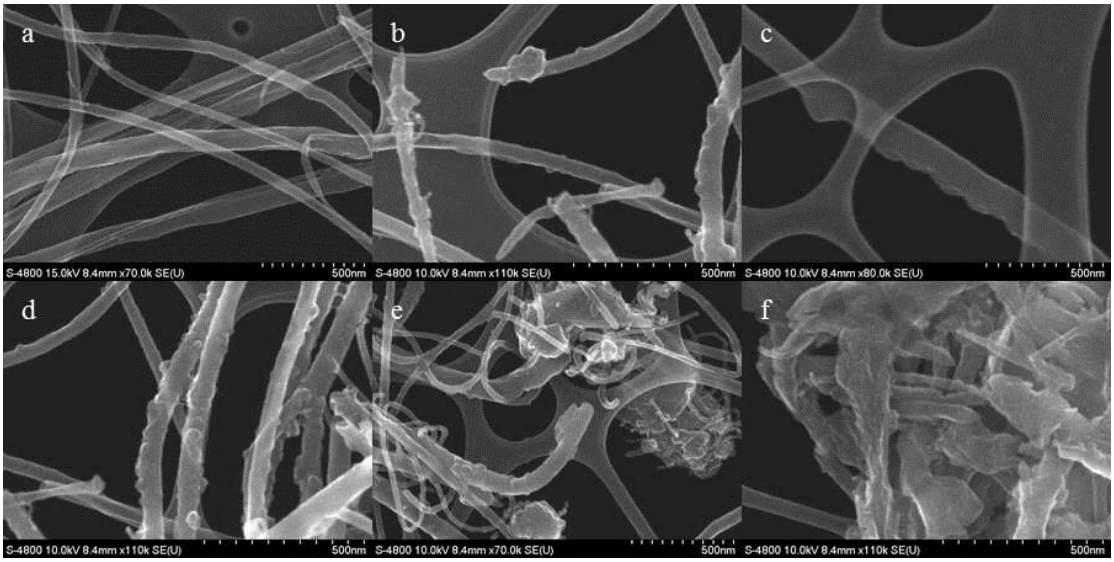

Figure 2-24 SEM images of G-N-MWCNTs treated with conc. HNO_3 after: a) 6h; b), and c) damages (surface etching and exfoliation) observed in few tubes after 6h; d) and e) 12h and f) 24h.

As reported based on TGA experiments conducted on oxidized MWCNTs, the thermal oxidative degradation is a multistage process[76] and it is likely that oxidative degradation of G-N-MWCNTs (Figure 2-23) is similar. The low-temperature weight loss can be attributed to evaporation of physisorbed water, decarboxylation and elimination of water from hydroxyl functionalities. The observed degradation at higher temperatures is a result of thermal oxidation of remaining disordered carbon. The decrease in the temperature of the onset of the oxidative decomposition upon increasing reflux time is an evidence of increasing G-N-MWCNT structural damage as suggested by SEM.

Treatment of MWCNTs with conc. HNO_3 results in shortening, fragmentation[81], and degradation of CNTs to carbonaceous materials[81, 92]. However, with G-N-MWCNTs no drastic change in length or in the fragmentation of CNT was observed (Figure 2-24). SEM images (Figure 2-24(a), (b) and (c)) of G-N-MWCNTs that had been refluxed in conc. HNO_3 for 6h showed limited damage on tubes, although initiation of exfoliation and etching of the surface was evident. While only partial exfoliation was seen after 12h (Figure 2-24(d) and (e)), greater exfoliation resulting in formation of carbonaceous material was observed after 24h (Figure 2-24(f)).

Oxidation with H_2SO_4/H_2O_2 (piranha oxidation) (2-65 and 66):

Specific conditions for oxidation of CNTs with piranha solution can bring about controlled cleavage of CNTs[75]. At higher temperatures, piranha solution attacks defect and damage sites, creating vacancies in the sidewalls. Increasing the exposure time produces shorter nanotubes resulting from further oxidation of these vacancies. Selective etching of smaller diameter nanotubes and significant sidewall damage are other results of this process[75]. At room temperature, piranha solution is not as efficient and results in less etching and less sidewall damage.

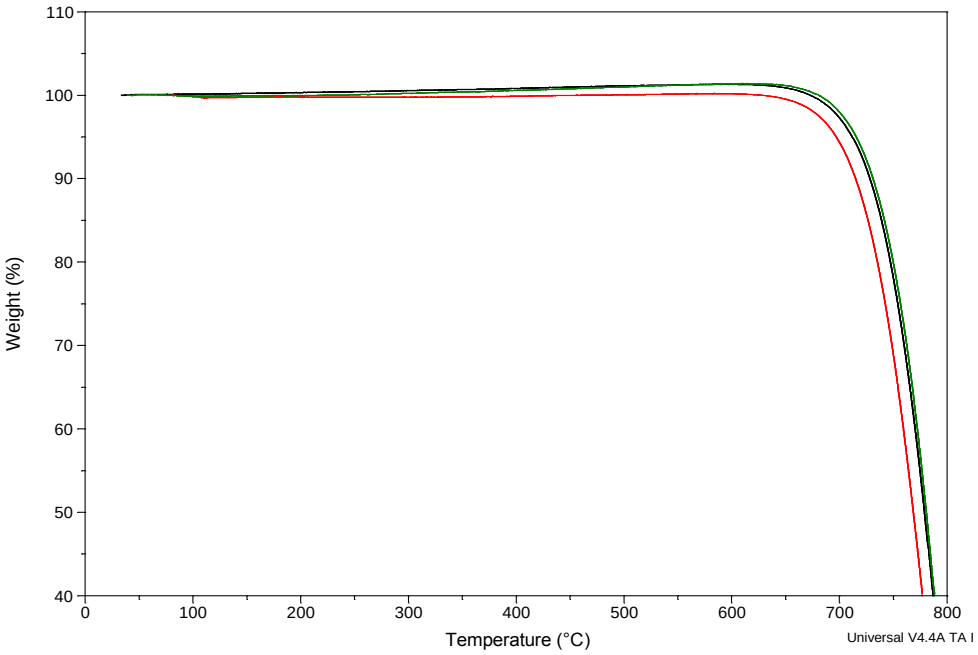

Figure 2-25 TGA plot comparing G-N-MWCNTs (black) with products of oxidation with piranha solution after: 12h (green) and 24h (red) of oxidation.

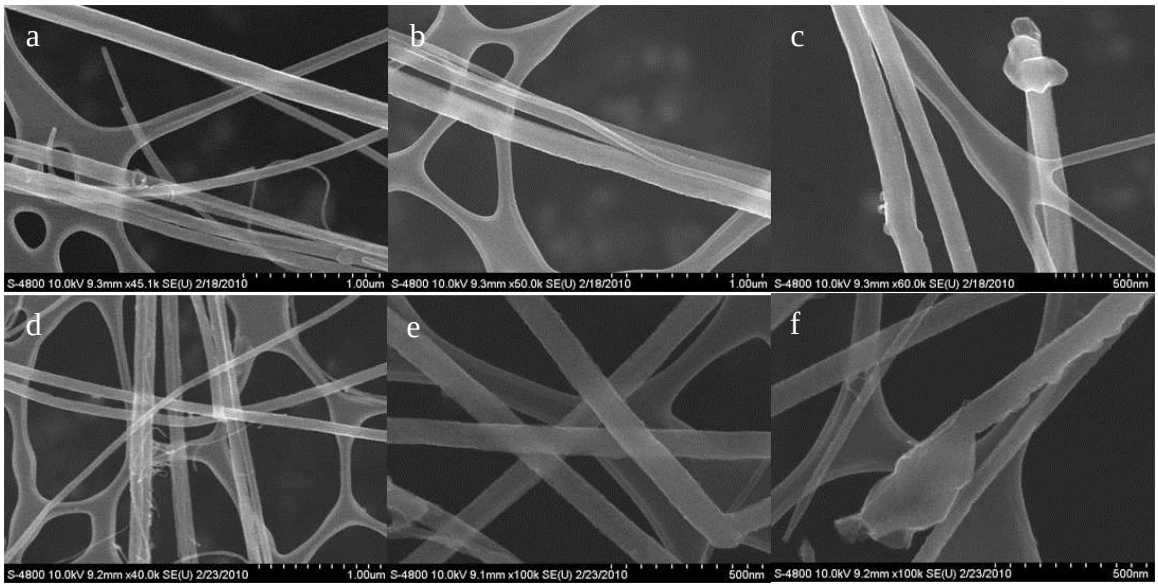

Figure 2-26 SEM images of G-N-MWCNTs treated with piranha solution after: a), b) & c) 12h ; d), e) & f) 24h.

Piranha solution appeared to be significantly milder than HNO_3 in its effects on G-N-MWCNTs. Stirring a suspension of G-N-MWCNTs with piranha solution at room temperature did not result in significant changes as reflected by TGA (Figure 2-25) until roughly 24h (red) of treatment. SEM results (Figure 2-26) supported the observations from TGA and indicated very little damage of the tubes from oxidation with piranha solution. The tubes appeared unaffected after 12h (Figure 2-26(a), (b) and (c)) of piranha treatment and most of the tubes were unaffected even after 24h (Figure 2-26(d) and (e)). Only few of the tubes appeared to have significantly damaged side-walls (Figure 2-26(f)).

Wang *et al.* have shown that a mixture of H_2O_2 and HCl can significantly increase purity relative to as-produced nanotube material[94]. They proposed that the presence of Fe particles in the as-produced material act as a catalyst for Fenton chemistry, producing hydroxyl radicals which are a more powerful oxidant than H_2O_2. The absence of Fe catalyst in our materials means that there is no iron source during piranha oxidation so no Fenton chemistry would occur, and this may be responsible for insignificant effect of piranha oxidation. This led us to explore the effects of Fenton oxidation.

Fenton oxidation (2-67):

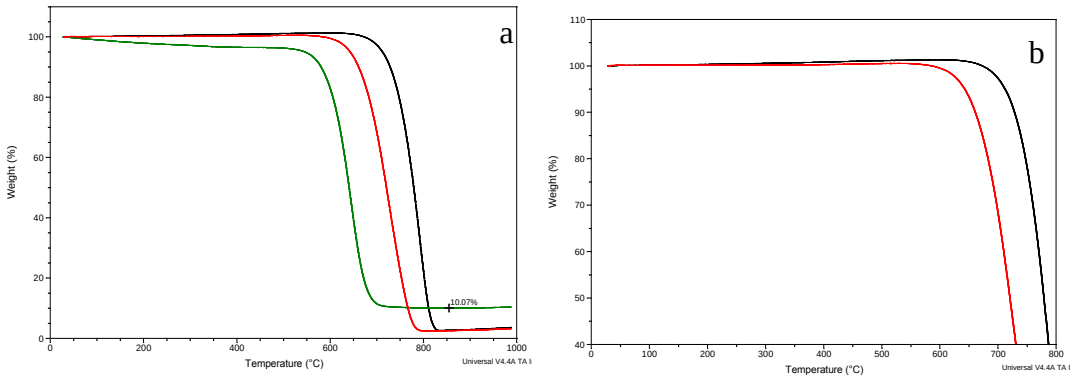

Figure 2-27 TGA plots: a) original and b) rescaled, comparing G-N-MWCNTs (black) with product of Fenton oxidation before HBr wash (green) and after HBr wash (red).

TGA (Figure 2-27) of the material obtained by treatment of G-N-MWCNTs with Fenton's reagent (Figure 2-27(a), green) at room temperature for 24h had two striking features. Comparing the thermal stability of Fenton oxidized material to that of G-N-MWCNTs, we can see that there is 150 ˚C difference between the T_o of two materials. There was also a 10% increase in residue, a red solid that is likely Fe_2O_3.

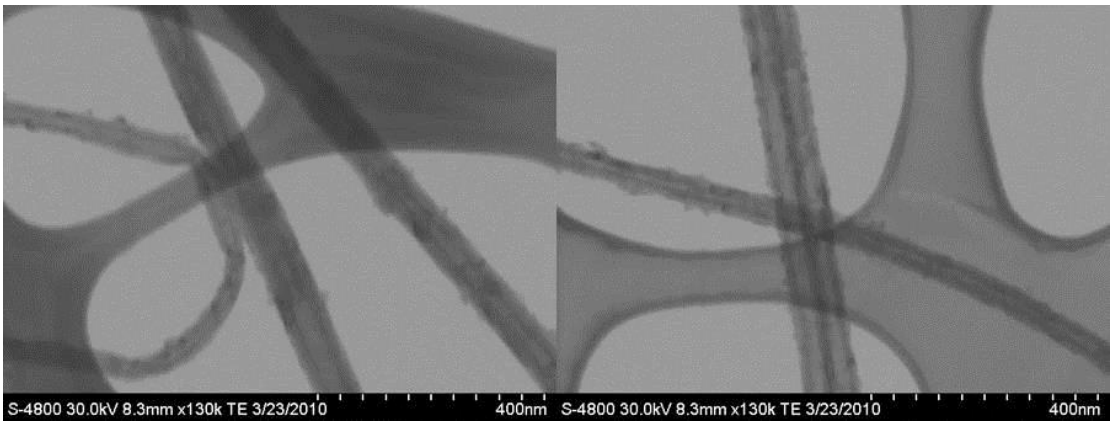

Figure 2-28 STEM images of G-N-MWCNTs treated with Fenton's reagent.

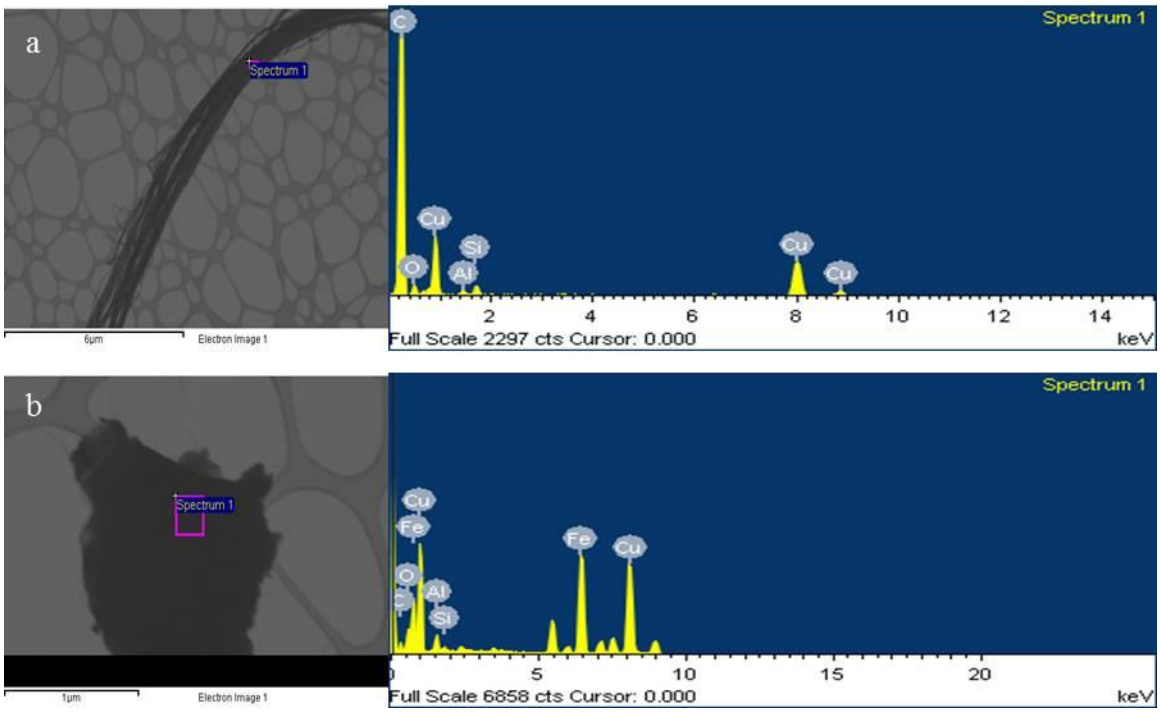

Figure 2-29 EDX on (a) Fenton oxidized tubes, shows mostly carbon without signs of Fe and (b) large fragments in Fenton oxidized tubes. (average carbon (16 %) signal may be from lacey carbon) (Cu from Cu grid, Al from sample holder, small amounts of Si is residue from synthesis, and small unlabeled peaks are Cr and Ca).

There were no noticeable dark spots on individual tubes (Figure 2-28) when the product was imaged using STEM. EDX (Figure 2-29(a)) on G-N-MWCNTs treated with Fenton's reagent showed no peaks from Fe. Instead, we observed few dark big pieces (Figure 2-29(b)) isolated from tubes under STEM and EDX on these showed Fe. So, we suspect these to be residual iron that showed as a residue in TGA. The product was treated with 48 wt% HBr in order to effectively remove iron. The difference was clearly seen in TGA (Figure 2-27 (a) and (b)), with red curve representing the oxidative thermal degradation of the HBr treated material following Fenton oxidation. Also, the difference in T_o was reduced from 150 ˚C to 70 ˚C, implying that residual iron having a catalytic role in oxidative thermal degradation.

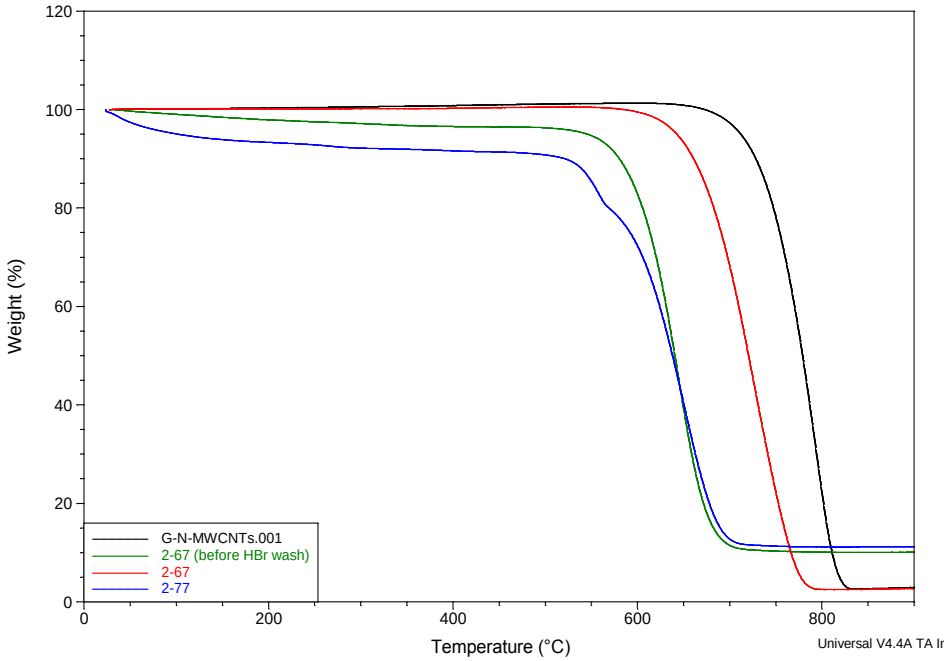

Figure 2-30 TGA plots comparing G-N-MWCNTs (black); product of Fenton oxidation before HBr wash (green) and after HBr wash (red) and product upon addition of Fe to HBr washed Fenton product (blue).

Catalytic role of Fe in oxidative thermal degradation was further analyzed by a control experiment (2-77) in which $FeSO_4.7H_2O$ was added to HBr treated Fenton oxidized product (2-67). The idea was to see whether added Fe will again lower T_o. TGA plot (Figure 2-30) illustrates the difference in T_o (compared to that of G-N-MWCNTs) increased from 70 ˚C (red) to 150 ˚C (blue) upon addition of Fe. The difference is same as seen in Fenton oxidized tubes before HBr wash. Hence the control experiment confirms the catalytic role of Fe in oxidative thermal degradation of the tubes.

Comparing piranha oxidation (Figure 2-25-red curve) with Fenton oxidation (Figure 2-27 (b)-red curve), it can be concluded that Fenton oxidation is harsher than piranha as the onset of oxidation is shifted to a lower temperature. STEM images (Figure 2-28) also suggest more side-wall damage in case of Fenton oxidation, supporting the TGA results. Based on these observations, the piranha oxidation of as-produced, iron-containing MWCNTs is likely a Fenton oxidation, resulting from oxidation of the iron catalyst particle to form Fe (II) ions that lead to Fenton chemistry.

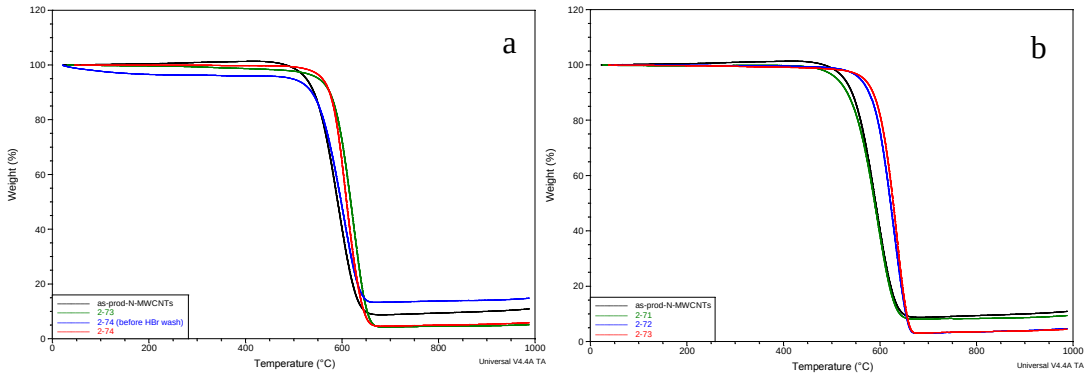

Figure 2-31 TGA plot comparing (a) product of piranha (green) and Fenton (blue, before HBr wash; red after HBr wash) on as-prod-N-MWCNTs (black) and (b) product of piranha oxidation (red) on Fe removed as-prod-N-MWCNTs (blue).

The observation was confirmed by control experiments. Figure 2-31(a) represents TGA of products of piranha oxidation (green) and Fenton oxidation (blue, before HBr wash; red after HBr wash) on as-prod-N-MWCNTs (black). The overlap of green and red curves suggests that piranha oxidation and Fenton oxidation have very similar effects on as-prod-N-MWCNTs. Figure 2-31(b) represents TGA of product of piranha oxidation (red) on catalyst (Fe) removed as-prod-N-MWCNTs (blue). The overlap of red and blue curves indicate insignificant effect of the treatment as seen in G-N-MWCNTs. Catalyst was removed from as-prod-N-MWCNTs (Figure 2-31(b), black curve) by HBr treatment prior to air oxidation of as-prod-N-MCNTs (Figure 2-31(b), green curve) at 400 °C for 4 h.

Oxidation with H_2SO_4/HNO_3 (2-68 and 69):

Treatment of MWCNTs with a mixture of H_2SO_4 and HNO_3 for 6 h or more purifies and oxidizes the nanotubes, but also causes opening of closed ends[95]. The highly curved surfaces at the end of nanotubes are fullerene-like, and it is easy to understand why these sites would be susceptible to oxidation. Recently Cho *et al.* reported radial followed by longitudinal unzipping of MWCNTs using a chemical method containing H_2SO_4 and HNO_3[96].

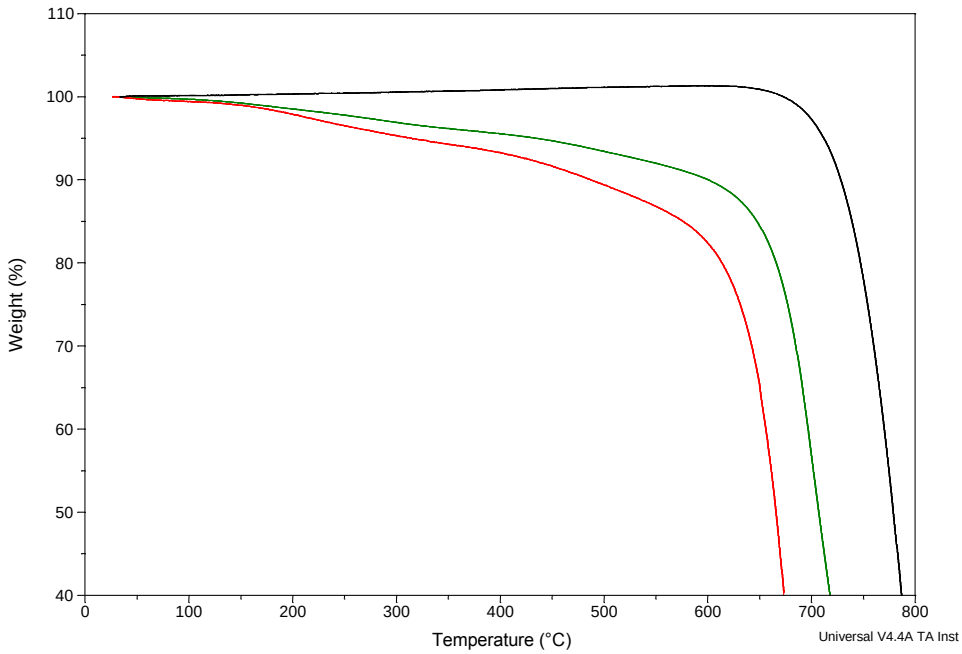

Figure 2-32 TGA plot comparing G-N-MWCNTs (black) with products of oxidation with a mixture of H_2SO_4/HNO_3 (3:1): 12h (green) and 24h (red).

Acid oxidation treatment of G-N-MWCNTs, with a mixture of H_2SO_4:HNO_3 (3:1) with sonication at room temperature (Figure 2-32) shifted the onset of oxidation to a lower temperature, both at 12h (green) and 24h (red) compared to that observed under treatments 1, 2 and 3 discussed above. This shift may likely be the result of increased damage to the tubes, consistent with what was found by SEM analysis.

Sonicating G-N-MWCNTs in a mixture of H_2SO_4/HNO_3 (3:1) for 12h resulted in the formation of spiraled ribbons (Figure 2-33). We have previously reported the phenomenon of longitudinal cutting in N-MWCNTs[72, 73] under dissolving metal reduction conditions (Li metal in liquid ammonia or ethylenediammine). The most common morphology of fractures observed after oxidation in this mixture was spiraled channels.

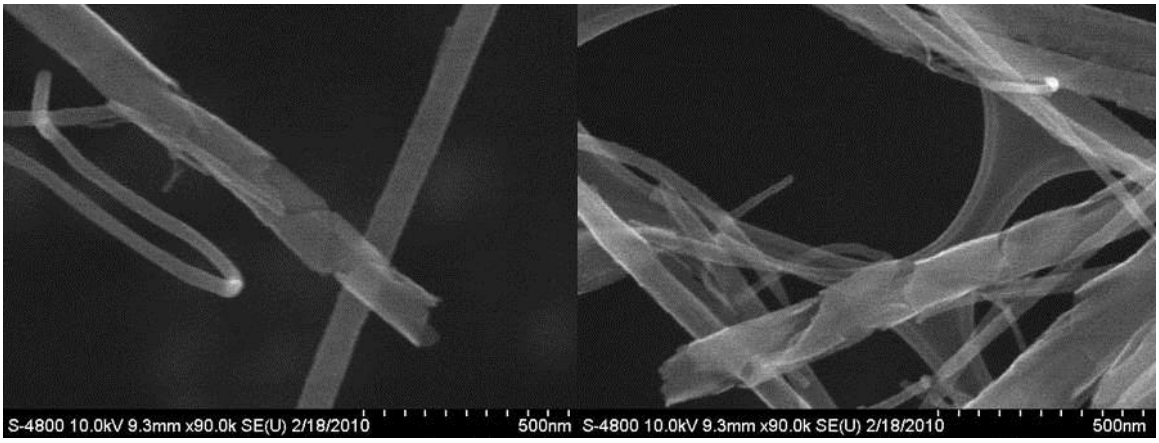

Figure 2-33 SEM images of G-N-MWCNTs treated with H_2SO_4/HNO_3 (sonication for 12h).

When the time period of sonication was increased from 12 to 24h, more damaged tubes were seen. The tubes became shorter as reflected by SEM (Figure 2-34). It has already been observed that sonication of SWCNTs in H_2SO_4/HNO_3 (3:1) mixture produces tubes of shorter lengths, as microscopic domains of high temperature produced by the collapse of cavitation bubbles in sonication, leads to the surface attack, leaving an open hole in the tube side[74]. The subsequent attack by acid mixture at this newly created defect cuts the tube cleanly.

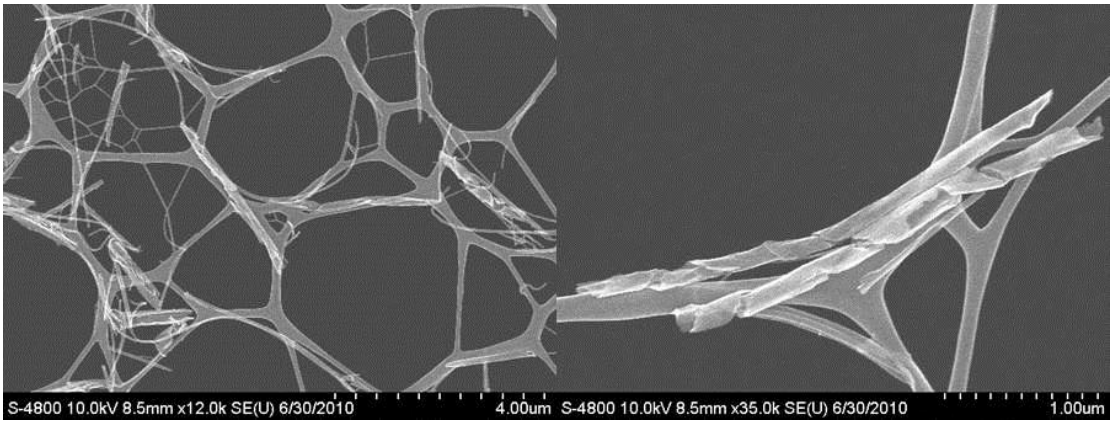

Figure 2-34 SEM images of G-N-MWCNTs treated with H_2SO_4/HNO_3 (sonication for 24h).

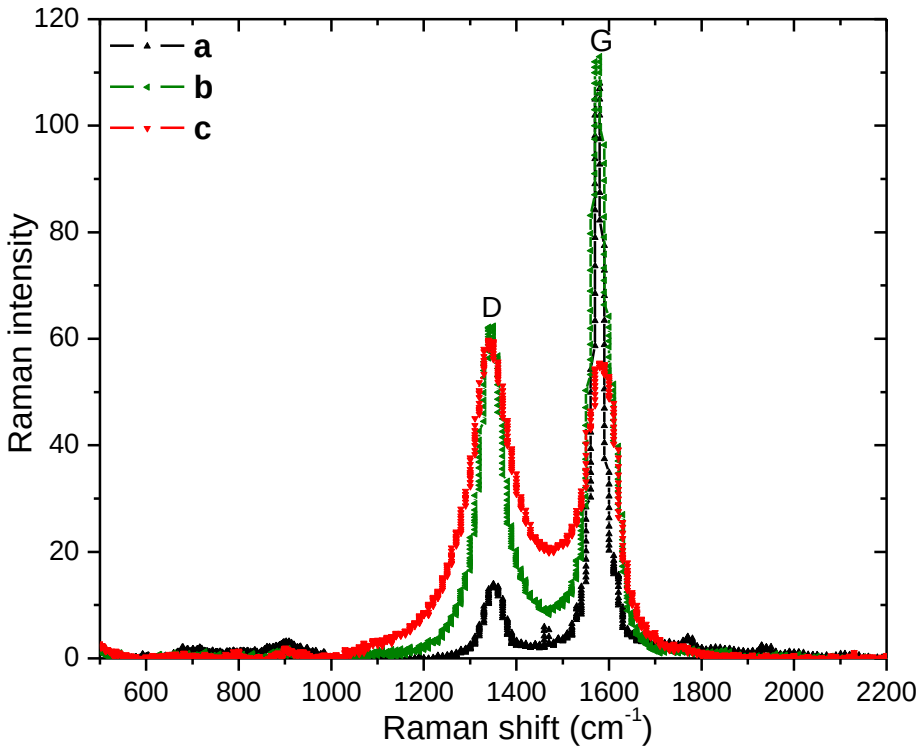

Figure 2-35 The Raman spectra of: a) G-N-MWCNTs; b) G-N-MWCNTs treated with H_2SO_4/HNO_3 (sonication for 24h) and c) G-N-MWCNTs treated with $KMnO_4/H_2SO_4$.

We further evaluated the structure of the G-N-MWCNTs before and after treatment using Raman spectroscopy. It was clear (Figure 2-35(a)) from the ratio of the integrated intensities of the D (1353 cm^{-1}) band to G (1576 cm^{-1}) band that G-N-MWCNTs have very few defects (I_D/I_G ~ 0.13) and upon oxidation (Figure 2-35(b)) with H_2SO_4/HNO_3 mixture the G band broadens a little with significantly increased intensity of the D band. It has been reported that oxygen-containing functionalities such as carbonyls, carboxyls and hydroxyls[97] exist at the edges and the surface[98], thereby disrupting the π-conjugated network, which result in broadened G band and increased intensity of D band[83].

We used XPS to determine the composition of oxidized compared to the starting G-N-MWCNTs which corresponds to the data shown in Figure 2-36. XPS spectroscopy also confirmed that the atomic concentration of oxygen increased from 3 to 12%.

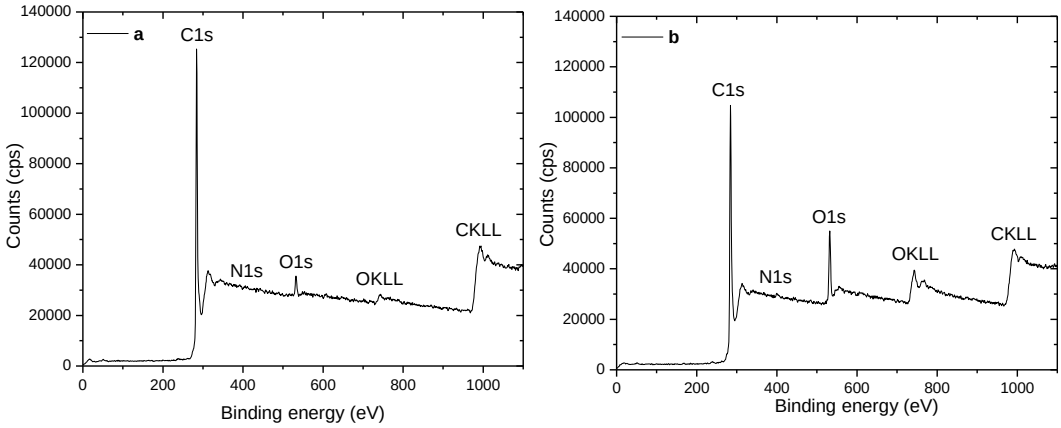

Figure 2-36 The XPS spectra of: a) G-N-MWCNTs and b) G-N-MWCNTs treated with H_2SO_4/HNO_3 (sonication for 24h).

Oxidation with $KMnO_4/H_2SO_4$ (2-70):

Lengthwise opening of MWCNTs along their axis was observed by Tour et al.[83] with a mixture of H_2SO_4 and $KMnO_4$. Among all the acid oxidative treatments on G-N-MWCNTs, $KMnO_4$ oxidation conditions remain the harshest. TGA (Figure 2-37, red curve) showed considerable low-temperature weight loss (~55%) attributed to evaporation of physisorbed water, decarboxylation, decarbonylation and elimination of hydroxyl functionalities[76] and also a maximum shift in the onset temperature of oxidation of remaining disordered carbon.

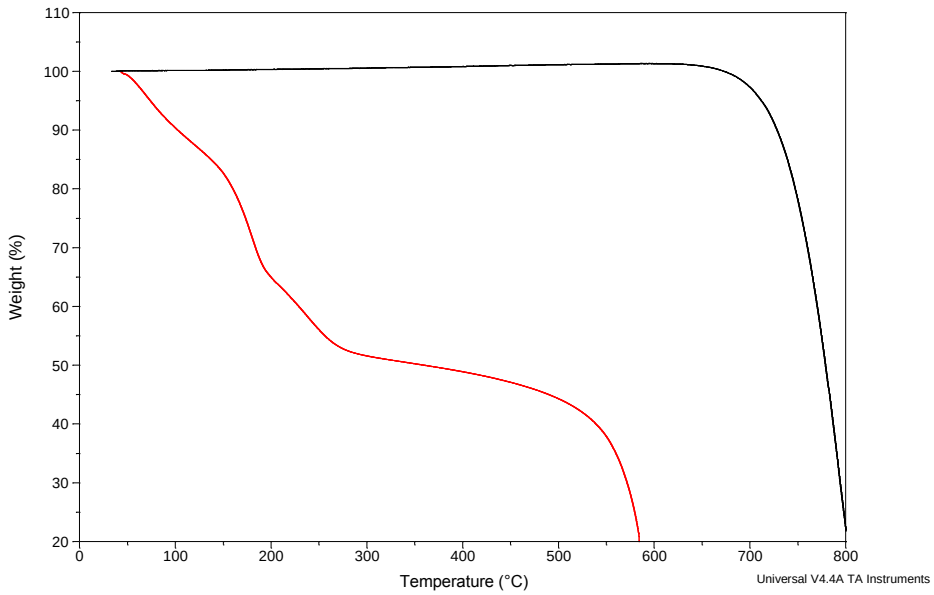

Figure 2-37 TGA plot comparing G-N-MWCNTs (black) with $KMnO_4/H_2SO_4$ oxidized product (red).

We also performed XRD analysis (Figure 2-38) to further investigate this high degree of oxidation as was observed from TGA. G-N-MWCNTs have 2θ values of ~26.18˚, corresponding to a d-spacing of 3.4 Å. $KMnO_4$ oxidized G-N-MWCNTs show a dominant peak at $2\theta = 10.7$˚, corresponding to a d-spacing of 8.3 Å, with minimal signal contributed by G-N-MWCNTs ($2\theta = 26$˚). The spectrum is similar to that of graphite oxide (GO) prepared by the Hummers method[97].

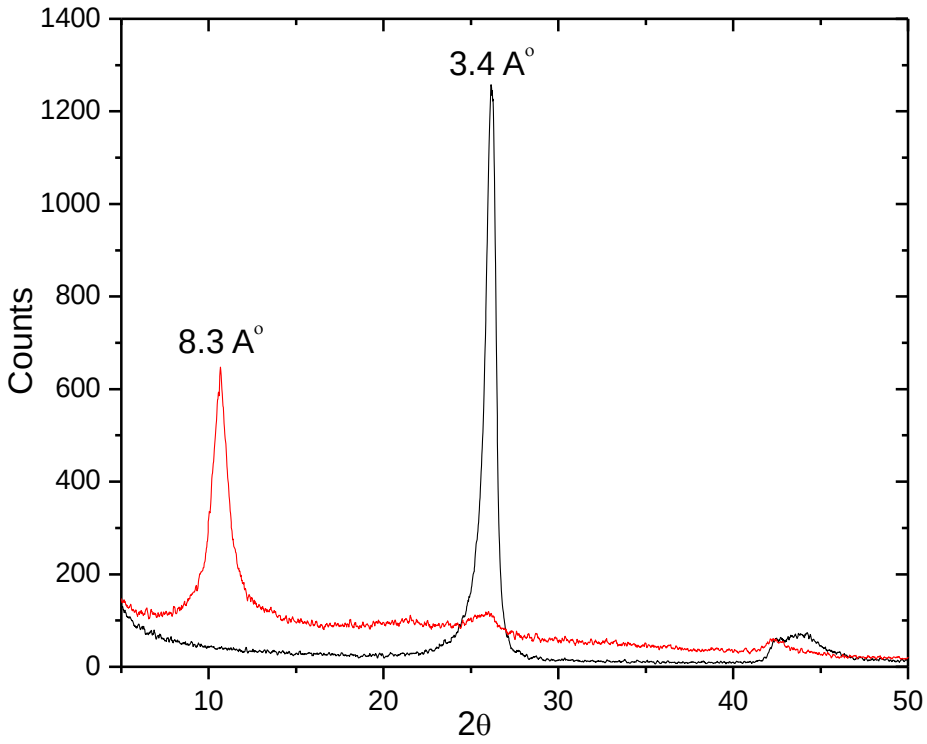

Figure 2-38 XRD analysis comparing G-N-MWCNTs (black) and $KMnO_4/H_2SO_4$ oxidized G-N-MWCNTs (red).

Raman spectroscopy also supported the increased level of disorder with the $KMnO_4$ oxidized material having $I_D/I_G \sim 1.1$ (Figure 2-35(c)) compared to $I_D/I_G \sim 0.13$ (Figure 2-35(a)) for G-N-MWCNTs. This behavior is similar to that observed for GO with a broadened G peak (1577 cm^{-1}) after oxidation along with the appearance of the D band at 1342 cm^{-1}.

Microscopy (Figure 2-39) revealed that $KMnO_4$ oxidation on G-N-MWCNTs produced the unusual spiraled ribbon textures. Shortening of tubes lengthwise was not

observed from the SEM (Figure 2-39) and TEM (Figure 2-40) images unlike upon oxidation with H_2SO_4/HNO_3 mixture. Also, the morphology of these spiraled ribbons was quiet different from the ones we had seen before with reducing[73] as well as oxidizing (H_2SO_4/HNO_3 mixture) conditions. The ribbon texture is more distinct, with the distance between the turns of the helix being 100-150 nm. We refer these as ***spiraled carbon nanoribbons (SCNs)***. A lot of new edges are formed in this newly formed ribbon texture as seen in TEM images (Figure 2-40, inset shown by black arrows). The formation of SCNs is discussed in chapter 3.

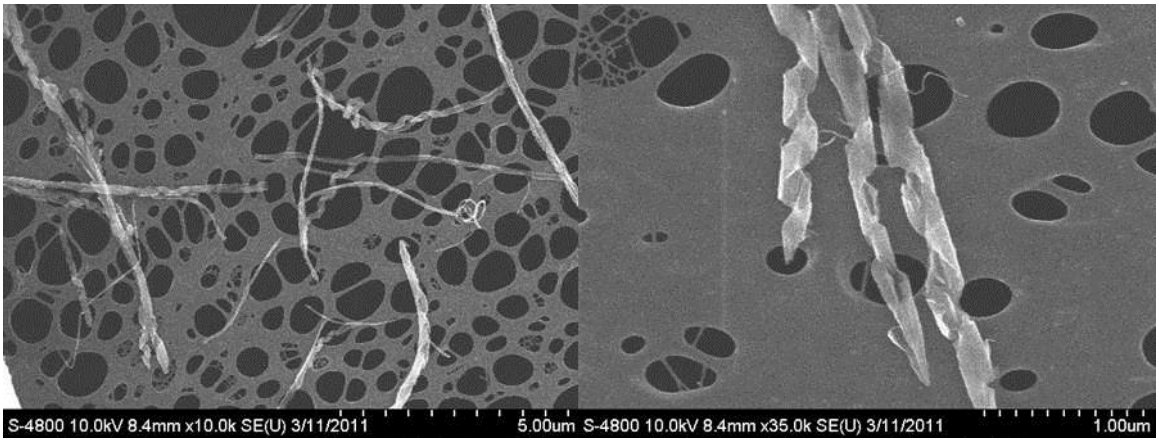

Figure 2-39 SEM images of $KMnO_4/H_2SO_4$ oxidized G-N-MWCNTs.

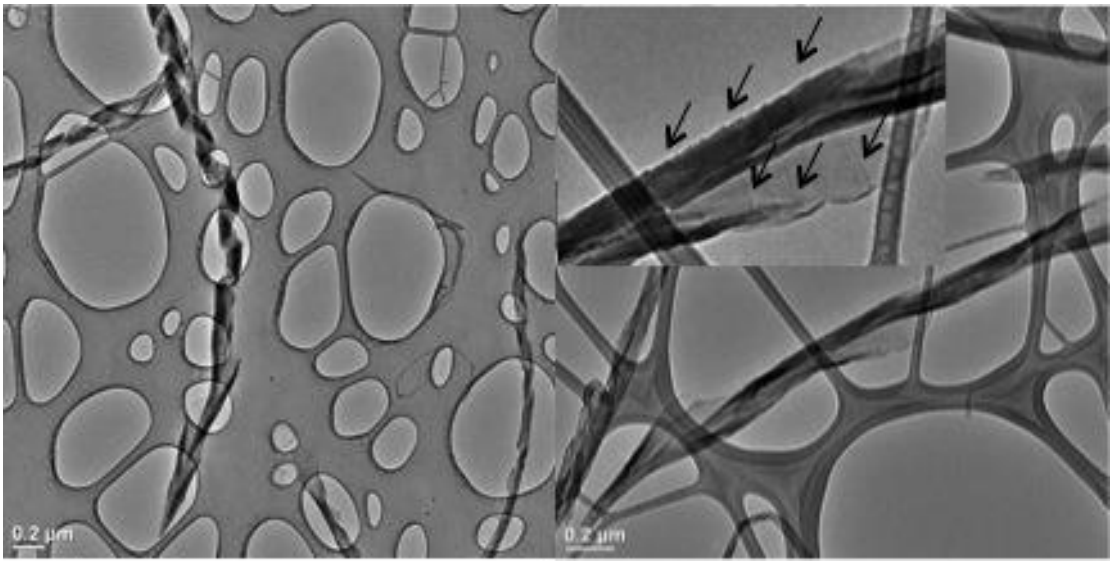

Figure 2-40 TEM images of $KMnO_4/H_2SO_4$ oxidized G-N-MWCNTs.

XPS and EELS analysis were further used to quantify the atomic concentration of oxygen. From the work of Tour *et al.*, in the XPS carbon 1*s* spectra (Figure 2-41(b)) of the $KMnO_4$ oxidized G-N-MWCNTs, the signals at 286 eV and 287 eV correspond to C–O and C=O, respectively and the shoulder at 289 eV is assigned to carboxyl groups[83]. In addition, the atomic concentration of oxygen increased from 3% to 20% as determined by XPS (Figure 2-41(a)).

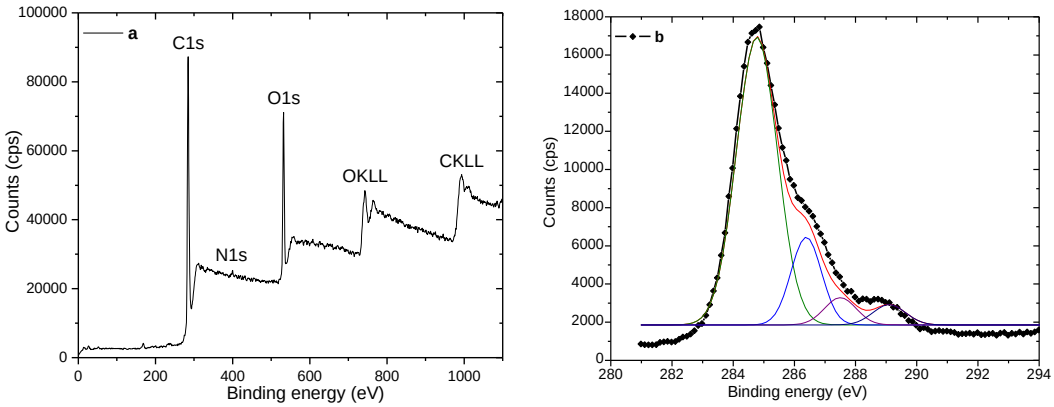

Figure 2-41 a) XPS and b) deconvoluted C 1*s* spectra of $KMnO_4/H_2SO_4$ oxidized G-N-MWCNTs.

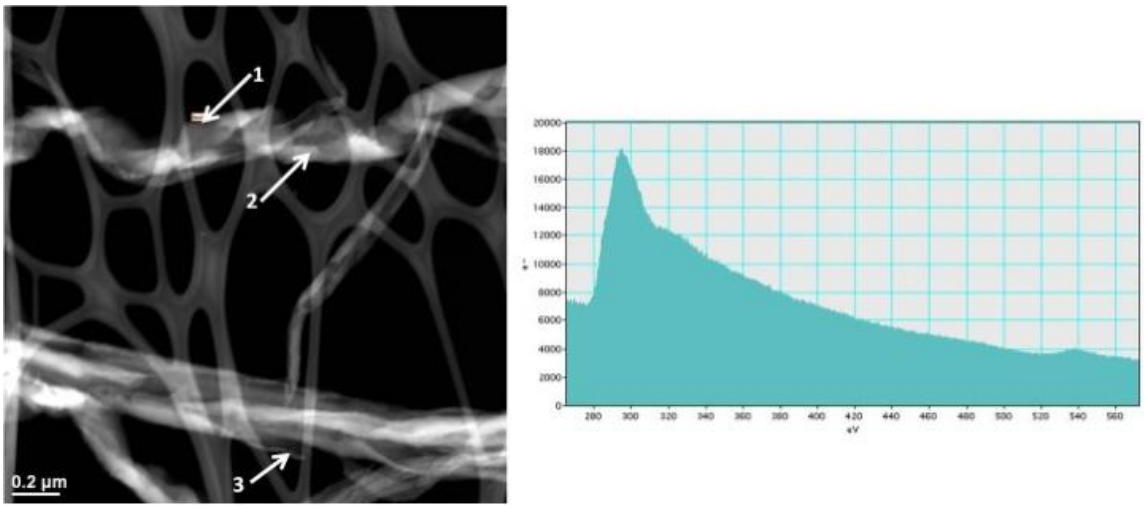

Figure 2-40 STEM image and the corresponding EELS plot for spot 1 of $KMnO_4/H_2SO_4$ oxidized G-N-MWCNTs.

EELS analyzed from individual oxidized tubes (STEM mode) exhibits the O-K edge at ~535 eV and the C-K edge at ~290 eV (Figure 2-42). It is clear (Table 2-1) that

oxygen-containing functional groups are distributed on the surface as well as the edges of the tubes. It can be seen that the average oxygen content from EELS is in accordance with that reported by XPS analysis, as a large fraction of oxygen atoms are located at or near to the surface.

Table 2-1 Quantitative atomic percent of C and O corresponding to three different spots (Figure 2-40) calculated from EELS.

Location	C (at. %)	O at. %
Spot 1	79	21
Spot 2	74	26
Spot 3	81	19

2.4. Conclusions

A novel characterization method for analysis of sites of reactivity was developed. Sulfur-containing ligands, as alkylating agents, were synthesized and were attached to the nanotubes. Commonly used approach to attach thiol groups to nanotubes involves multiple steps. This is achieved in a single step in our approach. The results from dissolving metal reduction followed by alkylation of G-N-MWCNTs suggested that the edges formed during reduction are the reactive sites for functionalization to take place. The original surface of N-MWCNTs seems to be unaffected. A detailed study about the structures of N-MWCNTs is under progress.

Another approach we used to modify N-MWCNTs was oxidation with various reagents. The effects of five commonly used wet chemical methods of oxidation (HNO_3, H_2SO_4/H_2O_2, $FeSO_4/H_2O_2$, H_2SO_4/HNO_3, $KMnO_4/ H_2SO_4$) were studied in terms of the extent of oxidation and on the texture of G-N-MWCNTs. TGA, XRD, Raman and XPS clearly revealed that $KMnO_4/ H_2SO_4$ was the most potent oxidant as it produced the highest fraction of oxygen-containing functional groups. Electron microscopy studies showed that the treatment of G-N-MWCNTs with H_2SO_4/HNO_3

and $H_2SO_4/KMnO_4$ mixtures lead to interesting spiraled ribbon texture, whereas treatment of G-N-MWCNTs with conc. HNO_3 resulted in exfoliation and formation of carbonaceous material. Piranha solution (H_2SO_4/H_2O_2) appeared to be significantly milder, and our results indicated that the piranha oxidation of as-produced MWCNTs is indistinguishable from a Fenton oxidation ($FeSO_4/H_2O_2$).

2.5. Experimental procedures

2.5.1. General Methods and Materials

N-MWCNTs were produced at the UK Center for Applied Energy Research from a pyridine feedstock containing dissolved ferrocene as catalyst, at a temperature of 800 °C using N_2 as the carrier gas in a 4 inch diameter tube reactor[41]. We refer to this material as as-produced N-MWCNTs (as-prod-N-MWCNTs).

Annealing was performed at the UK Center for Applied Energy Research by heating ~5 g samples of as-produced N-MCWNTs in a capped graphite crucible in a helium-purged vertical electric resistance tube furnace. The sample was heated from room temperature to the target temperature at 50 °C/min under a flowing He atmosphere maintained slightly above atmospheric pressure. Samples were held at the final temperature (~2800 °C) for 1 hour before being cooled to room temperature at 50 °C/min[87]. We refer to this material as G-N-MWCNTs.

TGA experiments were performed on TA 2950, TA Q500, and TA Q5000 instruments, with a standard heating rate of 10 °C/min from ambient temperature to 1000 °C under air. Results from different instruments are not compared to each other, due to differences in instrument behavior. All the TGA's were repeated at least two times, the reactions were also repeated few times, but the plots are reported from single experiment. All samples were ground to fine powder, with sample sizes approximately 8-10 mg.

DSC experiments were carried out on DSC Q20 coupled with refrigerated cooling system at 10 °C/min from -90 to 400 °C under N_2 atmosphere.

SEM studies were carried out using a Hitachi S-4800 FE-SEM operated at 5-10 kV. STEM observations were made on S-4800 FE-SEM equipped with a transmitted electron detector and an Oxford EDS system, operated at 30 kV. HRTEM, STEM, EDS, EELS were conducted using a JEOL 2010F TEM operated at 200 kV.

General procedure for sample preparation for imaging:

The samples for imaging were prepared by dispersing 1 mg of the sample in 10 ml EtOH or DMAc, and bath sonicated for 20 min to result in light grey dispersion. The dispersed samples were mounted on lacey carbon copper grids. These grids were vacuum dried for 24 h before imaging.

Surface area analysis of the samples was done using nitrogen physisorption at 77 K using an ASAP 2020 V3.00H instrument. All the runs were repeated at least two times with sample sizes ranging from 80-150 mg. Each time the samples were degassed prior to analysis. Surface areas and pore size distributions were calculated from the adsorption isotherms using the BET model.

XRD analysis was performed using a Bruker AXS (model D8 DISCOVER) at Kentucky Geological Survey facility with Cu Kα lamp. Sample sizes range from 100-150 mg for each run.

Raman spectroscopy was recorded with Thermo Scientific DXR Smart Raman (532 nm laser excitation). XPS of samples were recorded using a Physical Electronics PHI 5400 spectrometer with a magnesium X-ray source.

NMR spectra (^{1}H, ^{13}C) were measured on a 400MHz Varian Inova spectrometer. Samples were sonicated using Branson 1210 and 2200 bath sonicators.

Gold nanoparticles (2 nm, 10 nm) were brought from BBInternational. TEM grids used were lacey carbon type-A, 300 mesh, copper, with grid hole size of 63μm, and ordered from Ted Pella. Chemicals were ordered from Sigma-Aldrich (cysteamine.HCl, 4-aminothio phenol, 4-mercapto-1-butanol, EDC, lithium granular, ethylene diamine, pyridine, bromoacetic anhydride, chloroacetic anhydride, DMAP, 30% H_2O_2, $KMnO_4$), Alfa Aesar (ethyl bromoacetate, methyl iodide, chloroplatinic acid), Acros Organics (benzyl bromide, ethyl chloroacetate), Fluka (bromo acetylchloride, bromo acetylbromide) and Baker chemicals ($FeSO_4.7H_2O$). Absolute ethanol was ordered from Fischer, anhydrous THF from Sigma-Aldrich and extra dry DCM from Acros Organics. Acid such as H_2SO_4, HCl, HNO_3 were obtained from EMD chemicals.

2.5.2. General procedure for polyacylation of N-MWCNTs under Friedel-Crafts conditions:

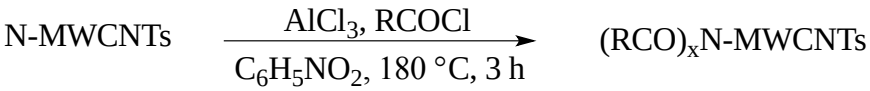

110 mL of dry nitrobenzene (dried and vacuum distilled over calcium chloride) and anhydrous aluminium chloride (8.7 g) were placed under a nitrogen atmosphere in a 500 mL three-necked flask equipped with a magnetic stirring bar, a dropping funnel with pressure equalizer, and a reflux condenser, all of which had been stored over-night in an oven at 110 °C. Under efficient stirring and cooling with water and ice, a solution of the acid chloride in 30 mL of nitrobenzene was added slowly through the dropping funnel. After addition was complete, the cooling bath was removed and the reaction was allowed to reach room temperature. The suspension of N-MWCNTs in nitrobenzene was added rapidly. This suspension was obtained by adding as-prod-N-MWCNTs (125 mg) in 55 mL of nitrobenzene and sonicating for two to five minutes in a bath sonicator. The reaction was heated under stirring at 180 °C for three hours after which it was stirred overnight at room temperature. The viscous reaction mixture was decomposed by cautious addition of ~250 g of crushed ice which had been treated with 5.5 mL of conc. hydrochloric acid. A very compact emulsion resulted and, after the ice melted, this was filtered on a Büchner funnel. On the filter paper remained a compact black powder, which was then washed with aqueous sodium hydrogen carbonate, water, EtOH and CH_2Cl_2. The resulting material was dried under vacuum overnight, weighed and then characterized.

Table 2-2 Acid chlorides used for polyacylation of N-MWCNTs.

Starting N-MWCNTs (mg)	Acid chloride (mL)	Compound # (quantity in mg)
As-prod-N-MWCNTs (125)	benzoyl chloride (6.63)	**2-1** (119)
As-prod-N-MWCNTs (250)	isobutyryl chloride (12)	**2-2** (215)
As-prod-N-MWCNTs (250)	decanoyl chloride (24)	**2-3** (237)
As-prod-N-MWCNTs (500) (in anhyd. CS_2)	acetyl chloride (4.7)	**2-4** (472)

2-5 (300)	benzoyl chloride (15.25)	**2-6** (268)
2-5 (300) (in anhyd. CS_2)	acetyl chloride (5.5)	**2-7** (442)

2.5.3. General procedure for polyalkylation of N-MWCNTs under dissolving metal conditions:

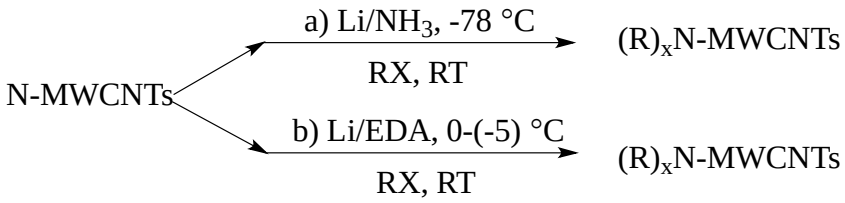

a) Using ammonia as solvent:

Approximately 175 mL of anhydrous ammonia was condensed using a Dewar condenser in a 250 mL three-necked round bottom flask in a dry ice-acetone bath under nitrogen. Li metal (250 mg) was added and the resulting blue solution was stirred for 5 min. To this solution was added acylated/as-prod-/G-N-MWCNTs (250 mg) and the resulting black suspension was stirred for 30 min. The alkyl halide was added dropwise using a syringe, and the mixture was stirred and allowed to warm to RT overnight until the ammonia had completely been evaporated from the flask. H_2O (200 mL) was added to the flask and stirred for 30 min. The resulting N-MWCNTs were then subsequently washed and filtered on 0.2 µm nylon membrane filters with H_2O until a neutral pH was reached. The polyalkylated N-MWCNTs were washed with EtOH and finally with CH_2Cl_2, dried under vacuum overnight, weighed and characterized.

Table 2-3 Electrophiles used in dissolving metal reaction conditions with NH_3 as solvent.

Starting N-MWCNTs (mg)	Electrophile (g/mL)	Compound # (quantity in mg)
2-1 (250)	ethyl bromoacetate (2.50)	**2-8** (272)
2-2 (150)	ethyl bromoacetate (1.38)	**2-9** (134)
2-3 (500)	ethyl bromoacetate (4.6)	**2-10** (486)

As-prod-N-MWCNTs (250)	ethyl bromoacetate (3.0)	**2-11** (238)
As-prod-N-MWCNTs (500)	ammonium chloride (3.4)	**2-5** (512)
G-N-MWCNTs (200)	ethyl bromoacetate (4.6)	**2-12** (213)
G-N-MWCNTs (100)	ammonium chloride (1.14)	**2-13** (100)
G-N-MWCNTs (50)	4-(benzylthio)butyl bromoacetate (0.35)	**2-14** (49)
G-N-MWCNTs (100)	4-(benzylthio)butyl chloroacetate (0.35)	**2-15** (112)
G-N-MWCNTs (100)	N-(4-(benzylthio)phenyl)-2-chloroacetamide (0.37)	**2-16** (100)
G-N-MWCNTs (100)	N-(4-(benzylthio)phenyl)-2-bromoacetamide (0.52)	**2-17** (103)
G-N-MWCNTs (500)	methyl iodide (6.50)	**2-18** (505)

b) Using EDA as solvent:

Approximately 175 mL of dry EDA was charged into a 250 mL three-necked round bottom flask and cooled to -5 $^{\circ}$C using salt-ice bath under nitrogen. Lithium metal (250 mg) was added and the resulting blue solution was stirred for 5 min. To this solution was added as-prod-/G-N-MWCNTs (250 mg) and the resulting black suspension was stirred for 30 min. The alkyl halide was added dropwise using a syringe, and the mixture was stirred and allowed to warm to RT overnight. Water (50 mL) was added to the flask and stirred for 30 min. The resulting N-MWCNTs were then subsequently washed and filtered on 0.2 µm nylon membrane filters with H_2O until a neutral pH was reached. The polyalkylated N-MWCNTs were washed with EtOH and finally with CH_2Cl_2, dried under vacuum overnight, weighed and characterized.

Table 2-4 Electrophiles used in dissolving metal reaction conditions with EDA as solvent.

Starting N-MWCNTs (mg)	Electrophile (g/mL)	Compound # (quantity in mg)
As-prod-N-MWCNTs (350)	ethyl bromoacetate (5.0)	**2-19** (377)
G-N-MWCNTs (500)	ethyl bromoacetate (7.2)	**2-20** (522)

G-N-MWCNTs (350)	methyl iodide (4.5)	**2-21** (370)
G-N-MWCNTs (50)	4-(benzylthio)butyl bromoacetate (0.25)	**2-22** (52)
G-N-MWCNTs (100)	4-(benzylthio)butyl chloroacetate (0.75)	**2-23** (98.5)
G-N-MWCNTs (100)	N-(4-(benzylthio)phenyl)-2-chloroacetamide (0.84)	**2-24** (98)
G-N-MWCNTs (50)	N-(4-(benzylthio)phenyl)-2-bromoacetamide (0.43)	**2-25** (55)
G-N-MWCNTs (100)	1-chloro butane (2.2)	**2-26** (105)

c) Dissolving metal reduction in EDA followed by in ammonia:
As-prod/G-N-MWCNTs were first reduced in EDA and then in ammonia using the above mentioned general procedures.

Table 2-5 Electrophiles used in dissolving metal reduction of G-N-MWCNTs (reduced in EDA) with NH_3 as solvent.

Starting N-MWCNTs (mg)	Electrophile (g/mL)	Compound # (quantity in mg)
2-21 (500)	ethyl bromoacetate (6.1)	**2-27** (503)
2-21 (50)	4-(benzylthio)butyl chloro acetate (0.35)	**2-28** (50)
2-21 (100)	N-(4-(benzylthio)phenyl)-2-bromoacetamide (0.55)	**2-29** (112)

2.5.4. General procedure for saponification of esterified N-MWCNTs (N-MWCNTs-$(CH_2COOC_2H_5)_x$):

$$(C_2H_5OOCCH_2)_x\text{N-MWCNTs} \xrightarrow[10\%\ HCl]{1M\ NaOH,\ 80\ ^\circ C,\ 24\ h} (HOOCCH_2)_x\text{N-MWCNTs}$$

To a 100 mL solution of 1M aqueous NaOH were added esterified N-MWCNTs (200 mg), and the mixture was heated to 80 °C and stirred for 24 h. The solution was cooled to room temperature and then subsequently washed and filtered on a Büchner funnel with H_2O until a neutral pH was reached. The resulting N-MWCNTs were washed off the filter paper to a 250 mL flask equipped with a magnetic stir bar. To this was added 85 mL of 10% HCl, the solution was stirred for 30 min and then subsequently washed and filtered on 0.2 µm nylon membrane filters with H_2O until a neutral pH was reached. The acidified N-MWCNTs were then washed with EtOH, dried under vacuum overnight, weighed and characterized.

Table 2-6 Saponification of esterified N-MWCNTs.

Starting N-MWCNTs (mg)	Compound # (quantity in mg)
2-11 (190)	**2-30** (155)
2-19 (300)	**2-31** (291)
2-20 (400)	**2-32** (399)
2-27 (100)	**2-33** (103)

2.5.5. General procedure of coupling of saponified N-MWCNTs (N-MWCNTs $(CH_2COOH)_x$) with cysteamine:

$$(HOOCCH_2)_xN\text{-MWCNTs} \xrightarrow[H_2NCH_2CH_2SH]{\text{EDC, DMF, RT, 24 h}} (HSCH_2CH_2HNCOCH_2)_xN\text{-MWCNTs}$$

Saponified N-MWCNTs (120 mg), cysteamine (1.54 g), N-(3-dimethylaminopropyl)-N'-ethyl-carbodiimidehydrochloride (EDC) (532 mg), and DMF (60 mL) were stirred at RT for 24 h under nitrogen. The resulting N-MWCNTs were then subsequently washed and filtered on 0.2 µm nylon membrane filters with H_2O. The resulting material was washed with EtOH and finally with CH_2Cl_2, dried under vacuum overnight, weighed and characterized.

Table 2-7 Coupling of saponified N-MWCNTs.

Starting N-MWCNTs (mg)	Compound # (quantity in mg)
2-30 (120)	**2-34** (123)
2-31 (200)	**2-35** (199)
2-32 (350)	**2-36** (351)
2-33 (100)	**2-37** (99)

2.5.6. General procedure for complexation of thiol functionalized N-MWCNTs:

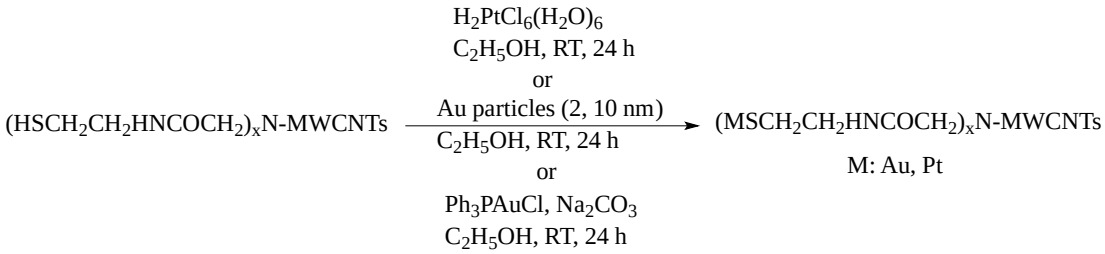

a) With Au nanoparticles:

Functionalized N-MWCNTs (10 mg) with thiol functionality, Au nanoparticles (2, 10 nm) (1.5 mL), and EtOH (2.5 mL) were stirred at RT for 24 h. The resulting N-MWCNTs were then subsequently washed and filtered on 0.2 µm nylon membrane filters with EtOH, dried under vacuum overnight, weighed and characterized.

b) With chloro(triphenylphosphine)-gold(I):

Thiol functionalized N-MWCNTs (50 mg) were dispersed in ethanol (20 mL) using bath sonicator and then stirred at room temperature under nitrogen. To this were added chloro(triphenylphosphine)-gold(I) (5 mg) dissolved in 2 mL of CH_2Cl_2 and sodium bicarbonate (5 mg). The resulting mixture was stirred at room temperature for 24 h. The resulting N-MWCNTs were then subsequently washed and filtered on 0.2 µm nylon membrane filters with water, EtOH and CH_2Cl_2, dried under vacuum overnight, weighed and characterized.

c) With chloroplatinic acid:

To functionalized N-MWCNTs (25 mg) with thiol functionality, 10 mL EtOH, was added chloroplatinic acid solution (50 wt. %) (33.15 mg) in EtOH (5 mL) and the resulting mixture was bath sonicated for 1 h. The mixture was either rot evaporated or filtered, dried under vacuum overnight, weighed and characterized.

Table 2-8 Metal complexation of thiol functionalized N-MWCNTs.

Starting N-MWCNTs	Complexing metal	Compound #
2-34	Au (2 nm)	**2-38**
2-34	Au (complex)	**2-39**
2-36	Au (2 nm)	**2-40**
2-36	Pt	**2-41**
2-37	Au (2 nm)	**2-42**
2-37	Pt	**2-43**
2-14	Au (2 nm)	**2-44**
2-14	Au (10 nm)	**2-45**
2-15	Au (2 nm)	**2-46**
2-15	Au (10 nm)	**2-47**
2-16	Au (10 nm)	**2-48**
2-17	Au (10 nm)	**2-49**
2-24	Au (10 nm)	**2-50**
2-25	Au (10 nm)	**2-51**
2-29	Au (10 nm)	**2-52**

2.5.7. Synthesis of thiol-containing ligands:

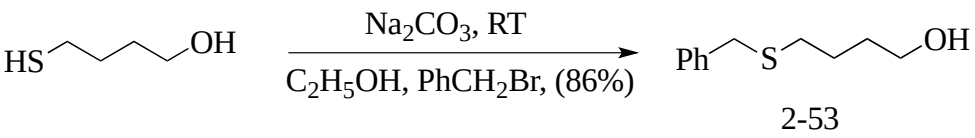

2-53

Synthesis of 4-(benzylthio)butan-1-ol (2-53):

Benzyl bromide (1.61 g, 9.42 mmol) was added to a stirred solution of 4-mercapto-1-butanol (1.00 g, 9.42 mmol) in 20 mL ethanol containing 2.00 g of sodium carbonate. The mixture was stirred under nitrogen for 12 h at room temperature. The solvent was removed *in vacuo* and the resulting residue was dissolved in CH_2Cl_2 and washed with 10% HCl and H_2O, dried over Na_2SO_4, and concentrated. The crude product was purified by flash column chromatography on silica gel using ethyl acetate:hexane as the eluent to give a colorless liquid (1.59 g, 86%). ^{1}H NMR (400 MHz, $CDCl_3$): δ 7.21 (5H, m, Ph*H*), 3.64 (2H, s, PhCH_2), 3.55 (2H, t, CH_2OH), 2.38 (2H, t, CH_2S), 1.57 (5H, m, CH_2-CH_2, O*H*). ^{13}C NMR (400 MHz, $CDCl_3$): δ 138.71, 129.04, 128.68, 127.15, 62.61, 36.44, 31.40, 31.26, 25.63.

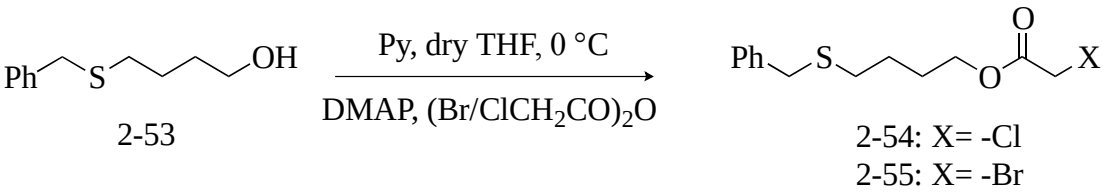

2-53

2-54: X= -Cl
2-55: X= -Br

General procedure for preparation of esters (2-54, -55):

To a cold solution of 4-(benzylthio)butan-1-ol (2-53) (0.50 g, 2.55 mmol) and pyridine (0.20 g, 2.55 mmol) in THF (5 mL), were added anhydride (2.55 mmol) and DMAP (0.03 g, 0.25 mmol) under nitrogen. The mixture was allowed to stand at room temperature for 10 h. The solvent was removed *in vacuo* and the resulting residue was dissolved in CH_2Cl_2, washed with 10% HCl and H_2O, dried over Na_2SO_4, and concentrated. The crude product was purified by flash column chromatography on silica gel using ethyl acetate:hexane as the eluent.

4-(benzylthio)butyl-chloroacetate (2-54):

Colorless liquid (0.514g, 74%). ^{1}H NMR (400 MHz, $CDCl_3$): δ 7.22 (5H, m, Ph*H*), 4.1 (2H, t, CH_2O), 3.97 (2H, s, CH_2Cl), 3.64 (2H, s, PhCH_2S), 2.38 (2H, t, SCH_2), 1.63 (2H, m, CH_2CH$_2$O), 1.57 (2H, m, CH_2CH$_2$S). ^{13}C NMR (400 MHz, $CDCl_3$): δ 167.53, 138.61, 129.03, 128.73, 127.22, 65.98, 41.08, 36.49, 30.99, 27.78, 25.69.

4-(benzylthio)butyl-bromoacetate (2-55):

Pale yellow liquid (0.542g, 67%). ^{1}H NMR (400 MHz, $CDCl_3$): δ 7.22 (5H, m, Ph*H*), 4.08 (2H, t, C*H*$_2$O), 3.74 (2H, s, C*H*$_2$Br), 3.64 (2H, s, PhC*H*$_2$S), 2.38 (2H, t, SC*H*$_2$), 1.67 (2H, m, C*H*$_2$CH$_2$O), 1.56 (2H, m, C*H*$_2$CH$_2$S). ^{13}C NMR (400 MHz, $CDCl_3$): δ 167.66, 138.59, 129.02, 128.71, 127.20, 65.99, 36.44, 30.95, 27.73, 26.03, 25.64.

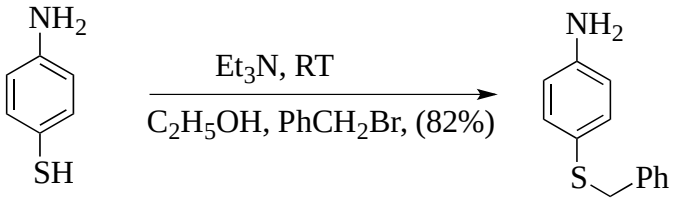

2-56

Synthesis of 4-Amino-S-benzylmercaptobenzene (2-56):

To a stirred solution of 4-aminothiophenol (2.00 g, 16 mmol) in 15 mL of EtOH, triethylamine (1.62 g, 16 mmol) and benzylbromide (2.74 g, 16 mmol) were added. The mixture was stirred at room temperature for 12 h. The solvent was removed *in vacuo* to yield a yellow oil. The oil was dissolved in CH_2Cl_2, washed with H_2O and saturated sodium bicarbonate solution, dried over Na_2SO_4, and concentrated. The crude product was purified by flash column chromatography on silica gel using ethyl acetate:hexane as the eluent to give a yellow liquid (4.25 g, 82%). ^{1}H NMR (400 MHz, $CDCl_3$): δ 7.29 (7H, m, Ph*H*), 6.67 (2H, m, Ph*H*), 4.04 (2H, s, SC*H*$_2$Ph), 3.79 (2H, bs, N*H*$_2$). ^{13}C NMR (400 MHz, $CDCl_3$): δ 146.41, 138.63, 134.94, 129.11, 128.48, 127.04, 123.12, 115.62, 41.97.

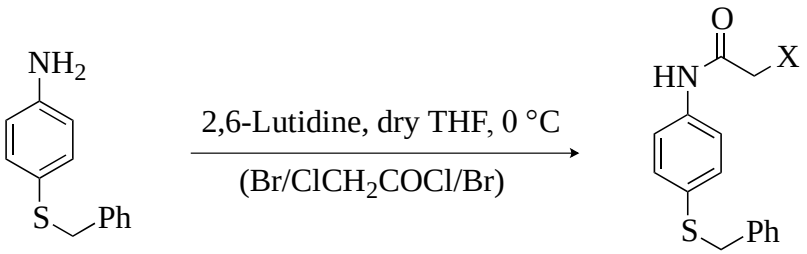

2-56

2-57: X= -Cl
2-58: X= -Br

General procedure for preparation of amides (2-57, -58):

To a cold solution of 4-amino-S-benzylmercaptobenzene (2-56) (1.50 g, 6.97 mmol) and 2,6- lutidine (0.82 g, 7.67 mmol) in THF (15 mL), acid halide (6.97 mmol) was added under nitrogen. The mixture was allowed to stand at room temperature for 8 h. The solvent was removed *in vacuo* and the resulting residue was dissolved in CH_2Cl_2, washed with 10% HCl and H_2O, dried over Na_2SO_4, and concentrated. The crude product was recrystallized from $CHCl_3$.

N-(4-(benzylthio)phenyl)-2-chloroacetamide (2-57):

yellow solid (1.52 g, 75%). ^{1}H NMR (400 MHz, $CDCl_3$): δ 8.18 (1H, br s, N*H*), 7.43 (2H, d, Ph*H*), 7.25 (7H, m, Ph*H*), 4.16 (2H, s, CH_2Cl), 4.05 (2H, s, SCH_2Ph). ^{13}C NMR (400 MHz, $CDCl_3$): δ 163.89, 137.66, 135.63, 132.62, 131.76, 129.04, 128.71, 127.42, 120.60, 43.05, 39.95.

N-(4-(benzylthio)phenyl)-2-bromoacetamide (2-58):

brown solid (1.87 g, 80%). ^{1}H NMR (400 MHz, $CDCl_3$): δ 8.09 (1H, bs, N*H*), 7.41 (2H, d, Ph*H*), 7.24 (7H, m, Ph*H*), 4.05 (2H, s, CH_2Br), 3.99 (2H, s, SCH_2Ph). ^{13}C NMR (400 MHz, $CDCl_3$): δ 163.41, 137.64, 135.85, 132.55, 131.72, 129.03, 128.71, 127.42, 120.51, 39.94, 29.65.

2.5.8. Control experiments:

a) G-N-MWCNTs and chloroplatinic acid solution (2-59):

To G-N-MWCNTs (25 mg), 10 mL EtOH, was added chloroplatinic acid solution (50 wt. %) (33.15 mg) in EtOH (5 mL) and the resulting mixture was bath sonicated for 1 h. The mixture was either rota-evaporated or filtered, dried under vacuum overnight, weighed and characterized.

b) G-N-MWCNTs and with Au nanoparticles (2-60):

G-N-MWCNTs (10 mg), Au nanoparticles (2, 10 nm) (1.5 mL), and EtOH (2.5 mL) were stirred at RT for 24 h. The resulting N-MWCNTs were then subsequently washed and filtered on 0.2 μm nylon membrane filters with EtOH, dried under vacuum overnight, weighed and characterized.

c) Me-G-N-MWCNTs and with Au nanoparticles (2-61):

G-N-MWCNTs reduced/alkylated (MeI) in EDA (2-21) (10 mg), Au nanoparticles (2, 10 nm) (1.5 mL), and EtOH (2.5 mL) were stirred at RT for 24 h. The resulting N-MWCNTs were then subsequently washed and filtered on 0.2 µm nylon membrane filters with EtOH, dried under vacuum overnight, weighed and characterized.

2.5.9. Treatment of G-N-MWCNTs with HNO_3[81]:

A suspension of 0.25 g of G-N-MWCNTs in 50 mL of nitric acid (70 wt%) was subjected to bath sonication for 30 minutes. The flask was then equipped with a condenser and a magnetic stir bar. The dispersion was stirred and heated at reflux for periods of 6, 12 and 24 hours. After that, the resulting dispersion was diluted in water, filtered and washed with water to neutral pH and then with ethanol. The resulting solid was dried in vacuum for overnight.

Table 2-9 HNO_3 oxidation of G-N-MWCNTs as a function of time.

Starting N-MWCNTs	Time of treatment	Compound #
G-N-MWCNTs	6 h	**2-62**
G-N-MWCNTs	12 h	**2-63**
G-N-MWCNTs	24 h	**2-64**

2.5.10. Treatment of G-N-MWCNTs with piranha solution[76]:

A suspension of 0.25 g of the G-N-MWCNTs in 50 mL of a 70:30 mixture of sulfuric acid (96 wt%) and hydrogen peroxide (30 wt%) in a 100 mL round bottom flask equipped with a condenser and the mixture was stirred at room temperature for periods of 12 and 24 hours. After that, the resulting dispersion was diluted in water, filtered and washed with water to neutral pH and then with ethanol. The resulting solid was dried in vacuum for overnight.

Table 2-10 Piranha treatment of G-N-MWCNTs with varying time.

Starting N-MWCNTs	Time of treatment	Compound #
G-N-MWCNTs	12 h	**2-65**
G-N-MWCNTs	24 h	**2-66**

2.5.11. Treatment of G-N-MWCNTs with Fenton reagent (2-67):

To 75 mL of water in 250 mL round bottom flask was added 0.25 g of G-N-MWCNTs. To the stirred suspension were added 125 mg of ferrous sulfate 7-hydrate and then 25 mL of 30% hydrogen peroxide. The mixture was allowed to stir for 24 hours, filtered, washed with water and ethanol and dried in vacuum for overnight. The residual iron was removed by stirring the product with 20 mL of 48 wt% hydrobromic acid for 6h.

2.5.12. Treatment of G-N-MWCNTs with H_2SO_4:HNO_3[82]:

To 0.25 g of the G-N-MWCNTs was added 60 mL of a 3:1 mixture of sulfuric acid (96 wt%) and nitric acid (70 wt%). The mixture was subjected to bath sonication at room temperature for periods of either 12 or 24 hours. After that, the resulting dispersion was diluted in water, filtered and washed with water to neutral pH and then washed with ethanol. The resulting solid was dried in vacuum overnight.

Table 2-11 H_2SO_4:HNO_3 treatment of G-N-MWCNTs with varying time.

Starting N-MWCNTs	Time of treatment	Compound #
G-N-MWCNTs	12 h	**2-68**
G-N-MWCNTs	24 h	**2-69**

2.5.13. Treatment of G-N-MWCNTs with $KMnO_4$:H_2SO_4[83] (SCNs) (2-70):

G-N-MWCNTs (0.15 g) were suspended in 150 ml of conc. H_2SO_4 for 24 h (bath sonication), then $KMnO_4$ (750 mg, 4.75 mmol) was added. After stirring for 1 h at room temperature, the mixture was heated at 55 °C for 30 min. The temperature was further increased to 65 °C for 15 min and finally to 70 °C. When the temperature stabilized at 70 °C, the reaction mixture was removed from heating and allowed to cool to room temperature. The mixture was poured into 400 ml of ice water containing 5 ml of 30% H_2O_2. The solid material was filtered under vacuum through a PTFE membrane. Following stirring of solid material in water (150 mL) for 30 min, it was subjected to bath-sonication for another 15 min. Addition of 20 vol% concentrated HCl (30 ml) flocculated the material that was again filtered through a PTFE membrane. The solid material obtained was stirred in ethanol (150 ml) for

30 min and then bath-sonicated for 15 min. Flocculation occurred on addition of ether (150 ml) and the product was collected by filtration through a PTFE membrane. Washing with ether (2x50 ml) and drying *in vacuo* afforded oxidized nanotubes.

2.5.14. Control experiments:

a) Air oxidation of as-prod-N-MWCNTs **(2-71):**
A sample of as-prod-N-MWCNTs on a crucible was inserted into a 25 cm long quartz tube. The quartz tube was placed in a tube furnace (Lindberg/Blue M tube furnace, model: TF55035A) and heated at 400 °C for 4 h in air.

b) HBr treatment to remove catalyst **(2-72):**
To air oxidized N-MWCNTs (2-72) (0.15g) was added 30 mL hydrobromic acid (48 wt%) and the resulting mixture was heated at 60 °C for 12h. After that, the resulting dispersion was diluted in water, filtered and washed with water to neutral pH and then washed with ethanol. The resulting solid was dried in vacuum overnight.

c) Piranha oxidation of as-prod-N-MCNTs **(2-73):**
A suspension of 0.25 g of as-prod-N-MCNTs in 50 mL of a mixture of sulfuric acid (96 wt%) and hydrogen peroxide (30 wt%) in ratio 70:30 in a 100 mL round bottom flask equipped with a condenser and the mixture was stirred at room temperature for 24 h. After that, the resulting dispersion was diluted in water, filtered and washed with water to neutral pH and then with ethanol. The resulting solid was dried in vacuum for overnight.

d) Fenton oxidation of as-produced N-MWCNTs **(2-74):**
Added 0.25 g of as-prod-N-MCNTs to 75 mL of water in 250 mL round bottom flask. To the stirred solution were added 125 mg of ferrous sulfate 7-hydrate and then 25 mL of 30% hydrogen peroxide. The solution was allowed to stir for 24 hours, filtered, washed with water and ethanol and dried in vacuum for overnight. The residual iron was removed by stirring the product with 48 wt% 20 mL hydrobromic acid for 6h.

e) Piranha oxidation of 2-73 (Fe removed as-prod-N-MWCNTs) **(2-75):**
A suspension of 0.05 g of 2-73 (Fe removed as-prod-N-MWCNTs) in 10 mL of a mixture of sulfuric acid (96 wt%) and hydrogen peroxide (30 wt%) in ratio 70:30 in a 100 mL round bottom flask equipped with a condenser and the mixture was stirred at room temperature for 24 h. After that, the resulting dispersion was diluted in water, filtered and washed with water to neutral pH and then with ethanol. The resulting solid was dried in vacuum for overnight.

f) Fenton oxidation of 2-73 (Fe removed as-prod-N-MWCNTs) **(2-76):**
Added 0.05 g of 2-73 (Fe removed as-prod-N-MWCNTs) to 15 mL of water in 25 mL round bottom flask. To the stirred solution were added 125 mg of ferrous sulfate 7-hydrate and then 5 mL of 30% hydrogen peroxide. The solution was allowed to stir for 24 hours, filtered, washed with water and ethanol and dried in vacuum for overnight. The residual iron was removed by stirring the product with 48 wt% 4 mL hydrobromic acid for 6h.

g) Fe oxidizes combustion of carbon **(2-77)**:
Added 0.01 g of Fenton oxidized G-N-MWCNTs **(2-67)** to a stirred solution of 5 mg of ferrous sulfate 7-hydrate in 3 mL of water. The dispersion was stirred for an h and then rota-evaporated and dried.

Chapter 3

Longitudinal Cutting of N-MWCNTs and ribbon formation[§]

3.1. Overview

This chapter presents the results and discussion of the channeling reaction observed in N-MCWNTs under reducing and oxidizing conditions. An investigation of the behavior of similar N-MCWNT structures was made to see how the MWCNT morphology determines the outcome of these reactions. To further unroll and exfoliate channeled materials, different techniques were applied. A detailed account on these attempts can be found later in the chapter. Based on observations from experiments and other analytical methods, a hypothesis on the origin of formation of spiraled and linear channels and spiraled carbon nanoribbons (SCNs) is presented.

3.2. Introduction

With the discovery of graphene in the twenty-first century[99, 100], researchers around the world are directing their studies towards the bulk synthesis of graphene and graphene nanoribbons (GNRs). Recently, unzipped MWCNTs have been used to form GNRs[83, 96, 101-109]. Several articles have reported processes for cutting open carbon nanotubes in the lengthwise (longitudinal) direction[83, 96, 101-109]. Figure 3-1 shows different ways in which MWCNTs could be unzipped to yield GNRs. Some of these processes include (Figure 3-1):

a) intercalation/exfoliation of MWCNTs;
   1) removal of the tube caps using acid treatments, followed by treatments in liquid NH_3 and Li, and then subsequent exfoliation by heat treatment[101];
   2) exposing pristine MWCNTs to hot potassium vapor followed by exfoliation using bath sonication in chlorosulfonic acid[102]

[§] A part of this chapter has already been published; Meier, M. S.; Selegue, J. P.; Cassity, K. B.; Kaur, A.; Qian, D. Journal of Physics: Condensed Matter 2010, 22, 334219.

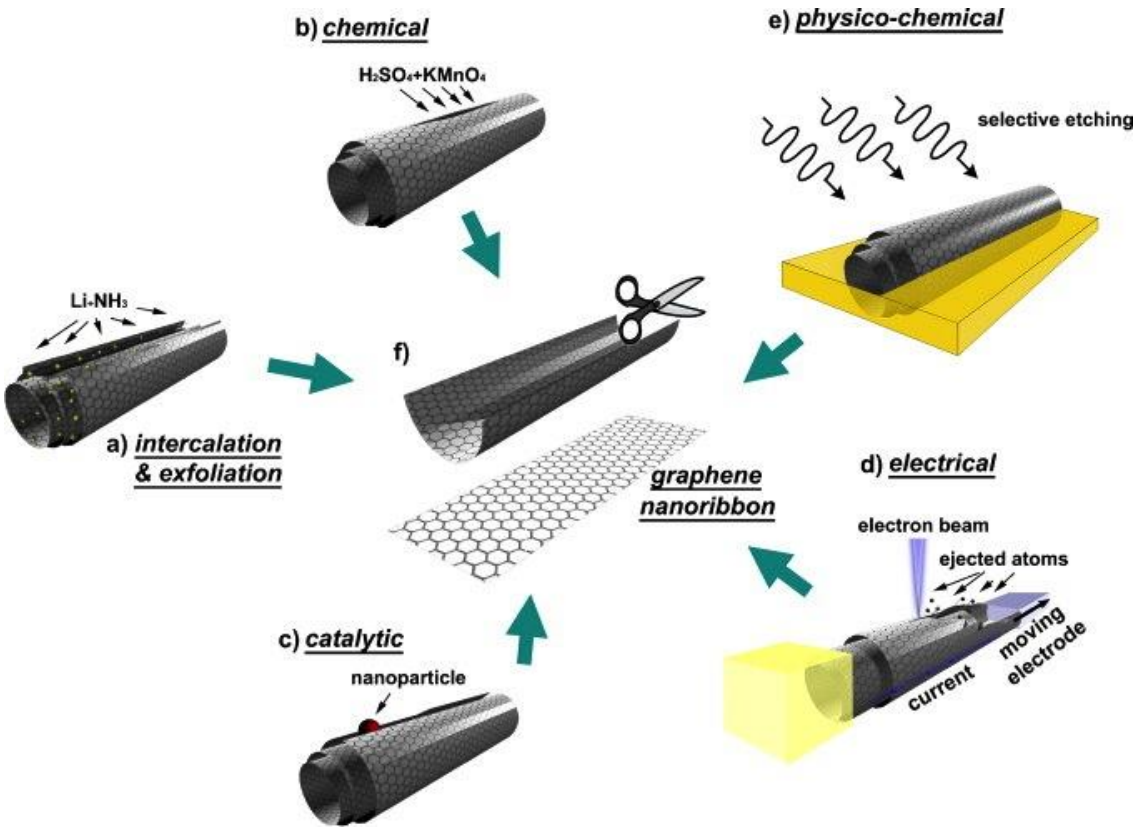

Figure 3-1 Sketch showing different ways to unzip MWCNTs to yield GNRs[110].

b) wet chemical methods, involving $H_2SO_4/KMnO_4$[83] and H_2SO_4/HNO_3[96] as oxidizing agents;

c) catalytic approach, in which metal nanoparticles cut the nanotube longitudinally like a pair of scissors[103];

d) electrical method, by passing an electric current through a nanotube[105];

e) physicochemical method, by embedding the CNTs in a polymer matrix followed by Ar plasma[104];

f) electrochemical method, which consists of the oxidation of CNTs at controlled potential, followed by reduction to form GNRs[109];

g) plasma treatment, in which MWCNTs are exposed to hydrogen/oxygen plasma in a DC-PECVD reactor at elevated temperatures[107];

h) STM tip, partial or total unzipping of the outer CNT layer functionalized by cycloaddition reaction, which is triggered by the STM tip, under specific operating conditions[108]; and

i) Unrolling ‘stacked-cup’ carbon nanotubes (CSCNTs) by the solution phase oxidation and reduction[106].

Other than longitudinal unzipping of MWCNTs, other textural changes are also observed upon physical/chemical treatment of carbon materials, in particular stacked carbon materials. Upon reduction with sodium naphthalenide in THF[111], cup-stacked carbon nanotubes consisting of truncated conical graphene layers, are known to un-stack rather than to tear open (Figure 3-2). N-MWCNTs undergo current-induced structural transformation; i.e., from the typical bamboo structure of N-MWCNTs to the stacked cones, when investigated using in situ TEM[112].

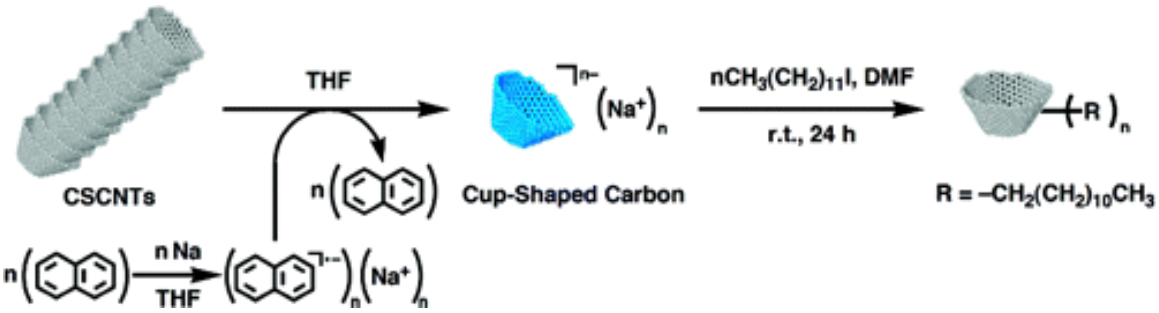

Figure 3-2 Sketch showing un-stacking of cones upon reduction with sodium naphthalenide[111].

In our previous publications, we reported longitudinal cutting in N-MWCNTs under dissolving metal reduction/alkylation conditions (Li/NH_3 and Li/EDA) that resulted in the formation of spiraled and linear channels[72, 73] in tubes. To our surprise, similar observations on channeling reaction were made under oxidative conditions (H_2SO_4/HNO_3 and H_2SO_4/$KMnO_4$). Presented below are the details of the channeling reaction under reducing and oxidizing conditions.

3.3. Results and discussion

3.3.1. Channeling reaction under dissolving metal reduction-alkylation conditions:

Treatment of G-N-MWCNTs with lithium in anhydrous ammonia and quenching with thiol-containing ligands, lead to the formation of tight spirals in tubes (Figure 2-11and 3-3). The channels extend into the inner core of the tubes, cutting through every layer of graphene. In some cases, a single helicity (either right or left-handed) is seen, but in many cases a double thread (both left- and right-handed spirals) is observed. The

triangular flaps seen in SEM (Figure 2-11and 3-3) are cuts at angles very close to 120° and 60°, as found in graphene lattice.

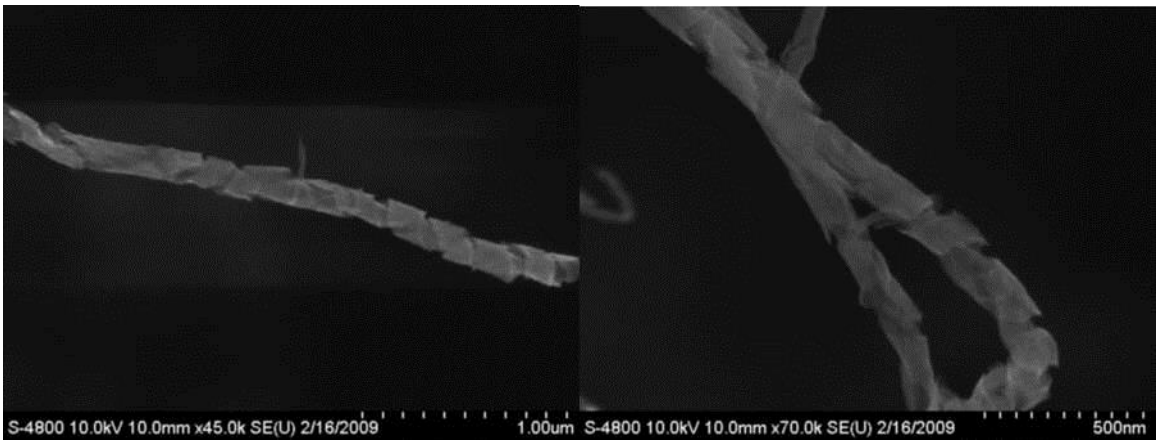

Figure 3-3 SEM of spiraled channels upon reduction/alkylation of G-N-MWCNTs in ammonia.

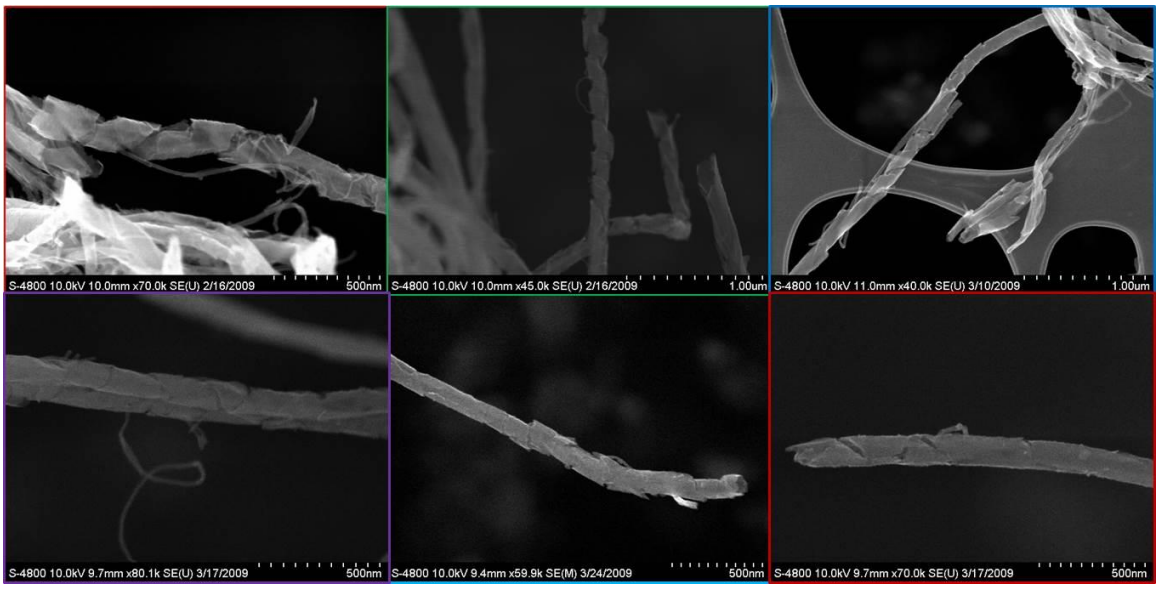

Figure 3-4 SEM of spiraled channels upon reduction/alkylation of G-N-MWCNTs in ammonia with different electrophiles.

We have found that the formation of spiral channels is independent of the electrophile; (4-(benzylthio)butyl chloroacetate, 4-(benzylthio)butyl bromoacetate, N-(4-(benzylthio)phenyl)-2-chloroacetamide, N-(4-(benzylthio)phenyl)-2-bromoacetamide, ethyl bromoacetate, ammonium chloride and methyl iodide) and also of the type of halide (chloride or bromide) being used in dissolving metal

reduction conditions. Figure 3-4 shows SEM images of samples that were treated with different electrophiles. Figure 3-5 represents STEM and TEM of the spiraled channeled samples. TEM reveals that these fractures are ~35-65 nm wide.

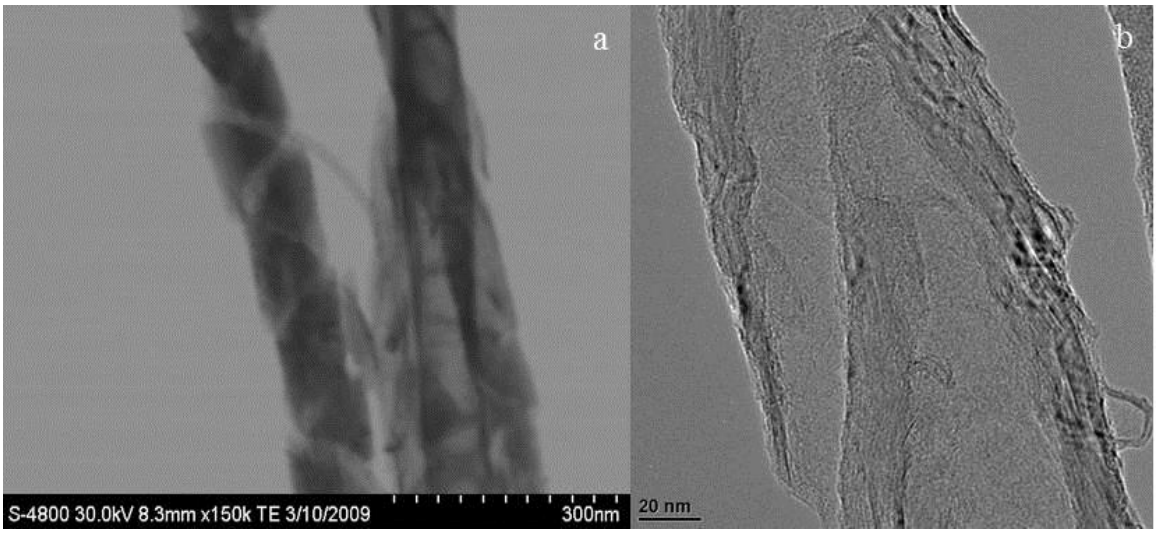

Figure 3-5 (a) STEM and (b) TEM of spiraled channels upon reduction/ alkylation of G-N-MWCNTs in ammonia.

The channeling reaction was not limited to individual tubes but it affected the bulk of the sample, as confirmed by TGA and surface area analysis. Bulk changes in sample were also observed by looking at different locations of the sample under SEM. SEM (Figure 3-6) revealed that spirals were formed throughout the sample.

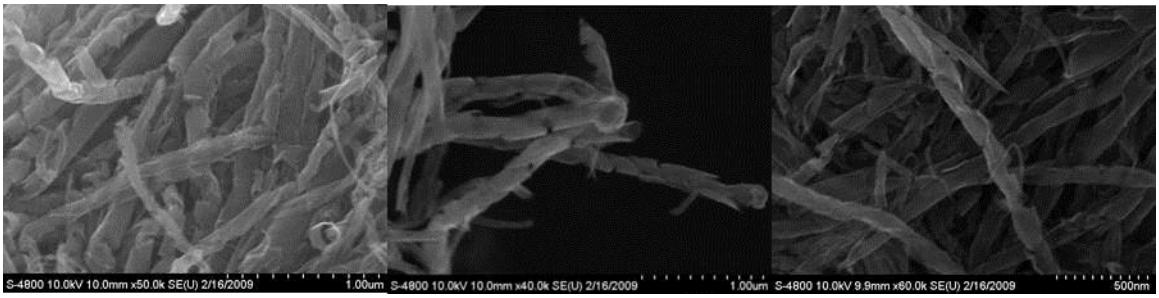

Figure 3-6 SEM of spiraled channels upon reduction/alkylation of G-N-MWCNTs in ammonia.

We anticipated that these spiral channeled materials would be thermally less stable than the starting G-N-MWCNTs. In Figure 3-7, is shown a derivative TGA plot comparing the T_o of various alkylated G-N-MWCNTs with T_o of G-N-MWCNTs. The shift in T_o in all the treated samples can be correlated with the damage done on the tubes suggested by the SEM. The black curve depicts G-N-MWCNTs that are thermally stable up to ~800 °C in air. A shift of ~150 °C is seen in sample treated with ammonium chloride (purple) This shift can be rationalized as resulting from the presence of reactive sp^3 sites available to initiate decomposition in the treated samples while only graphite-like sp^2 carbons are present in the untreated sample. Similar shifts were observed in the case of other samples treated with 4-(benzylthio)butyl bromoacetate (green), N-(4-(benzylthio)phenyl)-2-bromoacetamide (red) and ethyl bromoacetate (blue).

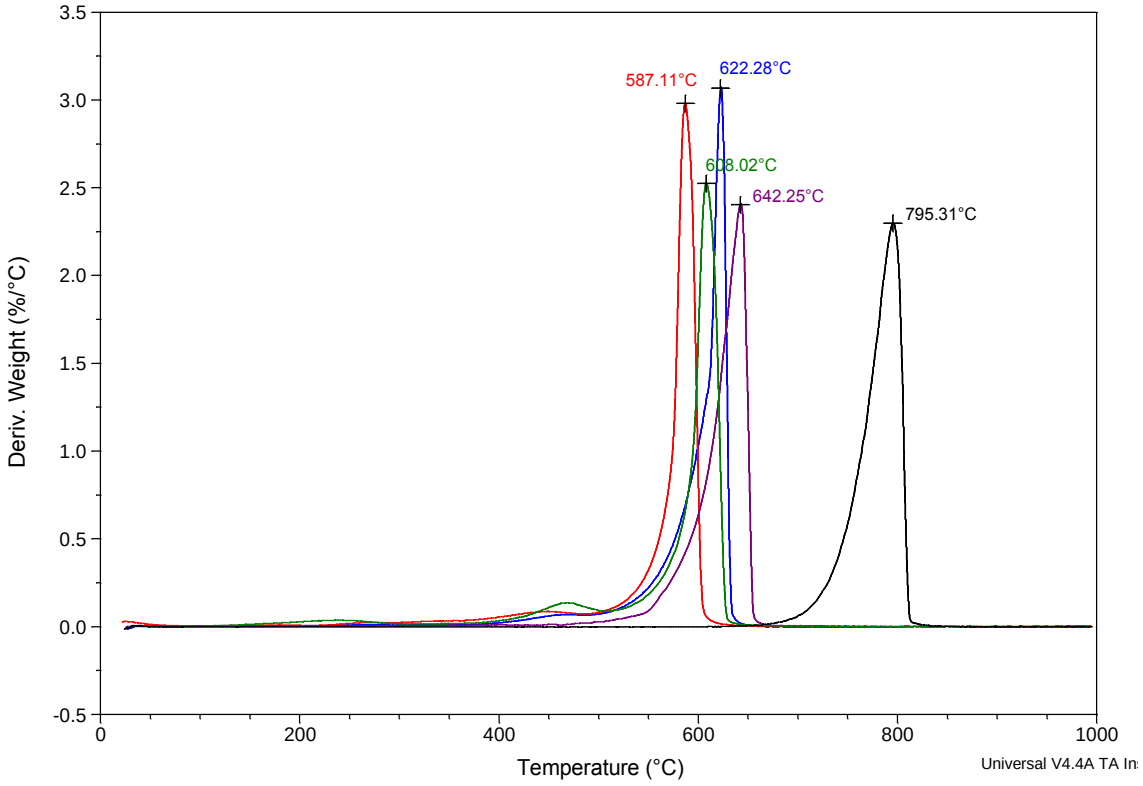

Figure 3-7 Derivative TGA plot comparing G-N-MWCNTs with products of dissolving metal reductions in ammonia with different electrophiles.

When reduction/alkylation of G-N-MWCNTs is carried out in EDA, the tubes are channeled in linear manner (Figure 3-8(a)). Subjecting these nanotubes to a second reduction/alkylation in ammonia, the initial linear channels open up significantly (Figure 3-8(b)).

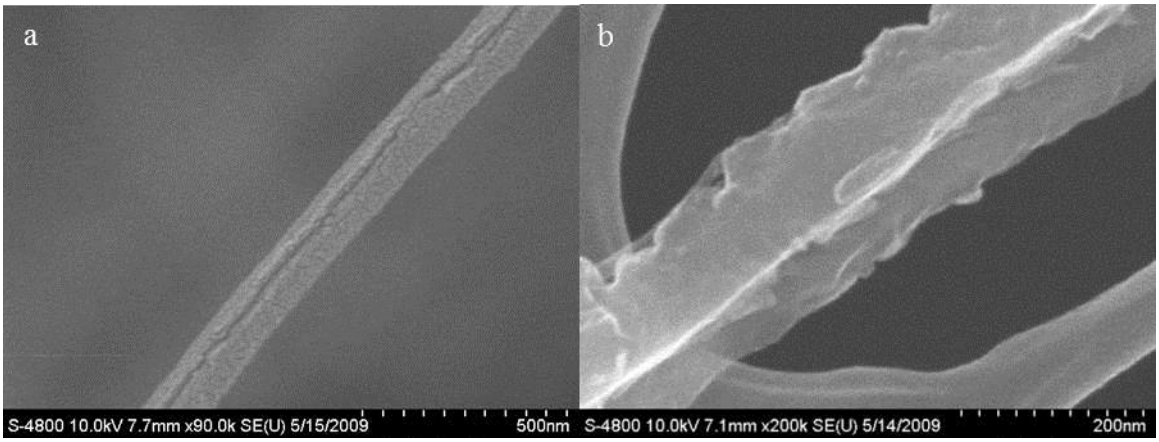

Figure 3-8 SEM of linear channels upon reduction/alkylation of G-N-MWCNTs (a) in EDA and (b) in EDA followed by in ammonia.

Table 3-1 lists the surface areas of G-N-MWCNTs and channeled tubes measured by nitrogen physisorption at 77 K using the BET model. Surface area analysis supports the TGA observations. These bulk measurements are consistent with impressions generated by the SEM analyses in Figures 3-6 and 3-8. Material that has been converted into a spiral has significantly greater surface area than G-N-MWCNTs (91 m^2/g compared to 34 m^2/g) and material with linear fractures (91 m^2/g compared to 69 m^2/g) with a concomitant tripling of the total pore volume. Similarly, the sample that has seen two reductions, first in EDA and then in ammonia, showed a similar increase in total surface area and total pore volume.

Surface area measurement confirms that the channeling reaction is not limited to a few individual nanotubes, but substantially changes the bulk material. A convenient classification of pores, according to their average diameter, is recommended by the International Union of Pure and Applied Chemistry (IUPAC):

- micropores, size less than 2 nm;
- mesopores, size between 2 nm and 50 nm; and

- macropores, size more than 50 nm

In a sample reduced in EDA, the increase in surface area may be largely due to a significant increase in the mesopore fraction of the pore size distribution, consistent with the observed size (~ 5-15 nm) of the channels in those samples. The spiral channeled sample shows a negligible increase in mesopore fraction and a considerable increase in macropore fraction. TEM reveals that these channels are ~ 35-65 nm wide. As the diameter of the spiral channeled material is on the border between mesopore and macropore sizes, it is hard to apply this nomenclature definitively. The porosity distribution of the sample that has been subjected to two separate reduction steps suggests that the increase in the surface area is mainly due to a significant increase in the macropore fraction that is consistent with the pore size, as suggested by SEM.

Table 3-1 Surface area analysis of channeled G-N-MWCNTs.

Sample	Surface area[a] (m^2/g)	Pore volume (cm^3/g)	Micropore (%) (< 2 nm)	Mesopore (%) (2-50 nm)	Macropore (%) (> 50 nm)
G-N-MWCNTs	34	0.12	4.5	46.2	49.3
G-N-MWCNTs alkylated[b] in NH_3	91	0.38	1.3	47.0	51.7
G-N-MWCNTs alkylated[b] in EDA	69	0.23	2.2	52.9	44.9
G-N-MWCNTs alkylated[b] in EDA and then in NH_3	86	0.36	0.9	40.4	58.7

[a] Average of three runs, [b] MeI was used as the alkylating agent.

3.3.2. Channeling reaction under oxidizing conditions:

Channeling of G-N-MWCNTs under oxidizing conditions (H_2SO_4/HNO_3 and $H_2SO_4/KMnO_4$) was surprising, as the results were different from oxidation with HNO_3, piranha and Fenton oxidations. The morphology of the channels formed with $H_2SO_4/KMnO_4$ was quite different. The ribbon texture here is more distinct with

distance between the turns of the helix being 100-150 nm (Figure 3-9). We refer these as SCNs.

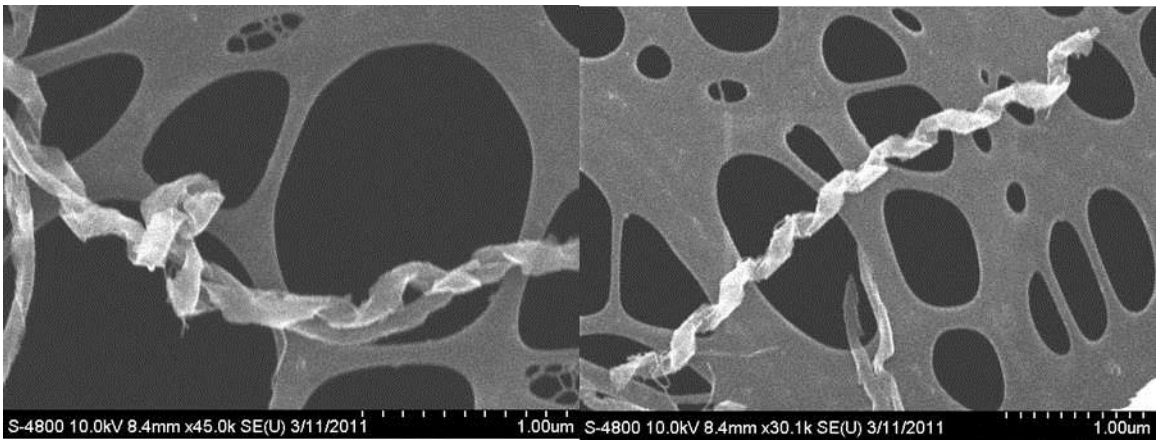

Figure 3-9 SEM of SCNs.

Channeling of G-N-MWCNTs with H_2SO_4/HNO_3 was observed under sonication conditions. The formation of spiraled channels in G-N-MWCNTs upon sonication in H_2SO_4/HNO_3 for 24 h was confirmed by running SEM and STEM consecutively (Figure 3-10).

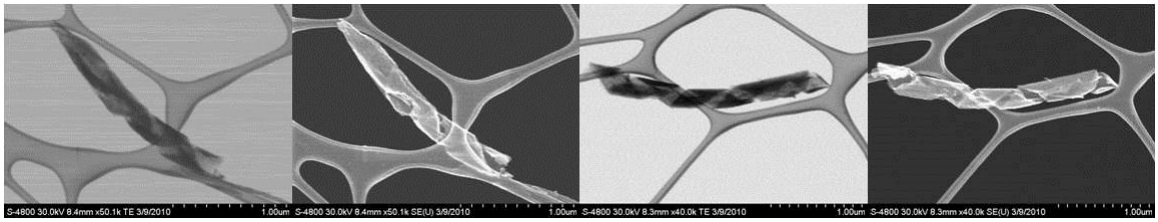

Figure 3-10 STEM and SEM images of G-N-MWCNTs treated with H_2SO_4/HNO_3 (sonication for 24h).

In order to determine if the oxidizing mixture (H_2SO_4/HNO_3) or the sonication were responsible for the formation of channels, a comparative study was done. In one study, the tubes were sonicated in water for 12 h (3-1) and in the other study the tubes were stirred in a H_2SO_4/HNO_3 (3:1) mixture for 12 h (3-2). SEM (Figure 3-11(a)) does not indicate formation of channels in G-N-MWCNTs that were sonicated in water. But G-N-MWCNTs stirred in H_2SO_4/HNO_3 showed formation of spiraled

channels (Figure 3-11(b)). The results suggest that oxidizing mixture is required for formation of channels. Sonication as such is not a requirement for channeling, although it might have an added effect in oxidizing mixtures.

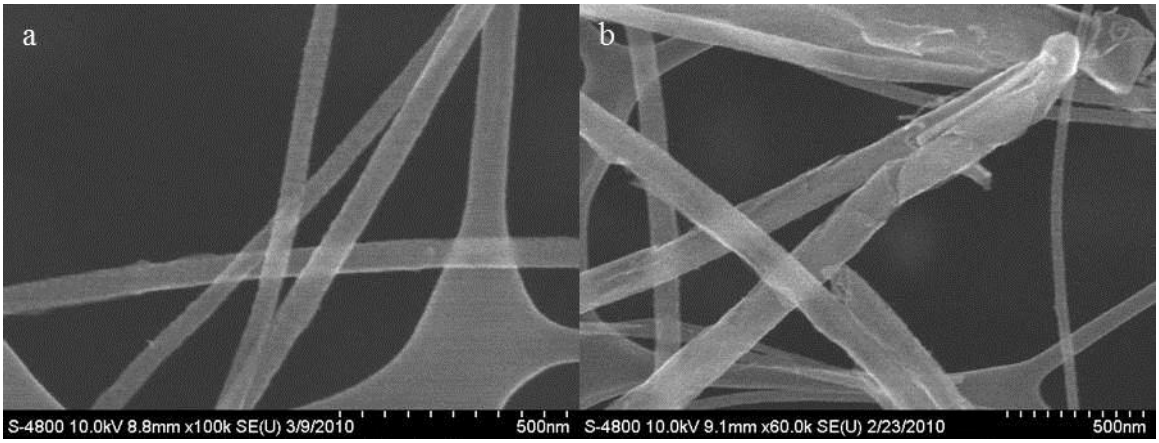

Figure 3-11 SEM images of G-N-MWCNTs treated with (a) water (sonication for 12 h) and (b) H_2SO_4/HNO_3 (stirring for 12 h).

The surface area of G-N-MWCNTs channeled under oxidizing conditions was determined by nitrogen physisorption. The results show that upon oxidation of G-N-MWCNTs with a mixture of H_2SO_4/HNO_3 (sonication for 24h), the surface area increased from 34 m^2/g to 63 m^2/g. This increase was not as large as the increase we have observed for samples treated under reducing conditions in ammonia, but it is similar to the increase we observed upon the reduction in EDA. Upon $KMnO_4$ oxidation of G-N-MWCNTs, the surface area increased to 240 m^2/g, with a total pore volume of 0.54 cm^3/g and the resulting material was highly mesoporous (~ 75%) which can easily be seen from the nitrogen adsorption isotherm (Figure 3-12(a)) and corresponding plot of incremental surface area vs. pore width (Figure 3-12(b)).

In general, physisorption isotherms can be grouped into six types shown in Figure 3-13. Type I isotherms are typical of adsorbents with microporous structures. The majority of pore filling occurs at a low relative pressure (below 0.1) and usually the process is completed by ~0.5 P/P_o. Type II isotherms are common to either non-porous solids or a mixture of micro and mesoporous solids. At relatively high pressures, monolayer coverage leads to multilayer formation. Type III and Type V

isotherms are convex to the relative pressure axis, depicting a weak adsorbate-adsorbent interaction. Adsorbate-adsorbate interactions accelerate the uptake at higher relative pressures. Type III isotherms typify nonporous and microporous solids, while Type V isotherms are associated with micro and mesoporous solids. Type IV isotherms (also Type V) possess a hysteresis loop. A hysteresis loop is associated with capillary condensation taking place in mesopores. Type VI isotherm represents stepwise adsorption with the step height being a measure of the monolayer capacity for each adsorbed layer. The step height remains nearly constant indicative of an extremely homogeneous material.

SCNs exhibit a type IV isotherm with a steep condensation step between 0.50 and 0.45 P/ P_o, indicating the formation of new mesopores[113], while G-N-MWCNTs showed virtually no hysteresis in the nitrogen desorption loop. The pronounced hysteresis loop seen in the Type IV nitrogen adsorption isotherm exhibited by this material is indicative of capillary condensation in mesopores, and likely reflects the addition of mesoporosity due to opening of the cores rather than addition of external surface roughness which would increase area but would result in a more conventional adsorption behavior without capillary effects. It should also be noted that the isotherm (Figure 3-12(a)) lacks a high pressure plateau, usually indicative of a narrow pore size distribution with pore sizes tending toward the smaller end of the mesopore regime, as exhibited here (Figure 3-12(b)).

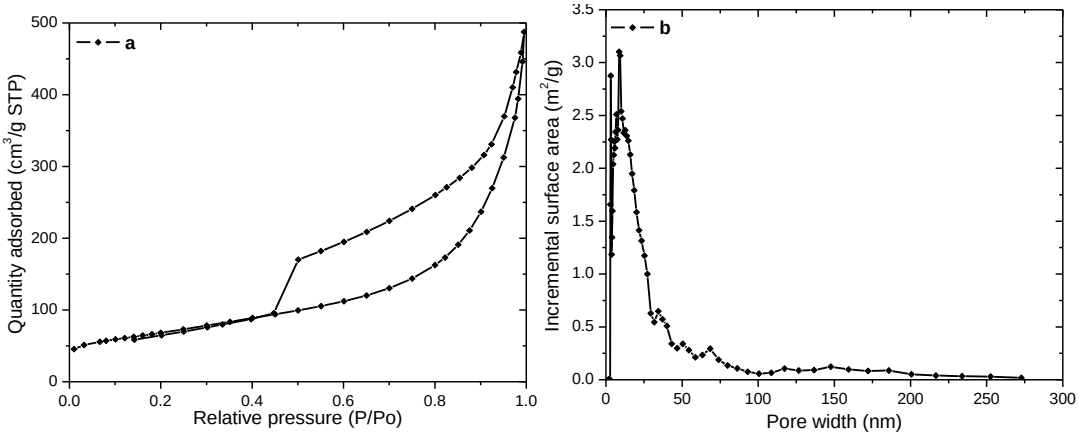

Figure 3-12 a) Adsorption isotherm and b) plot of incremental surface area vs. pore width in $KMnO_4/H_2SO_4$ oxidized G-N-MWCNTs (SCNs).

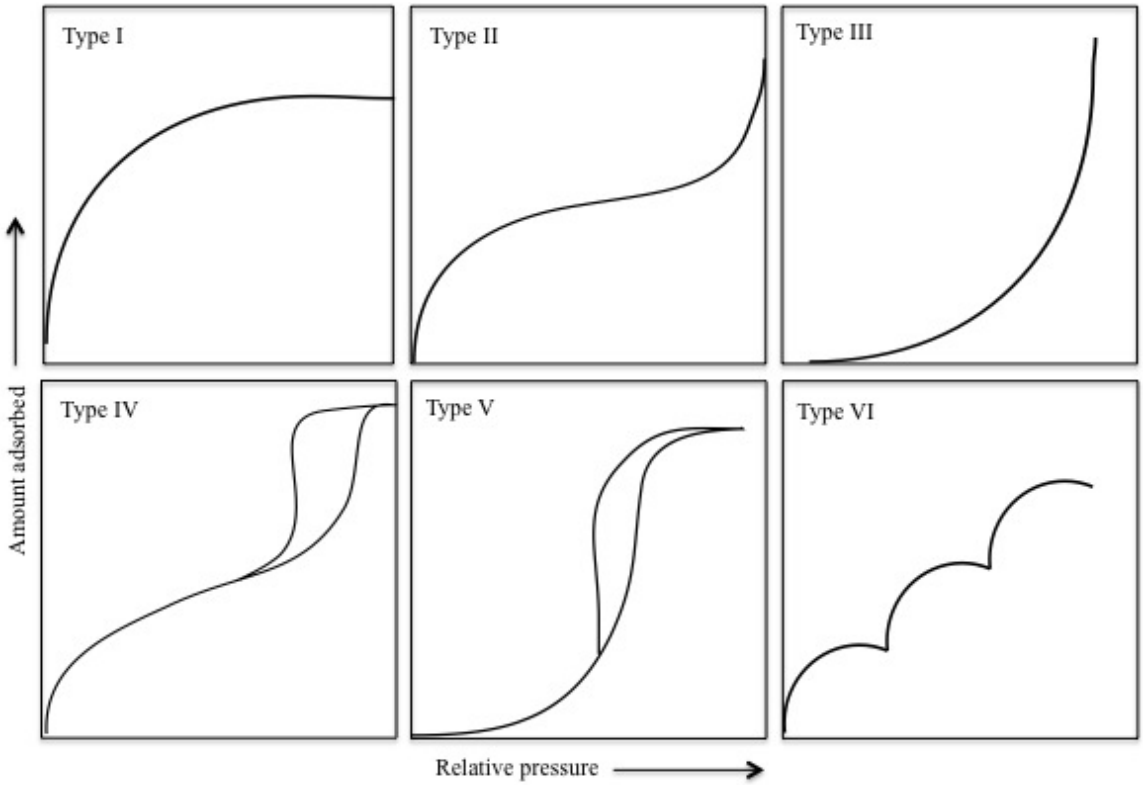

Figure 3-13 Six types of adsorption isotherms.

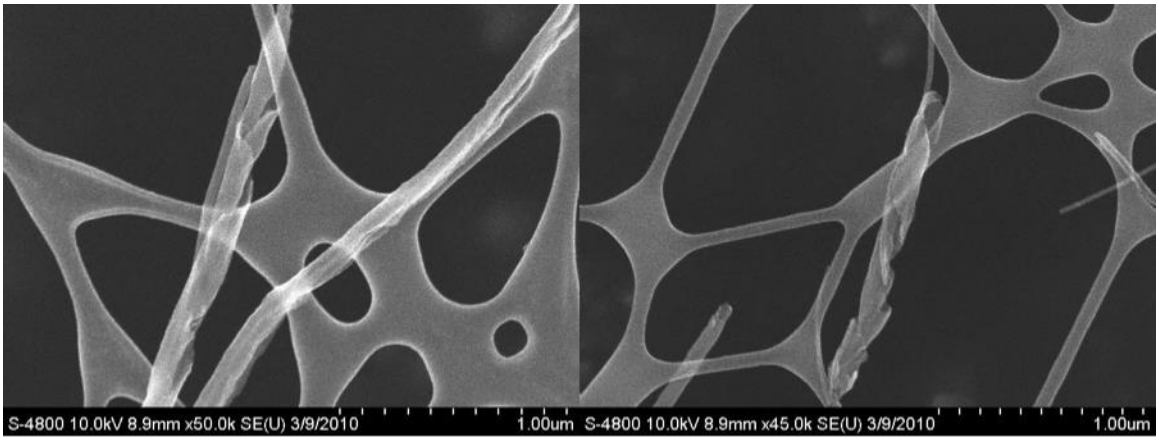

Figure 3-14 SEM of as-prod-N-MWCNTs treated with H_2SO_4/HNO_3.

We observed that both as-prod-N-MWCNTs and G-N-MWCNTs channel under dissolving metal reduction conditions. To find out if as-prod-N-MWCNTs channel under oxidizing conditions as well, they were subjected to treatment with H_2SO_4/HNO_3 (3-3) and H_2SO_4/$KMnO_4$ (3-4). Microscopy (Figures 3-14 and 3-15) suggests similar behavior to that seen with G-N-MWCNTs. Perhaps there is an underlying structural feature responsible for the formation of the channels, a feature that is sufficiently stable and is not removed by annealing at 2800 °C. Also, the

observation that the channeling reaction occurs on annealed material proves that the channeling process is independent of the presence of nitrogen.

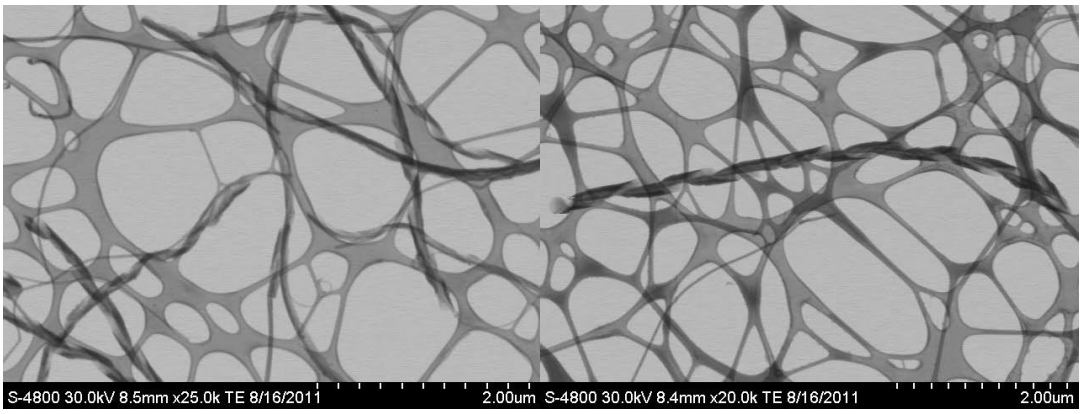

Figure 3-15 STEM of as-prod-N-MWCNTs treated with $H_2SO_4/KMnO_4$.

3.3.3. Channeling reaction in acetonitrile derived N-MWCNTs:

Thus far, the entire results reported on channeling reaction in this chapter have been performed on N-MWCNTs made from a pyridine feedstock in a 4-inch tube reactor. To confirm that channeling reaction is independent of the use of nitrogen containing hydrocarbon precursor during CVD, it was necessary to perform the reaction on N-MWCNTs that were derived from a different nitrogen source. We received a batch of as-prod-N-MWCNTs made from a mixture of acetonitrile and ferrocene in a 4-inch tube reactor, again produced at CAER. From TEM images, the acetonitrile derived N-MWCNTs look essentially identical in texture to pyridine derived N-MWCNTs.

When acetonitrile derived as-prod-N-MWCNTs were subjected to dissolving metal reduction/alkylation (3-5), the tubes were essentially just as susceptible to the channeling reaction as the pyridine derived as-prod-N-MWCNTs. TEM suggests formation of channels in almost every tube (Figure 3-16). When acetonitrile derived as-prod-N-MWCNTs were subjected to oxidizing conditions ($H_2SO_4/KMnO_4$) (3-6), similar spiraled ribbon structures were observed as with the pyridine derived as-prod-N-MWCNTs (Figure 3-17). The results suggest that the channeling reaction is not solely dependent on the use of pyridine derived N-MWCNTs, but are also independent of nitrogen source.

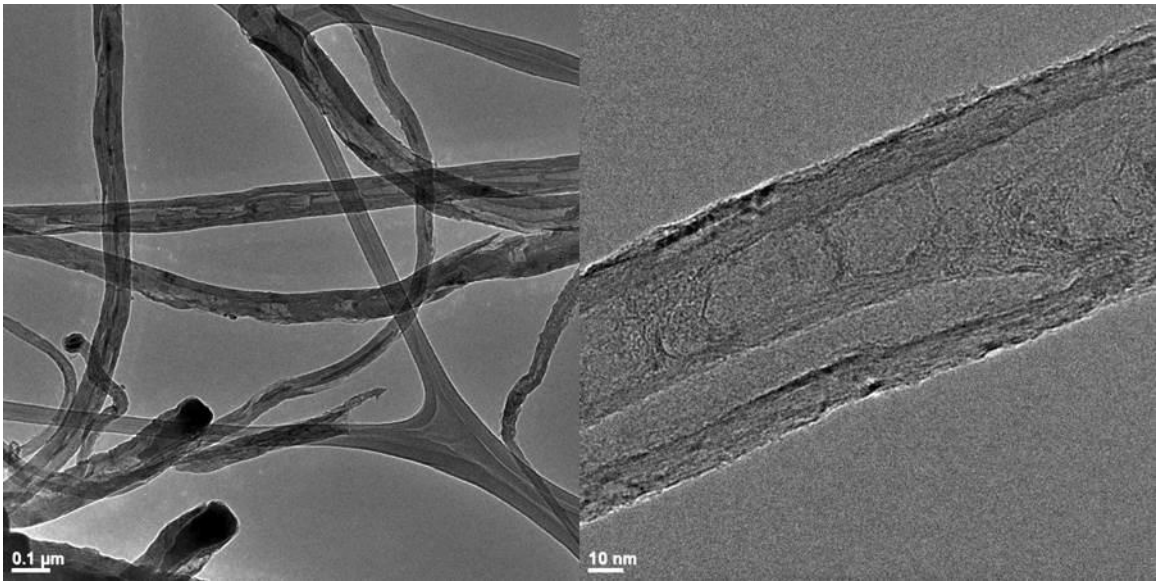

Figure 3-16 TEM of as-prod-N-MWCNTs (acetonitrile derived) upon reduction/alkylation.

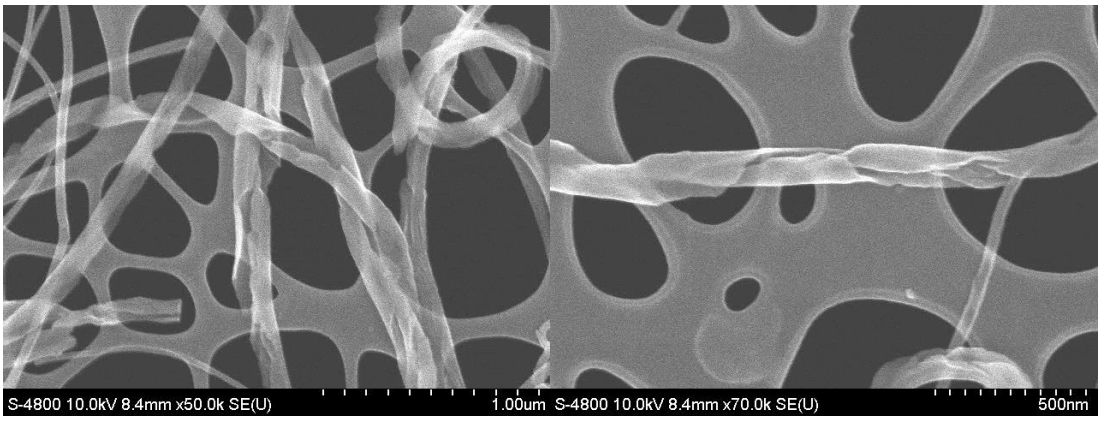

Figure 3-17 SEM of as-prod-N-MWCNTs (acetonitrile derived) upon treatment with $H_2SO_4/KMnO_4$.

To summarize the results so far, channels and spiraled ribbons are formed from N-MWCNTs under widely differing conditions (reducing conditions with Li/NH_3; Li/EDA and oxidizing conditions with $KMnO_4/H_2SO_4$; HNO_3/H_2SO_4). The channeling reaction changes the bulk of the material as suggested by surface area and TGA results. Spiraled channels are formed upon reduction in ammonia and oxidation in HNO_3/H_2SO_4, linear channels are formed on reduction in EDA and a new and interesting texture (SCNs) are formed upon oxidation in $KMnO_4/H_2SO_4$. SCNs are highly mesoporous; so they may have interesting applications. The channeling reaction is independent of:

- electrophile used under dissolving metal reduction conditions;
- presence of nitrogen and defects (annealable at 2800 °C); and
- source of nitrogen during CVD synthesis.

Regardless of the questions about the origin of the channels and spiraled ribbons in N-MWCNTs, there was an irresistible temptation to attempt to unroll them further to have some insight to their formation. Also, we were interested if it was possible to exfoliate these to single layers.

3.3.4. Attempts to unroll and exfoliate channeled N-MWCNTs:

We investigated several different methods that might result in substantial exfoliation of the channeled N-MWCNTs. We looked at physical methods, chemical methods, and thermal methods. Each one is discussed below.

Horn sonication

Horn sonication is a straightforward approach. We subjected these materials to high-power sonication (50% duty cycle) in 1 wt% aqueous surfactant solution (Pluronic F127, a polyethylene glycol-polypropylene glycol block copolymer). The material was then filtered using a porous alumina membrane filter (0.2 μm Anodisc), washed, and dried *in vacuo* and imaged while still on the filter after Au coating.

Microscopy on G-N-MWCNTs reduced/alkylated in ammonia and subjected to horn sonication(3-8) reveals that after 15 min of sonication (Figure 3-18(a)), there was initiation of unrolling in few nanotubes with other tubes still recognizable. After 25 min (Figure 3-18(b)), few nanotubes have partially unrolled and that after 60 min of sonication in surfactant solution (Figure 3-18(c) and (d)), most of them are partially unrolled and shortened in length. But we were unable to unroll them completely.

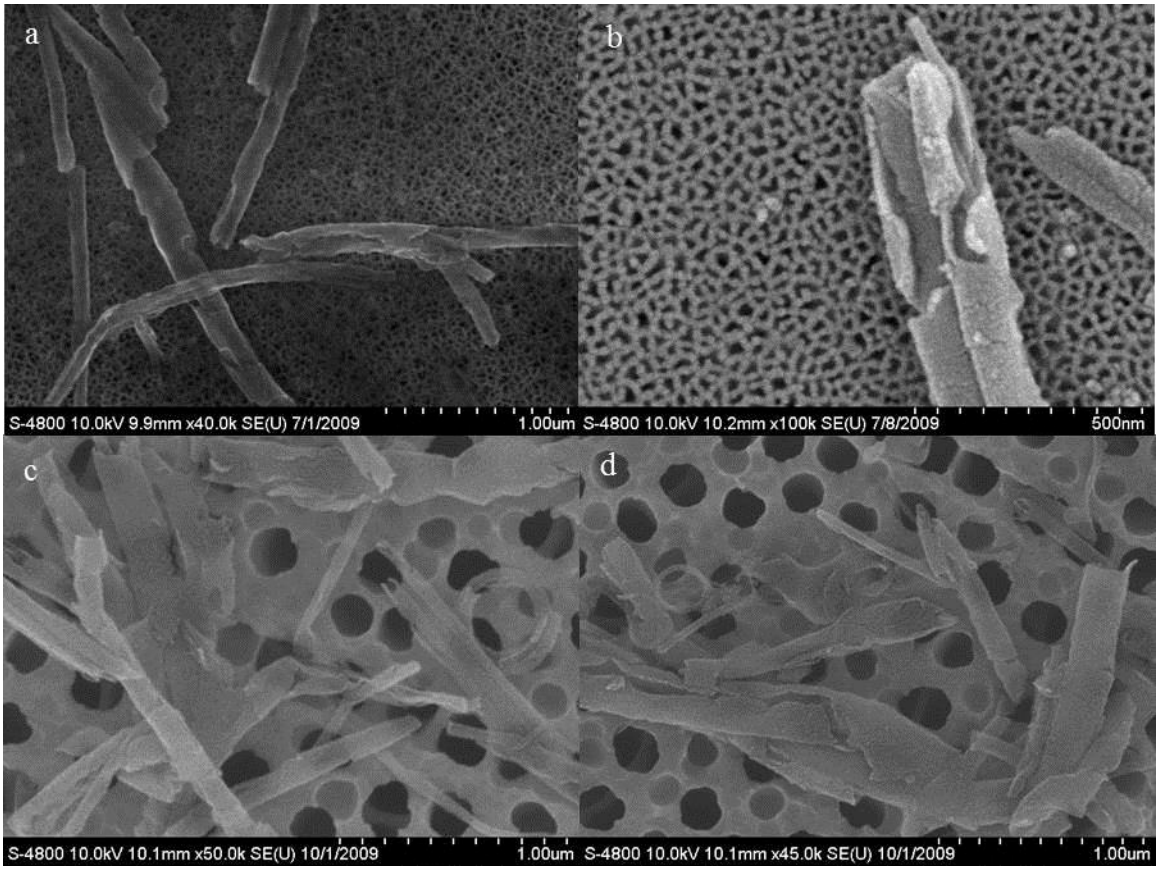

Figure 3-18 Horn sonication of G-N-MWCNTs reduced/alkylated (in ammonia) in surfactant F127 for (a) 15 min; (b) 25 min; and (c) and (d) 60 min.

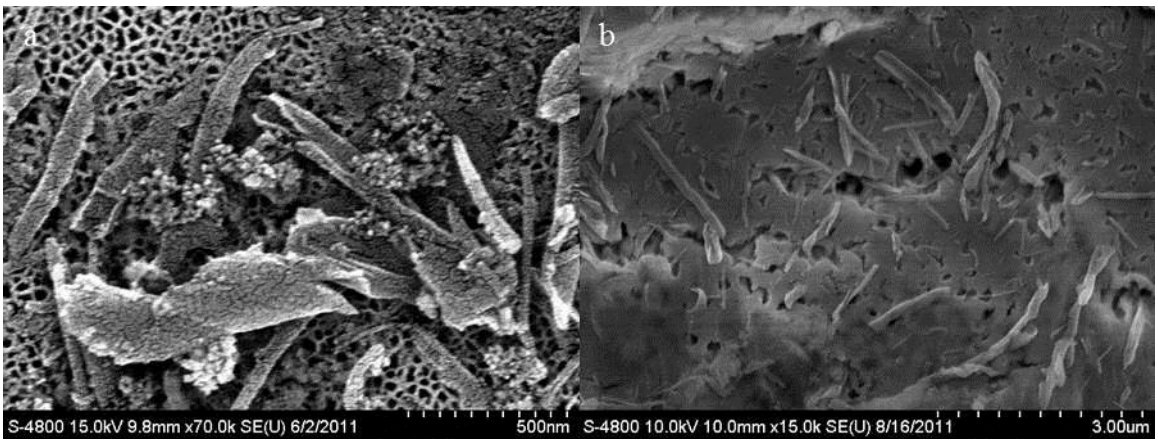

Figure 3-19 Horn sonication of G-N-MWCNTs treated with (a) HNO_3/H_2SO_4 and (b) $KMnO_4/H_2SO_4$ for 60 min.

Oxidized G-N-MWCNTs (HNO_3/H_2SO_4 and $KMnO_4/H_2SO_4$) were also subjected to high-power sonication (50% duty cycle) in 1 wt% aqueous surfactant solution

(Pluronic F127) for 60 min. SEM (Figure 3-19) images of both the materials (3-11 and 3-12) show that the tubes are shortened in length, but there is no indication of unrolling.

Treatment of SCNs with chlorosulfonic acid (3-13)

Chlorosulfonic acid has been shown to promote efficient exfoliation of graphite to few layers of graphene[114]. It has been described as a "true solvent" for CNTs; dissolving them by protonating the side walls[115]. SCNs were cut into very small pieces (Figure 3-20), but these small pieces were still multilayered. It seemed difficult to exfoliate them completely to form single layers.

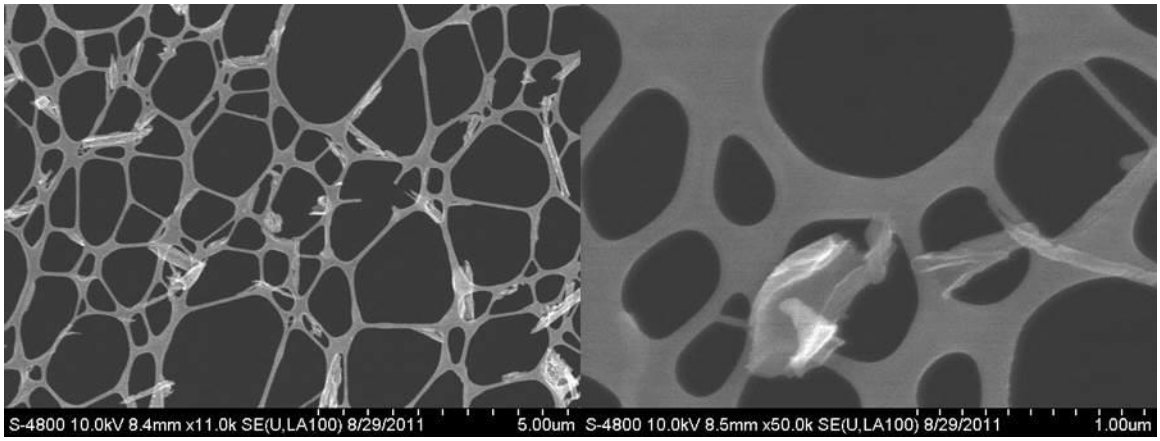

Figure 3-20 SCNs after sonication in chlorosulfonic acid for 24 h.

Thermal exfoliation of SCNs (3-14)

Rapid heating of graphite oxide results in expansion and delamination caused by rapid evaporation of intercalated water and evolution of gases produced by thermal pyrolysis of oxygen-containing functional groups[116]. When SCNs (Figure 3-21) were subjected to a similar heat treatment, some exfoliation of the material resulted, but this treatment was not able to split them to individual sheets.

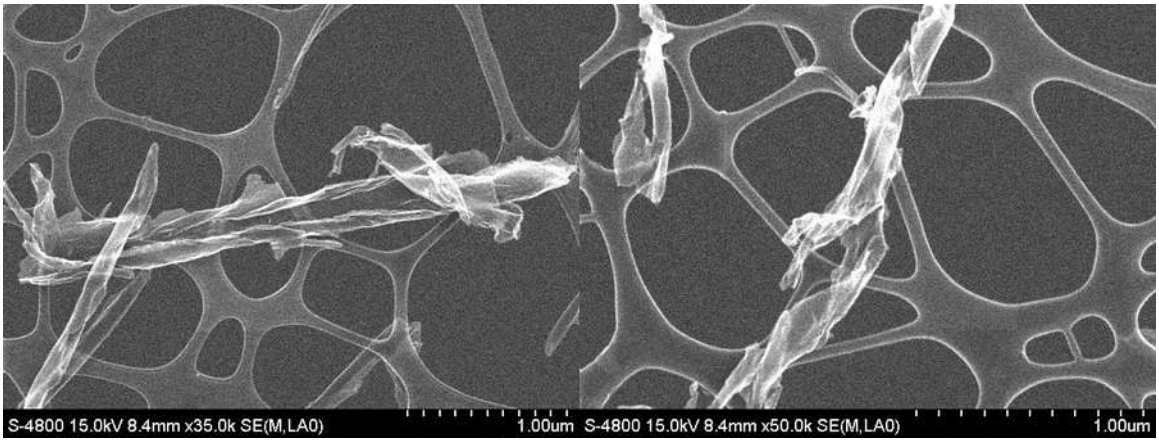

Figure 3-21 SCNs after thermal exfoliation.

Modified synthesis of SCNs (3-14 and 3-15)

G-N-MWCNTs were subjected to heating in $KMnO_4$ after sonication in H_2SO_4 at elevated temperature of 100 °C for 24 h. The resulting tubes have a spiraled ribbon texture (Figure 3-22), which is even more distinct than ones observed with original procedure. Increasing the amount of $KMnO_4$ from 5 to 6 weight equivalents and heating at 100 °C for 24 h, lead to yellow solution in which no black solid was visible. It appears that excess of $KMnO_4$ resulted in over-oxidation and destruction of the material.

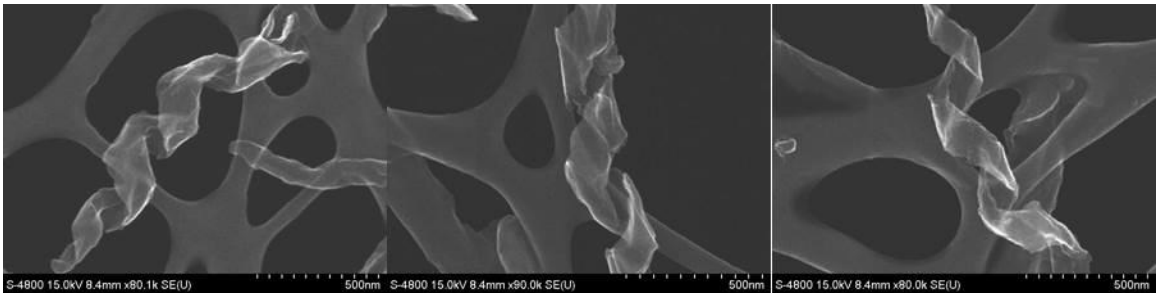

Figure 3-22 SCN formation at elevated temperature.

3.3.5. Origin of channels and ribbons:

Longitudinal cutting of N-MWCNTs under widely differing conditions (reducing conditions with Li/NH_3; Li/EDA and oxidizing conditions with $KMnO_4$/ H_2SO_4; HNO_3/ H_2SO_4), suggests that this material has a morphology that makes it predisposed to react in the manner described above. It appears that the process is

largely physical rather than chemical. Accordingly we believe that intercalation could be the driving force behind the observed changes from N-MWCNTs to SCNs and spiraled and linear channeled N-MWCNTs shown above and reported earlier[72, 73]. Lithium is known to form intercalation compounds with carbon materials such as graphite[117] and MWCNTs[118]. During the course of dissolving metal reduction/alkylation, lithium intercalation could push apart the graphene sheets to reveal the underlying architecture. Alkali metals can intercalate from the gas phase into MWCNTs, resulting in significant swelling but not tearing of the nanotubes[119]. Electrochemical intercalation of lithium into MWCNTs has been achieved[118, 120] without indication of the tearing process that we observe. Exfoliation has been reported in electrochemical intercalation when $LiPF_6$ dissolved in a mixture of ethylene carbonate, propylene carbonate and dimethyl carbonate (1:1:3) was used as an electrolyte[121]. This indicates that exfoliation may occur when a cointercalant is present.

It is possible that the solvent (ammonia or EDA) helps facilitate intercalation and results in a much higher amount of intercalated metal, or that the solvent diffuses in and occupies voids within the structure[122]. Intercalation of Li increases the interlayer spacing from 3.35 to 3.71 Å (LiC_6) in graphite[123]. The simultaneous intercalation of Li and ammonia in graphite increases the interlayer spacing to 6.62 Å ($Li(NH_3)_{1.6}C_{10.6}$)[124]. The stress induced by such a lattice expansion might be enough to tear the tubes. Formation of linear channels in EDA and spiraled channels in ammonia are difficult to explain on the basis of N-MWCNT structure. The process of channeling these tubes in a spiral manner or in a linear manner may be due to an interplay of solvent and lithium ion intercalation, coupled with the subtleties of the graphene morphology within the nanotube. EDA and ammonia are solvents with differing properties and may not be transported with lithium ions in the same manner into the graphite structure.

We further investigated the formation of SCNs ($KMnO_4/H_2SO_4$) by few control experiments. G-N-MWCNTs were subjected to sonication in H_2SO_4 (96 wt%) for 24 h (3-17). SEM (Figure 3-23 (a)) did not show any indication of channeling in G-N-MWCNTs.

Next we subjected G-N-MWCNTs to oxidation in $KMnO_4/H_2O$ (3-18) and $KMnO_4$/HCl (38 wt%) (3-19) following the same procedure as with $KMnO_4/H_2SO_4$. SEM images (Figure 3-23 (b) and (c)) indicated no sign of any channeling in G-N-MWCNTs. These results suggest that only the oxidizing mixture cannot be responsible for channeling. Also, H_2SO_4 appears to be the only acid that works for opening these tubes. Hence oxidation in H_2SO_4 seems to be the key requirement.

Like Li, sulfuric acid is also known to intercalate into graphite and MWCNTs[96]. Cho *et al.*[96] observed radial followed by longitudinal unzipping of MWCNTs in mixtures of HNO_3 and H_2SO_4 with high mixing ratio of H_2SO_4 (1:3 and 1:4). We observed longitudinal cutting in our material in a mixture of HNO_3/H_2SO_4 (1:3) and $KMnO_4/H_2SO_4$ but not upon refluxing in HNO_3. So under oxidizing conditions, intercalation of H_2SO_4 seems to be a key requirement, resulting in either separation of graphene layers or facilitating cleavage of C-C bonds, leading to formation of carbon spirals.

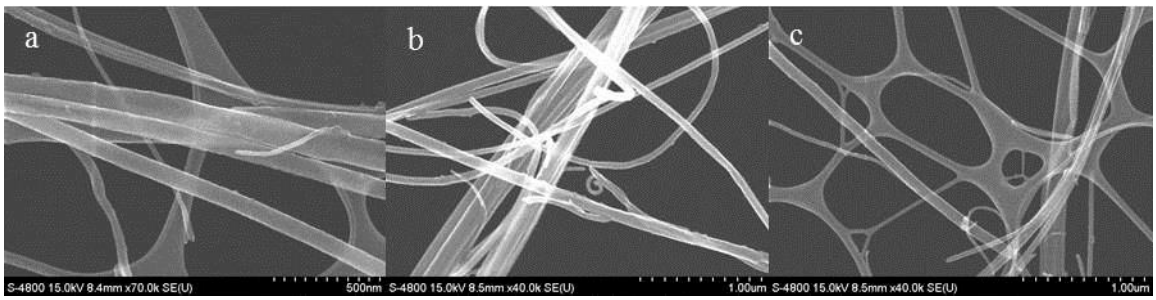

Figure 3-23 SEM images of G-N-MWCNTs subjected to (a) sonication in H_2SO_4 for 24 h; (b) oxidation in $KMnO_4/H_2O$ and (c) oxidation in $KMnO_4$/HCl.

Prolonged exposure to HNO_3 results in loss of tubular structure and formation of carbonaceous material. This is a different observation than in combination with H_2SO_4. Formation of carbonaceous material may be possible from an uncontrolled random attack of nitronium species on carbon atoms. In piranha oxidation, although sulfuric acid is present, the lower concentration seems to be ineffective in causing any change in G-N-MWCNTs. This again emphasizes requirement of higher concentration of H_2SO_4 in a mixture with other oxidant.

3.4. Conclusions

Longitudinal cutting of N-MWCNTs is observed under widely different reaction conditions. We hypothesize that intercalation (Li or H_2SO_4) is a key requirement under our reaction conditions for tearing N-MWCNTs. Channeling reaction results in bulk changes in the sample. Various attempts to unroll and exfoliate these materials further were unsuccessful.

Some interesting features about the structure are revealed by the different channel morphologies that result from the N-MWCNTs with only a change in the solvent used in the reduction/alkylation reaction and moving from reducing to oxidizing conditions. The consistency of the patterns observed suggests that an underlying structural feature is present. The formation of spiraled channels and SCNs are difficult to rationalize based on the reported stacked cup morphology of N-MWCNTs. The underlying structure of carbon appears to be more complex at least in the material under study. An attempt to develop a sructural model to explain various observations is made in the next chapter.

3.5. Experimental procedures

3.5.1. General Methods and Materials:

Horn sonication was performed using Vibra cell horn-sonicator (model: VC600, voltage: 120 V, Power: 600 watts, Frequency: 20 kHz) with time ranging from 1-60 min at a 50% duty cycle. Pluronic F127 surfactant was purchased from Sigma-Aldrich and chlorosulfonic acid was obtained from EMD chemicals.

3.5.2. Treatment of G-N-MWCNTs with DI water under sonication conditions (3-1):

To 0.10 g of the G-N-MWCNTs was added 24 mL of water. The mixture was subjected to bath sonication at room temperature for 12 h. After that, the resulting dispersion filtered and washed with ethanol. The resulting solid was dried in vacuum overnight.

3.5.3. Treatment of G-N-MWCNTs with H_2SO_4:HNO_3 under stirring conditions (3-2):

To 0.10 g of the G-N-MWCNTs was added 24 mL of a 3:1 mixture of sulfuric acid (96 wt%) and nitric acid (70 wt%). The mixture was subjected to stirring at room temperature for 12 h. After that, the resulting dispersion was diluted in water, filtered and washed with water to neutral pH and then washed with ethanol. The resulting solid was dried in vacuum overnight.

3.5.4. Treatment of pyridine derived as-prod-N-MWCNTs with H_2SO_4:HNO_3 (3-3):

To 0.25 g of as-prod-N-MWCNTs was added 60 mL of a 3:1 mixture of sulfuric acid (96 wt%) and nitric acid (70 wt%). The mixture was subjected to bath sonication at room temperature for periods of either 12 or 24 hours. After that, the resulting dispersion was diluted in water, filtered and washed with water to neutral pH and then washed with ethanol. The resulting solid was dried in vacuum overnight.

3.5.5. Treatment of pyridine derived as-prod-N-MWCNTs with $KMnO_4$:H_2SO_4[83] (3-4):

As-prod-N-MWCNTs (0.15 g) were suspended in 150 ml of conc. H_2SO_4 for 24 h (bath sonication), then $KMnO_4$ (750 mg, 4.75 mmol) was added. After stirring for 1 h at room temperature, the mixture was heated at 55 °C for 30 min. The temperature was further increased to 65 °C for 15 min and finally to 70 °C. When the temperature stabilized at 70 °C, the reaction mixture was removed from heating and allowed to cool to room temperature. The mixture was poured into 400 ml of ice water containing 5 ml of 30% H_2O_2. The solid material was filtered under vacuum through a PTFE membrane. Following stirring of solid material in water (150 mL) for 30 min, it was subjected to bath-sonication for another 15 min. Addition of 20 vol% concentrated HCl (30 ml) flocculated the material that was again filtered through a PTFE membrane. The solid material obtained was stirred in ethanol (150 ml) for 30 min and then bath-sonicated for 15 min. Flocculation occurred on addition of ether (150 ml) and the product was collected by filtration through a PTFE membrane. Washing with ether (2x50 ml) and drying *in vacuo* afforded oxidized nanotubes.

3.5.6. Dissolving metal reduction of acetonitrile derived as-prod-N-MWCNTs followed by methylation in NH_3 (3-5):

Approximately 170 mL of anhydrous ammonia was condensed using a Dewar condenser in a 250 mL three-necked round bottom flask in a dry ice-acetone bath under nitrogen. Li metal (230 mg) was added and the resulting blue solution was stirred for 5 min. To this solution were added as-prod-N-MWCNTs (230 mg) and the resulting black suspension was stirred for 30 min. Methyl iodide (3 mL) was added dropwise using a syringe, and the mixture was stirred and allowed to warm to RT overnight until the ammonia had completely been evaporated from the flask. H_2O (200 mL) was added to the flask and stirred for 30 min. The resulting N-MWCNTs were then subsequently washed and filtered on 0.2 µm nylon membrane filters with H_2O until a neutral pH was reached. The polyalkylated N-MWCNTs were washed with EtOH and finally with CH_2Cl_2, dried under vacuum overnight, weighed and characterized.

3.5.7. Treatment of acetonitrile derived as-prod-N-MWCNTs with $KMnO_4$:H_2SO_4[83] (3-6):

As-prod-N-MWCNTs (0.15 g) were suspended in 150 ml of conc. H_2SO_4 for 24 h (bath sonication), then $KMnO_4$ (750 mg, 4.75 mmol) was added. After stirring for 1 h at room temperature, the mixture was heated at 55 °C for 30 min. The temperature was further increased to 65 °C for 15 min and finally to 70 °C. When the temperature stabilized at 70 °C, the reaction mixture was removed from heating and allowed to cool to room temperature. The mixture was poured into 400 ml of ice water containing 5 ml of 30% H_2O_2. The solid material was filtered under vacuum through a PTFE membrane. Following stirring of solid material in water (150 mL) for 30 min, it was subjected to bath-sonication for another 15 min. Addition of 20 vol% concentrated HCl (30 ml) flocculated the material that was again filtered through a PTFE membrane. The solid material obtained was stirred in ethanol (150 ml) for 30 min and then bath-sonicated for 15 min. Flocculation occurred on addition of ether (150 ml) and the product was collected by filtration through a PTFE membrane. Washing with ether (2x50 ml) and drying *in vacuo* afforded oxidized nanotubes.

3.5.8. General procedure for horn sonication:

The material (1 mg) was suspended in a 1 wt% aqueous surfactant solution (Pluronic F127, polyethylene glycol-polypropylene glycol block copolymer) and subjected to high power horn sonication (50% duty cycle) for time intervals ranging from 1-60 min.

Starting N-MWCNTs	Compound #
G-N-MWCNTs	**3-7**
2-15	**3-8**
2-21	**3-9**
2-28	**3-10**
2-69	**3-11**
2-70	**3-12**

Sample preparation for imaging:

The dispersion was then filtered using a porous alumina membrane filter (0**.** 2 μm Anodisc), washed, and dried in *vacuo*. The material was then imaged while still on the filter after coating with Au.

3.5.9. Treatment of $KMnO_4$:H_2SO_4 oxidized G-N-MWCNTs with chlorosulfonic acid (3-13):

$KMnO_4$:H_2SO_4 oxidized G-N-MWCNTs (2-70) (0.05 g) were suspended in 75 ml of chlorosulfonic acid and bath sonicated for 24 h. The resulting dispersion was poured over ice, filtered under vacuum through a PTFE membrane, washed with ethanol and then dried in *vacuo*.

3.5.10. Thermal exfoliation of $KMnO_4$:H_2SO_4 oxidized G-N-MWCNTs in furnace (3-14):

To a clean pre-weighed crucible was added $KMnO_4$:H_2SO_4 oxidized G-N-MWCNTs (2-70) and weighed again. The crucible was then charged into 25 cm long quartz tube and kept in a furnace (Lindberg/Blue M tube furnace, model: TF55035A) and purged with Ar for 20 min. Argon inlet and outlet were inserted through a rubber stopper. The sample was heated at 150 °C for 10 min and then to 1000 °C. The sample was

kept at 1000 °C for 30 min, and then cooled down to 500 °C. The sample was then removed.

3.5.11. Treatment of G-N-MWCNTs with $KMnO_4$:H_2SO_4 at higher temperature (3-15):

G-N-MWCNTs (0.15 g) were suspended in 150 ml of conc. H_2SO_4 for 24 h (bath sonication), then $KMnO_4$ (750 mg, 4.75 mmol) was added. After stirring for 1 h at room temperature, the mixture was heated to 100 °C for 24 h. The reaction mixture was allowed to cool to RT and then was poured into 400 ml of ice water containing 5 ml of 30% H_2O_2. The solid material was filtered under vacuum through a PTFE membrane. Following stirring of solid material in water (150 mL) for 30 min, it was subjected to bath-sonication for another 15 min. Addition of 20 vol% concentrated HCl (30 ml) flocculated the material that was again filtered through a PTFE membrane. The solid material obtained was stirred in ethanol (150 ml) for 30 min and then bath-sonicated for 15 min. Flocculation occurred on addition of ether (150 ml) and the product was collected by filtration through a PTFE membrane. Washing with ether (2x50 ml) and drying *in vacuo* afforded oxidized nanotubes.

3.5.12. Treatment of G-N-MWCNTs with $KMnO_4$:H_2SO_4 (increasing amount of $KMnO_4$) (3-16):

G-N-MWCNTs (0.10 g) were suspended in 20 ml of conc. H_2SO_4 and stirred for an h. $KMnO_4$ (600 mg) was added over a period of 30 min at RT, and then after 15 min, the mixture was heated to 100 °C for 24 h. The reaction mixture was allowed to cool to RT and then was poured into 400 ml of ice water containing 5 ml of 30% H_2O_2. The solid material was filtered under vacuum through a PTFE membrane. Following stirring of solid material in water (150 mL) for 30 min, it was subjected to bath-sonication for another 15 min. Addition of 20 vol% concentrated HCl (30 ml) flocculated the material that was again filtered through a PTFE membrane. The solid material obtained was stirred in ethanol (150 ml) for 30 min and then bath-sonicated for 15 min. Flocculation occurred on addition of ether (150 ml) and the product was collected by filtration through a PTFE membrane. Washing with ether (2x50 ml) and drying *in vacuo* afforded oxidized nanotubes.

3.5.13. Control experiments:

a) Treatment of G-N-MWCNTs with H_2SO_4 **(3-17):**

G-N-MWCNTs (0.05 g) were suspended in 15 ml of conc. H_2SO_4 for 24 h (bath sonication), and then the mixture was poured into 400 ml of ice water. The solid material was filtrated under vacuum through a PTFE membrane. The product was washed with ethanol and dried *in vacuo*.

b) Treatment of G-N-MWCNTs with $KMnO_4$ in water **(3-18):**

G-N-MWCNTs (0.05 g) were suspended in 15 ml of DI water for 24 h (bath sonication), then $KMnO_4$ (250 mg, 1.6 mmol) was added. After stirring for 1 h at room temperature, the mixture was heated at 55 °C for 30 min. The temperature was further increased to 65 °C for 15 min and finally to 70 °C. When the temperature stabilized at 70 °C, the reaction mixture was removed from heating and allowed to cool to room temperature. The mixture was poured into 150 ml of ice water containing 1.6 ml of 30% H_2O_2. The solid material was filtered under vacuum through a PTFE membrane. Following stirring of solid material in water (50 mL) for 30 min, it was subjected to bath-sonication for another 15 min. Addition of 20 vol% concentrated HCl (10 ml) flocculated the material that was again filtered through a PTFE membrane. The solid material obtained was stirred in ethanol (50 ml) for 30 min and then bath-sonicated for 15 min. Flocculation occurred on addition of ether (50 ml) and the product was collected by filtration through a PTFE membrane. Washing with ether (2x10 ml) and drying *in vacuo* afforded the product.

c) Treatment of G-N-MWCNTs with $KMnO_4$ in HCl **(3-19):**

G-N-MWCNTs (0.05 g) were suspended in 15 ml of HCl for 24 h (bath sonication), then $KMnO_4$ (250 mg, 1.6 mmol) was added. After stirring for 1 h at room temperature, the mixture was heated at 55 °C for 30 min. The temperature was further increased to 65 °C for 15 min and finally to 70 °C. When the temperature stabilized at 70 °C, the reaction mixture was removed from heating and allowed to cool to room temperature. The mixture was poured into 150 ml of ice water containing 1.6 ml of 30% H_2O_2. The solid material was filtered under vacuum through a PTFE membrane. Following stirring of solid material in water (50 mL) for 30 min, it was subjected to bath-sonication for another 15 min. Addition of 20 vol% concentrated HCl (10 ml)

flocculated the material that was again filtered through a PTFE membrane. The solid material obtained was stirred in ethanol (50 ml) for 30 min and then bath-sonicated for 15 min. Flocculation occurred on addition of ether (50 ml) and the product was collected by filtration through a PTFE membrane. Washing with ether (2x10 ml) and drying *in vacuo* afforded oxidized nanotubes.

Chapter 4

The origin of ribbon-like structures: A proposal for a structural model of N-MWCNTs[**††]

4.1. Overview

The proposed models of N-MWCNTs in the literature - "bamboo type" or "stacked cups"- do not seem to support the observations made on our material. Chapters 2 and 3 gave an in-depth analysis of the textures produced under reductive and oxidative conditions, and it is difficult to rationalize the resulting textures if the starting point is a bamboo structure or a set of stacked cups. Using the observations from CNT-polymer composite experiments, the following chapter is an attempt to propose a plausible structure of the tubes under study.

4.2. Introduction

TEM is a widely used technique for characterization of microtextures in carbon materials. Since TEM is a two-dimensional cross-section of the material, it is sometimes difficult to fully characterize the original microstructure. For example, it is very difficult to distinguish nesting cylinders from scrolls in case of MWCNTs[125] and herringbone from stacked cups in the case of stacked CNTs[126]. Even though stacked cup CNTs have been synthesized under comparative conditions by CVD methods, their real structure is still a matter of some debate. Other models are proposed for explaining the texture of members of the "stacked cup" or herringbone family of filamentous carbons. These involve a discontinuous arrangement formed by stack of truncated graphitic cones[127-129] or a continuous texture formed by a helical graphene ribbon wrapped in a conical spiral[128-132].

[**] Part of this chapter is taken from our manuscript; Kaur, A.; Meier, M. S.; Andrews, R.; Qian, D. Discontinuous spiraled carbon nanoribbons resulting from coiling of thin graphite subunits formed during oxidation of N-doped multiwalled carbon nanotubes (Carbon, in Press).

[††] Figure 4-9: courtesy Prof. Mark S. Meier.

A structure of discontinuous truncated graphene cones, which look similar to herringbone CNTs, was proposed by Endo *et al.*[127]. Vera-Agullo *et al.* claimed a helical graphene ribbon structure for their "stacked cup CNTs" when they were able to directly peel long graphene ribbon from a single stacked cup CNT[130]. Yang *et al.* suggested that a single graphene sheet grown into a helical structure forms the basis of the structure of their fibers, which were synthesized via a CVD method by using Pd catalyst[131]. Terrones and co-workers produced high yields of graphitic conical nanofibers catalyzed by Pd[133]. Saito *et al.*[111] disassembled their cup stacked CNTs to individual cups after treatment with Na/naphthalene while Liu *et al.*[106] unrolled their cup stacked CNTs to graphene layers by permanganate treatment.

Monthioux *et al.*[128] found dramatic variations in type, diameter, inner texture and structure of filamentous carbon materials as a function of the catalyst composition and preparation method. They have estimated the relative proportions of various nanofilament types (platelet nanofibre to herringbone nanofibre to herringbone-bamboo nanotubes) depending on the angle (α) between graphene layers with respect to the nanofilament axis. Materials grown with graphene angles (α) that range from 30° to 180° take on herringbone nanofibre to herringbone-bamboo nanotube textures. In our material, the graphene layers are arranged with very narrow angles (α = 7-12°) relative to the nanotube axis (Figure 4-1(a)), compared to the 30˚ to 180˚ angles studied in previous reports. We observe catalyst particles (Figure 4-1(b)) that are sharp cones with angles ranging from 8˚ to 15°, significantly more pointed than the elongated conical catalyst particles (20˚ - 60°) observed by Monthioux *et al.*[128].

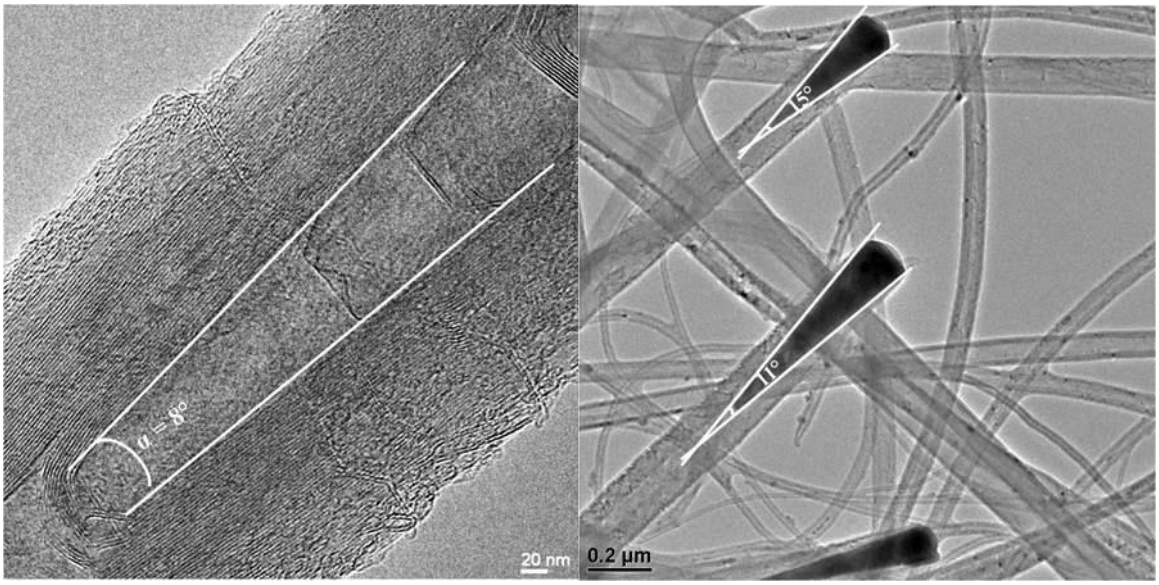

Figure 4-1 HRTEM images showing a) the α angle in G-N-MWCNTs; and b) the conical catalyst particles in N-MWCNTs before annealing

In our experiments (dissolving metal reduction/alkylation conditions and oxidizing conditions (H_2SO_4/HNO_3 and $H_2SO_4/KMnO_4$)), we observed formation of linear and spiral channels along with SCNs. Formation of spiraled channels and spiraled ribbons suggest that the underlying morphology is most likely not a set of stacked cups. In an effort to understand more about the texture we attempted to pull these spiraled ribbons lengthwise by stretching their polymer composites in the hopes that the underlying structure would unravel.

4.3. Results and discussion

CNT composites are made in order to disperse CNTs homogeneously throughout the matrix without destroying their integrity. The effective load transfer across CNT/ matrix depends upon good interfacial bonding. We started with dispersing G-N-MWCNTs in polystyrene (PS) using a melt method (4-1). G-N-MWCNTs were sonicated to suspend into PS solution. Adding excess ethanol precipitated the suspension. The resulting composite was dried and then was melted using heating mantle. Optical microscopy (Figure 4-2(a)) and SEM (Figure 4-2(b)) were used to analyze the melt sample. The images show that G-N-MWCNTs are well dispersed in PS. The melt was dispersed in chloroform by sonication, centrifuged and the

supernatant was spin cast to form a thin film on a glass slide. The film was coated with gold and analyzed by SEM.

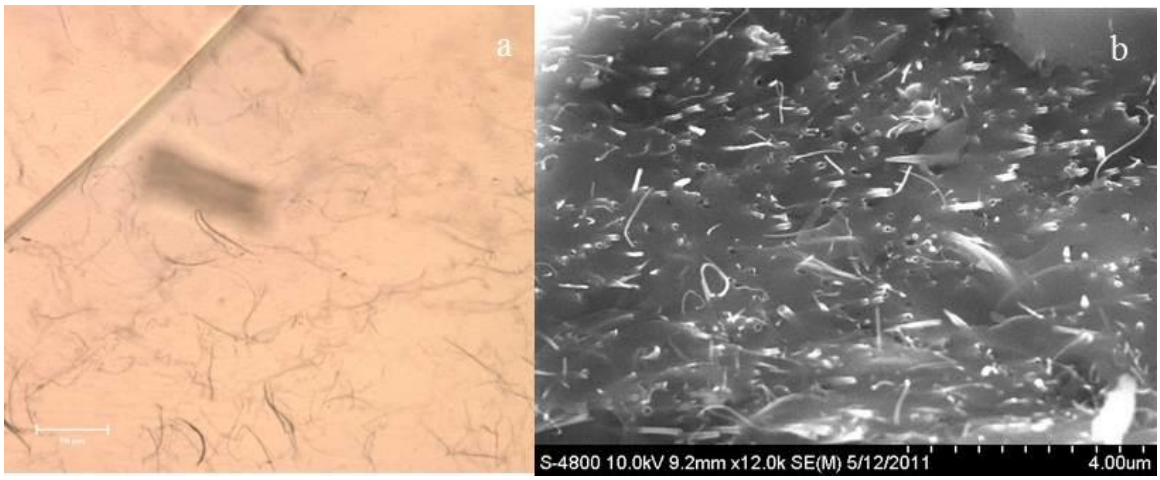

Figure 4-2 (a) Optical and (b) SEM of G-N-MWCNTs-PS melt composite.

SEM was not very informative as there were only few tubes visible in the film. This was probably due to limited solubility of the composite in chloroform, so a solution method for preparing composites was attempted.

Toluene was the first solvent used to make G-N-MWCNTs-PS composite (4-2). Optical microscopy (Figure 4-3(a)) shows that the tubes were poorly dispersed in PS. THF was then chosen as a solvent to make G-N-MWCNTs-PS composite (4-3). This resulted in a better dispersion as was seen under optical microscopy (Figure 4-3(b)). With this the method was optimized to make the PS composites.

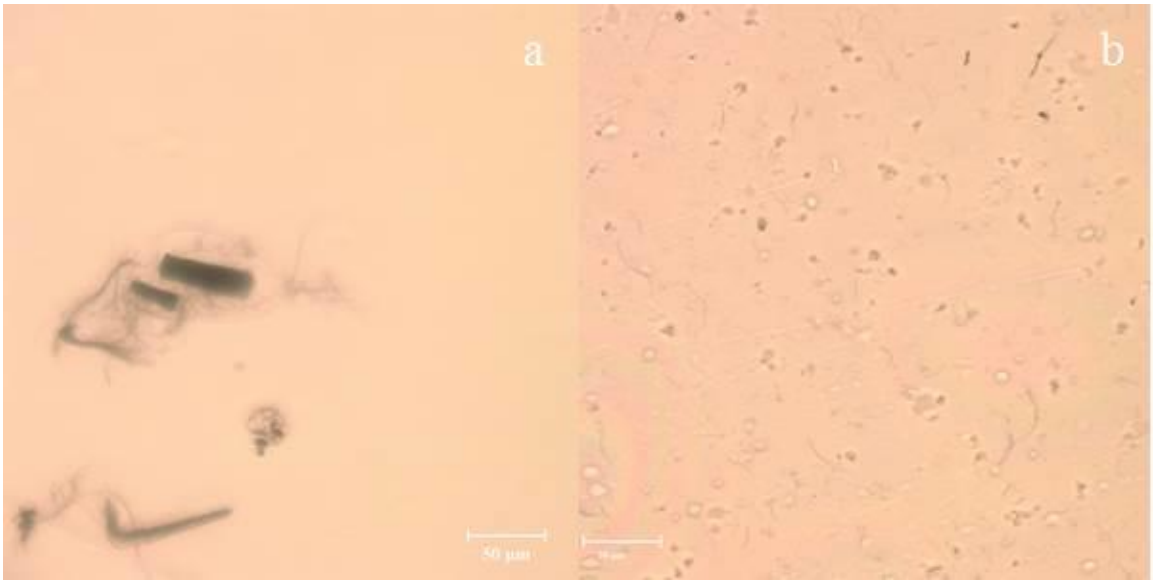

Figure 4-3 Optical microscopy of G-N-MWCNTs-PS solution composite in (a) toluene and (b) THF.

The composite of SCNs-PS (4-4) was made in THF and thin film was spin cast on a glass slide. The film, analyzed by SEM, shows the formation of circular structures on the surface (Figure 4-4(a)). This was not really due to an interaction between tubes and PS as similar appearance (Figure 4-4(b)) was observed with PS (without tubes) in THF. The glass slide was then cracked in liquid N_2. Figure 4-5 presents SEM of the cracked composite.

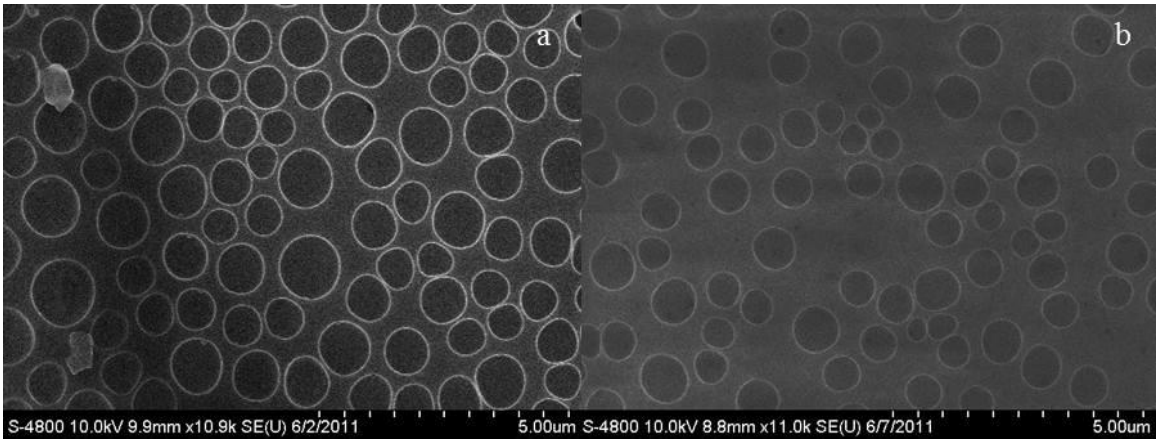

Figure 4-4 Low resolution of SEM of (a) G-N-MWCNTs-PS composite in THF and (b) PS in THF.

The image (Figure 4-5(a)) shows a crack in the polymer, but there are no tubes visible in the crack. As some SCNs (Figure 4-5(b)) are seen as such in the composite, they do not seem to have much interaction with PS. SCNs contain a lot of oxygen-containing functional groups on their surface and in between the layers. This may be responsible for their poor interaction with PS. We then tried saran wrap (polyethylene (PE)), to make composites with SCNs. This was not successful either.

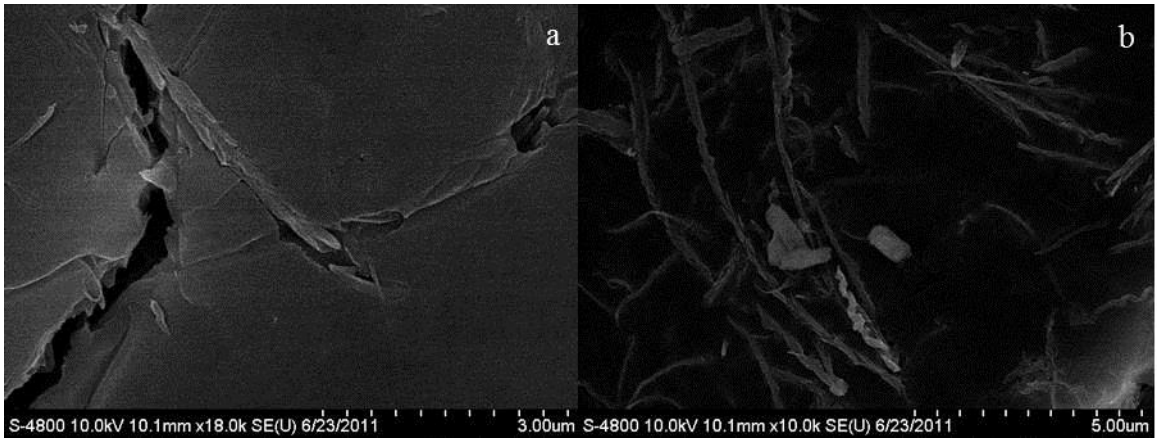

Figure 4-5 SEM of cracked SCNs-PS composite.

The next attempt was to use poly(methyl methacrylate) (PMMA). The composite (4-6) was formed by casting a suspension of SCNs in a solution of polymer dissolved in THF. Thin film on glass slide was analyzed by SEM (Figure 4-6(a) and (b)), after coating with Au. It was observed that focusing the electron beam on SCNs- PMMA composite in the SEM initiates cracks in the composite (Figure 4-6(a)), and this was used to an advantage in further preparation of SEM samples. Now the samples could be directly prepared on a copper grid and no additional steps to crack the composite were required. Figure 4-6(c) and (d) are SEM of the composite (4-9) on a copper grid. In situations where the spiraled ribbons are found exposed at the surface of the composite (Figure 4-6(b) and (d)), they appear to be composed of subunits with linear channels at one point, but that transform to spiraled ribbons farther along the ribbon. It appears as if the subunits that are apparent in a linear channel can rearrange to form a ribbon. Hence the two morphologies can be seen in a single tube. This observation is not polymer specific, as similar observations are made when SCNs were observed under SEM, STEM and TEM in the absence of polymers (Figure 4-7).

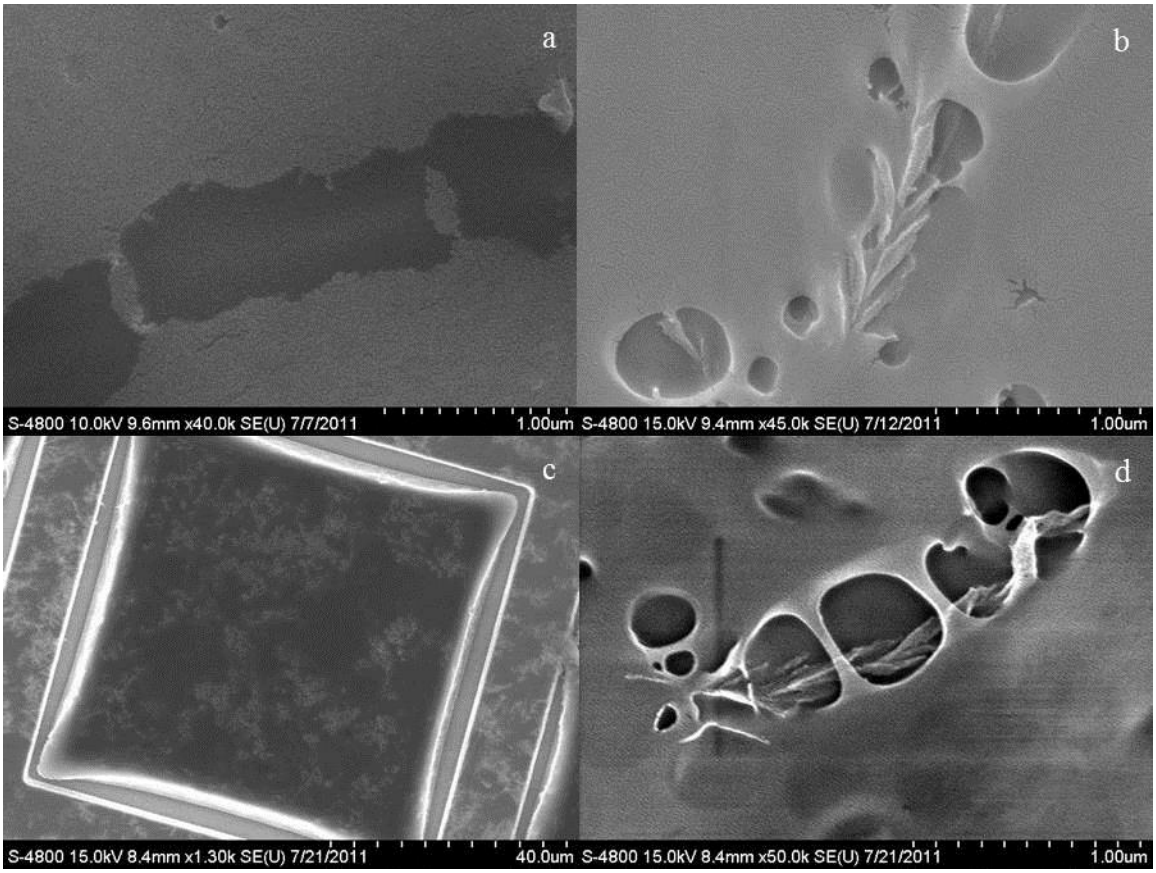

Figure 4-6 SEM of SCN-PMMA composite (a), (b) on a glass slide and (c), (d) on copper grid.

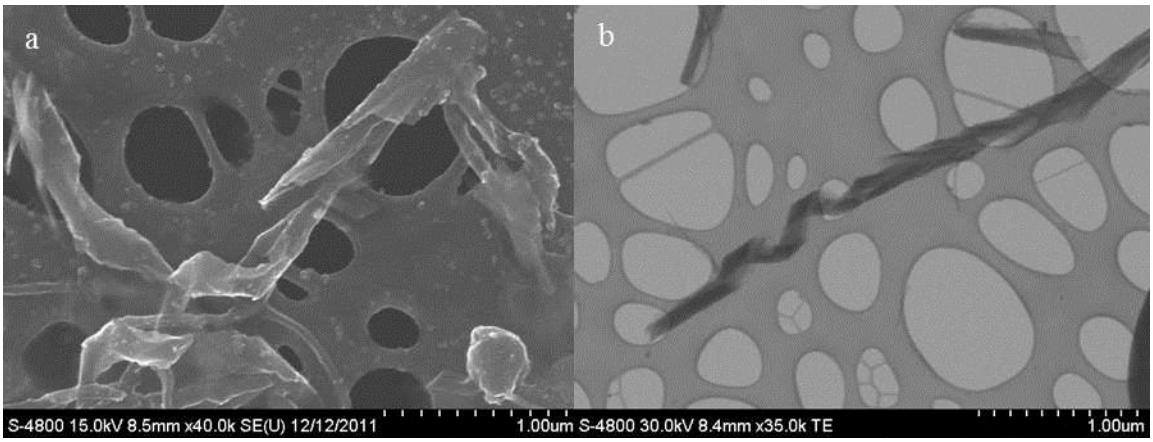

Figure 4-7 (a) SEM and (b) STEM of SCNs.

We found some examples of the ribbons unfurling as a result of the cracking of the composite. Figure 4-8 represents SEM images of the cracked composite. The images, with more clearly visible subunits, suggest that the structure that is composed of a stack of coiled subunits. We believe that the subunits visible in Figure 4-8 are composed of multiple graphene layers rather than a single sheet of graphene. Though

the tubes seen in the images do not represent a true ribbon, we can imagine rotation of individual subunits relative to another adjacent to form a coiled ribbon. All these observations suggest that SCNs are not composed of a continuous coiled ribbon but instead as a set of coiled subunits (Figure 4-7 and 4-8), even though they appear to be continuous.

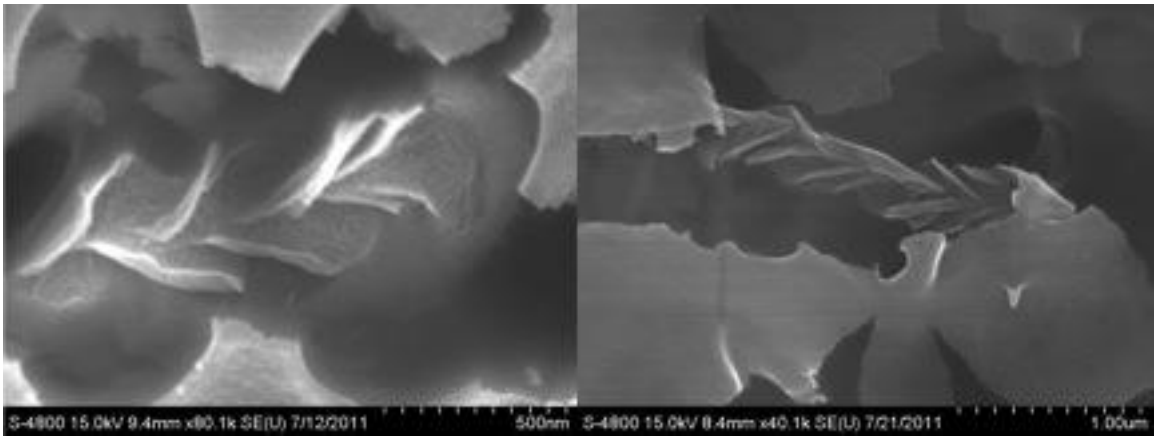

Figure 4-8 SEM image of SCNs exposed within a crack in the composite.

Formation of spiraled channels/carbon ribbon or linear channels, starting from the same material, can be rationalized as resulting from movement of the subunits that make up the structures in Figure 4-8 above. These processes are shown schematically in Figure 4-9, and are compared to textures we observe. Reduction/intercalation or oxidation/intercalation opens up the structure and permits the subunits to move relative to each other. If they do not rotate, the aligned edges of the subunits appear as a linear channel (A). If the edges of the subunits slip relative to each other (B), a curving channel is formed, and with slight rotation of subunit, a spiral ribbon forms (C), albeit a ribbon formed from the multiple subunits rather than from one continuous band of graphene.

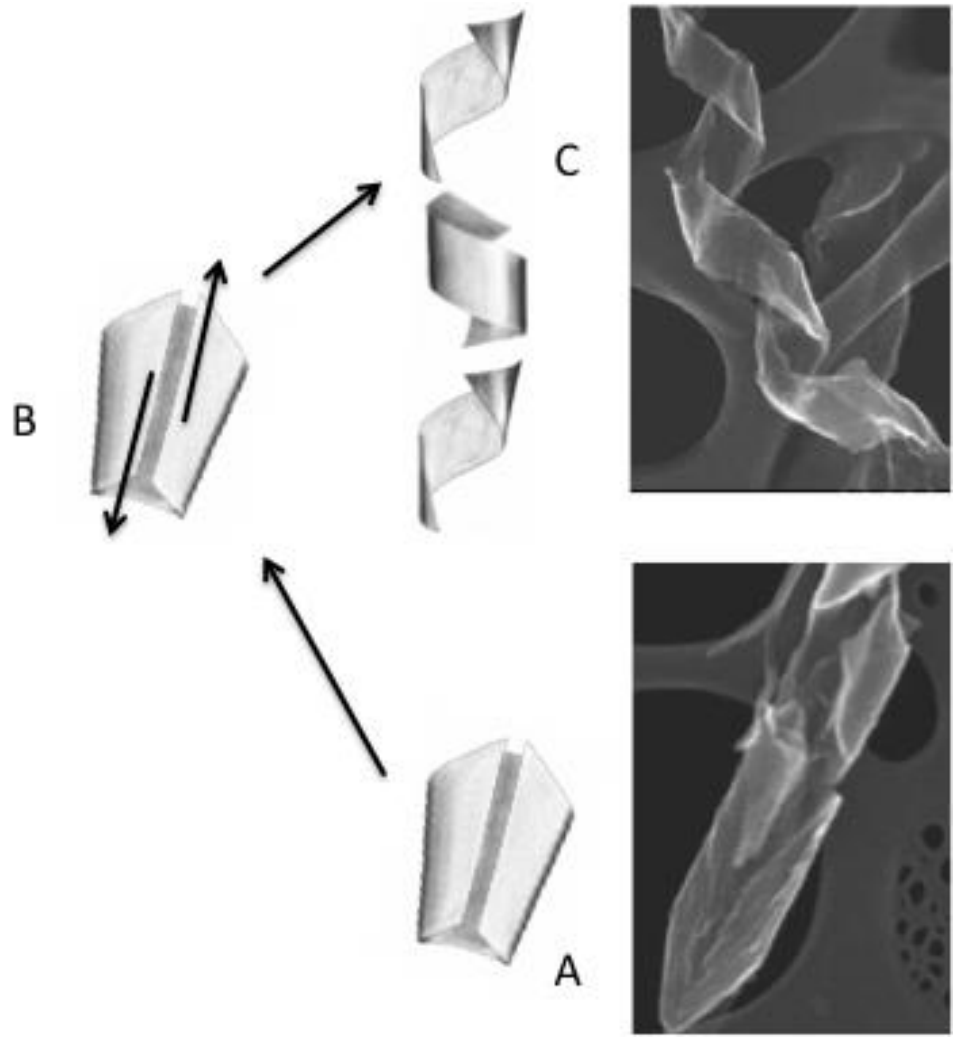

Figure 4-9 Schematic showing how simple curved subunits can form spiraled ribbon textures or filaments with linear channels.

When treated with a dilute polymer solution, the spiraled ribbons have a thin polymer coating on their surface. In some STEM images (Figure 4-10), this highlighted their surface texture, and in these images it is possible to see the edges of the individual subunits that together create the impression of a continuous coiled ribbon.

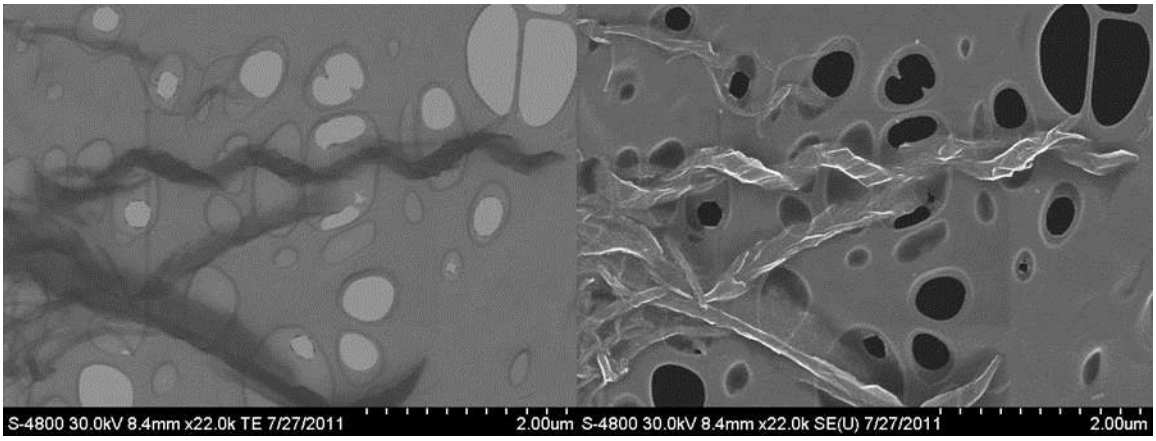

Figure 4-10 STEM-SEM images of SCNs-PMMA composite.

The motivation of preparing SCNs-polymer composites was to unfurl the tubes in order to gain insights on the microstructure of the tubes. These experiments revealed the underlying structure of many tubes and we did find few unfurled tubes. These observations were helpful in explaining the formation of different textures obtained from the same starting material, and gave us a confidence in proposing a structural model.

4.4. Conclusions

The results indicate that N-MWCNTs produced by CVD synthesis from pyridine/ferrocene in our reactor do not actually have the stacked-cup texture described previously but are instead a stack of coiled subunits. We believe that reduction/intercalation or oxidation/intercalation pushes apart the stacks, revealing and enabling the subunits to move relative to each other, resulting in formation of spiraled channels or carbon nanoribbons.

4.5. Experimental procedures

4.5.1. General Methods and Materials:

PS and PMMA were obtained from UK CAER and premium Saran wrap was used for PE. THF was ordered from Sigma-Aldrich and toluene from Pharmco-Aaper.

4.5.2. G-N-MWCNTs-Polystyrene composite (melt method) (4-1):

To G-N-MWCNTs (5 mg) was added polystyrene (1 g) and THF (10 mL) and sonicated to suspend G-N-MWCNTs into polystyrene solution. The suspension was rapidly precipitated by adding excess ethanol and the resulting composite was dried at 80 °C in vacuum. The composite was then melted using heating mantle at 250 °C for 30 min and stirred with glass rod. A sample of melt was taken for optical and scanning electron microscopy. The melt was cooled and dispersed in chloroform by sonication and then centrifuged for 15 min. The supernatant was analyzed by optical microscopy and spin cast to form a thin film on a glass slide, which was analyzed by SEM.

4.5.3. G-N-MWCNTs-Polystyrene composite (solution method) in toluene (4-2):

G-N-MWCNTs (5 mg) were dispersed in toluene (10 mL) with sonication for 30 min. Polystyrene (1 g) was then added and the mixture was stirred and heated at 100 °C for 2 h. A thin film was casted onto a glass slide, which was analyzed by optical microscopy.

4.5.4. G-N-MWCNTs-Polystyrene composite (solution method) in THF (4-3):

To G-N-MWCNTs (10 mg) was added polystyrene (1 g) and THF (10 mL) and the mixture was sonicated to suspend G-N-MWCNTs into polystyrene solution. A thin film was casted onto a glass slide, which was analyzed by optical microscopy and SEM.

4.5.5. $KMnO_4$ oxidized G-N-MWCNTs-polystyrene composite (solution method) in THF (4-4):

To $KMnO_4$ oxidized G-N-MWCNTs (2-70) (50 mg) was added polystyrene (1 g) and THF (10 mL) and the mixture was sonicated to suspend oxidized N-MWCNTs into polystyrene solution. A thin film was cast onto a glass slide, which was analyzed by SEM.

4.5.6. $KMnO_4$ oxidized G-N-MWCNTs-polyethylene composite in xylene (4-5):

Saran wrap (polyethylene) (0.5 g) was stirred and heated at 150 °C to dissolve in xylene (10 mL). To the solution was added $KMnO_4$ oxidized G-N-MWCNTs (2-70) (35 mg). A thin film was casted onto a glass slide, which was analyzed by SEM.

4.5.7. $KMnO_4$ oxidized G-N-MWCNTs-poly(methyl methacrylate) composite in THF (4-6):

To $KMnO_4$ oxidized G-N-MWCNTs (2-70) (25 mg) was added PMMA (0.5 g) and THF (5 mL) and the mixture was sonicated to suspend oxidized N-MWCNTs into PMMA solution. A thin film was casted onto a glass slide, which was analyzed by SEM.

4.5.8. G-N-MWCNTs-poly(methyl methacrylate) composite in THF (4-7):

To G-N-MWCNTs (25 mg) was added PMMA (0.5 g) and THF (5 mL) and the mixture was sonicated to suspend N-MWCNTs into PMMA solution. A thin film was cast onto a glass slide, which was analyzed by SEM.

4.5.9. As-prod-N-MWCNTs-poly(methyl methacrylate) composite in THF (4-8):

To As-prod-N-MWCNTs (25 mg) was added PMMA (0.5 g) and THF (5 mL) and the mixture was sonicated to suspend N-MWCNTs into PMMA solution. A thin film was cast onto a glass slide, which was analyzed by SEM.

4.5.10. General procedure for cracking polymer composites and preparation of samples for SEM analysis:

Thin film of CNT-Polymer composite on glass slide was cracked in liquid N_2 and analyzed by SEM with the film still on glass. A piece of this glass was glued to carbon tape already placed on SEM holder. The samples were Au coated prior to analysis.

4.5.11. $KMnO_4$ oxidized G-N-MWCNTs-poly(methyl methacrylate) composite in THF on Cu grid (4-9):

To $KMnO_4$ oxidized G-N-MWCNTs (2-70) (25 mg) was added PMMA (0.5 g) and THF (5 mL) and the mixture was sonicated to suspend oxidized N-MWCNTs into PMMA solution. A drop of composite was directly loaded onto Cu grid for SEM, STEM and TEM analysis and Cu grid was Au coated prior to analysis.

Chapter 5

N-MWCNT-derived materials as negative electrodes in lithium ion batteries

5.1. Overview

The commercialization of lithium ion batteries (LIBs) in early 1990s by Sony was a breakthrough in mobile energy technology. These batteries have become the most used portable source of mobile energy of the century[134-136]. However, the delivery of high energy/power density to meet escalating requirements of evolving new technologies[137, 138] remains a significant challenge. In collaboration with colleagues Prof. Y. T. Cheng and Dr. J. C. Li, at UK Chemical and Material Engineering, the performance of G-N-MWCNTs and functionalized N-MWCNTs for energy storage in LIBs is evaluated. Attention is paid to investigate the effect of microstructure and morphology of these materials on Li storage capacity.

5.2. Introduction

5.2.1. Electrochemical energy storage

When an electrochemical system is connected to an external source, a finite charge q is stored. The system converts the electric energy into the stored chemical energy during the charging process. When the system is connected to an external resistive circuit, it releases the finite q and drives a current through the external circuit. The system then converts the stored chemical energy into electric energy in the discharging process.

Based on the mechanism of energy storage, electrochemical energy storage systems can be classified as: capacitors, batteries and fuel cells. Batteries store energy in chemical reactants capable of generating charge, whereas electrochemical capacitors store energy directly as charge. In fuel cells, reactant is a fuel and its chemical energy is converted into electricity through a chemical reaction with oxygen or another oxidizing agent. A battery is composed of a positive electrode and a negative electrode separated by a porous separator immersed in an ionically conducting and electronically insulating electrolyte. The chemical driving force is due to the difference in the chemical potentials of the two electrodes, which can be expressed as

the *Gibbs free energy change per mole of reaction, ΔG*. The electrostatic energy per mole of an electrically charged species is *nFE*, where E is the voltage between the electrodes, F is the Faraday constant and n is the number of electrons involved (n=1 for Li ions). Hence under open-circuit conditions, the theoretical voltage of a cell is given:

$$\Delta G = -nFE$$

5.2.2. Lithium ion batteries (LIBs)

Development in the phenomenon of intercalation during 1970-80s, lead to the discovery of LIBs[137]. The idea was to substitute the negative and positive electrodes with host materials that can accommodate (release) Li ions in (from) the structure. Use of Li insertion compounds as negative electrodes overcame the limitations of periodic dissolution and deposition, extensive shape changes and side reactions with electrolyte associated with cycling of metallic Li[137]. The commonly-used negative electrode materials of LIBs mainly include different types of graphite[139], Si[140], Sn[140], Ge[141], TiO_2[142], and their alloys or composites. In Table 5-1, key characteristics of some of the commonly used active materials in negative electrodes are listed.

Table 5-1 Commonly used negative electrode materials[139, 143].

Negative electrodes in LIBs			
Reduced form	Oxidized form	E(Li/Li^+) (V)	q (mAh g^{-1}) (theoretical)
Li	Li^+	0.00	3861
Graphite based materials			
LiC_6	graphite	0.10	372
LiC_{12}	graphite	0.13	186
LiC_{18}	graphite	0.22	124
Alloys			
LiAl	Al	0.35	993
$Li_{22}Sn_5$	Sn	0.42-0.66	994
Li_3Sb	Sb	0.90	660
$Li_{21}Si_5$	Si	0.30	4000

The positive electrode materials are either layered-type lithium metal oxides[144-146] or olivine and spinel-type lithium metal phosphates, silicates or oxides[145, 146]. Table 5-2 lists characteristics of some positive electrode materials. During operation, the electrolyte transports lithium ions between the two electrodes. The electrolyte is usually composed of one or more solvents (Table 5-3) and one or more salts (Table 5-4) which dissociate and provide ions.

Table 5-2 Commonly used positive electrode materials[147].

Positive electrodes in LIBs			
Reduced form	Oxidized form	$E(Li/Li^+)$ (V)	q (mAh g^{-1}) (theoretical)
Layered compounds			
$LiTiS_2$	TiS_2	1.5-2.4	239
$Li_3V_2O_5$	V_2O_5	2.0-3.5	442
$LiCoO_2$	Li_xCoO_2	3.5-4.2	274
$LiNiO_2$	Li_xNiO_2	3.5-4.2	274
$LiMnO_2$	Li_xMnO_2	3.5-4.2	285
$Li(NiMnCo)O_2$	$Li_x(NiMnCo)O_2$	3.0-4.5	274
Spinels and Olivines			
$LiMnO_4$	Li_xMnO_4	3.0-4.0	213
$LiFePO_4$	$FePO_4$	3.4	170

Table 5-3 Common solvents used in electrolytes in LIBs[148].

Solvent	T_m (°C)	T_b (°C)	η (cP)	ε
EC	36.4	248	1.90[(a)]	89.8
PC	-48.8	242	2.50	64.9
DMC	4.6	91	0.59	3.1
DEC	-74.3	126	0.75	3.1
EMC	-53	110	0.65	2.9

T_m is melting temperature, T_b is boiling temperature, η is viscosity in centipoise measured at 25 °C, ((a) measured at 40 °C) and ε is the relative dielectric constant. EC stands for ethylene carbonate, PC for propylene carbonate, DMC for dimethyl carbonate, DEC for diethyl carbonate and EMC for ethyl methyl carbonate.

Table 5-4 Common salts used in electrolytes in LIBs[148].

Salts	σ (mS cm^{-1})	
	PC	EC:DMC
$LiBF_4$	3.4	4.9
$LiPF_6$	5.8	10.7
$LiAsF_6$	5.7	11.1
$LiClO_4$	5.6	8.4

σ is specific conductivity of salts in indicated solvents.

5.2.3. Terms and parameters in use

The energy contained in an electrochemical system is the integral of the voltage (V) multiplied by the charge capacity, i.e., the amount of charge (q) available.

$$E = \int Vdq$$

Usually the energy stored is expressed in watt-hours. The mathematical relationship for capacity (q) (amp-hours (Ah)) is the product of current and time.

$$q = I * t$$

The watt-hours (Wh) stored in a battery is approximated by multiplying the rated amp-hours by the voltage.

$$Wh = V * Ah$$

The terms specific energy (Wh/kg) and specific power (W/kg) are defined as the energy and power available per unit weight respectively. The amount of energy stored per unit volume is called the energy density (Wh/liter) and power per unit volume is power density (W/liter). The characteristics of a battery are often graphically illustrated using Ragone plots (named after D.V. Ragone)[149], in which the specific power is plotted against the specific energy.

Cycle life is the number of times a device can be effectively recharged before its performance degrades (the capacity has not diminished significantly). Coulombic efficiency is defined as the ratio of charge capacity to discharge capacity for a cycle.

$$\text{Coulombic efficiency (\%)} = \frac{q_{\text{charging}}}{q_{\text{discharging}}} * 100$$

A term that is often used to indicate the rate at which a battery is discharged is the C-rate. The discharge rate of a battery is expressed as C/R, where C is capacity and R is the number of hours required to completely discharge its nominal capacity. For example, if a cell has a nominal capacity of 5 Ah and discharges at the rate of C/10 (it discharges completely in 10 h), then the current available is 0.5 A. If the discharge rate is C/5, the discharge current is 1 A. It is important to consider the same C-rate while comparing the behavior of different materials and electrodes.

5.2.4. Carbon materials as negative electrodes for LIBs

For a long time, graphite powder was used as the negative electrode in rechargeable LIBs[150, 151]. Electrodes made of nanostructured materials could potentially increase the rate of Li insertion/removal and improve battery performance, as these materials can mitigate changes in volume associated with many other active electrode materials[152-154]. This leaves an opportunity for CNTs, with properties including high aspect ratio, channels for lithium ion intercalation and excellent conductivity (electrical and thermal)[155], to be considered as potential candidates in electrode research. There have been numerous reports evaluating the use of CNTs in LIBs[156-164]. Freestanding CNT paper acts as both active material and current collector, and in addition it offers low weight, flexible geometry and high temperature stability, each of which is necessary for specific applications[157, 165]. CNTs could be strategically used as conductive additives to establish an electrical percolation network in composite electrodes, with lower weight loadings when compared to conventional carbon additives. For example with SWCNTs, mass loadings of just 0.2% w/w can achieve a comparable conductivity as with spherical particles[166]. MWCNTs when used as an additive with $LiCoO_2$, $LiFePO_4$ and $LiNi_{0.7}Co_{0.3}O_2$ cathodes, show ~10%

improvement in the reversible capacity compared to carbon black counterparts[167, 168].

Li ion capacity in CNTs results from intercalation of Li ions between the MWCNT layers or in the interstitial sites of close-packed SWCNT bundles, and also from effective diffusion into stable sites located on the nanotube surface and/or inside individual nanotubes through endcap or sidewall openings[169-171]. Lin *et al.* concluded that Li^+ diffuses much faster into MWCNTs based on the diffusion coefficient value calculated from results of impedance and chronoamperometery techniques[172]. They found that Li^+ diffuses or intercalates mainly the graphite layers, accounting for reversible capacity. The corresponding irreversible capacity results from Li^+ diffusing into the hollow core of the MWCNTs or the pores formed by entangled nanotubes. Calculations also proposed a curvature-induced lithium condensation inside the core of the nanotubes[173]. Liu *et al.* observed lithiation of the individual MWCNTs by in situ TEM experiments, and reported lithiation-induced embrittlement which they attributed to the combined effects of mechanical and chemical weakening of C-C bonds by Li insertion, as well as the tensile hoop prestress[174]. Factors that influence the mechanism of Li insertion into a specific material are morphology, porosity and chemical composition.

Various modifications have been made to improve electrochemical performance of CNTs. Chemical etching in acid solution[175], dicing longer tubes to short segments (~200 nm)[176], short tubes from direct growth[177], and the use of vertically aligned CNTs[178] have all led to increased reversible capacity. CNT arrays and their composites show good capacity, excellent rate performance and long cycle life when used as electrode materials[179-181]. Elemental doping of CNTs has been also a recent tactic to improve electrochemical performance[182, 183].

Doping CNT anodes with heteroatoms influences the Li^+ storage capacity for LIBs. N-MWCNTs have been investigated as anodes and have shown reversible capacity from 135-494 $mAhg^{-1}$[67, 165, 184-188]. A higher reversible capacity is attributed to the incorporation of graphitic or pyridinic N-atoms that facilitate higher electrical conductivity and more defect sites for Li^+ storage[67, 165, 188, 189]. In this chapter we investigated G-N-MWCNTs, SCNs, SCNs-300, SCNs-2500.

5.2.5. Electrochemical techniques for LIB research

Half-cells are usually used for conducting fundamental research on LIB electrodes. A half cell is a cell with a single electrode (either positive or negative) as the working electrode (WE) and pure lithium metal as the counter electrode (CE) and also as the reference electrode (RE), whose electrochemical potential does not change and is set to zero. The performance of carbon is generally evaluated with the help of Li/C cells. Thus, carbon is positive electrode of the cells and Li intercalation is the discharge process, whereas it is the charge process in C/MO cells (real battery). The WE is composed of a mixture of active material (carbon), polymeric binder and often, carbon black. The role of carbon black is to increase the conductivity and the wettability of the electrode by the electrolyte. Electrochemical systems are usually evaluated using cyclic voltammetry and galvanostatic cycling.

Cyclic voltammetry:

In cyclic voltammetry the potential is swept towards a maximum and then returned to a minimum linearly. The procedure can be repeated (cycled) many times. During such experiments, the current is recorded as function of the potential and, in general, the shape of the I-V curve depends on the sweep rate.

Galvanostatic cycling:

In galvanostatic cycling experiments, the current intensity is imposed and kept constant. The potential is recorded as function of the total charge passed through the system. The sign of current intensity is changed once a maximum or a minimum potential difference is reached. The information obtained from galvanostatic cycling can be plotted in three ways, namely potential-capacity profile, differential potential-capacity profile, and cycling performance. Many examples are presented in this chapter. We can obtain information about phase transformations in electrodes, rate performance, potential range for practical use, cycle life and coulombic efficiency for LIBs from galvanostatic cycling.

5.3. Results and discussion

The materials being investigated are:

1. G-N-MWCNTs
2. Spiraled carbon nanoribbons (SCNs)
3. Spiraled carbon nanoribbons annealed @ 300 °C (SCNs-300)
4. Spiraled carbon nanoribbons annealed @ 2500 °C (SCNs-2500)

5.3.1. Characterization of materials

Following the process described in chapter 2, SCNs were synthesized by $KMnO_4/H_2SO_4$ oxidation of G-N-MWCNTs. Annealing at 300 °C (SCNs-300) (5-1) was used to remove the oxygen-containing functional groups. In addition, annealing the material at 2500 °C (SCNs-2500) (5-2) makes the carbon more graphitic. TGA plot of SCNs (Figure 5-1, curve green) showed considerable low-temperature weight loss (~55%) compared to G-N-MWCNTs (Figure 5-1, curve black). Also, the onset temperature of oxidation of remaining disordered carbon is shifted to a much lower temperature. In case of SCNs-300 (Figure 5-1, curve blue), there is almost no low-temperature weight loss. So the treatment was able to remove almost all of the oxygen-containing functional groups. The remaining disordered carbon is not significantly affected and the onset temperature is almost the same as for SCNs (Figure 5-1, curves green and blue). But, in the TGA of SCNs-2500 (Figure 5-1, curve red), there is not only almost zero low-temperature weight loss, but also the onset temperature of oxidation is very similar to the G-N-MWCNTs, which suggests that remaining carbon had been annealed back to a nearly graphitic state.

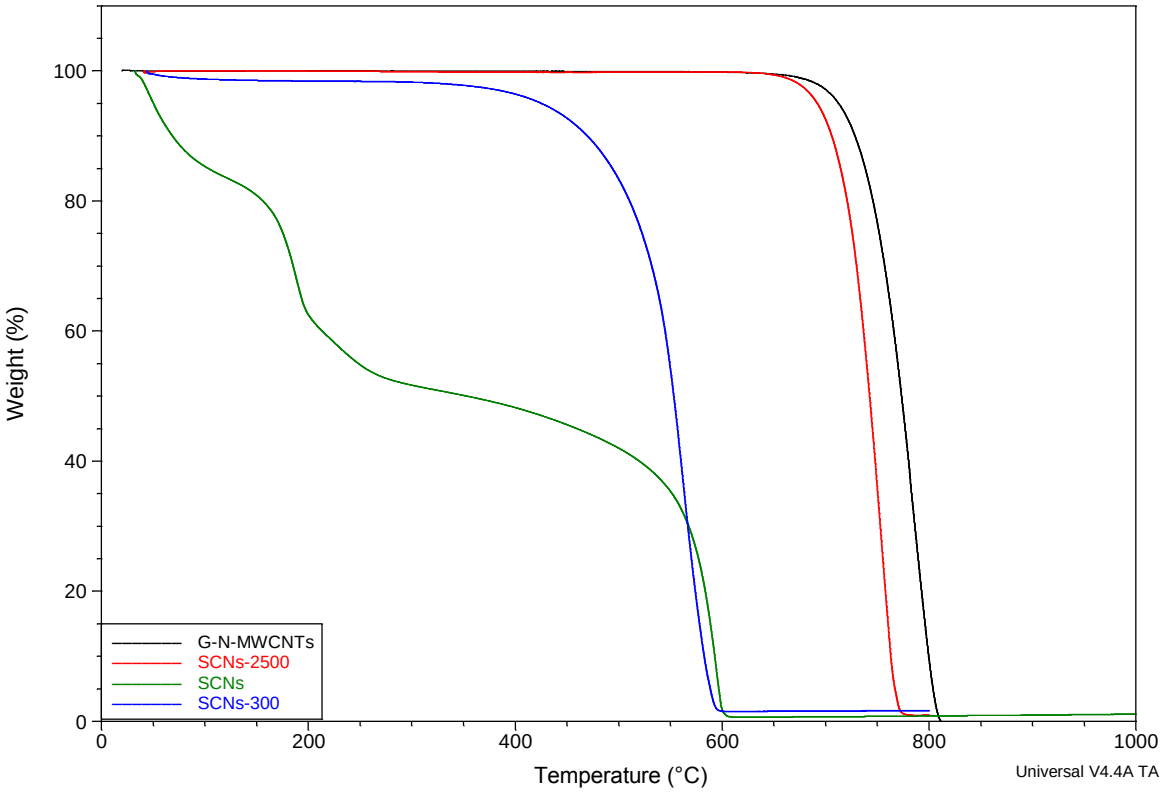

Figure 5-1 TGA plot comparing G-N-MWCNTs (black), SCNs (green), SCNs-300 (blue) and SCNs-2500 (red).

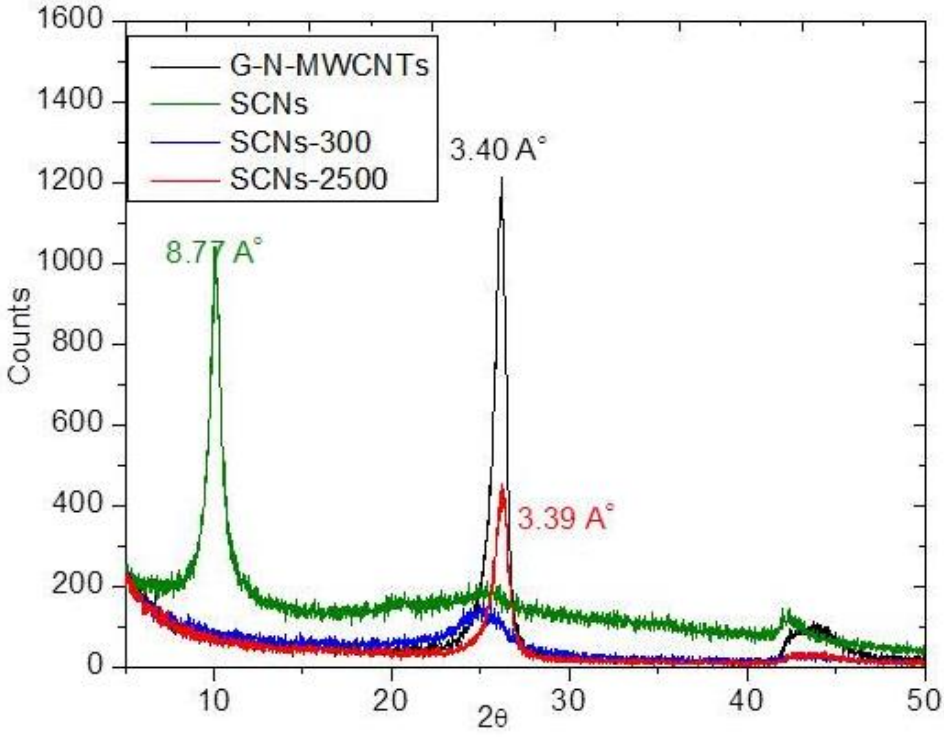

Figure 5-2 XRD plot comparing G-N-MWCNTs (black), SCNs (green), SCNs-300 (blue) and SCNs-2500 (red).

XRD (Figure 5-2) is used to evaluate crystalline structure of the materials. Starting tubes have 2θ values of ~26.18˚ (Figure 5-2, curve black). This corresponds to an average d_{002} spacing of 3.4 Å, exhibiting a high degree of graphitization. However, after oxidation (conversion to SCNs), the average d_{002} spacing increased to 8.77 Å (Figure 5-2, curve green). This is a more graphite oxide-like structure[97]. In SCNs-300, rapid heating of the SCNs causes violent formation of volatile gaseous species from oxygen-containing functionalities, forcing apart the adjacent graphene layers and producing a highly disordered material. Hence no distinct peak corresponding to a d_{002} spacing (Figure 5-2, curve blue) is observed, other than a small broad peak around 3.4 Å. But, the 2500 °C treatment reverses oxidation by thermally desorbing all the covalently attached species and repairing the defects. XRD (Figure 5-2, curve red) confirms the remarkable recovery of graphitic structure with an average d_{002} spacing of 3.39 Å.

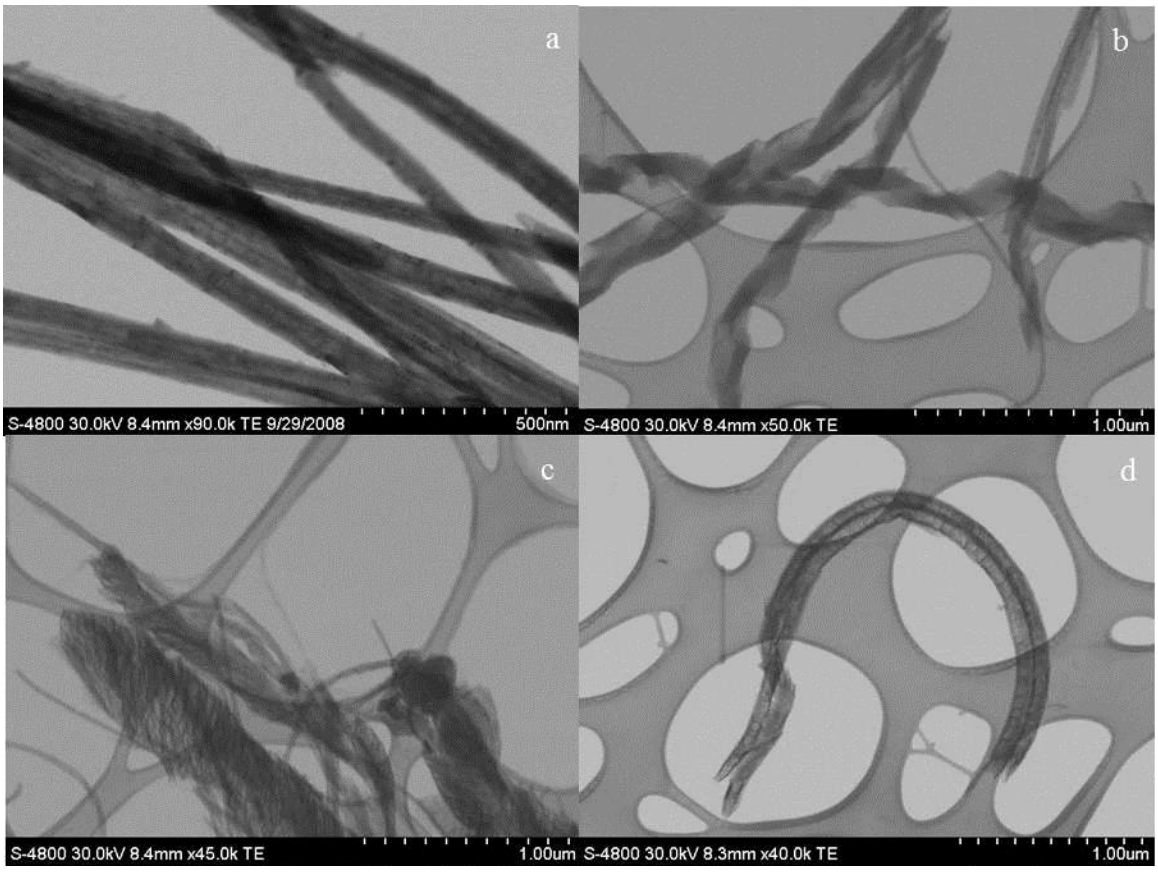

Figure 5-3 STEM of (a) G-N-MWCNTs, (b) SCNs, (c) SCNs-300 and (d) SCNs-2500.

Figure 5-3 and 5-4 respectively represent STEM and TEM of the four materials under discussion. Figure 5-3(a) represents STEM of starting tubes, G-N-MWCNTs and 5-3(b) of SCNs. Upon annealing of SCNs at 300 °C, the material has a wrinkled texture (Figure 5-3(c)). Rapid heating of the SCNs at 300 °C forces the adjacent graphene layers to move apart, giving rise to the texture seen in Figure 5-3(c). As mentioned earlier, SCNs are highly mesoporous (Chapter 3, Figure 3-12). Prior to calculation of pore size distribution and surface area using BET model, the material is degassed at 300 °C. SCNs, now SCNs-300, have a wrinkled texture and these wrinkles on the surface, as seen in Figure 5-3(c), are the new mesopores. Annealing of SCNs at 2500 °C, gives rise to a new texture (Figure 5-3(d)) that became more clear when analyzed by TEM.

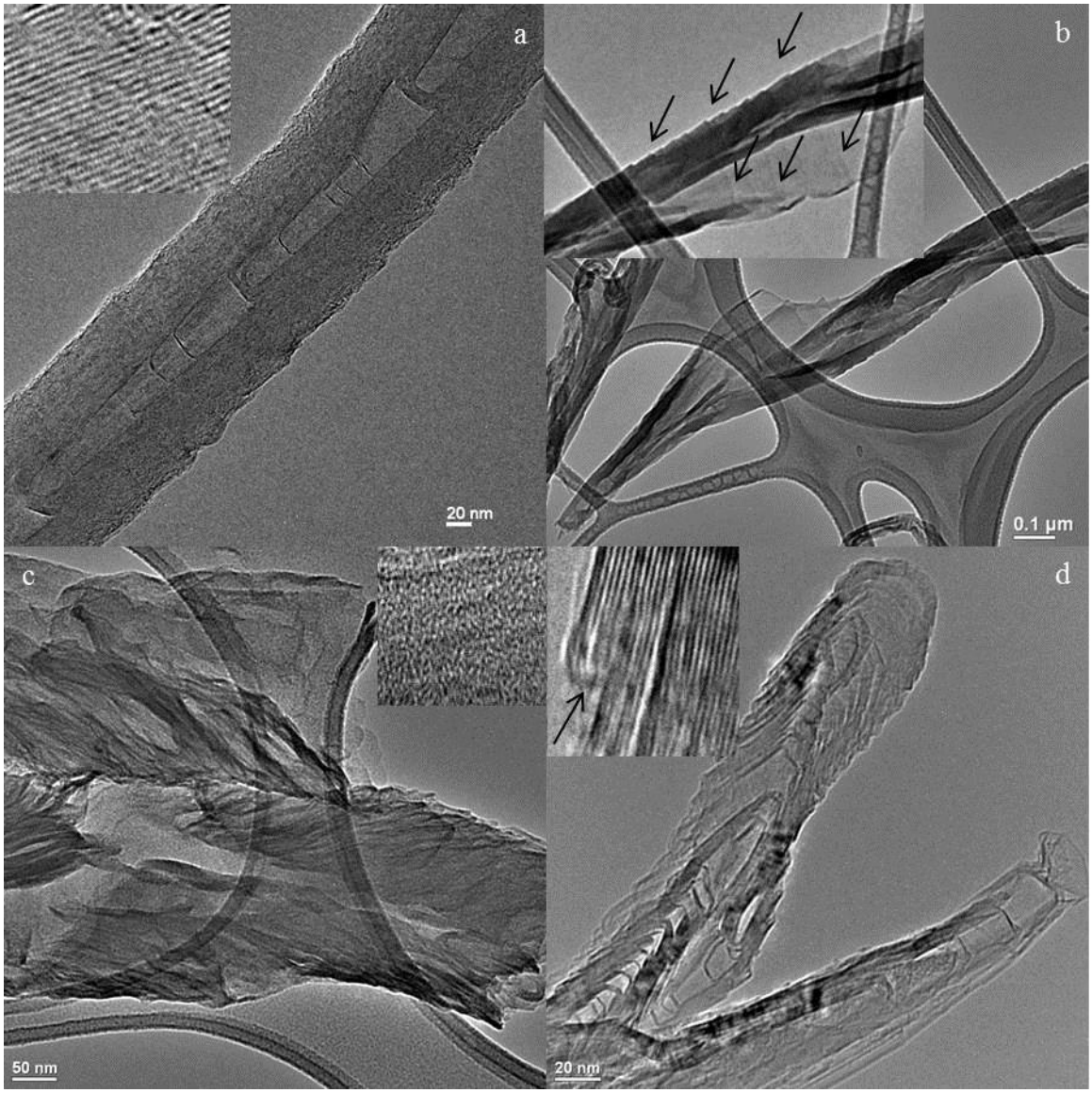

Figure 5-4 TEM of (a) G-N-MWCNTs, (b) SCNs, (c) SCNs-300 and (d) SCNs-2500.

Figure 5-4(a) shows a TEM image of G-N-MWCNTs and Figure 5-4(b) is for SCNs. SCNs-300 (Figure 5-4(c)) looked rumpled with highly distorted graphene planes. The inset shows no sign of any ordering of layers. The original texture of SCNs is still retained, but the material looks exfoliated. TEM (Figure 5-4(d) of the material annealed at 2500 °C showed an interesting morphological transformation. It exhibits a stacked cone type texture that may be formed by the healing[127, 133] of the open subunits that compose SCNs. Another feature of the SCNs-2500 is the formation of a loop between neighboring conical sheets (inset, shown by arrow). The carbon looks more ordered and the interlayer spacing is also retained.

5.3.2. Electrochemical performance

G-N-MWCNTs

The morphology of WEs consisting of G-N-MWCNTs as the active materials is shown in Figure 5-5. The white particles are the NaCMC binder. After coating and drying, the G-N-MWCNTs form a uniform, interconnected layer with no obvious orientation preference.

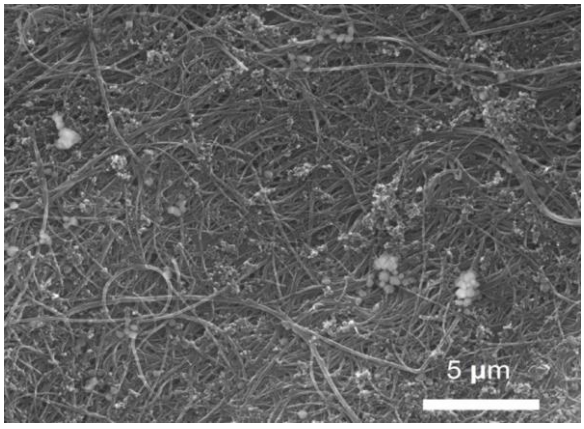

Figure 5-5 SEM image of working electrode.

Figure 5-6(a) compares the galvanostatic potential-capacity profiles of lithiation and de-lithiation of G-N-MWCNTs at the 1st, 2nd, and 70th cycle. The cycling rates are C/10 for 1st and 2nd cycles, and C/5 for 70th cycle. In this work, the C rate is calculated based on the theoretical capacity of graphite (372 mAh g^{-1}). Hence a rate of C/10 corresponds to a current (37 mA g^{-1}) necessary to (dis)charge the full theoretical capacity within 10 h. The first cycle for G-N-MWCNTs (Figure 5-6(a)) is characterized by a discharge capacity (C_{1st}) of 503 mAh g^{-1} and a charge capacity of

345 mAh g^{-1} ($C_{rev-1st}$). The loss of capacity, known as irreversible capacity, is 158 mAh g^{-1} ($C_{irrev-1st}$). $C_{rev-1st}$ of G-N-MWCNTs under C/10 is lower than the theoretical reversible capacity of graphite but similar to its practical capacity. $C_{irrev-1st}$ is mainly due to the irreversible formation of a solid-electrolyte interphase (SEI)[190] layer on the electrode surface. The electrochemical potential range for SEI formation is more clear in differential potential-capacity profile, as shown in Figure 5-6(b). Comparing the discharge (lithiation) curves at 1st and 2nd cycle, SEI formation on G-N-MWCNTs occurs mainly in the range of 1.0 to 0.1 V vs. Li/Li^+; the peak around 0.7 V (inset Figure 5-6(b)). This is consistent with observed potential range for SEI formation on carbonaceous materials[143]. SEI is formed nearly completely during 1st lithiation and does not decompose readily. After the 1st lithiation, the electrochemical performance of G-N-MWCNTs is so stable that the potential-capacity profiles of de-lithiation at 1st and 2nd cycles overlap with each other (Figure 5-6(b)).

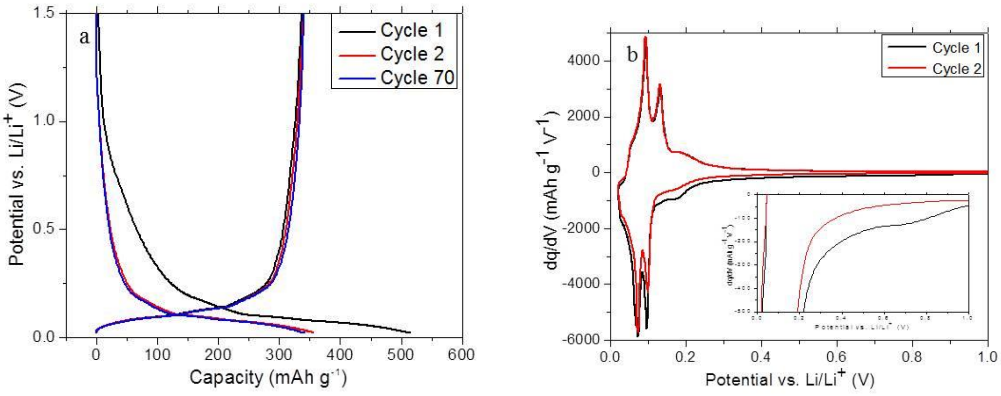

Figure 5-6 (a) Constant current potential-capacity profile; (b) Differential potential-capacity profile of Li in G-N-MWCNTs at selective cycles.

The mechanism of lithiation and de-lithiation of G-N-MWCNTs can be drawn from differential capacity profiles (Figure 5-6(b)). It is known that the existence of voltage plateaus correspond to transitions between different single phases and the end points of the plateaus give the composition. In G-N-MWCNTs, three reduction peaks (0.180V, 0.100V, and 0.075V) and the corresponding oxidation peaks (0.192V, 0.134V, and 0.097V) occur at potentials similar to known processes in graphite electrodes[139]. These follow a reaction mechanism shown below:

$$LiC_{72} \rightleftarrows LiC_{36} \cdots LiC_{18} \rightleftarrows LiC_{12} \rightleftarrows LiC_6$$

This suggests that G-N-MWCNTs have a structure that is primarily well-stacked and as ordered as graphite. G-N-MWCNTs also show a very stable reversible capacity upon extended cycling, as shown in Figure 5-7(a). The reversible capacity of 336 mAh g^{-1} for the 11th cycle shows essentially no decrease up to 70 cycles under a cycling rate of C/5. The capacity remains above 300 mAh g^{-1} after 300 cycles under an accelerated cycling rate of C/2. Coulombic efficiency upon extended cycling is greater than 99.9% (Figure 5-7(b)). High coulombic efficiency is needed by advanced LIBs for electric vehicles (EVs) whose cycle life is required to be as long as 5000 cycles.

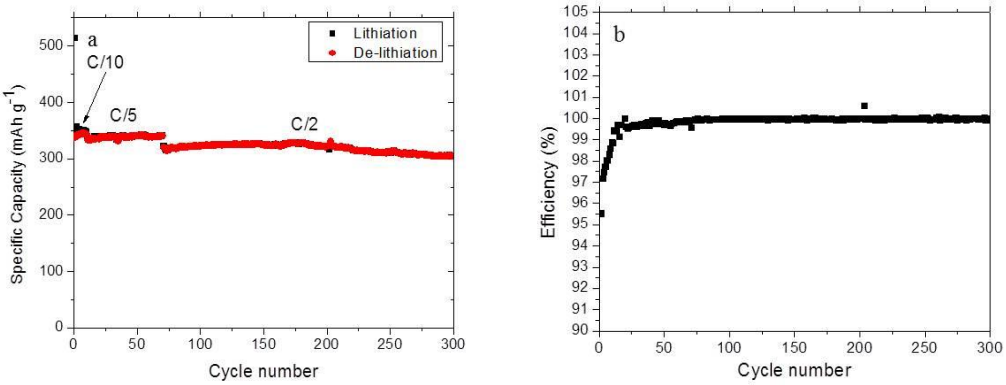

Figure 5-7 Constant current cycling performance of G-N-MWCNTs/Li half cells; (a) specific discharge/charge capacities (b) coulombic efficiency.

The constant current cycling performance of G-N-MWCNTs under different rates is summarized in Figure 5-8. The reversible capacity of G-N-MWCNTs is 348, 340, 322, and 287 mAh g^{-1} for cycling rate of C/10, C/5, C/2, and 1C respectively. However, when the cycling rate goes up to 2C, the capacity is only 180 mAh g^{-1}. It also drops to lower than 100 mAh g^{-1} at rates faster than 5C. This indicates that the performance of G-N-MWCNTs at high rates is not ideal. But, this material can be used at rates of 1C, which is practical for low power applications. Reducing the average length of G-N-MWCNTs and thus the mean diffusion distance for lithium could possibly enhance the performance of the anodes at a higher rate.

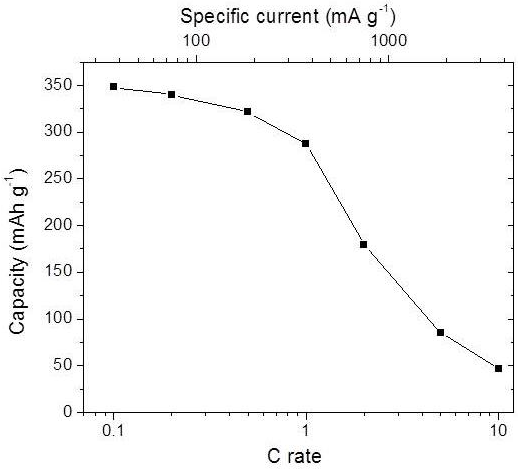

Figure 5-8 Rate performance of G-N-MWCNTs. C rates are calculated based on the theoretical capacity of graphite. 1C refers to a specific current of 372 mA g^{-1}.

Table 5-5 presents an overview of materials that are either MWCNTs or N-MWCNTs and their electrochemical performance. All the materials listed are produced by CVD method, but the recipe in each case is different including differences in hydrocarbon source and conditions. If we compare the initial reversible capacities, it is apparent that there is considerable variation among each material and also from theoretical capacity of graphite. Although this may not be considered as a thorough comparison since these materials are cycled at different rates, it gives an overall picture of their performance as negative electrodes for LIBs. The difference in behavior suggests that lithium ion storage in these materials depend strongly on crystallinity, microstructure and morphology of the materials. Another important battery parameter is efficiency, and these materials do not show a good cycling and coulombic efficiency except the last two entries. A recent report[67] on N-MWCNTs as negative electrodes demonstrated much higher capacity of 494 mAh g^{-1} with a capacity of 397 mAh g^{-1} in the 100^{th} cycle. So, the overall efficiency is 80% after 100 cycles when cycled at a relatively high current density of 100 mA g^{-1}. The authors attributed the improved performance to high concentration of nitrogen (16.4 at.%) in carbon nanotubes facilitating higher electrical conductivity and more defect sites in anodes providing more Li^+ storage in electrochemically active locations. G-N-MWCNTs we have studied retain 93% of the initial reversible capacity even after 300 cycles. This is at a higher rate (185 mA g^{-1}) than reported (100 mA g^{-1}) by Li *et al.*[67].

Table 5-5 Electrochemical performance of CNTs.

Material	Current density (mA g^{-1})	First reversible capacity (mAh g^{-1})	Cycle number	Remaining capacity (mAh g^{-1})
MWCNTs[160]	17	447	5	273
MWCNTs[191]	10	300	20	260
MWCNTs[162]	50	250	80	220
MWCNTs[172]	20	700	6	150
N-MWCNTs[184]	37	480	30	420
N-MWCNTs[187]	75	230	10	131
N-MWCNTs[188]	17	270	30	~ 270
N-MWCNTs[67]	100	494	100	397 (80%)
G-N-MWCNTs (this work)	185	322	300	300 (93%)

Annealing of N-MWCNTs removes nitrogen as suggested by XPS (Figure 2-10(d)) and EELS (chapter 2). These results establish that contrary to the explanation ventured by Li *et al.*[67], nitrogen has *little or no role* to play in the high stability observed in the electrochemical performance of our material. The morphology and microstructure of G-N-MWCNTs is likely to be responsible for the observed electrochemical characteristics.

Structure of G-N-MWCNTs after cycling

In order to examine stability of the material after electrochemical tests, *ex-situ* TEM and Raman spectroscopy are conducted on dissected coin cell electrodes. A TEM image of G-N-MWCNT after 80 cycles, shown in Figure 5-9(a), suggests that G-N-MWCNTs retain their original layered structure. There is no evidence of mechanical degradation or surface damage. A uniform 15 nm layer of SEI is formed on the surface.

Ex-situ Raman spectra of G-N-MWCNTs before and after 50 cycles are shown in Figure 5-9(b). The average I_D/I_G ratio is 0.34 after 50 cycles, similar to the 0.37 ratio observed before cycling. Raman spectroscopy also indicates that the structure of G-N-

MWCNTs is stable and does not change significantly during extended electrochemical cycling. As suggested by Raman and XRD (Figure 2-10(b) and (c)), annealing at 2800 °C resulted in a more graphitic material. Although the exact structural changes are still not clear, graphitization seems to ensure better stability of the structure in extended cycling and thus providing a better cycle life[192].

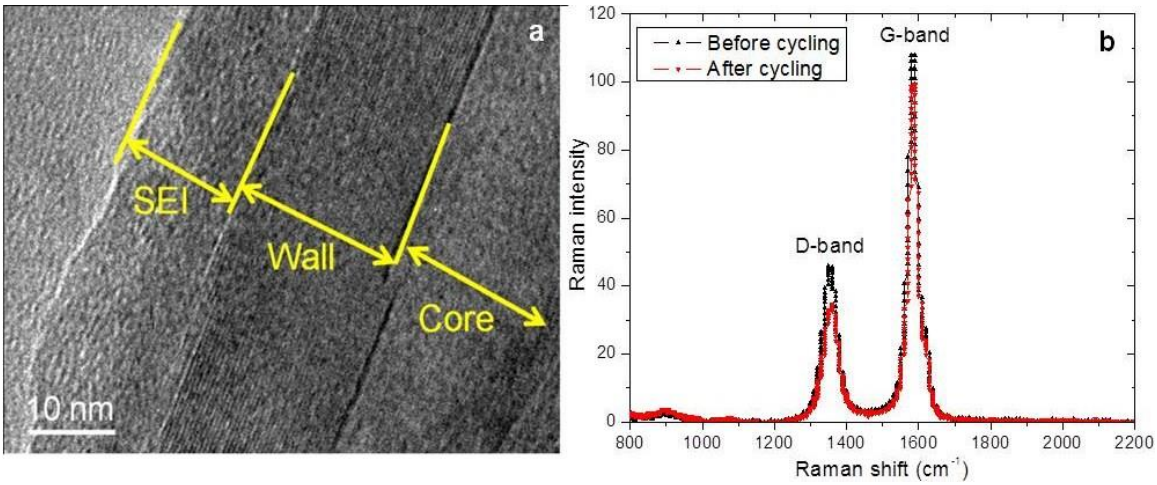

Figure 5-9 (a) *Ex-situ* TEM image of G-N-MWCNT after 80 cycles. (b) *Ex-situ* Raman spectra of G-N-MWCNTs before cycling and after 50 cycles.

The results indicate that the electrochemical performance of G-N-MWCNTs is similar to that of graphite. This suggests that the microstructure of as-produced N-MWCNTs evolve progressively towards a graphite microstructure when they are treated at a high temperature (up to 2800 °C) to produce G-N-MWCNTs.

SCNs

Figure 5-10(a) shows discharge-charge curves for cycles 1, 2 and 10 at a current rate of C/10 for SCNs. The first cycle for SCNs is characterized by a very high discharge capacity (C_{1st}) of 1700 mAh g^{-1}, a charge capacity of 980 mAh g^{-1} ($C_{rev\text{-}1st}$) and a irreversible capacity of 720 mAh g^{-1} ($C_{irrev\text{-}1st}$). The potential profile differs considerably from graphite[139] and G-N-MWCNTs with respect to curve slopes, without considerable plateaus with a charge/discharge voltage hysteresis. The behavior is similar to graphitizing (soft) and non-graphitizing (hard) carbons prepared below 900 °C that show very high specific charges and exhibit a hysteresis[143]. The extent of the hysteresis is proportional to the hydrogen content in the carbon. The attachment of Li starts from 3.0 V in the first cycle. The charge capacity is 2.6 times

that of the theoretical capacity of graphite (372 mAh g^{-1}), suggesting existence of other storage mechanisms in SCNs. It has been reported that oxygen-containing functional groups induce the formation of a much stable, chemically bonded SEI, resulting in loss of capacity during first few cycles[193].

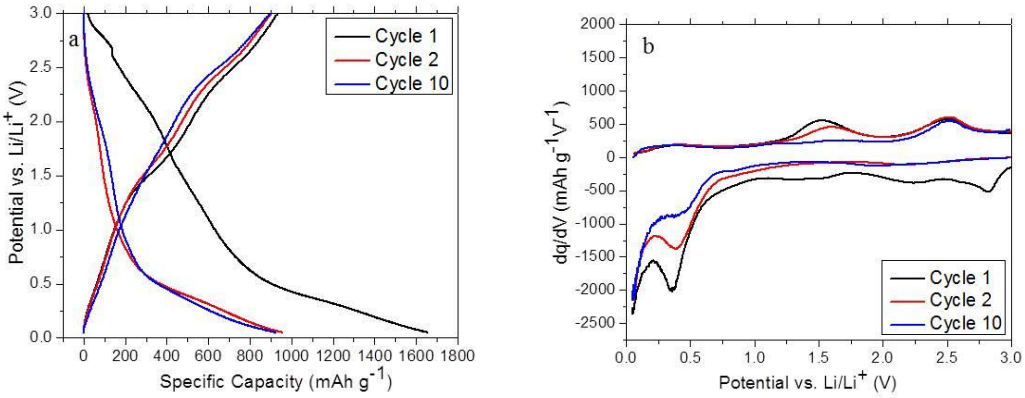

Figure 5-10 (a) Constant current potential-capacity profile; (b) Differential potential-capacity profile of Li in SCNs at selective cycles.

To get better insights, we plotted the differential capacity plot. The differential capacity vs. voltage plots of SCNs (Figure 5-10(b)) show a considerable capacity between 3-1.0 V in the first cycle in SCNs, which contributes the most to $C_{irrev\text{-}1st}$. Oxidation induces different types of oxygen-containing functional groups like, carboxyl, hydroxyl, carbonyl, epoxide, ether, lactone etc. These functional groups can react with Li ions during the first Li intercalation process to form -COOLi, -OLi etc. Peled *et al.*[193] proposed that these can be bonded to the solvent reduction products, e.g., Li_2CO_3, to form a chemically bonded SEI. Clearly, the reaction of Li ions with the functional groups during the first Li intercalation is an irreversible reaction resulting in a considerable loss of capacity in the first cycle[194]. The plot lacks any distinguishable peak around 0.7 V, which is usually the observed potential for SEI formation on carbonaceous materials[143]. The capacity below 0.75 V can be attributed to intercalation of Li into graphene layers[194]. The potential-capacity profile shows hysteresis and Li is de-inserted at higher potentials. The two oxidation peaks at 1.5 V and 2.5 V may be because of de-insertion of Li and it appears that Li has been removed from two different environments. Shenoy *etal.*[195] studied the lithiation of graphene oxide (GO) as a function of O-coverage using first-principles.

They observed that in GO with oxygen content 12.5 %, Li atoms can attach both by forming bonds with oxygen atoms and by forming LiC_6. The combined lithiation mechanism allows greater potential and capacity (approximately twice that of graphite). Recent studies have shown that carbonyl groups can be reduced by Li^+ and reversibly oxidized in the voltage range from 3.5 to 1.5 V vs. Li, in aromatic carbonyl derived materials such as poly(2,5-dihydroxy-1,4-benzoquinone-3,6-methylene)[196] and $Li_2C_6O_6$[197]. So, a high charge capacity in SCNs is probably due to attachment of Li to both oxygen and carbon atoms. In order to confirm the role functional groups in providing high capacity, SCNs were compared to SCNs-300.

SCNs-300

As mentioned earlier, the treatment successfully removes almost all of the oxygen-containing functional groups. Figure 5-11(a) represents discharge-charge curves for cycles 1, 2 and 10 at a current rate of C/10 for SCNs-300. Surprisingly, the first cycle for SCNs-300 is also characterized by a very high discharge capacity (C_{1st}) of 1700 mAh g^{-1}, a charge capacity of 880 mAh g^{-1} ($C_{rev\text{-}1st}$) and a irreversible capacity of 820 mAh g^{-1} ($C_{irrev\text{-}1st}$). The potential curve slopes without considerable plateaus with a charge/discharge voltage hysteresis. But the potential profile differs from SCNs in terms that there is almost no capacity in 3.0-1.0 V range. A considerable loss of capacity in the first cycle is therefore not because of the functional groups. This again is consistent with the expected result of heat treatment at 300 °C.

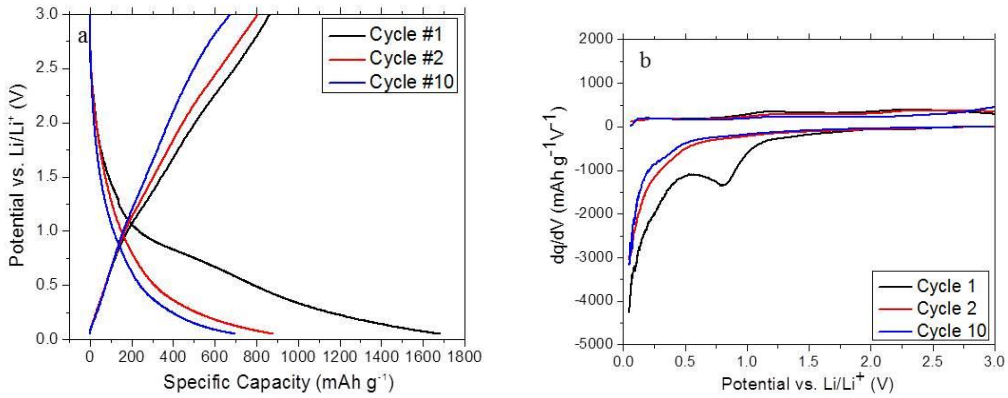

Figure 5-11 (a) Constant current potential-capacity profile; (b) Differential potential-capacity profile of Li in SCNs-300 at selective cycles.

The differential capacity vs. voltage plots of SCNs-300 (Figure 5-11(b)) clearly differs from that of SCNs (Figure 5-10(b)). It lacks a capacity between 3-1.0 V, which contributes mainly to $C_{irrev\text{-}1st}$ in the first cycle in SCNs and the two distinguishable peaks at 1.5 and 2.0 V seen in SCNs. Hence functional groups have no role in either $C_{rev\text{-}1st}$ or $C_{irrev\text{-}1st}$ in SCNs-300. But there is a huge capacity at around 0.8 V in SCNs-300 that contributes to $C_{irrev\text{-}1st}$, the observed potential for the formation of SEI in carbonaceous materials[143]. Thus the nature of SEI in both materials is different, one being chemically bonded and the other one being regular SEI formed in most carbonaceous materials in first cycle in organic electrolytes.

The main attraction of SCNs and SCNs-300 is that the reversible capacity of the electrodes is found to be very high and quite stable even after extended cycling; 530 mAh g^{-1} after 250 cycles in SCNs (Figure 5-12(a)) and 500 mAh g^{-1} after 350 cycles in SCNs-300 (Figure 5-12(b)), both higher than theoretical capacity of graphite. Although the coulombic efficiency is low for the first cycle (56 % for SCNs and 51 % for SCNs-300), after stabilization of capacity in few cycles (35 for SCNs and 50 for SCNs-300), the overall coulombic efficiency is good (99.5 % for SCNs and 98.5 % for SCNs-300). It is still lower than the excellent coulombic efficiency seen in G-N-MWCNTs. The rate capability of the materials is shown in Figure 5-13. At a high charging/discharging rate of 2 C, SCNs (Figure 5-13(a)) show a reversible capacity of ~400 mAh g^{-1}. SCNs-300 (Figure 5-13(b)) show a reversible capacity of ~300 mAh g^{-1} at much faster rate of 5 C.

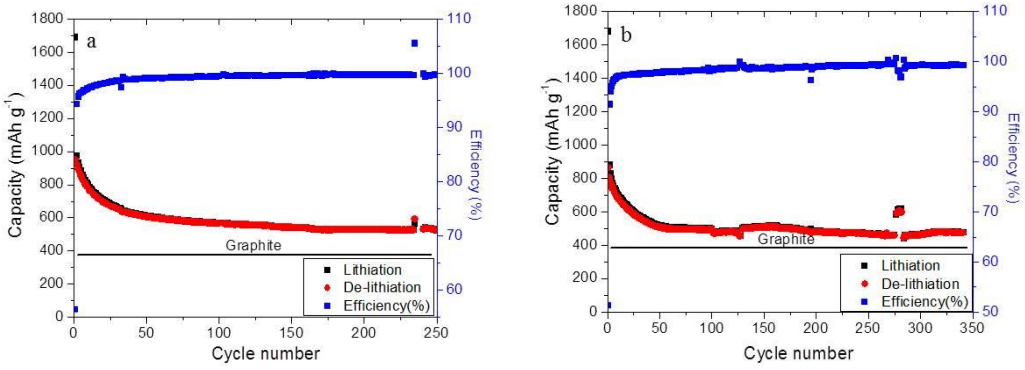

Figure 5-12 Constant current cycling performance (a) specific discharge/charge capacities and coulombic efficiency of SCNs/Li half cells; (b) specific discharge/charge capacities and coulombic efficiency of SCNs-300/Li half cells.

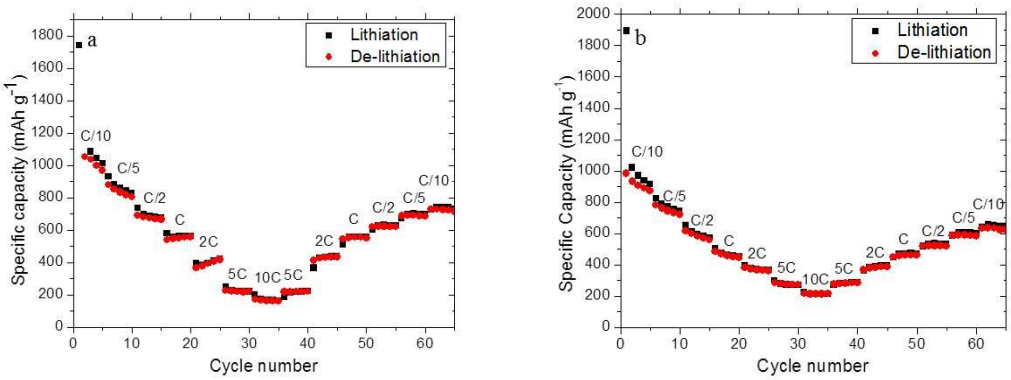

Figure 5-13 Rate performance of (a) SCNs and (b) SCNs-300.

The performance of both the materials, SCNs and SCNs-300, is better than graphite and G-N-MWCNTs. Table 5-6 lists some of the high capacity carbon materials. These include SWCNTs, porous carbons, carbon fibers, spheres and nanocages. The reported high capacity for MWCNTs is from graphene nanoribbons obtained by unzipping MWCNTs by permanganate oxidation, with a reversible capacity of 800 mAh g^{-1}.

Table 5-6 High capacity carbon materials.

Material	Current density (mA g^{-1})	First reversible capacity (mAh g^{-1})	Cycle number	Remaining capacity (mAh g^{-1})
SWCNTs[198]	50	942	60	150
Ordered mesoporous carbon[199]	50	3083	50	500
Hierarchical porous carbon[200]	75	1500	40	500
Carbon nanofibers[201]	100	680	25	260
Carbon spheres[202]	50	950	135	400
Carbon nanocages[203]	100	1050	50	520
Oxidized graphene	37	1400	15	490

nanoribbons[204]				
SCNs (this work)	37	1700	250	530
SCNs-300 (this work)	37	1700	350	500

Several mechanisms have been proposed to explain high capacity of certain materials. Peled *et al.*[205] suggested that the extra capacity gained upon mild oxidation of graphite is due to the accommodation of Li at the zigzag and armchair faces between two adjacent crystallites, and in the vicinity of defects. According to Xiang and co-workers[206], the role of the edges of carbon layers is essential for enhanced battery performance. Sato *et al.*[207] proposed that in addition to the regular site occupation leading to LiC_6, Li molecules (Li_2) will also occupy nearest neighbor sites in intercalated carbons. This conclusion was based on ^{7}Li NMR measurements which showed two bands with chemical shifts of 10 and 0 ppm, attributed to regular intercalated Li and Li_2 molecules respectively. Yata *et al.*[208] discussed the possibility of formation of LiC_2 in carbons with high d spacing (4.0 Å). From X-ray diffraction and small angle X-ray scattering experiments,[209] it was proposed that lithium can be adsorbed onto internal surfaces of nanopores formed by single-layer, bi-layer and tri-layer groups of graphene sheets which are arranged like a `house of cards'. Yazami *et al.*[210] proposed the formation of lithium multilayers on graphene sheets. In porous carbons, the 3D network of pores provide favorable transport channels for Li insertion, hence high reversible capacity and superior rate performance[211]. Size of pore should be small to avoid the reaction of stored lithium with the electrolyte[212, 213]. In addition to microporosity, microtexture should also be regarded[214].

Explanation for enhanced performance

Important structural features of the materials under study are tabulated in Table 5-7. This table is used as a guide to find key reasons for differences in reversible storage capacity we obtained from our material by different treatments. This would further be utilized to understand the Li storage mechanism.

Table 5-7 Important structural parameters of materials being tested.

Sample	XRD (Figure 5-2)	Raman (Figure 5-14)	Surface area (Figure 5-15)	TGA (Figure 5-1)
	d spacing (nm), L_c (nm), no. of layers	**I_D/I_G, L_a (nm)**	**area (m^2/g), % meso porosity**	**% low-temp. wt. loss, temp. of oxidative degradation**
G-N-M WCNTs	0.34, 11, 34	0.13, 145	42, 51	~ 0, 784
SCNs	0.87, 27, 31	1.06, 17.8	N/A	~ 60, 590
SCNs-300	N/A	1.08, 17.4	266, 78	~ 5, 562
SCNs-2500	0.34, 9, 27	0.11, 171	81, 57	~ 0, 755

Estimation on number of layers and L_c was calculated based on XRD data (Figure 5-2). Scherrer equation is used in X-ray diffraction and crystallography to find the dimensions of the crystallite. The stacking length in the c-direction L_c, in carbon materials can be determined from the Bragg peak (002) by Scherrer formula[215]:

$$L_c = \frac{0.9\lambda}{B\cos\theta}$$

Here, λ is X-ray wavelength, θ is Bragg angle and B is the line broadening at half the maximum intensity. The number of layers in c-direction is calculated by dividing L_c by spacing between the layers (d_{002}). The degree of order of the layers within the materials was examined using Raman spectroscopy, shown in Figure 5-14. In G-N-MWCNTs the ratio of intensities of D band to G band is 0.13, indicating that high-temperature annealing reduces the defect density producing more perfect structure.

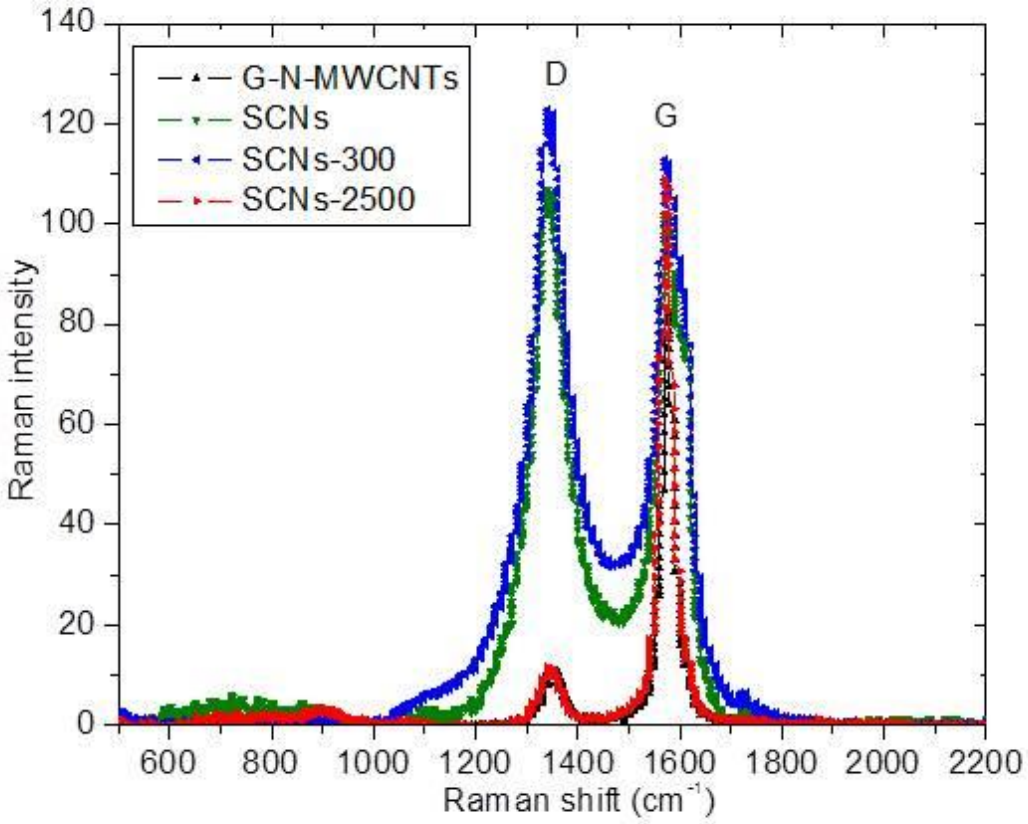

Figure 5-14 Raman analysis of G-N-MWCNTs (black), SCNs (green), SCNs-300 (blue) and SCNs-2500 (red).

$KMnO_4$ oxidation of G-N-MWCNTs increased I_D/I_G ratio to 1.06. In SCNs-300, the ratio of intensities is similar to SCNs. The treatment is able to remove almost all the functional groups, but the degree of disorderness remains the same. The length in the a-direction, L_a, can be calculated from intensity ratio I_D/I_G[216]:

$$L_a = \frac{560}{E_l^4}\left(\frac{I_D}{I_G}\right)^{-1}$$

where E_l is the excitation energy of the laser used in the Raman experiment in eV. Table 5-7 suggests that the microstructure of SCNs and SCNs-300 is different from G-N-MWCNTs. G-N-MWCNTs are highly ordered (Figure 5-4(a), inset), with d_{002} spacing close to that of graphite, whereas SCNs and SCNs are disordered with I_D/I_G approximately ten times that of G-N-MWCNTs. The larger I_D/I_G ratio of SCNs and SCNs-300 in comparison to that of G-N-MWCNTs indicates more disorder, defects,

and smaller sp^2 domains.

The capacity of carbons is largely affected by crystallite size. Endo *etal.*[217] showed that the minimum capacity is obtained when L_c is of the order of 100 Å. For L_c>100 Å, a classical intercalation process should occur, governed by the L_c value, as shown for example in the case of sulfuric acid intercalation[218]. On the other hand for L_c<100 Å, the occurrence of a different process of doping and undoping, namely the formation of covalent Li_2 molecules which could act as a Li ion reservoir. Substantial disorder leads to a decrease in L_a and increase in the capacity. The increased number of edge sites at the periphery of the sp^2 nanodomains and other defects are suggested to accommodate additional Li[88]. The crystallite dimensions change dramatically upon treatment of G-N-MWCNTs to form SCNs and SCNs-300 (Table 5-7). In case of SCNs, L_c is increased ~2.4 times as *d* spacing increases from 0.34 to 0.87 nm by the introduction of functional groups, although the number of layers are similar when compared to G-N-MWCNTs. While, L_a is decreased from 145 to 18 nm in SCNs obtained from oxidation of G-N-MWCNTs. The value of L_a remains the same upon further treatment of SCNs to make SCNs-300. Hence we believe that the defects at edge sites of the nanodomains embedded in graphene nanosheets (formed as of reduction in L_a), whose existence is confirmed by Raman spectroscopy, is one of the reason for greatly enhanced reversible capacities observed in SCNs and SCNs-300.

TEM image (Figure 5-4(b), inset shown by arrows) suggests that SCNs have a layered structure with new edges available in this new texture to bind additional Li. Thus, in SCNs the enhanced capacity is because of intercalation of Li in between the layers, Faradaic reactions at oxygen-containing functional groups, additional binding of Li to the new edges and defects at edge sites of the nanodomains. STEM and TEM (Figure 5-3(c) and 5-4(c)) of SCNs-300 show that the material has a wrinkled morphology with highly distorted graphene planes. In order to account for similar I_D/I_G ratio in SCNs and SCNs-300, we think that (based on electron microscopy) that SCNs could have inner defects in the layered graphene structure whereas SCNs-300 have defects more in the form of surface defects. Hence the defect-based reversible storage of Li dominates in SCNs-300. Also, the large voltage hysteresis is related to these active defects. It may be possible that the breaking of the relatively strong bonds of Li with

the defects in charge processes requires higher voltages, thus resulting in the voltage hysteresis.

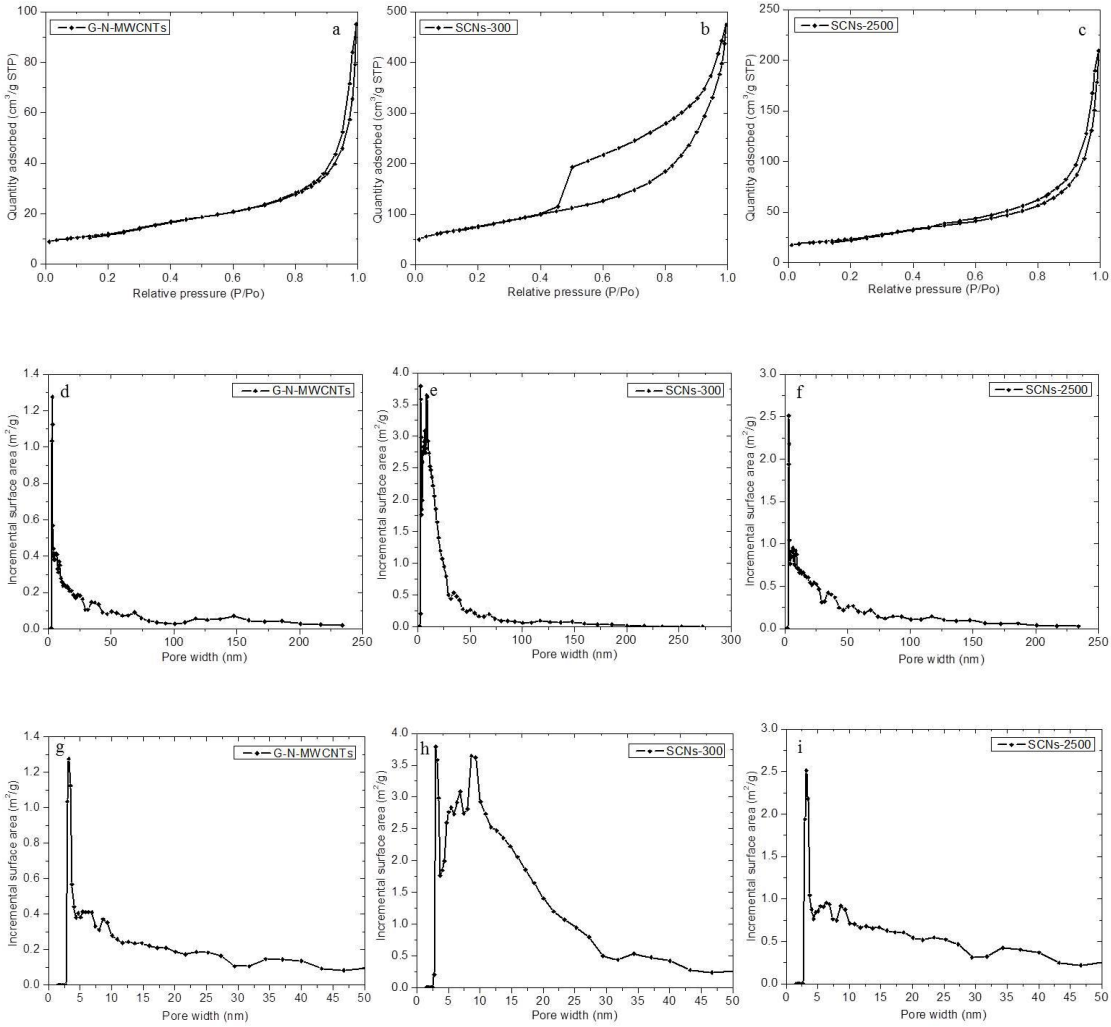

Figure 5-15 Surface area isotherms, plots of incremental surface area vs. pore width and rescaled plots of incremental surface area vs. pore width for G-N-MWCNTs (a, d and g), SCNs-300 (b, e and h), and SCNs-2500 (c, f and i) respectively.

The porous structure and specific surface area of these materials are investigated by nitrogen isothermal adsorption using BET model (Figure 5-15). G-N-MWCNTs reveal a Type II isotherm (Figure 5-15(a)), which indicates that the material has very little microporosity and is mostly bulk surface area (42 m^2/g). SCNs-300 (Figure 5-15(b)), however, exhibit a Type IV isotherm with a well-defined capillary

condensation step between 0.50 and 0.45 P/P_o, indicating formation of new mesopores. A plot of incremental surface area vs. pore size (Figure 5-15(e) and (h)) shows an additional peak at ~10 nm for these new mesopores, whereas there is no peak in the corresponding plot of G-N-MWCNTs (Figure 5-15(d) and (g)). The wrinkles seen in the STEM and TEM images on the surface of SCNs-300 are likely to be the new mesopores. The surface area increases to 266 m^2/g and the material is ~ 80% mesoporous. So, the huge irreversible capacity in first cycle of SCNs-300 is attributed to their high specific surface area.

The rate performance of LIBs is limited by diffusion of Li ions[219, 220]. Pores formed by the increased interlayer spacing and edges in SCNs may be responsible for their improved rate performance compared to G-N-MWCNTs. The increased mesoporosity of SCNs-300 provides fast transport channels for the ions, largely reducing the diffusion length[221]. This improves their rate performance compared to G-N-MWCNTs and SCNs.

We hypothesized that the texture of SCNs is formed by relative motion of thin graphite subunits (SEM, TEM and STEM) (roughly trapezoidal). So, the flexibility of the texture may act as buffer to the volume changes during the (dis)charging processes, provide enough stability to the electrode and hence better cycling stability and coulombic efficiency. The mesoporous structure permits excellent cycling stability by shortening diffusion lengths. But as of their negative effects, mesopores and defects are responsible for the low coulombic efficiency of SCNs-300 as compared to G-N-MWCNTs and SCNs.

SCNs-2500

The next material we tested is SCNs-2500. The treatment not only removes the functional groups but also anneals the carbon back to a graphitic form. It lacks both high discharge and charge capacity compared to SCNs and SCNs-300. The first charge and discharge capacity (Figure 5-16(a)) is similar to that of graphite and G-N-MWCNTs. This seems reasonable as the material retains a d_{002} spacing of 0.34 nm from 0.87 nm upon treatment. Healing of defects at the edge sites is indicated by the increase in La from18 to 170 nm. Also the I_D/I_G ratio reverts to the ratio observed in

G-N-MWCNTs. These reveal a Type II isotherm (Figure 5-15(c)) similar to G-N-MWCNTs (Figure 5-15(a)). Plot of incremental surface area vs. pore size (Figure 5-15(f) and (i)) is also similar to that of G-N-MWCNTs (Figure 5-15(d) and (g)).

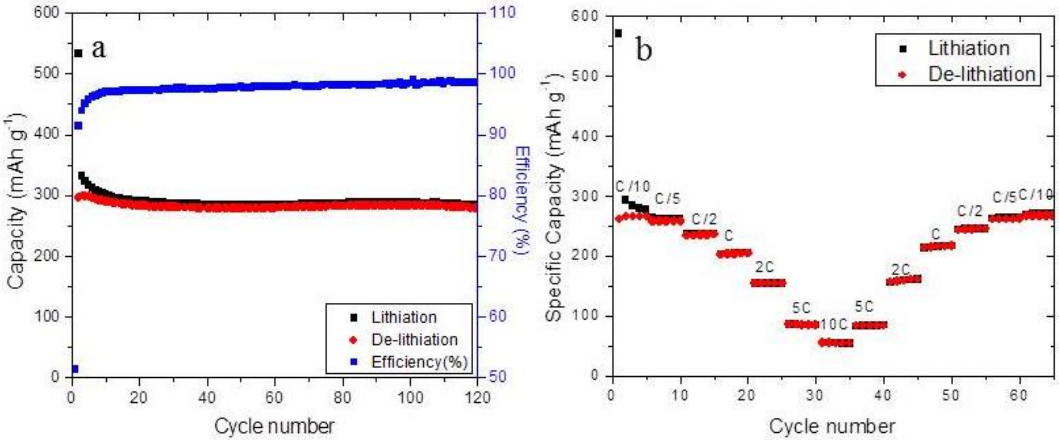

Figure 5-16 (a) specific discharge/charge capacities and coulombic efficiency of SCNs-2500/Li half cells and (b) rate performance of SCNs-2500.

The material shows an excellent efficiency through 150 cycles (Figure 5-16(a)). After that the capacity starts deteriorating and almost becomes zero in 200 cycles. The results indicate that the structure of SCNs-2500 is not stable under extended cycling, unlike G-N-MWCNTs. The rate performance (Figure 5-16(b)) of SCNs-2500 looks ordinary with a capacity of 200 mAh g^{-1} and 150 mAh g^{-1} at faster rates of C and 2C respectively. The capacity is below 100 200 mAh g^{-1} at the much faster rate of 5C. SCNs-2500 show an average performance compared to G-N-MWCNTs, SCNs and SCNs-300. The annealing process is able to convert the microstructure back to original (G-N-MWCNTs), it may be that the new texture of SCNs-2500 is not stable to extended cycling.

5.4. Conclusions

Table 5-8 Electrochemical performance of materials under study.

Material	C_{1st} (mAh g^{-1})	$C_{irrev-1st}$ (mAh g^{-1})	$C_{rev-1st}$ (mAh g^{-1})	% loss of $C_{rev-1st}$ after 250 cycles
Graphite[143]	390	55	335	N/A
G-N-MWCNTs	468	158	310	3
SCNs	1700	720	980	47
SCNs-300	1700	820	880	43
SCNs-2500	520	220	300	100

Table 5-8 tabulates the electrochemical performance of all the materials under study. The results suggest that Li intercalation and de-intercalation strongly depends on the crystalline phase, microstructure and morphology of these materials. In G-N-MWCNTs, the reversible capacity is similar to graphite and is obtained by intercalation of Li between layers. In SCNs, the enhanced capacity is because of intercalation of Li between the layers, Faradaic reactions at oxygen-containing functional groups, additional binding of Li to the new edges and defects at edge sites of the nanodomains. On the other hand, the enhanced capacity in SCNs-300 comes from storage of Li in defects. Hence, by careful modification of our material we present different CNTs that can be accordingly used in different applications. The materials are easily tunable. SCNs are produced from G-N-MWCNTs by $KMnO_4/H_2SO_4$ oxidation. SCNs-300 are obtained by thermal treatment of SCNs at 300 °C. SCNs are annealed at high temperature (2500 °C) to produce SCNs-2500.

5.5. Experimental procedures

5.5.1. General Methods and Materials:

Galvanostatic cycling of coin cells was conducted using a potentiostat (Bio-Logic, MPG2) with cut-off potentials of 1.5 V and 0.02 V. Cycling rates were calculated based on the theoretical capacity of graphite, and 1 C corresponds to a specific current of 372 mA g^{-1} of the active materials.

For *ex-situ* Raman characterization of electrodes, working electrodes (WEs) consisting of 85 wt.% active material and 15 wt.% sodium carboxymethyl cellulose (NaCMC) were used in the cells in order to eliminate the influence of carbon black on Raman signals. For TEM characterization, active material directly loaded on Cu grid was used as the WEs. The cycled cells were disassembled in glove box and the WEs were rinsed in DMC (99%) before Raman and TEM tests.

Chemicals were ordered from Alfa Aesar (NaCMC, DMC and Li metal foil), Timcal (carbon black), Novolyte (electrolyte) and Celgard (polypropylene separators). The glove box used is from MBraun.

5.5.2. Annealing of $KMnO_4$ oxidized G-N-MWCNTs at 300 °C (SCNs-300) (5-1):

Annealing was performed using degassing port of ASAP 2010 surface area analyzer. 0.25 g sample of $KMnO_4$ oxidized G-N-MWCNTs (2-70) was added to a sealed sample probe and the probe was placed in a isothermal jacket. The sample was heated from room temperature to the target temperature of 300 °C for 6 h.

5.5.3. Annealing of $KMnO_4$ oxidized G-N-MWCNTs at 2500 °C (SCNs-2500) (5-2):

High-temperature annealing was performed at the UK Center for Applied Energy Research by heating 0.5 g samples of $KMnO_4$ oxidized G-N-MWCNTs (2-70) in a capped graphite crucible in a helium-purged vertical electric resistance tube furnace. The sample was heated from room temperature to the target temperature of 2500 °C at 50 °C/min under a flowing He atmosphere maintained slightly above atmospheric pressure. Sample was held at the final temperature for 1 hour before being cooled to room temperature at 50 °C/min[87].

5.5.4. General procedure for preparation of WEs:

A slurry consisting of 75 wt.% active material, 15 wt.% NaCMC binder, and 10 wt.% conducting additive (carbon black, Super C65) suspended in deionized water, was coated on Cu foils. After drying at 90 °C for 12 hrs, samples of the proper size were punched from the coated foil and used as the WEs. The counter electrodes (CEs) were pure Li metal foils (99.9%), and the electrolyte was a solution of 1M $LiPF_6$ dissolved in ethylene carbonate/dimethyl carbonate (EC/DMC, 1:1 by vol.). The WEs and CEs were separated by polypropylene separator. CR2025 coin cells were assembled in an argon-filled glove box where the oxygen and moisture content were both maintained below 0.1 ppm.

Active materials tested include G-N-MWCNTs, SCNs, SCNs-300 and SCNs-2500.

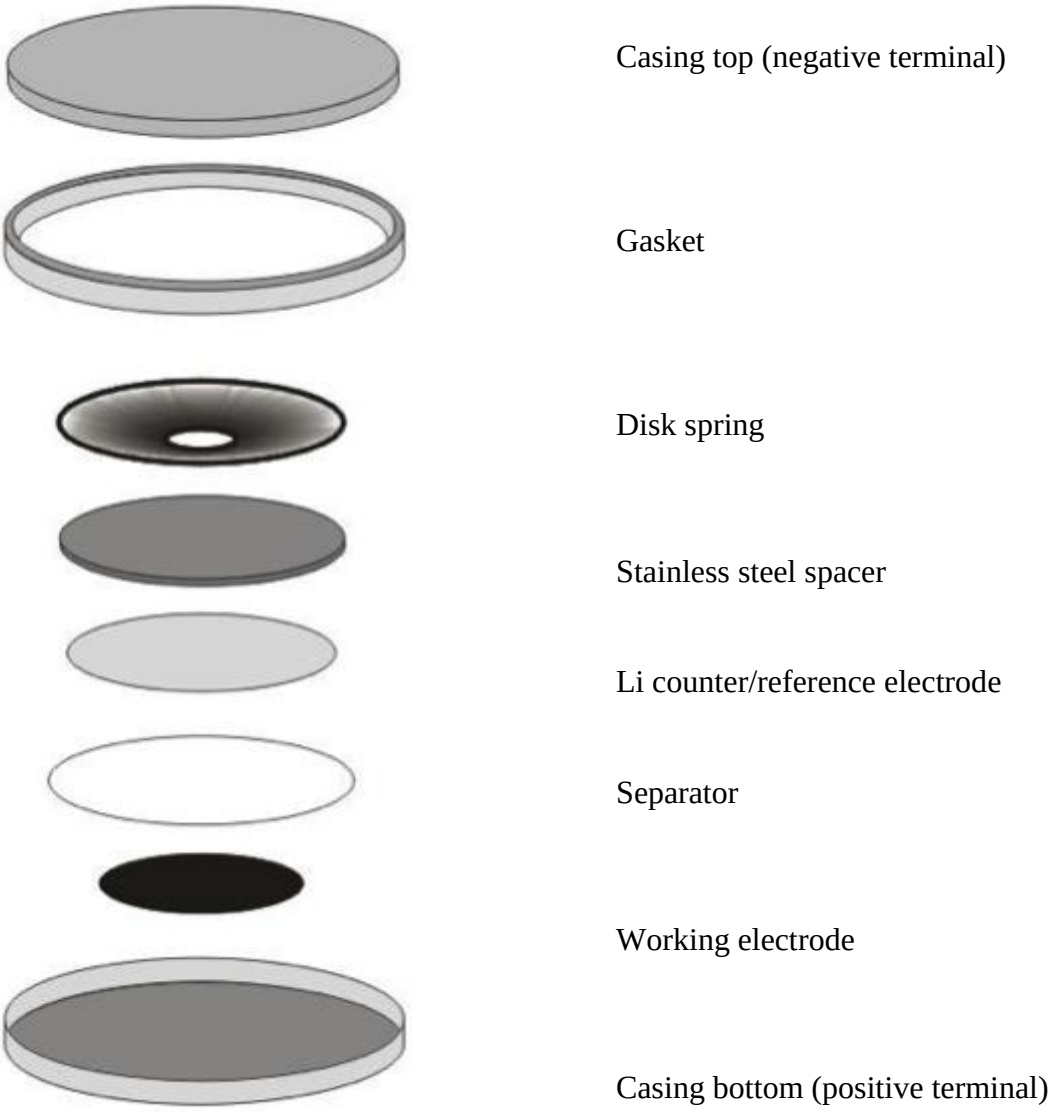

Figure 5-17 Cartoon showing different parts of a coin cell.

SUMMARY

This research study involved modification and characterization of carbon materials, specifically N-MWCNTs, and their application as possible negative electrodes for Li-ion batteries. This research is highly cross-disciplinary, combining facets of chemistry and engineering. Compared to the conventional CNTs, N-MWCNTs command greater attention due to their modified physical and chemical properties.

Functionalization of carbon materials is important to fine-tune the chemistry and physics required for their use in different applications. We have used dissolving metal reduction/alkylation and oxidations to modify N-MWCNTs which lead to textural modification (formation of linear and spiral channels and spiraled carbon nanoribbons). The chemically modified materials were characterized by TGA, DSC, SEM, STEM, TEM, EDX, EELS, surface area analysis using N_2 BET model, micro-Raman, XPS and powder X-ray diffraction.

In an attempt to unfurl the observed ribbon textures further, we fabricated polymer-CNT composites using various methods (melt method, solution methods) and pulled on the composites to understand the formation of these textures and answer some key questions about the structure of starting CNTs. The observations from this study were helpful in explaining the formation of different textures obtained from the same starting material, and gave us a confidence in proposing a structural model. The ultimate experiment, still to be performed, for a detailed underlying texture would be in-situ pulling the ribbons in an electron microscope, preferably SEM.

In collaboration with engineers at UK, we have shown that N-MWCNTs and functionalized N-MWCNTs hold potential to be used as negative electrode for Li-ion batteries. We observed that the Li ion storage capacity depends on microstructure and morphology of these materials. Hence synthetic control in material designs could lead to breakthrough in key energy storage parameters. With SCNs, varying the degree of oxidation may lead to a balance between capacity and cycling stability of the electrode. Also, fabricating nanostructured C-templated electrodes may improve the Li ion capacity associated with carbon and the short cycle life associated with silicon. For example, materials based on a CNT-Si hybrid electrode may combine the advantages of high storage capacity (Si) and long cycle life (C).

REFERENCES

[1] Monthioux M, Kuznetsov VL. Who should be given credit for the discovery of carbon nanotubes? Carbon. 2006;44:1621-3.
[2] Iijima S. Helical microtubules of graphitic carbon. Nature. 1991;354(6348):56-8.
[3] Oberlin A, Endo M, Koyama T. Filamentous growth of carbon through benzene decomposition J Cryst Growth 1976;32(3):335-49.
[4] Dresselhaus MS, Dresselhaus G, Avouris P. Carbon nanotubes : synthesis, structure, properties, and applications. Berlin ; New York: Springer; 2001.
[5] Wei BQ, Vajtai R, Ajayan PM. Reliability and current carrying capacity of carbon nanotubes. Appl Phys Lett. 2001;79(8):1172-4.
[6] Baughman RH, Zakhidov AA, de Heer WA. Carbon Nanotubes--the Route Toward Applications. Science. 2002;297(5582):787-92.
[7] Charlier JC, Blase X, Roche S. Electronic and transport properties of nanotubes. Reviews of Modern Physics. 2007;79(2):677-732.
[8] Keller N, Maksimova NI, Roddatis VV, Schur M, Mestl G, Butenko YV, et al. The catalytic use of onion-like carbon materials for styrene synthesis by oxidative dehydrogenation of ethylbenzene. Angew Chem Int Ed Engl. 2002;41(11):1885-8.
[9] Wagner HD, Vaia RA. Nanocomposites: issues at the interface. Materials Today. 2004;7(11):38-42.
[10] De Volder MFL, Tawfick SH, Baughman RH, Hart AJ. Carbon Nanotubes: Present and Future Commercial Applications. Science. 2013;339(6119):535-9.
[11] Banks CE, Davies TJ, Wildgoose GG, Compton RG. Electrocatalysis at graphite and carbon nanotube modified electrodes: edge-plane sites and tube ends are the reactive sites. Chem Commun. 2005(7):829-41.
[12] Stephan O, Ajayan PM, Colliex C, Redlich P, Lambert JM, Bernier P, et al. Doping Graphitic and Carbon Nanotube Structures with Boron and Nitrogen. Science. 1994;266(5191):1683-5.
[13] Kong J, Zhou CW, Yenilmez E, Dai HJ. Alkaline metal-doped n-type semiconducting nanotubes as quantum dots. Appl Phys Lett. 2000;77(24):3977-9.
[14] Jourdain V, Stephan O, Castignolles M, Loiseau A, Bernier P. Controlling the morphology of multiwalled carbon nanotubes by sequential catalytic growth induced by phosphorus. Adv Mater. 2004;16(5):447-+.
[15] Fagan SB, Mota R, Da Silva AJR, Fazzio A. Substitutional Si doping in deformed carbon nanotubes. Nano Lett. 2004;4(5):975-7.
[16] Lafdi K, Chin A, Ali N, Despres JF. Cobalt-doped carbon nanotubes: Preparation, texture, and magnetic properties. J Appl Phys. 1996;79(8):6007-9.
[17] Glenis S, Nelson AJ, Labes MM. Sulfur doped graphite prepared via arc discharge of carbon rods in the presence of thiophenes. J Appl Phys. 1999;86(8):4464-6.
[18] Jorio A, Dresselhaus G, Dresselhaus MS. Carbon nanotubes : advanced topics in the synthesis, structure, properties, and applications. Berlin ; New York: Springer; 2008.
[19] Miyamoto Y, Cohen ML, Louie SG. Theoretical investigation of graphitic carbon nitride and possible tubule forms. Solid State Commun. 1997;102(8):605-8.

[20] Nevidomskyy AH, Csanyi G, Payne MC. Chemically active substitutional nitrogen impurity in carbon nanotubes. Phys Rev Lett. 2003;91(10).
[21] Liu AY, Wentzcovitch RM. Stability of Carbon Nitride Solids. Phys Rev B. 1994;50(14):10362-5.
[22] Terrones M, Ajayan PM, Banhart F, Blase X, Carroll DL, Charlier JC, et al. N-doping and coalescence of carbon nanotubes: synthesis and electronic properties. Appl Phys A: Mater Sci Process. 2002;74(3):355-61.
[23] Kim DP, Lin CL, Mihalisin T, Heiney P, Labes MM. Electronic-Properties of Nitrogen-Doped Graphite Flakes. Chem Mater. 1991;3(4):686-92.
[24] Maldonado S, Morin S, Stevenson KJ. Structure, composition, and chemical reactivity of carbon nanotubes by selective nitrogen doping. Carbon. 2006;44:1429-37.
[25] Czerw R, Terrones M, Charlier JC, Blase X, Foley B, Kamalakaran R, et al. Identification of Electron Donor States in N-Doped Carbon Nanotubes. Nano Lett. 2001;1:457-60.
[26] Sumpter BG, Meunier V, Romo-Herrera JM, Cruz-Silva E, Cullen DA, Terrones H, et al. Nitrogen-mediated carbon nanotube growth: Diameter reduction, metallicity, bundle dispersability, and bamboo-like structure formation. Acs Nano. 2007;1(4):369-75.
[27] Becker M, Bender H, Jansen M, Kienle L, Assenmacher W. Efficient access to bamboo-like carbon micro and nanofibres by pyrolysis of zinc cyanamide. J Phys Chem Solids. 2001;62(8):1431-3.
[28] Han WQ, Kohler-Redlich P, Seeger T, Ernst F, Rühle M, Grobert N, et al. Aligned CNx nanotubes by pyrolysis of ferrocene/C60 under NH3 atmosphere. Appl Phys Lett. 2000;77:1807-9.
[29] Jang JW, Lee CE, Lyu SC, Lee TJ, Lee CJ. Structural study of nitrogen-doping effects in bamboo-shaped multiwalled carbon nanotubes. Appl Phys Lett. 2004;84(15):2877-9.
[30] Lu Y, Zhu Z, Su D, Wang D, Liu Z, Schlögl R. Formation of bamboo-shape carbon nanotubes by controlled rapid decomposition of picric acid. Carbon. 2004;42:3199-207.
[31] Lee CJ, Park J. Growth model of bamboo-shaped carbon nanotubes by thermal chemical vapor deposition. Appl Phys Lett. 2000;77:3397-9.
[32] Jiang K, Eitan A, Schadler LS, Ajayan PM, Siegel RW, Grobert N, et al. Selective Attachment of Gold Nanoparticles to Nitrogen-Doped Carbon Nanotubes. Nano Lett. 2003;3(3):275-7.
[33] Suenaga K, Johansson MP, Hellgren N, Broitman E, Wallenberg LR, Colliex C, et al. Carbon nitride nanotubulite – densely-packed and well-aligned tubular nanostructures. Chem Phys Lett. 1999;300:695-700.
[34] Le Normand F, Hommet J, Szorenyi T, Fuchs C, Fogarassy E. XPS study of pulsed laser deposited CNx films. Phys Rev B. 2001;64(23).
[35] Choi HC, Park J, Kim B. Distribution and structure of N atoms in multiwalled carbon nanotubes using variable-energy X-ray photoelectron spectroscopy. J Phys Chem B. 2005;109(10):4333-40.
[36] Nath M, Satishkumar BC, Govindaraj A, Vinod CP, Rao CNR. Production of bundles of aligned carbon and carbon–nitrogen nanotubes by the pyrolysis of precursors on silica-supported iron and cobalt catalysts. Chem Phys Lett. 2000;322:333-40.

[37] Lu Y, Zhu ZP, Su DS, Wang D, Liu ZY, Schlogl R. Formation of bamboo-shape carbon nanotubes by controlled rapid decomposition of picric acid. Carbon. 2004;42(15):3199-207.
[38] Saito Y, Yoshikawa T. Bamboo-Shaped Carbon Tube Filled Partially with Nickel. J Cryst Growth. 1993;134(1-2):154-6.
[39] Andrews R, Jacques D, Rao AM, Derbyshire F, Qian D, Fan X, et al. Continuous production of aligned carbon nanotubes: A step closer to commercial realization. Chem Phys Lett. 1999;303(5-6):467-74.
[40] Lee CJ, Lyu SC, Kim HW, Lee JH, Cho KI. Synthesis of bamboo-shaped carbon–nitrogen nanotubes using C2H2–NH3–Fe(CO)5 system. Chem Phys Lett. 2002;359:115-20.
[41] Qian D, Andrews R, Jacques D, Kichambare P, Lian G, Dickey EC. Low-Temperature Synthesis of Large-Area CNx Nanotube Arrays. J Nanosci Nanotech. 2003;3:93-7.
[42] Terrones M, Terrones H, Grobert N, Hsu WK, Zhu YQ, Hare JP, et al. Efficient route to large arrays of CNx nanofibers by pyrolysis of ferrocene/melamine mixtures. Appl Phys Lett. 1999;75:3932-4.
[43] Terrones M, Grobert N, Olivares J, Zhang JP, Terrones H, Kordatos K, et al. Controlled production of aligned-nanotube bundles. Nature. 1997;388(6637):52-5.
[44] Che R, Peng L-M, Chen Q, Duan XF, Gu ZN. Fe2O3 particles encapsulated inside aligned CNx nanotubes Appl Phys Lett. 2003;82:3319-21.
[45] Tang CC, Bando Y, Golberg D, Xu FF. Structure and nitrogen incorporation of carbon nanotubes synthesized by catalytic pyrolysis of dimethylformamide. Carbon. 2004;42(12-13):2625-33.
[46] Wang XB, Hu WP, Liu YQ, Long CF, Xu Y, Zhou SQ, et al. Bamboo-like carbon nanotubes produced by pyrolysis of iron(II) phthalocyanine. Carbon. 2001;39(10):1533-6.
[47] Schaper AK, Hou HQ, Greiner A, Phillipp F. The role of iron carbide in multiwalled carbon nanotube growth. J Catal. 2004;222(1):250-4.
[48] Sun XC, Reyes-Gasga J, Dong XL. Formation and microstructure of carbon encapsulated superparamagnetic Co nanoparticles. Mol Phys. 2002;100(19):3147-50.
[49] Nishitani SR, Ishihara KN, Suzuki RO, Shingu PH. Metastable Solid Solubility Limit of Carbon in the Ni-C System. J Mater Sci Lett. 1985;4(7):872-5.
[50] van Dommele S, Romero-Izquirdo A, Brydson R, de Jong KP, Bitter JH. Tuning nitrogen functionalities in catalytically grown nitrogen-containing carbon nanotubes. Carbon. 2008;46(1):138-48.
[51] Bahr JL, Mickelson ET, Bronikowski MJ, Smalley RE, Tour JM. Dissolution of small diameter single-wall carbon nanotubes in organic solvents? Chem Commun. 2001(2):193-4.
[52] Monthioux M, Smith BW, Burteaux B, Claye A, Fischer JE, Luzzi DE. Sensitivity of single-wall carbon nanotubes to chemical processing: an electron microscopy investigation. Carbon. 2001;39(8):1251-72.
[53] Holzinger M, Vostrowsky O, Hirsch A, Hennrich F, Kappes M, Weiss R, et al. Sidewall functionalization of carbon nanotubes. Angew Chem Int Edit. 2001;40(21):4002-+.
[54] Lim JK, Yun WS, Yoon MH, Lee SK, Kim CH, Kim K, et al. Selective thiolation of single-walled carbon nanotubes. Synthetic Met. 2003;139(2):521-7.
[55] Hamwi A, Alvergnat H, Bonnamy S, Beguin F. Fluorination of carbon nanotubes. Carbon. 1997;35(6):723-8.

[56] Chen J, Hamon MA, Hu H, Chen Y, Rao AM, Eklund PC, et al. Solution Properties of Single-Walled Carbon Nanotubes. Science. 1998;282(5386):95-8.
[57] Stephenson JJ, Sadana AK, Higginbotham AL, Tour JM. Highly Functionalized and Soluble Multiwalled Carbon Nanotubes by Reductive Alkylation and Arylation: The Billups Reaction. Chem Mater. 2006;18:4658-61.
[58] Walker PL. Carbon - an Old but New Material Revisited. Carbon. 1990;28(2-3):261-79.
[59] Bom D, Andrews R, Jacques D, Anthony J, Chen B, Meier MS, et al. Thermogravimetric Analysis of the Oxidation of Multiwalled Carbon Nanotubes: Evidence for the Role of Defect Sites in Carbon Nanotube Chemistry. Nano Lett. 2002;2:615-9.
[60] Belin T, Epron F. Characterization methods of carbon nanotubes: a review. Materials Science and Engineering B. 2005;119(2):105-18.
[61] Wepasnick KA, Smith BA, Bitter JL, Fairbrother DH. Chemical and structural characterization of carbon nanotube surfaces. Analytical and Bioanalytical Chemistry. 2010;396(3):1003-14.
[62] Lambin P, Loiseau A, Culot C, Biró LP. Structure of Carbon Nanotubes Probed by Local and Global Probes. Carbon. 2002;40:1635-48.
[63] Hemraj-Benny T, Wong SS. Silylation of Single-Walled Carbon Nanotubes. Chem Mater. 2006;18(20):4827-39.
[64] Engtrakul C, Davis MF, Gennett T, Dillon AC, Jones KM, Heben MJ. Protonation of Carbon Single-Walled Nanotubes Studied Using 13C and 1H−13C Cross Polarization Nuclear Magnetic Resonance and Raman Spectroscopies. J Am Chem Soc. 2005;127(49):17548-55.
[65] Xiao K, Liu Y, Hu Pa, Yu G, Sun Y, Zhu D. n-Type Field-Effect Transistors Made of an Individual Nitrogen-Doped Multiwalled Carbon Nanotube. Journal of the American Chemical Society. 2005;127(24):8614-7.
[66] Maiyalagan T, Viswanathan B, Varadaraju UV. Nitrogen containing carbon nanotubes as supports for Pt – Alternate anodes for fuel cell applications. Electrochemistry Communications. 2005;7(9):905-12.
[67] Li X, Liu J, Zhang Y, Li Y, Liu H, Meng X, et al. High concentration nitrogen doped carbon nanotube anodes with superior Li+ storage performance for lithium rechargeable battery application. J Power Sources. 2012;197(0):238-45.
[68] Villalpando-Páez F, Romero AH, Muñoz-Sandoval E, Martı, amp, x, et al. Fabrication of vapor and gas sensors using films of aligned CNx nanotubes. Chem Phys Lett. 2004;386(1–3):137-43.
[69] Martin CR, Kohli P. The emerging field of nanotube biotechnology. Nature Reviews Drug Discovery. 2003;2(1):29-37.
[70] Andrews R, Weisenberger MC. Carbon nanotube polymer composites. Current Opinion in Solid State & Materials Science. 2004;8(1):31-7.
[71] Hirsch A, Vostrowsky O. Functionalization of Carbon Nanotubes. Top Curr Chem. 2005;245:193-237.
[72] Meier MS, Andrews R, Jacques D, Cassity KB, Qian D. Tearing Open Nitrogen-Doped Multiwalled Carbon Nanotubes. J Mater Chem. 2008;18:4143-5.
[73] Meier MS, Selegue JP, Cassity KB, Kaur AP, Qian D. Linear and spiral forms of longitudinal cuts in graphitized N-doped multiwalled carbon nanotubes (g-N-MWCNTs) Journal of Physics: Condensed Matter 2010;22(33):334219-24.
[74] Liu J, Rinzler AG, Dai H, Hafner JH, Bradley RK, Boul PJ, et al. Fullerene Pipes. Science. 1998;280(5367):1253-6.

[75] Ziegler KJ, Gu Z, Peng H, Flor EL, Hauge RH, Smalley RE. Controlled Oxidative Cutting of Single-Walled Carbon Nanotubes. J Am Chem Soc. 2005;127(5):1541-7.
[76] Datsyuk V, Kalyva M, Papagelis K, Parthenios J, Tasis D, Siokou A, et al. Chemical oxidation of multiwalled carbon nanotubes. Carbon. 2008;46(6):833-40.
[77] Zhang J, Zou H, Qing Q, Yang Y, Li Q, Liu Z, et al. Effect of Chemical Oxidation on the Structure of Single-Walled Carbon Nanotubes. The Journal of Physical Chemistry B. 2003;107(16):3712-8.
[78] Spitalský Z, Krontiras CA, Georga SN, Galiotis C. Effect of oxidation treatment of multiwalled carbon nanotubes on the mechanical and electrical properties of their epoxy composites. Composites Part A: Applied Science and Manufacturing. 2009;40(6-7):778-83.
[79] Hu C-C, Su J-H, Wen T-C. Modification of multi-walled carbon nanotubes for electric double-layer capacitors: Tube opening and surface functionalization. J Phys Chem Solids. 2007;68(12):2353-62.
[80] Hu H, Zhao B, Itkis ME, Haddon RC. Nitric Acid Purification of Single-Walled Carbon Nanotubes. The Journal of Physical Chemistry B. 2003;107(50):13838-42.
[81] Rosca ID, Watari F, Uo M, Akasaka T. Oxidation of multiwalled carbon nanotubes by nitric acid. Carbon. 2005;43(15):3124-31.
[82] Marshall MW, Popa-Nita S, Shapter JG. Measurement of functionalised carbon nanotube carboxylic acid groups using a simple chemical process. Carbon. 2006;44(7):1137-41.
[83] Kosynkin DV, Higginbotham AL, Sinitskii A, Lomeda JR, Dimiev A, Price BK, et al. Longitudinal unzipping of carbon nanotubes to form graphene nanoribbons. Nature. 2009;458(7240):872-6.
[84] Hiura H, Ebbesen TW, Tanigaki K. Opening and purification of carbon nanotubes in high yields. Adv Mater. 1995;7(3):275-6.
[85] Simmons JM, Nichols BM, Baker SE, Marcus MS, Castellini OM, Lee CS, et al. Effect of ozone oxidation on single-walled carbon nanotubes. J Phys Chem B. 2006;110(14):7113-8.
[86] Balaban TS, Balaban MC, Malik S, Hennrich F, Fischer R, Rösner H, et al. Polyacylation of Single-Walled Carbon Nanotubes under Friedel–Crafts Conditions: An Efficient Method for Functionalizing, Purifying, Decorating, and Linking Carbon Allotropes Adv Mater. 2006;18:2763-7.
[87] Andrews R, Jacques D, Qian D, Dickey EC. Purification and structural annealing of multiwalled carbon nanotubes at graphitization temperatures. Carbon. 2001;39:1681-7.
[88] Pan D, Wang S, Zhao B, Wu M, Zhang H, Wang Y, et al. Li Storage Properties of Disordered Graphene Nanosheets. Chem Mater. 2009;21(14):3136-42.
[89] Shioyama H. The interactions of two chemical species in the interlayer spacing of graphite. Synth Met. 2000;114(1):1-15.
[90] Nalimova VA, Sklovsky DE, Bondarenko GN, AlvergnatGaucher H, Bonnamy S, Beguin F. Lithium interaction with carbon nanotubes. Synth Met. 1997;88(2):89-93.
[91] Koreeda M, Yang W. The Chemistry of 1,2-Dithiins: Synthesis of 1,2-Dithiin and 3,6-Disubstituted 1,2-Dithiins. Synlett. 1994;1994(03):201-3.
[92] Bower C, Kleinhammes A, Wu Y, Zhou O. Intercalation and partial exfoliation of single-walled carbon nanotubes by nitric acid. Chem Phys Lett. 1998;288(2-4):481-6.

[93] Martínez MT, Callejas MA, Benito AM, Cochet M, Seeger T, Ansón A, et al. Sensitivity of single wall carbon nanotubes to oxidative processing: structural modification, intercalation and functionalisation. Carbon. 2003;41(12):2247-56.
[94] Wang YH, Shan HW, Hauge RH, Pasquali M, Smalley RE. A highly selective, one-pot purification method for single-walled carbon nanotubes. J Phys Chem B. 2007;111(6):1249-52.
[95] Zhang H, Guo H, Deng X, Gu P, Chen Z, Jiao Z. Functionalization of multi-walled carbon nanotubes via surface unpaired electrons. Nanotechnology. 2010;21(8).
[96] Cho S, Kikuchi K, Kawasaki A. Radial followed by longitudinal unzipping of multiwalled carbon nanotubes. Carbon. 2011;49(12):3865-72.
[97] Hummers WS, Offeman RE. Preparation of Graphitic Oxide. J Am Chem Soc. 1958;80(6):1339-.
[98] Lerf A, He H, Forster M, Klinowski J. Structure of Graphite Oxide Revisited. The Journal of Physical Chemistry B. 1998;102(23):4477-82.
[99] Novoselov KS, Geim AK, Morozov SV, Jiang D, Zhang Y, Dubonos SV, et al. Electric Field Effect in Atomically Thin Carbon Films. Science. 2004;306(5696):666-9.
[100] Novoselov KS, Jiang D, Schedin F, Booth TJ, Khotkevich VV, Morozov SV, et al. Two-dimensional atomic crystals. Proceedings of the National Academy of Sciences of the United States of America. 2005;102(30):10451-3.
[101] Cano-Márquez AG, Rodriguez-Macias FJ, Campos-Delgado J, Espinosa-González CG, Tristán-López F, Ramirez-González D, et al. Ex-MWNTs: Graphene Sheets and Ribbons Produced by Lithium Intercalation and Exfoliation of Carbon Nanotubes. Nano Lett. 2009;9(4):1527-33.
[102] Tour JM, Kosynkin DV, Lu W, Sinitskii A, Pera G, Sun ZZ. Highly Conductive Graphene Nanoribbons by Longitudinal Splitting of Carbon Nanotubes Using Potassium Vapor. ACS Nano. 2011;5(2):968-74.
[103] Elías AL, Botello-Méndez AR, Meneses-Rodrigues D, Jehová-González V, Ramirez-González D, Ci L, et al. Longitudinal Cutting of Pure and Doped Carbon Nanotubes to Form Graphitic Nanoribbons Using Metal Clusters as Nanoscalpels. Nano Lett. 2010;10:366-72.
[104] Jiao L, Zhang L, Wang X, Diankov G, Dai H. Narrow graphene nanoribbons from carbon nanotubes. Nature. 2009;458(7240):877-80.
[105] Kim K, Sussman A, Zettl A. Graphene Nanoribbons Obtained by Electrically Unwrapping Carbon Nanotubes. ACS Nano. 2010;4(3):1362-6.
[106] Liu Q, Fujigaya T, Nakashima N. Graphene unrolled from ‘cup-stacked’ carbon nanotubes. Carbon. 2012;50(15): 5421-8.
[107] Mohammadi S, Kolahdouz Z, Mohajerzadeh S. Hydrogenation-assisted unzipping of carbon nanotubes to realize graphene nano-sheets. Journal of Materials Chemistry C. 2013;1(7):1309-16.
[108] Paiva MCa, Xu W, Fernanda ProencÌ§a M, Novais RM, LÃ¦gsgaard E, Besenbacher F. Unzipping of Functionalized Multiwall Carbon Nanotubes Induced by STM. Nano Letters.10(5):1764-8.
[109] Shinde DB, Debgupta J, Kushwaha A, Aslam M, Pillai VK. Electrochemical Unzipping of Multi-walled Carbon Nanotubes for Facile Synthesis of High-Quality Graphene Nanoribbons. Journal of the American Chemical Society. 2011;133(12):4168-71.
[110] Terrones M, Botello-Méndez AR, Campos-Delgado J, López-Urías F, Vega-Cantú YI, Rodríguez-Macías FJ, et al. Graphene and graphite nanoribbons:

Morphology, properties, synthesis, defects and applications. Nano Today. 2010;5(4):351-72.
[111] Saito K, Ohtani M, Fukuzumi S. Electron-Transfer Reduction of Cup-Stacked Carbon Nanotubes Affording Cup-Shaped Carbons with Controlled Diameter and Size. J Am Chem Soc. 2006;128:14216-7.
[112] Aslam Z, Nicholls R, Koós A, Nicolosi V, Grobert N. Current-Induced Restructuring and Chemical Modification of N-Doped Multi-walled Carbon Nanotubes. Adv Funct Mater. 2011;21(20):3933-7.
[113] Patrick JW. Porosity in carbons: characterization and applications. New York: Halsted Press; 1995.
[114] Behabtu N, Lomeda JR, Green MJ, Higginbotham AL, Sinitskii A, Kosynkin DV, et al. Spontaneous high-concentration dispersions and liquid crystals of graphene. Nat Nano. 2010;5(6):406-11.
[115] Parra-Vasquez ANG, Behabtu N, Green MJ, Pint CL, Young CC, Schmidt J, et al. Spontaneous Dissolution of Ultralong Single- and Multiwalled Carbon Nanotubes. ACS Nano.4(7):3969-78.
[116] McAllister MJ, Li J-L, Adamson DH, Schniepp HC, Abdala AA, Liu J, et al. Single Sheet Functionalized Graphene by Oxidation and Thermal Expansion of Graphite. Chemistry of Materials. 2007;19(18):4396-404.
[117] Guerard D, Herold A. Intercalation of Lithium into Graphite and other Carbons. Carbon. 1975;13:337-45.
[118] Lin K, Xu Y, He G, Wang X. The Kinetic and Thermodynamic Analysis of Li Ion in Mulit-walled Carbon Nanotubes. Materials Chemistry and Physics. 2006;2006(99):190-6.
[119] Mordkovich VZ, Baxendale M, Chang RPH, Yoshimura S. Intercalation into Carbon Nanotubes without Breaking the Tubular Structure. Synth Met. 1997;86(1):2049-50.
[120] Leroux F, Méténier K, Gautier S, Frackowiak E, Bonnamy S, Béguin F. Electrochemical insertion of lithium in catalytic multi-walled carbon nanotubes. Journal of Power Sources. 1999;81-82:317-22.
[121] Maurin G, Bousquet C, Henn F, Bernier P, Almairac R, Simon B. Electrochemical lithium intercalation into multiwall carbon nanotubes: a micro-Raman study. Solid State Ionics. 2000;136:1295-9.
[122] Scharff P, Alheid H. Ammonia Occlusions in Graphite Cavities. Phys Stat Sol (a). 2000;177:93-7.
[123] Dresselhaus MS, Dresselhaus G. Intercalation Compounds of Graphite. Adv Physics. 2002;51:1-186.
[124] Enoki T, Suzuki M, Endo M. Graphite intercalation compounds and applications. New York: Oxford University Press; 2003.
[125] Berber S, Tomanek D. Stability differences and conversion mechanism between nanotubes and scrolls. Phys Rev B: Condens Matter Mater Phys. 2004;69(23):233404/1-/4.
[126] Kim Y-A, Hayashi T, Naokawa S, Yanagisawa T, Endo M. Comparative study of herringbone and stacked-cup carbon nanofibers. Carbon. 2005;43(14):3005-8.
[127] Endo M, Kim YA, Hayashi T, Fukai Y, Oshida K, Terrones M, et al. Structural characterization of cup-stacked-type nanofibers with an entirely hollow core. Applied Physics Letters. 2002;80(7):1267-9.

[128] Monthioux M, Noe L, Dussault L, Dupin JC, Latorre N, Ubieto T, et al. Texturising and structurising mechanisms of carbon nanofilaments during growth. Journal of Materials Chemistry. 2007;17(43):4611-8.
[129] Cheng H-Y, Zhu Y-A, Sui Z-J, Zhou X-G, Chen D. Modeling of fishbone-type carbon nanofibers with cone-helix structures. Carbon. 2012;50(12):4359-72.
[130] Vera-Agullo J, Varela-Rizo H, Conesa JA, Almansa C, Merino C, Martin-Gullon I. Evidence for growth mechanism and helix-spiral cone structure of stacked-cup carbon nanofibers. Carbon. 2007;45(14):2751-8.
[131] Yang Y, Rosalie J, Bourgeois L, Webley PA. Bulk synthesis of carbon nanostructures: Hollow stacked-cone-helices by chemical vapor deposition. Materials Research Bulletin. 2008;43(8–9):2368-73.
[132] Xu FF, Bando Y, Golberg D. The tubular conical helix of graphitic boron nitride. New Journal of Physics. 2003;5(1):118.
[133] Terrones H, Hayashi T, Muñoz-Navia M, Terrones M, Kim YA, Grobert N, et al. Graphitic cones in palladium catalysed carbon nanofibres. Chemical Physics Letters. 2001;343(3–4):241-50.
[134] Nagaura T, Tozawa K. Prog Batteries Sol Cells. 1990;9:209.
[135] Stura E, Nicolini C. New nanomaterials for light weight lithium batteries. Anal Chim Acta. 2006;568(1–2):57-64.
[136] Armand M, Tarascon JM. Building better batteries. Nature. 2008;451(7179):652-7.
[137] Tarascon JM, Armand M. Issues and challenges facing rechargeable lithium batteries. Nature. 2001;414(6861):359-67.
[138] Landi BJ, Cress CD, Raffaelle RP. High energy density lithium-ion batteries with carbon nanotube anodes. J Mater Res. 2010;25:1636-44.
[139] Ohzuku T, Iwakoshi Y, Sawai K. Formation of Lithium-Graphite Intercalation Compounds in Nonaqueous Electrolytes and Their Application as a Negative Electrode for a Lithium Ion (Shuttlecock) Cell. J Electrochem Soc. 1993;140(9):2490-8.
[140] Huggins RA. Lithium alloy negative electrodes. J Power Sources. 1999;81:13-9.
[141] Laforge B, Levan-Jodin L, Salot R, Billard A. Study of germanium as electrode in thin-film battery. J Electrochem Soc. 2008;155(2):A181-A8.
[142] Yang ZG, Choi D, Kerisit S, Rosso KM, Wang DH, Zhang J, et al. Nanostructures and lithium electrochemical reactivity of lithium titanites and titanium oxides: A review. J Power Sources. 2009;192(2):588-98.
[143] Winter M, Besenhard JO, Spahr ME, Novák P. Insertion Electrode Materials for Rechargeable Lithium Batteries. Adv Mater. 1998;10(10):725-63.
[144] Itou Y, Ukyo Y. Performance of LiNiCoO2 materials for advanced lithium-ion batteries. J Power Sources. 2005;146(1-2):39-44.
[145] Li H, Wang ZX, Chen LQ, Huang XJ. Research on Advanced Materials for Li-ion Batteries. Adv Mater. 2009;21(45):4593-607.
[146] Goodenough JB, Kim Y. Challenges for Rechargeable Li Batteries. Chem Mater. 2010;22(3):587-603.
[147] Whittingham MS. Lithium batteries and cathode materials. Chem Rev. 2004;104(10):4271-301.
[148] Xu K. Nonaqueous Liquid Electrolytes for Lithium-Based Rechargeable Batteries. Chem Rev. 2004;104(10):4303-418.
[149] Ragone DV. Review of Battery Systems for Electrically Powered Vehicles. Sae Transactions. 1968;77:131-&.

[150] Schalkwijk WAv, Scrosati B. Advances in lithium-ion batteries. New York, NY: Kluwer Academic/Plenum Publishers; 2002.
[151] Nazri G, Pistoia G. Lithium batteries : science and technology. Boston: Kluwer Academic Publishers; 2004.
[152] Arico AS, Bruce P, Scrosati B, Tarascon J-M, van Schalkwijk W. Nanostructured materials for advanced energy conversion and storage devices. Nat Mater. 2005;4(5):366-77.
[153] Bruce PG, Scrosati B, Tarascon J-M. Nanomaterials for Rechargeable Lithium Batteries. Angew Chem Int Ed. 2008;47(16):2930-46.
[154] Guo Y-G, Hu J-S, Wan L-J. Nanostructured Materials for Electrochemical Energy Conversion and Storage Devices. Adv Mater. 2008;20(15):2878-87.
[155] Harris PJF. Carbon nanotube science : synthesis, properties and applications. Rev. and updated ed. Cambridge, UK ; New York: Cambridge University Press; 2009.
[156] Centi G, Perathoner S. Carbon Nanotubes for Sustainable Energy Applications. ChemSusChem. 2011;4(7):913-25.
[157] Che G, Lakshmi BB, Fisher ER, Martin CR. Carbon nanotubule membranes for electrochemical energy storage and production. Nature. 1998;393(6683):346.
[158] Esplandiu MJ, Pacios M, Bellido E, Valle Md. Carbon Nanotubes and Electrochemistry. Z Phys Chem. 2007;221(9-10):1161-73.
[159] Frackowiak E, Béguin F. Electrochemical storage of energy in carbon nanotubes and nanostructured carbons. Carbon. 2002;40(10):1775-87.
[160] Frackowiak E, Gautier S, Gaucher H, Bonnamy S, Beguin F. Electrochemical storage of lithium in multiwalled carbon nanotubes. Carbon. 1999;37(1):61-9.
[161] Landi BJ, Ganter MJ, Cress CD, DiLeo RA, Raffaelle RP. Carbon nanotubes for lithium ion batteries. Energy & Environmental Science. 2009;2(6):638-54.
[162] Shin H-C, Liu M, Sadanadan B, Rao AM. Electrochemical insertion of lithium into multi-walled carbon nanotubes prepared by catalytic decomposition. J Power Sources. 2002;112(1):216-21.
[163] Wang GX, Ahn J-h, Yao J, Lindsay M, Liu HK, Dou SX. Preparation and characterization of carbon nanotubes for energy storage. J Power Sources. 2003;119–121(0):16-23.
[164] Yang Z-h, Wu H-q. Electrochemical intercalation of lithium into carbon nanotubes. Solid State Ionics. 2001;143(2):173-80.
[165] Landi BJ, Dileo RA, Schauerman CM, Cress CD, Ganter MJ, Raffaelle RP. Multi-Walled Carbon Nanotube Paper Anodes for Lithium Ion Batteries. Journal of Nanoscience and Nanotechnology. 2009;9(6):3406-10.
[166] Landi BJ, Raffaelle RP, Heben MJ, Alleman JL, VanDerveer W, Gennett T. Single Wall Carbon Nanotube−Nafion Composite Actuators. Nano Lett. 2002;2(11):1329-32.
[167] Li X, Kang F, Bai X, Shen W. A novel network composite cathode of LiFePO4/multiwalled carbon nanotubes with high rate capability for lithium ion batteries. Electrochem Commun. 2007;9(4):663-6.
[168] Li X, Kang F, Shen W. A Comparative Investigation on Multiwalled Carbon Nanotubes and Carbon Black as Conducting Additive in LiNi[sub 0.7]Co[sub 0.3]O[sub 2]. Electrochem Solid-State Lett. 2006;9(3):A126-A9.
[169] Garau C, Frontera A, Quiñonero D, Costa A, Ballester P, Deyà PM. Lithium diffusion in single-walled carbon nanotubes: a theoretical study. Chem Phys Lett. 2003;374(5–6):548-55.

[170] Nishidate K, Hasegawa M. Energetics of lithium ion adsorption on defective carbon nanotubes. Phys Rev B. 2005;71(24):245418.
[171] Song B, Yang J, Zhao J, Fang H. Intercalation and diffusion of lithium ions in a carbon nanotube bundle by ab initio molecular dynamics simulations. Energy & Environmental Science. 2011;4(4).
[172] Lin K, Xu Y, He G, Wang X. The kinetic and thermodynamic analysis of Li ion in multi-walled carbon nanotubes. Mater Chem Phys. 2006;99(2–3):190-6.
[173] Zhao M, Xia Y, Mei L. Diffusion and condensation of lithium atoms in single-walled carbon nanotubes. Phys Rev B. 2005;71(16):165413.
[174] Liu Y, Zheng H, Liu XH, Huang S, Zhu T, Wang J, et al. Lithiation-Induced Embrittlement of Multiwalled Carbon Nanotubes. ACS Nano. 2011;5(9):7245-53.
[175] Eom JY, Kwon HS, Liu J, Zhou O. Lithium insertion into purified and etched multi-walled carbon nanotubes synthesized on supported catalysts by thermal CVD. Carbon. 2004;42(12–13):2589-96.
[176] Wang XX, Wang JN, Chang H, Zhang YF. Preparation of Short Carbon Nanotubes and Application as an Electrode Material in Li-Ion Batteries. Adv Funct Mater. 2007;17(17):3613-8.
[177] Wang XX, Wang JN, Su LF. Preparation and electrochemical performance of ultra-short carbon nanotubes. J Power Sources. 2009;186(1):194-200.
[178] Welna DT, Qu L, Taylor BE, Dai L, Durstock MF. Vertically aligned carbon nanotube electrodes for lithium-ion batteries. J Power Sources. 2011;196(3):1455-60.
[179] Zhang H, Cao G, Yang Y. Carbon nanotube arrays and their composites for electrochemical capacitors and lithium-ion batteries. Energy & Environmental Science. 2009;2(9).
[180] Zhang H, Cao G, Wang Z, Yang Y, Shi Z, Gu Z. Carbon nanotube array anodes for high-rate Li-ion batteries. Electrochim Acta. 2010;55(8):2873-7.
[181] Zhao J, Gao QY, Gu C, Yang Y. Preparation of multi-walled carbon nanotube array electrodes and its electrochemical intercalation behavior of Li ions. Chem Phys Lett. 2002;358(1–2):77-82.
[182] Flandrois S, Simon B. Carbon materials for lithium-ion rechargeable batteries. Carbon. 1999;37(2):165-80.
[183] Mukhopadhyay I, Hoshino N, Kawasaki S, Okino F, Hsu WK, Touhara H. Electrochemical Li Insertion in B-Doped Multiwall Carbon Nanotubes. J Electrochem Soc. 2002;149(1):A39-A44.
[184] Zhong DY, Zhang GY, Liu S, Wang EG, Wang Q, Li H, et al. Lithium storage in polymerized carbon nitride nanobells. Appl Phys Lett. 2001;79(21):3500-2.
[185] Wang Q, Li H, Chen L, Huang X, Zhong D, Wang E. Investigation of Lithium Storage in Bamboo-like CNTs by HRTEM. J Electrochem Soc. 2003;150(9):A1281-A6.
[186] Shanmugam S, Gedanken A. Electrochemical properties of bamboo-shaped multiwalled carbon nanotubes generated by solid state pyrolysis. Electrochem Commun. 2006;8(7):1099-105.
[187] Zou L, Lv R, Kang F, Gan L, Shen W. Preparation and application of bamboo-like carbon nanotubes in lithium ion batteries. J Power Sources. 2008;184(2):566-9.
[188] Bulusheva LG, Okotrub AV, Kurenya AG, Zhang H, Zhang H, Chen X, et al. Electrochemical properties of nitrogen-doped carbon nanotube anode in Li-ion batteries. Carbon. 2011;49(12):4013-23.
[189] Li XL, Du K, Huang JM, Kang FY, Shen WC. Effect of carbon nanotubes on the anode performance of natural graphite for lithium ion batteries. J Phys Chem Solids. 2010;71(4):457-9.

[190] Liu X-M, Huang Zd, Oh Sw, Zhang B, Ma P-C, Yuen MMF, et al. Carbon nanotube (CNT)-based composites as electrode material for rechargeable Li-ion batteries: A review. Compos Sci Technol. 2012;72(2):121-44.
[191] Maurin G, Henn F, Simon B, Colomer JF, Nagy JB. Lithium Doping of Multiwalled Carbon Nanotubes Produced by Catalytic Decomposition. Nano Lett. 2001;1(2):75-9.
[192] Wu GT, Wang CS, Zhang XB, Yang HS, Qi ZF, He PM, et al. Structure and Lithium Insertion Properties of Carbon Nanotubes. J Electrochem Soc. 1999;146(5):1696-701.
[193] Peled E, Menachem C, Bar-Tow D, Melman A. Improved Graphite Anode for Lithium-Ion Batteries Chemically. J Electrochem Soc. 1996;143(1):L4-L7.
[194] Klink S, Ventosa E, Xia W, La Mantia F, Muhler M, Schuhmann W. Tailoring of CNT surface oxygen groups by gas-phase oxidation and its implications for lithium ion batteries. Electrochem Commun. 2012;15(1):10-3.
[195] Stournara ME, Shenoy VB. Enhanced Li capacity at high lithiation potentials in graphene oxide. J Power Sources. 2011;196(13):5697-703.
[196] Le Gall T, Reiman KH, Grossel MC, Owen JR. Poly(2,5-dihydroxy-1,4-benzoquinone-3,6-methylene): a new organic polymer as positive electrode material for rechargeable lithium batteries. J Power Sources. 2003;119–121(0):316-20.
[197] Chen H, Armand M, Demailly G, Dolhem F, Poizot P, Tarascon J-M. From Biomass to a Renewable LiXC6O6 Organic Electrode for Sustainable Li-Ion Batteries. ChemSusChem. 2008;1(4):348-55.
[198] Li J-X, Zhao Y, Guan L-H. Lithium storage in single-walled carbon nanotubes. Electrochem Commun. 2010;12(4):592-5.
[199] Li H-Q, Liu R-L, Zhao D-Y, Xia Y-Y. Electrochemical properties of an ordered mesoporous carbon prepared by direct tri-constituent co-assembly. Carbon. 2007;45(13):2628-35.
[200] Hu YS, Adelhelm P, Smarsly BM, Hore S, Antonietti M, Maier J. Synthesis of Hierarchically Porous Carbon Monoliths with Highly Ordered Microstructure and Their Application in Rechargeable Lithium Batteries with High-Rate Capability. Adv Funct Mater. 2007;17(12):1873-8.
[201] Deng D, Lee JY. One-Step Synthesis of Polycrystalline Carbon Nanofibers with Periodic Dome-Shaped Interiors and Their Reversible Lithium-Ion Storage Properties. Chem Mater. 2007;19(17):4198-204.
[202] Tien B, Xu M, Liu J. Synthesis and electrochemical characterization of carbon spheres as anode material for lithium-ion battery. Mater Lett. 2010;64(13):1465-7.
[203] Li G, Xu L, Hao Q, Wang M, Qian Y. Synthesis, characterization and application of carbon nanocages as anode materials for high-performance lithium-ion batteries. RSC Advances. 2012;2(1):284-91.
[204] Bhardwaj T, Antic A, Pavan B, Barone V, Fahlman BD. Enhanced Electrochemical Lithium Storage by Graphene Nanoribbons. J Am Chem Soc. 2010;132(36):12556-8.
[205] Menachem C, Peled E, Burstein L, Rosenberg Y. Characterization of modified NG7 graphite as an improved anode for lithium-ion batteries. J Power Sources. 1997;68(2):277-82.
[206] Xiang HQ, Fang SB, Jiang YY. Carbonaceous anodes for lithium-ion batteries prepared from phenolic resins with different cross-linking densities. J Electrochem Soc. 1997;144(7):L187-L90.
[207] Sato K, Noguchi M, Demachi A, Oki N, Endo M. A Mechanism of Lithium Storage in Disordered Carbons. Science. 1994;264(5158):556-8.

[208] Yata S, Kinoshita H, Komori M, Ando N, Kashiwamura T, Harada T, et al. Structure and Properties of Deeply Li-Doped Polyacenic Semiconductor-Materials Beyond C6li Stage. Synth Met. 1994;62(2):153-8.
[209] Zheng T, Xue JS, Dahn JR. Lithium insertion in hydrogen-containing carbonaceous materials. Chem Mater. 1996;8(2):389-93.
[210] Yazami R, Deschamps M. The Carbon-Lithium Negative Electrode for Lithium-Ion Batteries in Polymer Electrolyte. MRS Online Proceedings Library. 1994;369:165.
[211] Zhou H, Zhu S, Hibino M, Honma I, Ichihara M. Lithium Storage in Ordered Mesoporous Carbon (CMK-3) with High Reversible Specific Energy Capacity and Good Cycling Performance. Adv Mater. 2003;15(24):2107-11.
[212] Zheng T, Liu YH, Fuller EW, Tseng S, Vonsacken U, Dahn JR. Lithium Insertion in High-Capacity Carbonaceous Materials. J Electrochem Soc. 1995;142(8):2581-90.
[213] Xue JS, Dahn JR. Dramatic Effect of Oxidation on Lithium Insertion in Carbons Made from Epoxy-Resins. J Electrochem Soc. 1995;142(11):3668-77.
[214] Sonobe NI, T.; Masuko, J. carbonaceous electrode material for secondary battery and process for production thereof. US Patent. 1996;5 527 643.
[215] Warren BE. X-Ray Diffraction in Random Layer Lattices. Physical Review. 1941;59(9):693-8.
[216] Cancado LG, Takai K, Enoki T, Endo M, Kim YA, Mizusaki H, et al. General equation for the determination of the crystallite size L[sub a] of nanographite by Raman spectroscopy. Appl Phys Lett. 2006;88(16):163106.
[217] Endo M, Nishimura Y, Takahashi T, Takeuchi K, Dresselhaus MS. Lithium storage behavior for various kinds of carbon anodes in Li ion secondary battery. J Phys Chem Solids. 1996;57(6–8):725-8.
[218] Inagaki M, Iwashita N, Hishiyama Y. Criteria for the Intercalation of Sulfuric Acid. Molecular Crystals and Liquid Crystals Science and Technology Section A Molecular Crystals and Liquid Crystals. 1994;244(1):89-94.
[219] Wang Q, Li H, Huang X, Chen L. Determination of Chemical Diffusion Coefficient of Lithium Ion in Graphitized Mesocarbon Microbeads with Potential Relaxation Technique. J Electrochem Soc. 2001;148(7):A737-A41.
[220] Levi MD, Aurbach D. Diffusion Coefficients of Lithium Ions during Intercalation into Graphite Derived from the Simultaneous Measurements and Modeling of Electrochemical Impedance and Potentiostatic Intermittent Titration Characteristics of Thin Graphite Electrodes. The Journal of Physical Chemistry B. 1997;101(23):4641-7.
[221] Guo B, Wang X, Fulvio PF, Chi M, Mahurin SM, Sun X-G, et al. Soft-Templated Mesoporous Carbon-Carbon Nanotube Composites for High Performance Lithium-ion Batteries. Adv Mater. 2011;23(40):4661-6.

VITA

Aman Preet Kaur

EDUCATION:

Master of Science (H.S.) (2004-2006), Organic Chemistry, Panjab University, Chandigarh, India

Bachelor of Science (H.S.) (2001-2004), Chemistry, Panjab University, Chandigarh, India

SERVICE/LEADERSHIP RESPONSIBILITIES:

Laboratory chemical inventory coordinator, 2010-present

Laboratory safety coordinator, 2010-present

PROFESSIONAL AFFILIATIONS:

Student Member, American Chemical Society

Student Member, Material Research Society

Treasurer, UK-MRS chapter, 2010-11

FELLOWSHIPS, HONORS AND AWARDS:

Awarded Kentucky Opportunity Fellowship for 2008-09

Outstanding Teaching Assistant Award, Department of Chemistry, UK for 2010-11

100% plus research award, Department of Chemistry, UK

PUBLICATIONS & PRESENTATIONS

Publications

Meier, M. S.; Selegue, J. P.; Cassity, K. B.; Kaur, A.; Qian, D. *Journal of Physics: Condensed Matter* 2010, *22,* 334219.

Harman-Ware, A. E.; Crocker, M.; Kaur, A.; Meier, M. S.; Kato, D.; Lynn, B. *Journal of Analytical and Applied Pyrolysis* 2013, *99,* 161.

Kaur, A.; Meier, M. S.; Andrews, R.; Qian, D. Discontinuous spiraled carbon nanoribbons resulting from coiling of thin
graphite subunits formed during oxidation of N-doped multiwalled carbon nanotubes (*Carbon,* in Press).

Kaur, A.; Li, J.; Meier, M. S.; Cheng, Y.-T. Relation between the microstructure and lithium storage of MWCNTs (in preparation).

Patil, N.; Kaur, A.; Meier, M. S. Oxidative deconstruction of lignin model compounds (in preparation).

Contributed presentations

Kentucky Academy of Science, Annual Meeting 2008, University of Kentucky, Lexington, KY – Oral presentation

Kentucky Academy of Science, Annual Meeting 2009, Northern Kentucky University, Highland Heights, Lexington, KY – Oral presetation

CARBON 2010, International Carbon Conference, Clemson University, Clemson, SC – Oral presetation

ACS National Meeting, Spring 2012, San Diego, CA – Oral presetation

MRS meeting, Fall 2012, Boston, MA – co-author